Studies of transverse properties of relativistic electrons from laser wakefield accelerator

by
Grace Gloria Manahan

A thesis presented in the fulfilment of the requirements for the degree of Doctor of Philosophy in Physics.
Physics Department, University of Strathclyde

Supervisors:
Prof. Dino A. Jaroszynski
Dr. Enrico Brunetti

2013

Signed:
Date:

Abstract

Laser wakefield acceleration (LWFA) can occur when the ponderomotive force of high power ultra short laser pulses produce wakefields in underdense plasma. The structure of these wakefields are similar to those in rf cavities of conventional linear accelerators, but are characterised by large fields that can accelerate particles to high energies over much shorter distances. Compactness and inherent short bunch duration make LWFAs potential candidates for laboratory-scale coherent radiation sources. Currently, theoretical and experimental studies are being pursued to obtain in-depth understanding of LWFAs, in particular the injection mechanisms, as these will lead to better control and improved quality of the electron beams. Experimental effort is being directed towards the design of suitable diagnostics to measure the most important properties of the electron beam, one of which is the emittance. Emittance is a good figure of merit as it describes the beam distribution in phase space and provides information on the beam focusability.

This work presents a numerical and experimental study of the potential of LWFA as a next generation table-top accelerator. The first part of the thesis investigates the transport of LWFA produced electron beams using conventional devices. To provide a "usable" beam, the transport system should be capable of preserving the transverse emittance. Possible sources of emittance growth are examined, focusing on the effects of energy spread, divergence and pointing stability on the emittance. The second part of the thesis presents direct single shot measurements of the transverse emittance using the pepper-pot technique. This method is also used to quantify the performance of high-gradient miniature permanent quadrupoles.

Acknowledgement

The completion of my Ph. D. career will not be possible without the help of the following:

- Prof. Dino Jaroszynski, for accepting me as his student, for letting me explore the wonders of Laser Wakefield Acceleration and for helping me in my research career.
- Dr. Enrico Brunetti for being my mentor and my good friend, for constantly encouraging me to be at my best, for the valuable discussions and great ideas to improve my Ph. D. project, for sharing his great mind about Python and GEANT4 and for editing my manuscript.
- The thesis examiners, Dr. Yuri Saveliev and Dr. Wenlong Hu for fruitful discussions and helpful insights in improving my manuscript.
- Dr. Gregor Welsh and Dr. Riju Issac for extending their expertise on laser system and helping us in experimental works.
- Dr. Mark Wiggins for designing and constructing the pepperpot mask for emittance measurements and great inputs to improve my experiments.
- Constantin Aniculaesei (my lab partner), Maria Pia Anania (my trainer), Dr. Silvia Cipiccia (my motivator), Ania Subiel (my sista) and David Grant (my stress absorber) for being my everyday companions in the experiments and even staying late just to obtain enough data.
- David Clark and Tom McCanny for the technical support.
- The theoretical group of SILIS, particularly Dr. Bernhard Ernsfeld and Dr. Ranaul Islam for the valuable theoretical discussions and providing the PIC simulation used in this thesis.
- My colleagues of the SILIS group, who are not mentioned by name, for the fruitful discussions.
- My family for their moral guidance and Daniele for selfless support in my Glasgow adventure.

My sincerest gratitude to all.

Role of the author

The numerical simulations presented in this thesis were designed by the author with the supervision of Dr. Enrico Brunetti. The experiments were performed by the author with the help of Constantin Aniculaesei. The experimental setup and data obtained by the first emittance measurements (first part of Chapter 4) were from Dr. Richard Shank, while the design of pepperpot mask with the quadrupoles was from the author. Calculation of the emittance and all of the data analysis were done by the author, with constant supervision of Dr. Enrico Brunetti. The mask used in the pepperpot experiments was designed and constructed by Dr. Mark Wiggins, while the installation of the permanent quadrupoles is courtesy of Maria Pia Anania.

List of Publications

1. **G. G. Manahan**, E. Brunetti, C. Aniculaesei, M. P. Anania, S. Cipiccia, R. C. Issac, M. R. Islam, B. Ersfeld, G. H. Welsh, S. M. Wiggins, and D. A. Jaroszynski, "Characterisation of laser-driven electron beams with a permanent quadrupole triplet and pepper-pot mask", *in preparation.*

2. E. Brunetti, **G. G. Manahan**, R. P. Shanks, M. R. Islam, B. Ersfeld, M. P. Anania, S. Cipiccia, R. C. Issac, G. Vieux, G. H. Welsh, S. M. Wiggins and D. A. Jaroszynski, "Characterisation of electron beams from laser-driven particle accelerators", in AIP Conference Proceedings (2012).

3. **G. G. Manahan**, E. Brunetti, R.P. Shanks, M.R. Islam, B. Ersfeld, M.P. Anania, S. Cipiccia, R.C. Issac, G. Raj, G. Vieux, G.H. Welsh, S.M. Wiggins, and D.A. Jaroszynski, "High resolution, single shot emittance measurement of relativistic electrons from laser-driven accelerator", in Proc. SPIE 8079 (Prague, Czech Republic, 2011), pp. 807909-807909-6.

4. **G. G. Manahan**, M.P. Anania, C. Aniculaesei, E. Brunetti, S. Cipiccia, B. Ersfeld, M.R. Islam, R.C.Issac, R.P. Shanks, G.H. Welsh, S.M. Wiggins and D.A. Jaroszynski "Emittance and energy spread measurements of relativistic electrons from laser-driven accelerators", Proc. DIPAC (Hamburg, Germany, 2011).

5. S. M. Wiggins, R. C. Issac, G. H. Welsh, E. Brunetti, R. P. Shanks, M. P. Anania, S. Cipiccia, **G. G. Manahan**, C. Aniculaesei, B. Ersfeld, M. R. Islam, R. T. L. Burgess, G. Vieux, W. A. Gillespie, A. M. MacLeod, S. B. van der Geer, M. J. de Loos, and D. A. Jaroszynski,"High quality electron beams from a laser wakefield accelerator", Plasma Phys. Control. Fusion 52, 124032 (2010).

6. E. Brunetti, R. P. Shanks, **G. G. Manahan**, M. R. Islam, B. Ersfeld, M. P. Anania, S. Cipiccia, R. C. Issac, G. Raj, G. Vieux, G. H. Welsh, S. M. Wiggins, and D. A. Jaroszynski, "Low emittance, high brilliance relativistic electron beams from a laser-plasma accelerator", Phys. Rev. Lett. 105, 215007 (2010).

Contents

Chapter 1

Introduction

Particle accelerators are of great interest in many fields of science both for fundamental research and practical applications. For instance, high-energy charged particle beams are used in studying the basic structure of matter. One of the largest sources of high-energy particles is the Large Hadron Collider (LHC) at CERN, which aims to validate fundamental laws of particle physics, one of which is the existence of elementary particles like the Higgs boson. High-energy electrons are also capable of emitting coherent synchrotron and gamma radiation as well as driving free electron lasers [1–3]. These types of radiation sources are in demand for possible applications in medical imaging and radiation therapy [4, 5].

One well established conventional accelerator design is the linear accelerator (linac), which is capable of generating high energy electron beams without changing the beam propagation direction. They use large potential differences to extract particles from a cathode, e.g. radio frequency (rf) electron guns, into an accelerating (high) vacuum chamber, which consists of resonant cavities, to produce strong electric fields. These electric fields are then responsible for accelerating particles to high energies.

In conventional rf linacs, the maximum energy is approximately proportional to the size of the resonant cavities, which results in very long accelerators. The accelerating fields are limited by breakdown of the chamber walls, which occurs around 100 MV/m. To date, the longest rf linac is the Stanford Linear Accelerator, where electrons are accelerated up to 50 GeV over a distance of 3.2 km. Since the energy is approximately proportional to the length of the chamber, so is the cost to build it. Moreover, the size of the infrastructures limits the possible locations where they can be built. Clearly, there is a need to develop new sources of charged particles which are less expensive and more compact.

T. Tajima and J.M. Dawson conceptualized the laser-plasma electron accelerator in 1979 [6]. They proposed using the large collective forces from an intense laser to excite plasma waves known as the "wakefields." Plasma offers many advantages as compared with conventional rf linacs. For one, ideally, there is no need for external injectors as plasma is itself a good source of electrons. Moreover, the accelerating field gradient from the wakefield, E, depends on the plasma

density, n_e (i.e. $E[\mathrm{V/m}] \simeq 96\sqrt{n_e\,[\mathrm{cm}^{-3}]}$) and can exceed by two to three order of magnitudes than the fields achievable with conventional rf linacs. For instance, a plasma with $n_e = 10^{18}$ cm^{-3} can sustain a field of $\sim 96\,\mathrm{GV/m}$, without breakdown. Since the acceleration length is determined by the plasma density, it is possible to realise compact, small-scale accelerators. Ref [6] predicted that the maximum electron energy for a 1 cm single-stage, plasma accelerator can reach GeV scale. Since then many researchers have shown interest in the possibility of using plasma-based accelerators as small-scale table-top particle accelerators. The rapid progress in this field for over three decades follows the advances in laser technology. Today, state of the art laser facilities are able to deliver high power ($\sim$ TW) and ultra short ($\sim$ fs) pulses by employing the chirped pulse amplification (CPA) technique, pioneered by G. Mourou and D. Strickland in 1985 [7]. In CPA, the pulse is temporally and spectrally stretched (typically by using a grating) before the amplification.

There are many ways to create wakefields. In the self-modulated laser wakefield acceleration, a laser with long pulse duration is used as a driver and the plasma modulates the laser amplitude to transform it into a train of short pulses. It is also possible to use two long laser pulses with different frequencies to excite a wakefield, a scheme known as the plasma beat wave accelerator. On the other hand, when an ultra-short laser is used as driver for the wakefield, the process is called laser wakefield acceleration (LWFA). A big drawback of plasma-based accelerators is their vulnerability to laser-plasma instabilities. However, most of these instabilities develop in time scales slower than the LWFA (which is in the order of the plasma frequency). Therefore, LWFA offers an advantage over other plasma-based acceleration methods in terms of plasma stability and it has been shown to be a viable candidate for the development of the next generation of radiation sources [8–10]. However, the future of LWFAs can only be realised if they can be controlled to produce high quality electron beams with characteristics such as low divergence, small energy spread and high charge. It is therefore important to study the properties of laser-produced electron beams and establish a link with the physical processes occurring in the interaction between high power lasers and plasma.

Towards a high-quality electron beam

A typical experimental setup for laser wakefield acceleration is illustrated in Figure 1.1, where an intense ultra-short laser is focused into plasma and the ac-

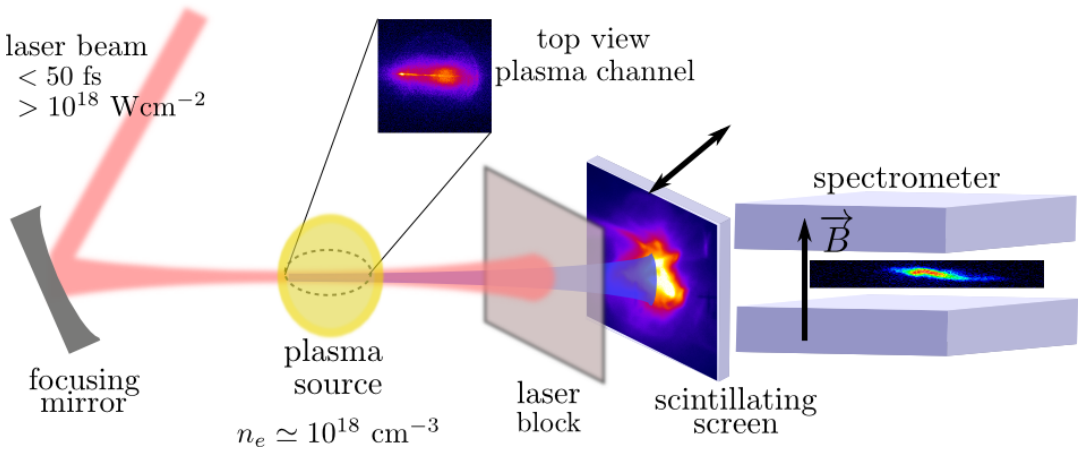

Figure 1.1: Typical set-up for laser-plasma electron acceleration. The laser beam is focused into plasma. The accelerated electrons are detected using removable scintillating screens. Electron energy is measured using dipole magnets coupled to scintillating screens. A laser beam block is usually placed before the diagnostics to prevent damages of optical detectors.

celerated electron beam propagates downstream to diagnostics and applications. Helium is the usual gas target, which is fully ionised by the leading edge of the laser, creating a plasma that is exposed to the full laser intensity.

The first evidences of electron acceleration from laser-induced plasma waves were obtained using external injection [11] and self-injection from picosecond [12] and femtosecond [13] lasers, where accelerating gradients of the order of 100 GV/m were obtained. However, the electron beam had poor quality. Although the estimated charge is high ($\simeq$ 1 nC), the number of electrons decreases exponentially as the energy increases, resulting in large energy spread. Most of the charge is in energies below 50 MeV with angular spread greater than 8 – 10 mrad and estimated transverse emittance of $\sim 5\,\pi$ mm mrad. These parameters are quite far from what is routinely achievable using conventional rf linacs.

One of the most important milestones in LWFA was obtained in 2004 when three different groups (including a University of Strathclyde led group - ALPHA-X) observed quasi-monoenergetic electron beams (80 – 170 MeV) by focusing intense ($\sim$10 TW), ultra short ($<$ 60 fs) lasers onto the edge of underdense plasma, thereby reaching the blow-out or bubble regime [14–16] discussed in Section 1.1.6. Plasma channels 2–3 mm long were created and self-injected electrons were accelerated. Since then, there has been further progress in LWFAs using lasers with powers up to 100–200 TW, improving the electron beam quality. Other plasma targets such as gas-filled capillary discharge waveguides and gas cells have enabled to increase the maximum electron energy by extending the interaction length in

comparison with gas jets. Today, energies in the range of ~ 0.2 – 1 GeV with charges up to < 100 pC are achieved [17–20]. However, it is very challenging to improve several electron beam parameters at the same time. Electron energies greater than 1 GeV suffer from poor reproducibility. The shot-to-shot energy and pointing fluctuations have been improved only at low energies. These quality issues arise from the fact that electron self-injection and acceleration in the bubble regime are combinations of many complex nonlinear processes that are hard to control. Moreover, the process of stopping the injection is still not well understood and therefore the overall energy spread is large. Recently, energy spreads down to 5 % for a 0.46 GeV electron beams were obtained using two-stage acceleration, where electrons are first produced in a shorter gas cell and then accelerated using a second longer gas cell [20]. However, simulations show that the staging mechanism can induce transverse emittance growth of one to two orders of magnitude during injection if the electron beam properties are not properly matched to the wakefield properties [21, 22].

Transverse beam emittance

The transverse properties of an electron beam can be quantified using the emittance, which measures the volume occupied by the particle distribution in phase space and which will be discussed in detail in Chapter 2. A low emittance value indicates a beam where electrons move along trajectories characterised by a high level of parallelism. The beam is therefore well-focused and capable of driving high quality radiation sources. Different measurements of transverse emittance of beams accelerated in the bubble regime have been carried out. The first direct measurements were provided in [23–25], using the pepper-pot technique. Here, transverse emittances of the order of $> 1\,\pi$ mm mrad are achieved limited by the experimental resolution. However, very recently, more accurate measurements have shown that LWFA can indeed produce emittances less than $1\,\pi$ mm mrad [26–28].

Objectives and coverage

This thesis aims to investigate the possibility of using electron beams from LWFAs as drivers of compact accelerators. In particular, this work focuses on diagnostics to characterise the transverse quality of the electron beam by measuring the emittance before and after passing through a focusing (transport) device. Numerical studies on the transport of electron beams using conventional devices will

be presented to understand the possible sources of emittance growth.

The first chapter briefly discusses the theoretical foundations of laser wakefield acceleration (LWFA), presenting the linear, 1D nonlinear and 3D nonlinear (bubble) regimes. With the support of the high power laser community, LWFAs are able to operate in the bubble regime, which has the potential of generating high-quality electrons despite challenges such as control of the injection mechanism.

In order to use LWFAs as drivers for many applications, transport systems are required. Chapter 2 discusses the transport of laser-produced electron beams along a simple beamline based on the current design of the ALPHA-X accelerator at the University of Strathclyde.

Chapter 3 describes the ALPHA-X laser system, electron beam diagnostics and experimental methods used for accelerating and optimising the electrons. Measurements of electron beams produced at the ALPHA-X accelerators are also discussed.

Chapter 4 and 5 present transverse emittance measurements using the pepper-pot technique and show that focusing elements do not degrade the quality of the electron beam. Moreover, an alternative diagnostic for simultaneous measurement of electron transverse emittance and energy spectrum in a single shot is discussed. Evidence of structured electron beams is also reported.

1.1 Theory of laser-wakefield acceleration

The experiments performed in this thesis are all based on LWFA. Depending on the laser intensity, different behaviours and properties of the accelerated electrons will be observed. Understanding the physics behind laser-plasma interaction helps experimentalists to improve the quality of the accelerated electrons.

This section discusses the theoretical foundations of laser-wakefield acceleration. General properties of lasers and plasmas are first presented. Excitation of plasma waves and electron injection are then described for linear, 1D nonlinear and 3D nonlinear (bubble) regimes. This chapter is mainly based on Ref. [29,30].

1.1.1 Plasma

Plasma is an ionised gas consisting of freely moving electrons and ions. The total charge of electrons and ions is ideally the same, making the plasma quasi-neutral.

Characteristics

Plasma is capable of screening an external electric field within a distance known as the Debye length, λ_D, which is given by

$$\lambda_D = \sqrt{\frac{k_B T}{4\pi n_e e^2}}\,, \tag{1.1}$$

where T and n_e are the temperature and density of the plasma electron, k_B is the Boltzmann constant and e is the electron charge. This equation assumes that the ions are immobile with respect to the electrons and that charges can be described by the Boltzmann distribution [29].

The Debye screening indicates that for a sphere with radius λ_D, known as the Debye sphere, the interaction between charges occurs within λ_D and charges outside are effectively invisible. If many particles are included within the Debye sphere, the net effect of collisions vanishes and the collective behaviour of the plasma becomes important. This type of plasma is termed "collisionless plasma." In the following sections, a collisionless plasma is assumed.

When the electrons within the Debye sphere are displaced by a distance very small compared to λ_D, the charge separation creates a restoring Coulomb force, which pulls back the electrons to their initial position. The electrons, owing to their gained kinetic energy, overshoot and perform harmonic oscillations around

the initial position at a characteristic frequency, ω_p,

$$\begin{aligned} \omega_p &= \sqrt{\frac{4\pi n_e\, e^2}{m_e}} \\ \omega_p\,[\mathrm{fs}^{-1}] &\simeq 56.4\times 10^{-12}\sqrt{n_e[\mathrm{cm}^{-3}]}\,, \end{aligned} \tag{1.2}$$

where m_e is the electron mass. A similar expression can be derived for the background ions, with corresponding mass m_i and density n_i. However, since $m_i \gg m_e$, ions move slower than the electrons, and for the timescale of laser wakefield acceleration they can be considered immobile. The plasma wavelength is,

$$\begin{aligned} \lambda_p &= \frac{2\,\pi c}{\omega_p} \\ \lambda_p\,[\mu\mathrm{m}] &\simeq 3.3\times 10^{10}/\sqrt{n_e[\mathrm{cm}^{-3}]}\,, \end{aligned} \tag{1.3}$$

where c is the speed of light. For instance, $\omega_p \simeq 0.18\,\mathrm{fs}^{-1}$ and $\lambda_p \simeq 10\,\mu\mathrm{m}$ for a plasma with density $n_e = 10^{19}$ cm^{-3}.

Plane wave propagation in plasma

When a monochromatic electromagnetic wave travels through an unmagnetized cold plasma, the dispersion relation which describes the dependence of the wave angular frequency, ω, on the wave number, k is

$$\begin{aligned} \omega^2 &= c^2\,k^2 + \omega_p^2 \\ k &= \frac{\omega}{c}\sqrt{1-\frac{\omega_p^2}{\omega^2}}\,, \end{aligned} \tag{1.4}$$

As shown in Figure 1.2, waves with frequencies $\omega < \omega_p$ are reflected since k becomes imaginary, and the plasma is called "overdense", while for $\omega > \omega_p$, waves propagate and the plasma is called "underdense". This defines a critical density:

$$n_{cr}\,[\mathrm{cm}^{-3}] = \frac{m_e}{4\pi e^2}\,\omega^2 \simeq \frac{1.12\times 10^{21}}{\lambda^2[\mu\mathrm{m}]}. \tag{1.5}$$

The critical density for a laser beam with wavelength $\lambda = 0.8\,\mu\mathrm{m}$ is $n_{cr} \simeq 1.75\times 10^{21}$ cm^{-3}. For laser wakefield acceleration, plasma sources usually have densities in the range between 10^{17} and 10^{19} cm^{-3}, and therefore plasma is underdense.

The phase, v_p, and group, v_g, velocities for tranverse electromagnetic fields in

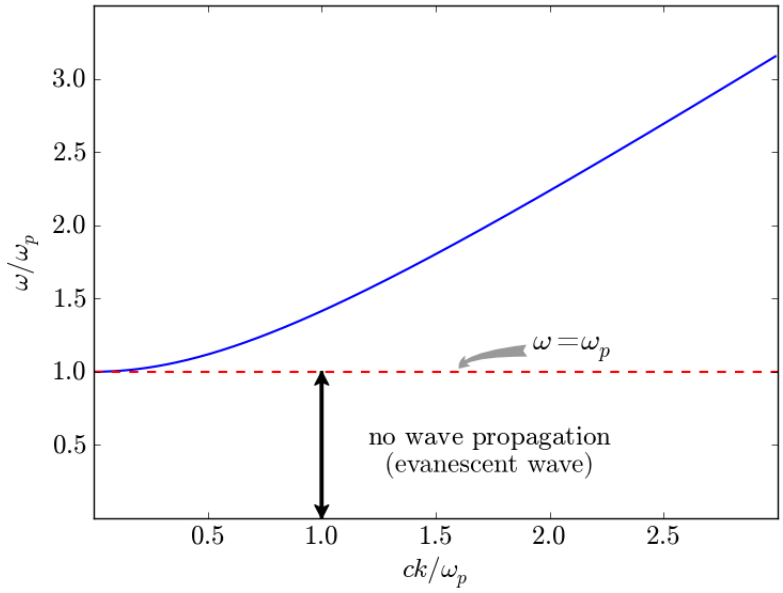

Figure 1.2: Dispersion relation of electromagnetic waves in an unmagnetized plasma (from Equation 1.4).

plasma are calculated from Equation 1.4,

$$\begin{aligned} v_p &= \frac{\omega}{k} = \frac{c}{\eta} \quad \text{and} \quad v_g = \frac{\partial \omega}{\partial k} = c\,\eta\,, \\ \text{with} \quad \eta &= \sqrt{1 - \frac{\omega_p^2}{\omega^2}} = \sqrt{1 - \frac{n_e}{n_{cr}}} \end{aligned} \tag{1.6}$$

as the plasma refractive index. For underdense plasma, the refractive index is always less than one, therefore the phase velocity of an electromagnetic wave is larger than the speed of light, whereas the group velocity is always less than the speed of light.

1.1.2 Laser interaction with electrons in relativistic limits

This section introduces some parameters and nonlinear effects that are important in the interaction of intense lasers with plasma. The parameters describing the laser and plasma are typically expressed in normalised units:

- momentum to $m_e c$, $\mathbf{p} \rightarrow \mathbf{p}/m_e c$
- vector potential to $e/m_e c^2$, $\mathbf{A} \rightarrow e\mathbf{A}/m_e c^2$
- speed to c, $\beta = v/c$

- time to ω, $t \to \omega t$
- distance to k, $z \to kz$

Laser strength parameter

The boundary between classical and relativistic regimes is defined by the laser strength parameter a_0, which is the peak amplitude of the normalised vector potential,

$$\begin{aligned} \mathbf{a} &= \frac{e\mathbf{A}}{m_e c^2} \\ a_0 &= \frac{eA}{m_e c^2} \simeq \frac{eE_L}{\omega m_e c} \,, \end{aligned} \tag{1.7}$$

where $\mathbf{A}$ is the vector potential, ω and E_L are the laser angular frequency and electric field peak amplitude. For a linearly polarised Gaussian beam, a_0 is related to the laser peak intensity I by the expression,

$$a_0 \simeq 0.85 \times 10^{-9} \lambda[\mu\text{m}] \, \left(I[\text{W/cm}^2]\right)^{1/2} \,. \tag{1.8}$$

The laser power in terms of a_0 is $P[\text{GW}] \simeq 21.5(a_0 r_0/\lambda)^2$, where r_0 and λ are the laser spot size and wavelength [30]. The factor a_0 sets the boundary between the linear ($a_0 < 1$) and relativistic ($a_0 \geq 1$) regimes. For instance, a laser with $\lambda = 0.8\,\mu\text{m}$, $r_0 = 15\,\mu\text{m}$ and $a_0 = 1$, has $I = 2.2 \times 10^{18}\text{W/cm}^2$ and $P = 7.6\,\text{TW}$.

When an electron interacts with an intense laser field, it will oscillate transversely known as the quiver motion. The amplitude of this motion in normalised units is $|\mathbf{a}|$, based on the conservation of canonical transverse momentum,

$$\begin{aligned} p_t - eA/c &= \text{constant} \\ \Rightarrow a &= \frac{p_t}{m_e c} \,. \end{aligned} \tag{1.9}$$

By definition, the Lorentz factor $\gamma = 1/(1-\beta^2)^{1/2} = (1 + p^2/m_e^2 c^2)^{1/2}$. Hence, the corresponding gamma factor, γ_t is related to a as,

$$\gamma_t = \sqrt{1 + a^2} \,. \tag{1.10}$$

The trajectory of an electron is illustrated in Figure 1.3 for different laser strengths. If the laser intensity is low (i.e. nonrelativistic interaction), electrons only oscillate trasversely. As the laser becomes intense, electrons begin to both oscillate and drift in the laser propagation direction. In the frame moving at the average drift velocity in one period of the laser field, the electron motion describes

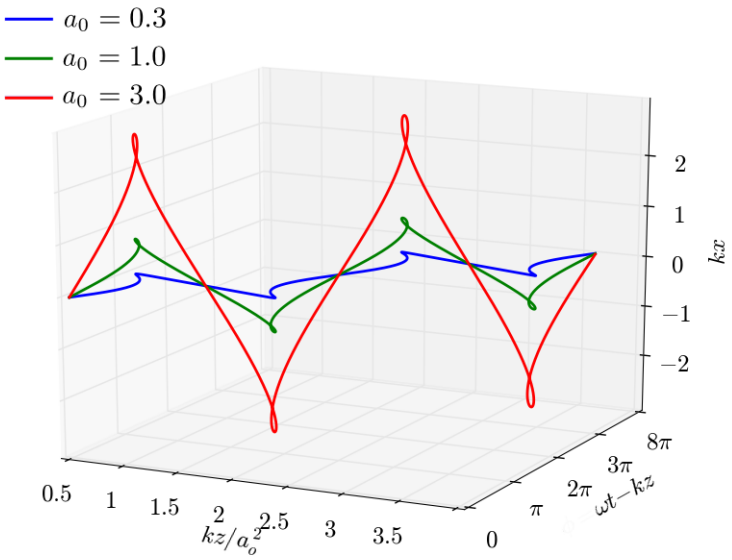

(a)

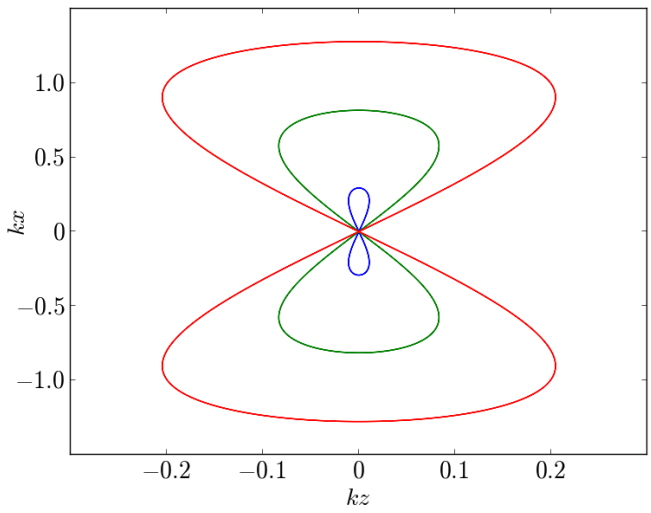

(b)

Figure 1.3: (a) Motion of an electron immersed in a linearly polarised laser ($\lambda = 0.8\,\mu\text{m}$) for different laser strength parameters, where $\omega t - kz$ is the laser phase (plots are in normalised coordinates). (b) shows the same electron orbit in a frame moving at the average drift velocity.

the well-known "figure-of-eight" orbit, as shown in Figure 1.3-b.

Ponderomotive force

A tightly focused laser beam creates a strong radial intensity gradient. Electrons interacting with this inhomogeneous field are pushed away from the regions where the intensity is higher by the ponderomotive force, $\mathbf{F}_p$. In laser-driven accelerators, this is the mechanism responsible for the excitation of plasma waves, as will be discussed in Section 1.1.4.

For a laser with an electric field $\mathbf{E}(\mathbf{r}, t) = \mathbf{E}(\mathbf{r}) \cos \omega t$, the linear ponderomotive force is given by [29, 30],

$$\mathbf{F}_p = -\frac{e^2}{4\, m_e\, \omega^2} \nabla \mathbf{E}^2 = -m_e c\, \nabla \left(\frac{a^2}{2} \right) , \tag{1.11}$$

assuming that the dominant motion of an electron is due to the quiver momentum. Equation 1.11 implies that the direction of $\mathbf{F}_p$ is the same for positively and negatively charged particles. However, its effect is much stronger on the electrons since their mass is light as compared to the ions. The strength of $\mathbf{F}_p$ depends strongly on the $\nabla \mathbf{E}^2$ term. For a focused laser with a radial Gaussian profile, the intensity gradient is higher close to the centre and decreases along the tail. Therefore, the effect of ponderomotive force is to push the electrons away from the centre of the laser axis, as a radiation pressure. The ponderomotive force is also proportional to λ^2, hence, it is stronger for longer wavelength.

Plasma self wave guiding

The transverse intensity profile (in normalised units) of a Gaussian beam in free-space is,

$$\begin{aligned} & a^2 = a_0^2 \left(\frac{r_0}{r_s(z)} \right)^2 \exp \left(-\frac{2r^2}{r_s^2(z)} \right) , \\ & \text{where} \quad r_s(z) = r_0 \sqrt{1 + \left(\frac{z}{z_R} \right)^2} , \\ & \text{and} \quad z_R = \frac{\pi r_0^2}{\lambda} \end{aligned} \tag{1.12}$$

is the Rayleigh length, which defines the region where the beam can be considered focused. A laser with $\lambda = 0.8\,\mu\text{m}$ focused to a spot size of $r_0 = 15\,\mu\text{m}$ yields $z_R \simeq 900\,\mu\text{m}$. For high power lasers, effective laser-plasma interaction occurs within this range.

When a low power laser travels in an underdense plasma, the refractive index

of the plasma is given by Equation 1.6 and is approximately constant. However, as the laser intensity increases such that $a_0 \geq 1$, η evolves due to changes in the electron distribution and relativistic effects leading to variation in electron mass (i.e. $\eta = \eta(r)$). The variation in the radial profile of the refractive index can be clearly seen when the plasma frequency for very high intensity laser is expressed as

$$\omega_p^2 = \omega_{p,0}^2 \frac{1}{\gamma(r)} \frac{n(r)}{n_e} \ , \tag{1.13}$$

where $\omega_{p,0}$ is the unperturbed plasma frequency. At this condition, the quiver motion of the electrons dominates and therefore the momentum is mainly $\mathbf{p}_t = m_e c\mathbf{a}$ (also refer to Equation 1.9). This implies that $\gamma \simeq \gamma_t = (1 + a^2)^{1/2}$ (from Equation 1.10). For a typical laser profile, the intensity is higher on axis, and electrons in this region gain more energy than the electrons off axis. This leads to lowering of the plasma frequency on axis due to the relativistic effects. Therefore the refractive index is higher on axis resulting in a negative refractive index gradient (from Equation 1.6), i.e. $\partial\eta/\partial r < 0$. A negative $\partial\eta/\partial r$ implies that the phase velocity of the laser is faster off axis than on axis, leading to curvature of the phase front. This results in beam focusing through the nonlinear effect known as relativistic self focusing (RSF). The laser power for RSF must exceed the threshold power, P_c, given by [30],

$$P_c\,[\mathrm{GW}] \simeq 17.4 \left(\frac{\omega}{\omega_{p,0}}\right)^2 \ . \tag{1.14}$$

Note that this threshold neglects the effect of variation in the electron density. When the critical power is achieved, the limit for laser diffraction is overcome, and guiding in the plasma is obtained, which can be a few times z_R. If $P = P_c$, the laser is guided and maintains its spot size over a few z_R. On the other hand, when $P > P_c$, the laser beam self-focuses.

The ponderomotive force of an intense laser also causes variations in n_e. The plasma density is reduced in the region where the laser field gradient is high along the radial axis, due to the expulsion of the plasma electrons. Hence, η is higher on axis as compared to the low gradient region off axis, resulting in $\partial\eta/\partial r < 0$. This process, which is known as ponderomotive self-focusing (PSF), enhances RSF but cannot guide laser beam alone [30].

Moreover, the effect of PSF is only significant for long laser pulses ($c\tau \gg \lambda_p$) while the RSF dominates for short laser pulses ($c\tau > \lambda_p$), which is the time scale for laser wakefield acceleration. For a laser with $\lambda = 0.8\,\mu\mathrm{m}$ propagating through a plasma with $n_e = 10^{19}$ cm^{-3}, the critical power for RSF to occur is $\simeq 3\,\mathrm{TW}$,

which is easily achieved with current CPA-driven laser systems. Also note that the critical power for RSF is higher for lower plasma densities.

Early simulations (using a 2D fluid model) have shown that in the limit of $c\tau \leq \lambda_p$, RSF is not effective in beam guiding [31] even if $P \geq P_c$ since $\eta(r)$ changes in time scales comparable to the plasma frequency and not to the laser frequency. This indicates that an external optical guiding is needed in order to increase the interaction length for LWFA. However, as will be discussed in Section 1.1.6, RSF can be effective in laser wakefield acceleration in the bubble regime.

Pulse self-compression

Variations in refractive index (for example due to relativistic mass increase and variations in plasma density) also modify the longitudinal laser profile. As the laser front edge pushes the electrons, the plasma density is higher at the front than at the back edge of the laser. Therefore a variation in the laser group velocity is obtained [32], with the v_g higher for lower densities, leading to pulse compression. As the pulse self-compress, the intensity gradient at the front edge increases, which results in a higher overall peak intensity.

1.1.3 Excitation of plasma waves

When an intense laser propagates in an underdense plasma, the head of the laser pushes the plasma electrons away from the vicinity of the pulse, leaving the heavy ions behind. This motion results in charge separation, creating a restoring Coulomb force from the stationary ions that pulls the electrons back after the laser has passed, causing the electrons to oscillate. This results in density perturbations leading to the creation of plasma waves or wakefields, as illustrated in Figure 1.4. The electric fields from the plasma waves are capable of trapping and accelerating background or externally injected electrons. Depending on the laser strength, the excited plasma wave can have a linear ($a_0 \ll 1$) or nonlinear ($a_0 \simeq 1$) behaviour.

The discussion of plasma waves excitation in this section is only valid when the following conditions are satisfied:

- A small perturbation (δn) in the plasma density is assumed, i.e. $\delta n/n_e \ll 1$.
- The plasma electrons are treated as a fluid, i.e. electrons move in laminar flow and trajectory crossing does not occur.
- The laser should not evolve significantly over the time it takes to travel through one plasma wavelength (quasi-static approximation). This also

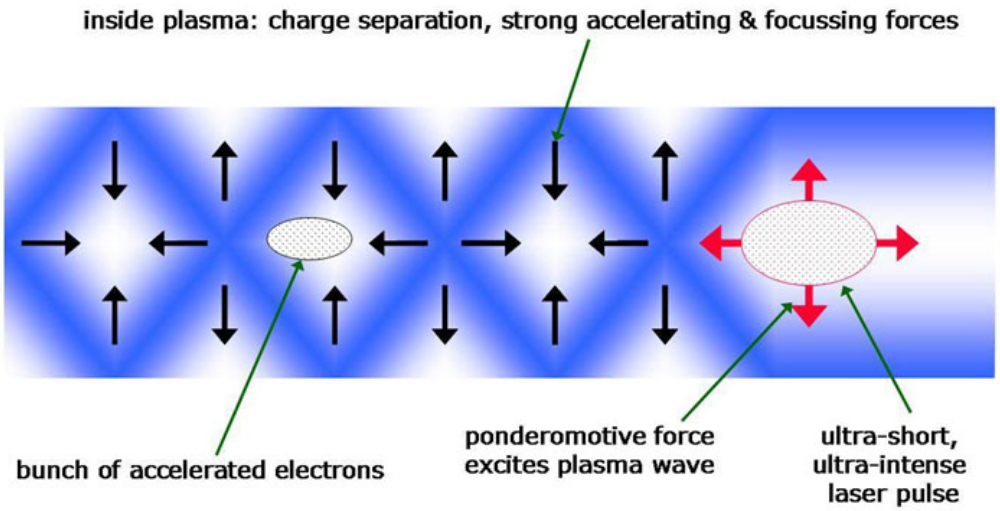

Figure 1.4: Illustration of plasma wave excitation due to strong ponderomotive force [33]. The electrons (shade of blue) are expelled by the ponderomotive force (red arrows) leading to excitation of plasma waves.

implies a laser beam with broad radial dimension, i.e. $k_p r_0 \gg 1$.

With these assumptions, the cold fluid equations can be linearised:

- Continuity equation to account for the density perturbation time variation.
- Fluid momentum equation, which represents the fluid/laminar flow of the plasma.
- Poisson's equation, which gives the potential due to the plasma density distribution.

Linear plasma waves

The plasma waves in the linear regime are excited by a laser when $a_0 \ll 1$. An in-depth analytical study of linear plasma waves is given in [30, 34]. The solutions of the linearised fluid equations show that the density perturbation, δn, and longitudinal electric field, E_z, are sinusoidal functions, out of phase by $\pi/2$. Figure 1.5a shows $\delta n/n_e$ and E_z profiles for a Gaussian laser pulse. Efficient excitation of linear wakefields is obtained when the laser pulse duration matches the plasma wavelength ($c\tau \simeq \lambda_p/2$). The longitudinal electric field consists of accelerating and decelerating regions oscillating at the plasma frequency, ω_p, and moving at a phase velocity, v_ϕ, equal to the laser group velocity, i.e.

$$v_\phi \simeq v_g \simeq c\sqrt{1 - \frac{\omega_p^2}{\omega^2}}\,. \tag{1.15}$$

The plasma waves also generate transverse wakefields, E_r and B_θ with $E_r \sim E_z \sim a^2$ and $B_\theta \sim a^4$ when $a^2 \ll 1$. These transverse fields provide the focusing and defocusing regions and the corresponding radial forces cancel out on axis. Background electrons travelling in the plasma waves with speed, v_z, close to c will experience both longitudinal acceleration and transverse focusing forces within $\lambda_p/4$ of the plasma wave period, as shown in Figure 1.5b.

An important property of plasma waves is that they can sustain extremely large field amplitudes. To estimate the peak amplidude, E_{max}, of the electric field, a uniform plasma with almost all electrons oscillating at the same frequency, ω_p, is assumed. The maximum amplitude for a linear plasma wave is equal to

$$\begin{aligned} E_{max} = E_0 &= \frac{c m_e \omega_p}{e} \\ &\simeq 96\sqrt{n_e\,[\mathrm{cm}^{-3}]} \quad [\mathrm{V/m}]\,. \end{aligned} \qquad thequiver \tag{1.16}$$

The parameter E_0 is called the cold, linear wave breaking field [35]. For a plasma with density $n_e = 10^{19}$ cm^{-3}, the wave breaking field can reach up to $E_0 \simeq 300\,\mathrm{GV/m}$.

Nonlinear plasma waves

For lasers with $a_0 \geq 1$, interaction becomes relativistic, the plasma waves behave nonlinearly and the electric field can exceed E_0 ($E_z \gg E_0$). The behavior of the nonlinear fields in 1D can be obtained analytically using the quasi-static approximation, where the laser is assumed to be non-evolving over the transit time through a plasma wavelength. These assumptions are necessary to make laser and plasma waves functions of the longitudinal coordinate, $z - v_\phi t$ only. References [36, 37] provide detailed derivations leading to the 1D analytical solutions for the density perturbation and longitudinal fields of the nonlinear plasma waves.

Solutions for a Gaussian laser pulse are presented in Figure 1.6, showing that both profiles are no longer sinusoidal. The front edge of the plasma waves becomes curved with increasing wave amplitude, resulting in longitudinal field steepening. As such, E_z has a "sawtooth" profile. The steepness of the field front increases as the peak field amplitude, E_{max}, increases. Furthermore, the density perturbation oscillates strongly, and in between the maxima the longitudinal fields are approximately linear. The plasma wave period is no longer constant, but lengthens with increasing E_{max}. The wavelength associated with the nonlinear plasma waves is known as nonlinear plasma wavelength, λ_{Np}.

For higher laser intensities, it is possible for E_{max} to exceed the cold, linear

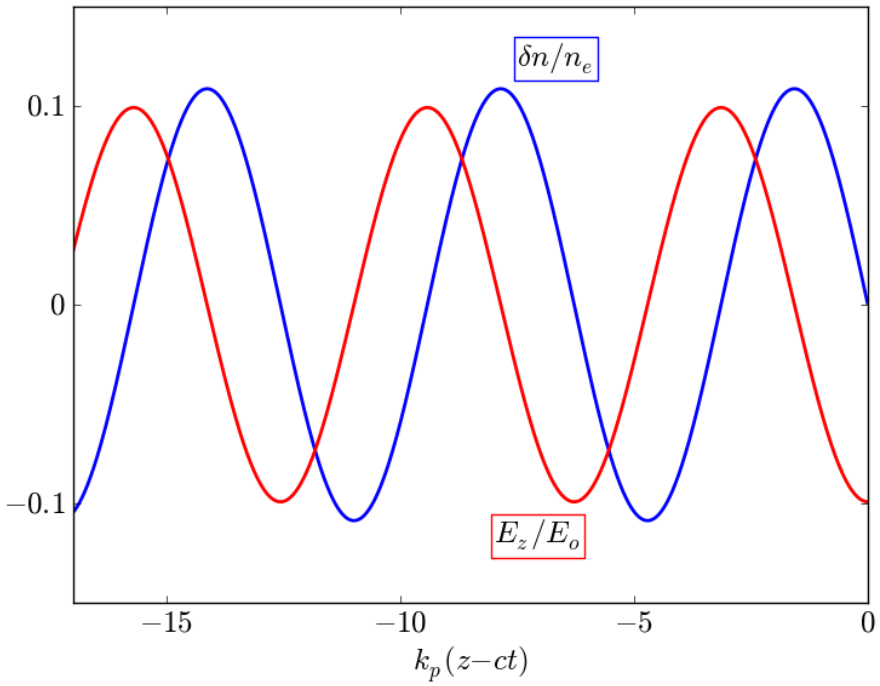

(a)

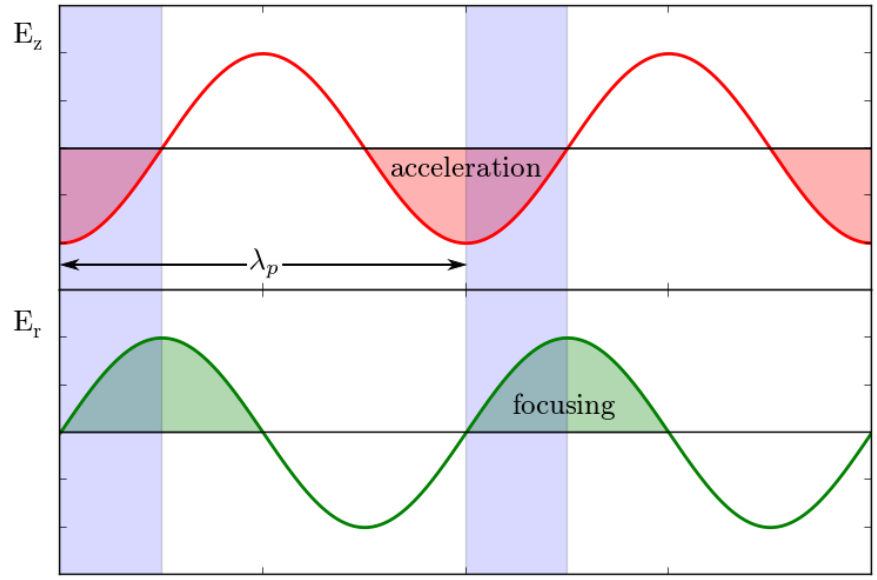

(b) A relativistic electron experiences both longitudinal force (acceleration) and transverse compression (focusing) in $\lambda_p/4$ of the phase region (indicated by the shaded regions).

Figure 1.5: Linear plasma waves. (a) Averaged variation of the density ($\delta n/n_e$) and normalised longitudinal (E_z/E_0) and (b) transverse, E_r, fields of linear plasma waves driven by a Gaussian laser pulse with $a_0 = 0.5$ [30, 34]. The fields are taken in the co-moving frame $k_p(z - ct)$.

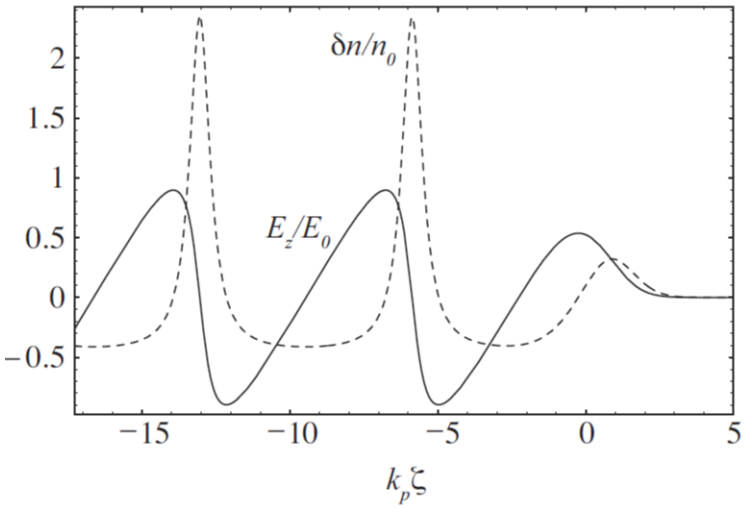

Figure 1.6: Density perturbation and longitudinal electric field profiles of a nonlinear plasma wave excited by a Gaussian laser pulse with $a_0 = 2$, where $k_p\zeta = k_p(z - v_\phi t)$ [30].

wave breaking field. The maximum amplitude field, E_{WB}, that a nonlinear plasma wave can sustain is derived using a 1D nonlinear cold fluid model [38] obtaining

$$E_{WB} = \sqrt{2\left(\gamma_p - 1\right)}\, E_0 \ , \tag{1.17}$$

where γ_p is the Lorentz factor associated with the phase velocity of the wakefield. Using the dispersion relation from Equation 1.4 and noting that $v_\phi \simeq v_g$, γ_p can be approximated as

$$\gamma_p = \left(1 - \frac{v_\phi^2}{c^2}\right)^{-1/2} \simeq \frac{\omega}{\omega_p} \ , \tag{1.18}$$

in the 1D low laser intensity limit. For a laser with $\lambda = 0.8\,\mu\text{m}$ interacting with a plasma with density $n_e = 10^{19}$ cm^{-3}, $\gamma_p \simeq 13$ and $E_{WB} = 5E_0$. Nonlinear plasma waves in the three dimensional high-intensity regime are discussed in Section 1.1.6.

1.1.4 Electron trapping in plasma waves

In the previous section, it was shown that plasma waves are capable of sustaining high electric fields, both in the linear and nonlinear limits. In both cases, the maximum longitudinal amplitude that these plasma waves can have, are E_0 (linear) and E_{WB} (nonlinear). When the fields reach these thresholds, the plasma electrons gain energy that is sufficient for their trajectories to begin to cross, a phenomenon known as "sheath crossing." This leads to plasma wave breaking and

simultaneously trapping of the electrons. Mathematically, wave breaking implies that the assumptions given at the beginning of Section 1.1.3 are no longer valid, which precludes the use of the fluid equations. For electron self-trapping (and therefore for acceleration) to be possible, longitudinal wave breaking is necessary. The conditions for trapping are discussed in the following sections.

Linear regime

The electrostatic potential, ψ, of a linear plasma waves can be expressed as $\psi = \psi_o \cos(k_p\zeta)$, where $\psi_o = E_{max}/E_0$ is the amplitude, $k_p\zeta = k_p(z - v_\phi t)$ is the phase and v_ϕ is the wave phase velocity. For ζ between $(-\pi, \pi)$, the maximum accelerating length is $\lambda_p/2$, which is at $-\pi < \zeta < 0$. The maximum energy gain is achieved within this length. The motion of background electrons initially located at $\zeta = 0$ is considered. The background electrons gain energy as they move backward with respect to the plasma wave. If the electron velocity, v_z, exceeds the phase velocity at $\zeta = -\pi$, i.e. $v_z > v_\phi$, then the electron is trapped and performs a closed orbit motion. Otherwise, if $v_z < v_\phi$ at $\zeta = -\pi$, it will just slip away and continue moving backward. The boundary of the trajectories between trapped (close orbit) and untrapped electrons (open orbit) is determined by the separatrix in phase space.

1D nonlinear regime

The electron trapping in 1D nonlinear plasma wave has been analysed by E. Esarey and M Pilloff by describing the electron motion with the Hamiltonian dynamics and the plasma waves by the quasi-static cold fluid equation [38]. The nonlinear plasma waves are assumed to have an electrostatic potential ψ oscillating between minima and maxima ($\psi_{min} < \psi < \psi_{max}$) at a period given by λ_{Np}. The minimum and maximum amplitude of the potential is dictated by the peak amplitude, E_{max}, of the plasma wave.

The plasma electrons are trapped if their normalised minimum momentum, $\bar{p}_t$, upon reaching the accelerating phase of the plasma wave reaches the value [38]

$$\bar{p}_t(m_e c) = \gamma_p\beta_p(1 - \gamma_p\Delta\psi) - \gamma_p[(1 + \gamma_p\Delta\psi)^2 - 1]^{1/2} , \tag{1.19}$$

where $\gamma_p \simeq \omega/\omega_p$, $\beta_p = v_\phi/c$ is the normalised plasma wave phase velocity and $\Delta\psi = \psi_{max} - \psi_{min}$. Figure 1.7 plots $\bar{p}_t$ for different plasma wave amplitudes (E_{max}/E_0) and γ_p with $\beta_p \approx 1$. It shows that as the plasma amplitude increases, the minimum momentum for electron trapping decreases. Moreover, working with

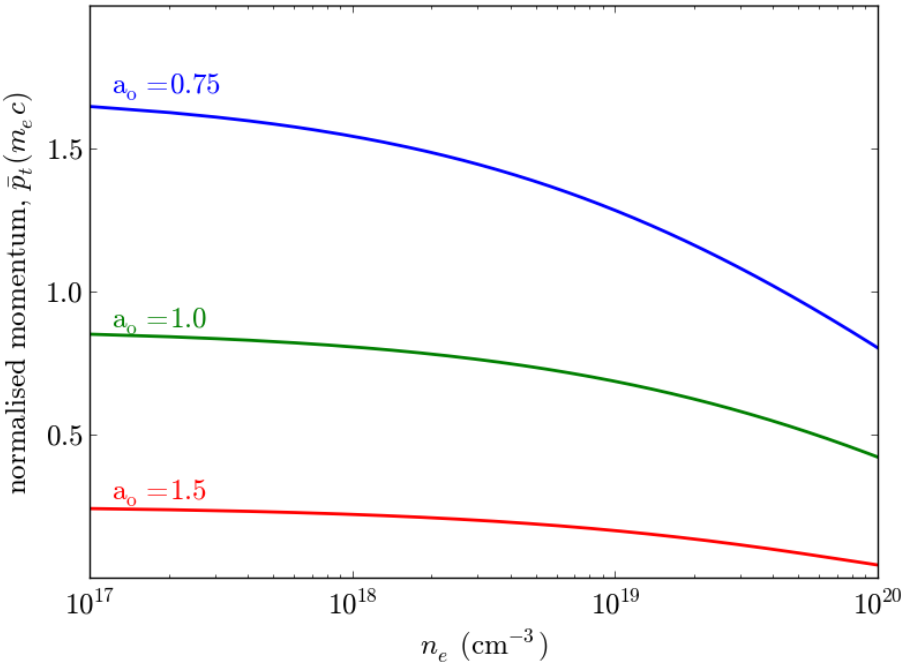

Figure 1.7: The required minimum momentum for an electron to be trapped in the nonlinear plasma waves using Equation 1.19.

lower densities (higher γ_p) decreases the threshold for trapping electrons. The width of the separatrix depends on λ_{Np}, which increases with peak amplitude. This implies that an electron trapped in nonlinear plasma waves can gain much more energy than with linear plasma waves. Electron trapping in the 3D high-intensity regime is discussed in Section 1.1.6.

1.1.5 Electron acceleration

Section 1.1.3 shows that the excitation of plasma waves is due to the balance between the ponderomotive and restoring Coulomb forces, while Section 1.1.4 describes the conditions for electron trapping in both linear and nonlinear limits. The fields of plasma waves (wakefields) have both longitudinal and transverse components which are responsible for simultaneously focusing and accelerating the self-trapped plasma electrons. This gives rise to laser wakefield acceleration (LWFA).

The trapped electrons gain energy from the wakefield, reaching speeds comparable with c, while the wakefield phase velocity remains constant. After some time, the electrons overrun the accelerating region and enter the decelerating region. The distance over which the electrons slip before they decelerate is known as the dephasing length, L_d, which is equivalent to $\lambda_p/2$. Therefore, L_d can be

expressed as,

$$\begin{aligned}(c - v_\phi)L_d &\simeq c\lambda_p \\ L_d &\simeq \gamma_p^2 \lambda_p\end{aligned} \tag{1.20}$$

The trapped electrons continuously gain energy until they reach L_d. Hence, the maximum energy gain is $W_{max} = eE_{max}L_d$ which is approximately equal to

$$\begin{aligned}W_{max} &\simeq eE_{max}L_d \\ W_{max} &\simeq 2\pi m_e c^2 \gamma_p^2 \left(\frac{E_{max}}{E_0}\right) ,\end{aligned} \tag{1.21}$$

assuming that the electrons are accelerated by the maximum field amplitude, which is dependent on the profile of the laser. Since the energy gain scales with γ_p^2 and E_{max}, higher electron energy is obtained for either low plasma densities or high intensity lasers. For nonlinear wakefields, λ_{Np} lengthens, resulting in an increase with the field amplitude E_{max}/E_0. Therefore, the dephasing length is longer and the trapped electrons obtain higher energy than in linear wakefields.

1.1.6 The "bubble" regime

Previous sections have described electron acceleration for (1) $a_0 \ll 1$ using linear theory, where the plasma waves oscillate sinusoidally and for (2) $a_0 \geq 1$, where the nonlinear plasma waves are treated using quasi-static approximation. In the high intensity limit in three dimensions (where the laser spot size approaches the plasma wavelength), the assumption that the laser is slowly evolving is no longer valid and wakefields have to be modelled numerically. The transverse ponderomotive force of the laser becomes comparable with its longitudinal counterpart, leading to an increase in the transverse motion of electrons, which can be completely blown away, creating an ion cavity on the first and subsequent plasma periods. In addition, the plasma wave front steepens, which causes the peak amplitude to grow considerably. At this point, E_{max} reaches and exceeds E_{WB}, leading to wave breaking and electron trajectory crossing. For these situations, the interplay between nonlinearities are difficult to include in a single theory. Hence, wakefields are best understood by numerically modeling the laser evolution in the plasma in 3D.

The high-intensity limit is called the "blow-out" or "bubble" regime, because of the nearly spherical cavity formed behind the driver [39]. This regime is typically modeled using particle-in-cell (PIC) codes. The laser field evolution is followed on time scales comparable with the laser pulse duration. It requires

long computations, making it difficult to explore a large parameter space. Figure 1.8a is a snapshot from simulations using the 3D PIC code OSIRIS [40], showing the formation of a nearly spherical ion cavity that is trailing the laser. Trapped electrons are visible inside the bubble as well as in a second bubble with very different structure.

In contrast to the prediction of 2D fluid models, simulations using PIC codes have shown that relativistic self-focusing over long distances is possible for ultra short pulsed lasers ($L \leq \lambda_p$, provided that $P \geq P_c$), thereby a preformed plasma channel is not necessary [41]. Moreover, simulations using PIC codes demostrate that the bubble regime is stable and the acceleration parameters are scalable [42].

There has been great interest in understanding acceleration in the bubble regime, both in experimental and theoretical works, because this regime has the potential of generating monoenergetic electrons with low divergence and transverse emittance, which are necessary conditions for the future of laser-driven particle accelerators [41, 42]. In many of LWFA experiments, the initial laser intensity and pulse duration are not high enough to directly enter the bubble regime. However, during the interaction with the plasma, the laser can evolve, reaching the threshold for complete ion cavitation.

Self-injection mechanisms

Up to now, in-depth understanding of injection mechanisms in this regime are still open for research and discussion. Nevertheless, there are theoretical models predicting trapping in the case of stationary [43] or evolving [44] bubble. Both theories assume laser powers in excess of P_c, so that relativistic self-focusing takes place.

As shown in Figure 1.8a, the bubble is trailing the laser. W. Lu et al. have shown that the bubble phase velocity is slower than the laser group velocity due to the laser front edge local pump depletion [39]. They estimated, using numerical simulations, the value of γ_p associated with the bubble phase velocity, $\gamma_p \simeq (1/\sqrt{3})(\omega/\omega_p)$. The plasma electrons surround the bubble forming a thin sheath just outside the ion channel. Trajectory crossing occurs, mostly at the back of the bubble, resulting in a very high plasma density and strong longitudinal electric fields. Within the bubble, this longitudinal field is approximately linear with $\zeta = z - v_\phi t$ (as illustrated in Figure 1.8b) and in the transverse direction. The electric field is maximum at the back of the bubble and minimum at the bubble center, $\zeta = 0$, which results in the bubble potential having a minimum at the back of the bubble and a maximum at the center.

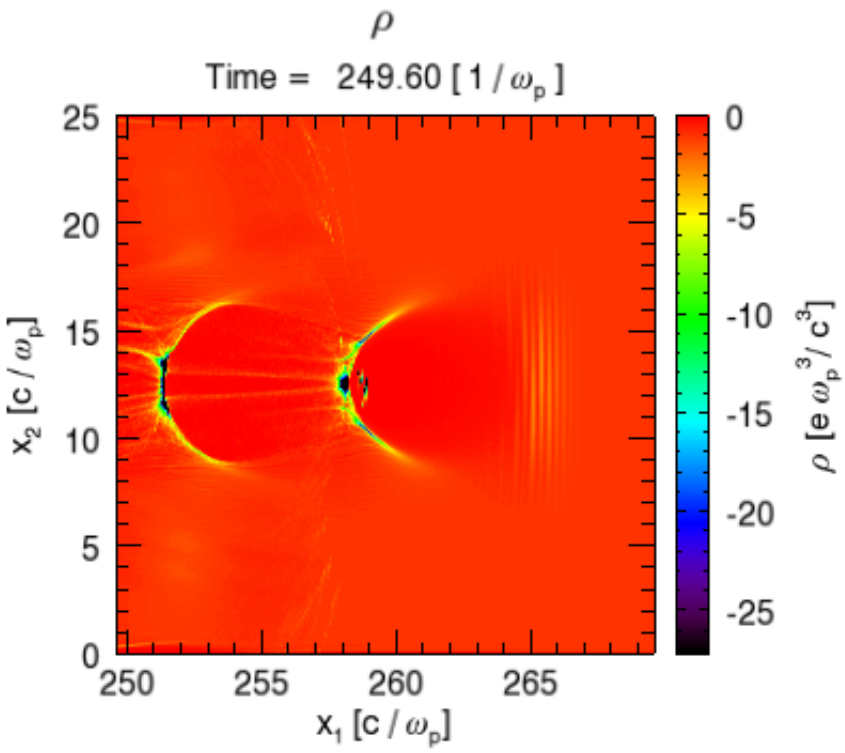

(a)

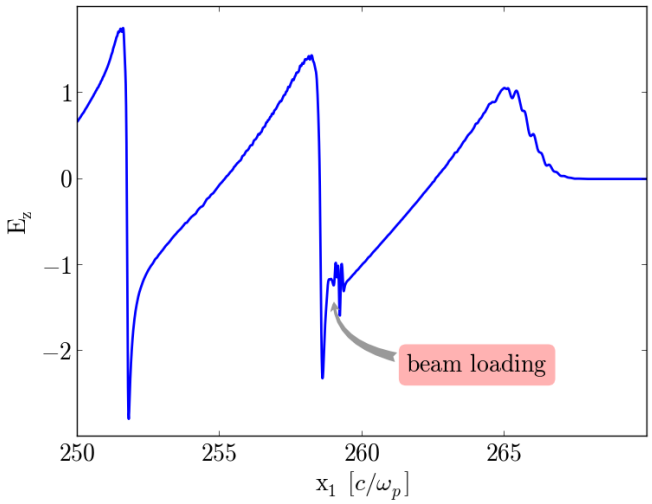

(b)

Figure 1.8: (a) Snapshot from 3D PIC code OSIRIS showing the spherically formed ion cavity, taken at the time when electrons are trapped in the first bubble and (b) the corresponding longitudinal electric field, E_z, for $a_0 = 2$ and $n_e = 10^{-19}$ cm^{-3}. Beam loading is evident with the distortion of the longitudinal electric field in the first bubble. Here, x_1 and x_2 are the propagation and transverse directions (courtesy of M.R. Islam).

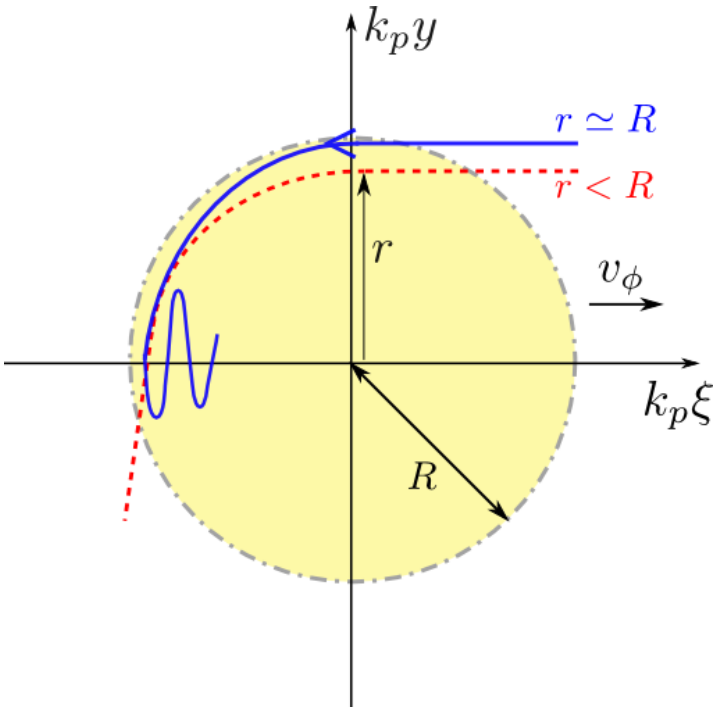

Figure 1.9: Trajectory of trapped ($r \simeq R$, solid blue line) and untrapped ($r < R$, dashed red line) electrons in the bubble regime based on the self-trapping condition of Kostyukov et al. [43].

In the linear and 1D nonlinear limits, wave breaking occurs due to electron trajectory crossing, and electron trapping happens simultaneously. However, in 3D nonlinear regime, this definition of wave breaking is not sufficient because sheath crossover always occurs and the fluid model always breaks down.

Kostyukov et al. provide an analytical model for the condition of electron self-trapping in 3D nonlinear plasma waves for a spherical shape with radius R [43]. In their model, the self-injection depends on the initial electron position, r, with respect to the bubble radius. If $r > R$, electrons are lost, scattered away from the bubble by the laser tail. On the other hand, if $r < R$, electrons will enter the bubble in the decelerating region (at $\zeta > 0$) and will gain a negative momentum upon reaching $\zeta = 0$, as shown in Figure 1.9 (red dotted line). As they approach the accelerating region, the energy gain can be so large to exceed the bubble velocity. The accelerating field is not strong enough to reverse the motion and electrons will not be trapped. However, different scenarios can happen for electrons at $r \simeq R$ initially at rest at $\zeta = 0$ (blue solid line). These electrons will encounter an accelerating field after entering the bubble when they reach the back of the bubble. Their longitudinal speed will be comparable to the bubble phase velocity. These electrons have a high probability of being trapped and accelerated to high energies. In general, the condition for electron self-injection

is

$$\frac{\gamma_p}{R} \leq \frac{1}{\sqrt{2}} \,. \tag{1.22}$$

In this type of injection, where trapping is dependent on the position, different electrons will be accelerated over different distances. Thus, the electron spectrum is composed of a narrow high energy peak with a long low energy tail. The gamma factor, $\gamma_p \simeq (1/\sqrt{3})\omega/\omega_p$, is inversely proportional to plasma density. Hence, if one chooses to go to lower densities to increase L_d and obtain high energy gain, then γ_p increases and condition given in Equation 1.22 will be difficult to realise.

On the other hand, in the model of Kalmykov et al., bubble temporal expansion is a necessary condition for electron self-injection [44]. In particular, electrons are trapped at the onset of a rapid expansion of the bubble which can occur when a tightly focused laser beam starts to diffract, leading to a growth in bubble radius. However, to produced monoenergetic electron bunches, this model requires that the bubble expansion must be followed by a contraction to stop the injection.

Similar to linear regime, both models show that to have trapping, the electrons must catch up with the bubble phase velocity. However, effects of bubble deformation due to the trapped electron bunch are not included in the 3D PIC codes of these two models (Kostyukov and Kalmykov models). When the number of trapped electrons increases, a wakefield is generated that strongly affects the back of the bubble. Simulations show that this leads to a slowing down of the bubble rear part, while the bubble front edge moves faster, resulting in an elongation of the bubble. Since electron self-injection occurs at the back, it is more appropriate to use the speed of the back of the bubble in the trapping condition for a non-evolving bubble given in Equation 1.22. As such, the required bubble radius is reduced for self-injection [43]. It is also possible that the trapped electrons form a bunch that repels electrons at the back of the bubble, stopping completely the injection.

Conditions and scaling laws

Electron acceleration in the bubble regime is very complex, as it is based on many interplaying nonlinear processes. However, theoretical works, supported by numerous 3D PIC simulations, have shown the existence of simple scalings laws connecting laser, plasma and electron parameters.

The bubble generation is optimised when the plasma density, laser spot size

and laser intensity satisfy the condition (in the limit of $a_0 \geq 2$) [39],

$$k_p\, R \simeq k_p\, r_0 \simeq 2\,\sqrt{a_0}\ . \tag{1.23}$$

This condition is obtained by balancing the ponderomotive force creating the bubble and the force from the ion channel. The bubble radius R, is approximately equal to the laser spot size ($R \simeq r_o \simeq (2/k_p)\sqrt{a_0}$). It shows that the generation of the bubble strongly depends on the evolution of the laser properties, i.e. spot size and pulse duration. This condition also assumes a laser power larger than the critical power for self-guiding, i.e. $P/P_c \gg 1$. It has been shown that for short pulses, relativistic self guiding is possible when $P \gg P_c$ [41]. This is mainly due to the depletion of the laser front edge before it starts to diffract, while the laser back edge is guided in the ion cavity.

As a consequence of pump depletion, the dephasing length must be matched to the pump depletion length to obtain the maximum electron energy. For $2 < a_0 < 4$, W. Lu et al. [39] have shown that the bubble is nearly spherically shaped and are able to obtain a scaling for the maximum energy gain after reaching the dephasing length, given by

$$E_{Lu} \simeq m_e c^2 \left(\frac{P}{P_{rel}}\right)^{1/3} \left(\frac{n_{cr}}{n_e}\right)^{2/3}\ , \tag{1.24}$$

where $P_{rel} = 85\,\mathrm{GW}$. On the other hand, for ultra-relativistics laser plasmas ($a_0 \gg 1$), A. Pukhov et al. [45] obtained a scaling law for the energy gain using similarity theory,

$$E_{Pukhov} \simeq 0.16\, m_e c^2\, \frac{c\,\tau}{r_0} \left(\frac{P}{P_{rel}}\right)^{2/3} \left(\frac{n_{cr}}{n_e}\right)^{1/3} \tag{1.25}$$

A. Pukhov's formula is strongly dependent on the laser properties whereas W. Lu's theory emphasizes scaling with the plasma density, as shown in Figure 1.10. The difference is a consequence of the regime considered by Lu et al. , where the acceleration length is limited by the pump depletion, which increases the laser etching velocity. This results in a plasma wave with phase velocity less than the laser group velocity, therefore the acceleration stops even before the electrons reach the dephasing length. On the other hand, A. Pukhov considers ultrarelativistic regimes where laser etching does not occur, and the plasma wave moves at the laser group velocity.

Nevertheless, both scalings show that to reach energies beyond GeV in a single

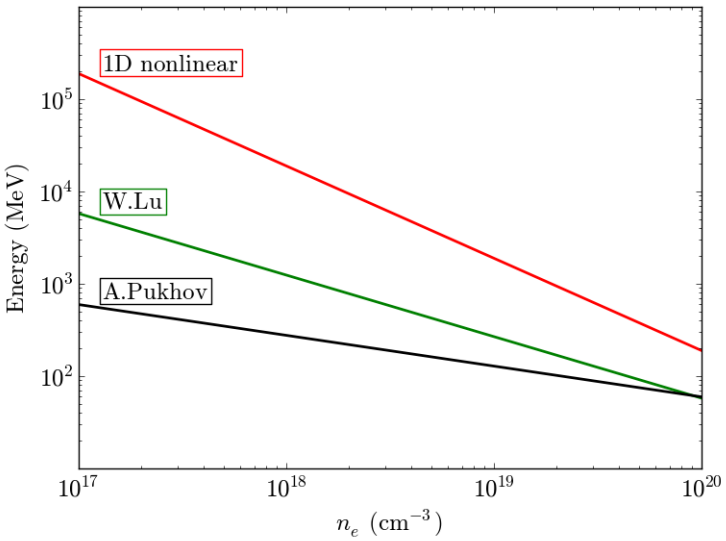

(a)

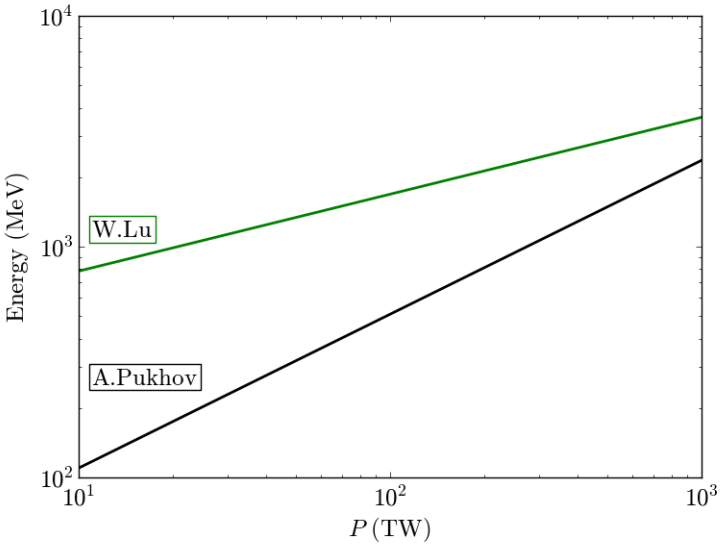

(b)

Figure 1.10: Comparison of the scaling laws for electron energy using Equations 1.24 and 1.25 for varying (a) plasma densities at laser power of 40 TW ($a_0 = 2.3$) and (b) laser power for plasma density of 10^{18} cm^{-3}. A linearly polarised laser beam with Gaussian radial profile, $\lambda = 0.8\,\mu$m and spot size of $r_o = 15\,\mu$m are assumed.

stage accelerator, it is necessary to go to lower densities. However, the critical power for relativistic self-focusing is higher for low densities, thus higher laser power is needed, or external guiding must be used and not rely on self-focusing.

1.1.7 Limitations to electron acceleration

The maximum energy gain is dictated by the acceleration length, which in turn depends on laser and plasma parameters that both evolve during the interaction. Important parameters that can possibly limit the acceleration length are discussed below.

Diffraction

As mentioned in Section 1.1.2, the laser diffracts and the beam size evolves according to Equation 1.12 in free-space propagation. The highest intensity is reached at the focal region where the beam size is smallest. Strong laser-plasma interaction can occur only over a few Rayleigh lengths, therefore limiting the acceleration length. If the laser power is not high enough for relativistic self-focusing, a pre-formed plasma channel waveguide can be used to optically guide the laser and increase the acceleration length. This is usually necessary for acceleration in the linear regime.

Dephasing and pump depletion

The maximum electron energy is limited by the dephasing length because the electron velocity exceeds the wakefield phase velocity. On the other hand, the laser energy decreases by sustaining the wakefield, leading to pump depletion. This results in a reduction of the laser group velocity, and hence a decrease in wakefield phase velocity.

Esarey et al. derived the dephasing, L_d, and pump depletion, L_{pd}, lengths for a linearly polarised square profile laser assuming a pulse duration $L = \lambda_{Np}/2$ [46, 47]. A comparison of the dephasing and pump depletion lengths for linear and 1D nonlinear limits is shown in Figure 1.11, where the gaps indicate the boundary between classical and relativistic regimes. Here, they assumed that the laser pulse shape does not evolve significantly. Both L_d and L_{pd} scale with $n_e^{-3/2}$, hence they can be further increased by going to lower densities. In the linear regime (indicated by the dashed curves), $L_d < L_{pd}$, hence the acceleration length and maximum energy gain are limited by the dephasing of trapped electrons. On the other hand, in the 1D nonlinear regime (indicated by the solid curves),

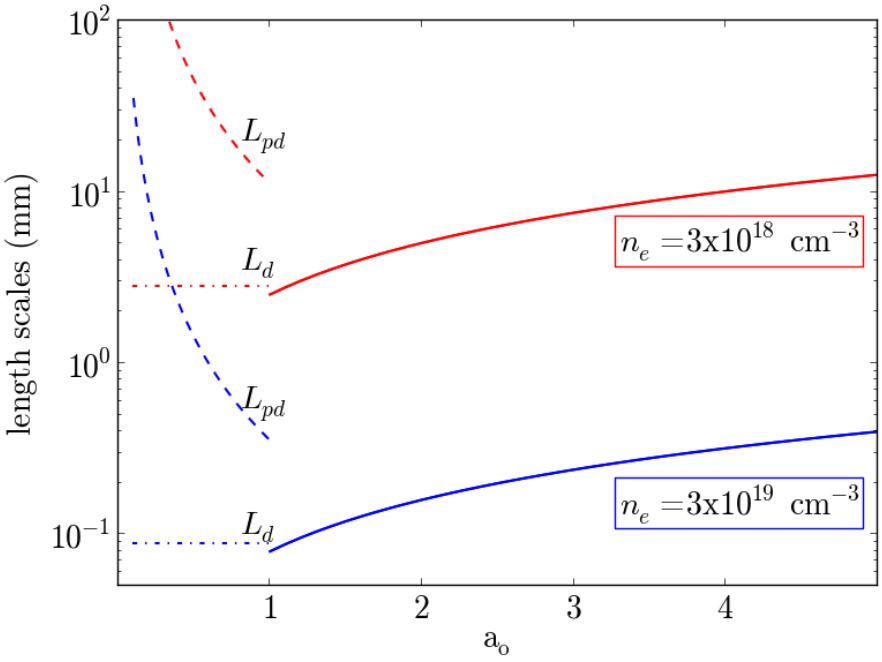

Figure 1.11: Comparison of dephasing and pump depletion lengths linear (dashed curves) and 1D nonlinear regime (solid curves) for two different plasma densities. The gap between the curves are the boundary between the two different regimes. These curves were calculated based from [46].

$L_d \sim L_{pd}$. Hence, the maximum obtainable electron energy is determined by the conversion efficiency of the laser energy to the wakefield.

Beam loading

It is possible for relativistic electrons to excite a wakefield by a mechanism similar to the ponderomotive force of the laser driver. A bunch of relativistically massive electrons pushes the relativistically less massive electrons away due to its space charge force, creating a wakefield. This process is most effective for an electron bunch with very small dimensions, where the charge density is high. The excited wakefield is detrimental since it is out of phase with the laser-induced wakefield, resulting in a reduction in wakefield amplitude. Beam loading occurs when the laser-driven wakefield profile is significantly changed by the electron bunch-induced wakefield, leading to degradation of the accelerated electron beam. This can be seen in the profile of E_z in the first bucket of Figure 1.8b. This effect sets an upper limit on the maximum number of electrons, N_{max}, that can be trapped in the wakefield before these electrons collectively generate their own wakefield, stopping further trapping.

Beam loading also has an effect on the electron energy spread. As the number of electrons, N, approaches N_{max}, the electrons in the front edge gain energy from the un-degraded wakefield, while those in the back edge gain energy from the degraded wakefield, resulting in a different energy gain. Katsouleas et al. [48] showed that the energy spread due to beam loading scales with N. Therefore when N reaches N_{max}, the induced energy spread becomes very large, possibly up to 100 %.

Wakefield phase velocity

In laser wakefield acceleration, the wakefield phase velocity, v_ϕ, is a crucial parameter because it determines:

- the minimum energy for electrons to be trapped,
- the dephasing length,
- and therefore the maximum energy gained by trapped electrons.

In the linear limit, v_ϕ is estimated to be equal to the laser group velocity, v_g. Using the dispersion relation in Equation 1.6, the Lorentz factor associated with v_ϕ is $\gamma_p \simeq \omega/\omega_p$ (Equation 1.18).

In the 1D nonlinear regime, analytical calculations have shown that v_ϕ is less than v_g [32, 49]. However, the calculations of v_g from the dispersion relation become inexact due to the dependence of individual waves on the field amplitude. C. Decker et al. [32, 50] argued that the laser loses energy by sustaining the wakefield, and therefore the front of the laser effectively moves backward at a rate given by the etching velocity v_{etch}. In their paper, the laser energy depletion for very high intensity was analysed in 1D using quasi-static approximation and obtained exact analysis using PIC simulations, where the etching velocity is estimated as $v_{etch} \simeq c\,(\omega_p/\omega)^2$. As the laser energy is used to generate the nonlinear plasma waves, the laser pulse profile steepens, forming a sharp front edge. Moreover, a large density spike (with a narrow width) in front of the laser is also formed. The v_{etch} is estimated by the rate at which the laser energy is depleted along the density spike. Therefore the 1D nonlinear wakefield phase velocity is the difference between the laser group velocity and the etching velocity,

$$\begin{aligned} v_\phi = v_g - v_{etch} &\simeq c\left[1 - \frac{1}{2}\left(\frac{\omega_p}{\omega}\right)^2 - \left(\frac{\omega_p}{\omega}\right)^2\right] \\ &\simeq c\left[1 - \frac{3}{2}\left(\frac{\omega_p}{\omega}\right)^2\right] . \end{aligned} \tag{1.26}$$

Following this argument, W. Lu et al. estimated (and refined using PIC codes) that the Lorentz factor associated with the 1D nonlinear v_ϕ is $\gamma_p = \sqrt{a_0}\ \omega/\omega_p$ and for 3D nonlinear limit is $\gamma_p = (1/\sqrt{3})\omega/\omega_p$ [39]. Since $v_\phi < v_g$, the trapping threshold for electrons is lowered. This also indicates that the dephasing length is reduced, limiting the maximum energy gain. Since in 3D nonlinear regime, the acceleration length is approximately the bubble radius, R, the dephasing length is then estimated as [39],

$$L_d \simeq \frac{c}{c - v_\phi} R \simeq \frac{2}{3} R \left(\frac{\omega}{\omega_p}\right)^2 . \tag{1.27}$$

1.1.8 Characteristics of electrons from LWFA

In a useful accelerator, it is important that the conversion efficiency of the laser driver to the plasma wave is high. This implies that the dephasing length is well matched to the pump depletion length, $L_d/L_{pd} \simeq 1$ [51],

$$\begin{aligned} L_d &\simeq L_{pd} \\ \frac{\omega_o^2}{\omega_p^2}\lambda_p &\simeq 2\frac{\omega_o^2}{\omega_p^2}\lambda_p a_o^{-2} , \end{aligned} \tag{1.28}$$

in the linear limit, leading to the condition that the laser driver conversion efficiency to the wakefield is proportional to $a_0^2/2$. Hence, to obtain high efficiency, the laser intensity should be very high ($a_0 > 1$). This suggests in the bubble regime the conversion efficiency is high.

The accelerated electrons should also have good quality.

- **High energy**. Both linear and 1D nonlinear limits scale equally with a_0^2 and γ_p^2, which means that higher energy is achieved by either going to high intense lasers or lower plasma densities. However, in the 3D nonlinear limit, the energy gain only scales linearly with a_0 and it is important to use lower densities. Comparisons of the maximum energy achieved for these three different regimes are shown in Figure 1.10.

- **Electron bunch duration**. An intrinsic property of laser accelerated electrons is the ultra-short bunch duration (σ_z), which is a fraction of the plasma wavelength and independent of the laser strength parameter. Since the simultaneous focusing and accerating occurs at $\lambda_p/4$, it can be estimated that $\sigma_z \geq \lambda_p/4$. For the densities considered in LWFAs, this duration is in the order of femtoseconds.

- **Tranverse beam emittance**. Emittance is a figure of merit that describes the particles distribution in phase space. Typically, the beam emittance is estimated at the beam waist, where it is approximately equal to the product of the source size, σ_r, and divergence, σ_r' (since at focus σ_r and σ_r' are uncorrelated). The source size is the statistical variation of the electron transverse position, while the divergence is the spread of its transverse momenta. The transverse fields have focusing and defocusing regions. The focusing region causes the electrons to oscillate transversely (betatron oscillations) at the betatron frequency, $\omega_\beta = 2\pi c/\lambda_\beta$. As the amplitude of betatron oscillation grows, the beam divergence increases. Katsouleas et al. showed that to suppress betatron oscillations, the electron beam size should be smaller than the bubble radius, which in turn, is dictated by the laser spot size [48]. However, if one chooses to go to lower densities (to have larger energy gain), the laser spot size is bigger and therefore the emittance is larger.

  In the bubble regime, both the transverse and longitudinal forces are linear, hence the transverse normalised emittance is approximately constant. This implies that the emittance is determined by the initial trajectories of the electrons trapped in the bubble. The emittance is therefore related to the self-injection process. If the electrons are trapped on axis, then the transverse forces are small and the emittance is low. This will reduce the initial beam size and divergence.

  However, this changes if the laser parameters are not well matched to the bubble radius. If the pulse duration is constant and larger than the bubble radius, then the emittance will grow for higher densities since there is a higher probability that the injected electrons will interact with the back of the laser driver [26, 52].

The evolution of the electron bunch properties after self-injection are calculated, as shown in Figure 1.12. These were obtained using the 3D PIC code OSIRIS for the same conditions of Figure 1.8a. Self-injected electrons with initial energy $\gamma = 100$ ($\sim 51\,\mathrm{MeV}$) are monitored as they propagate through the bubble and their properties (i.e. emittance, energy and transverse and longitudinal bunch sizes) are calculated. The beam source size is initially large at the onset of self injection, and then fluctuates. However, the average of the width variations is approximately constant. It shows that the growth in emittance is determined by the transverse forces experienced by the electrons during the self-injection mechanism, and remains constant inside the bubble. The slight growth of the

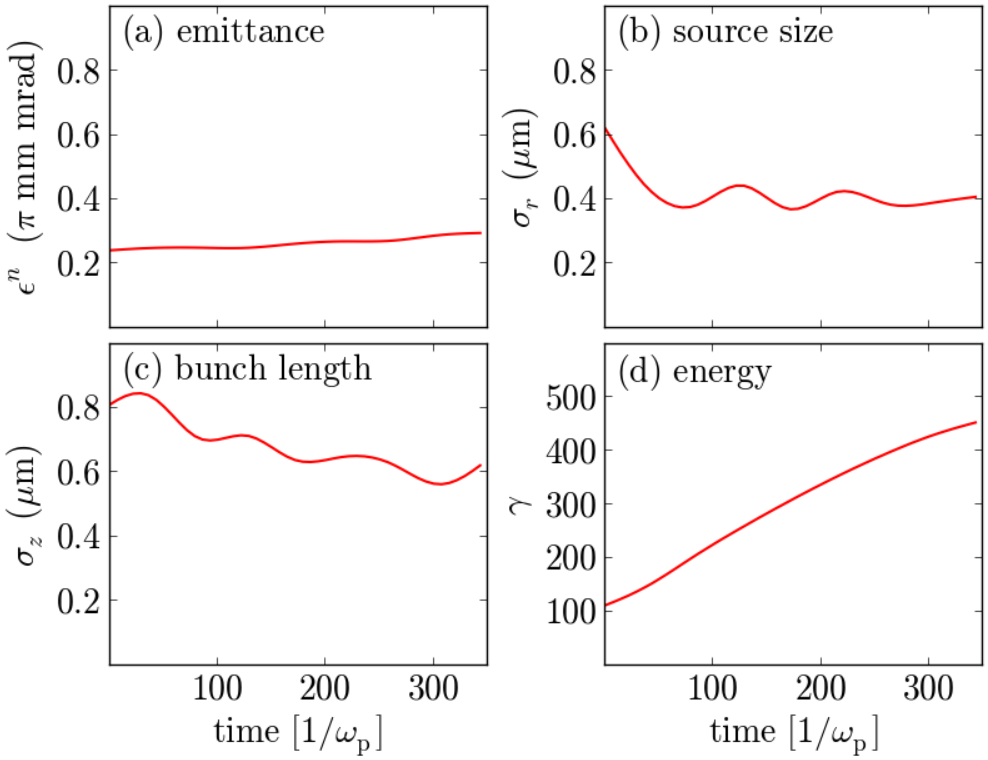

Figure 1.12: Electron beam evolution from 3D PIC code OSIRIS simulations with $a_0 = 2$ and $n_e = 10^{19}\text{cm}^3$. Electron beams are tracked and the following quantities are calculated: (a) emittance (b) source size and (c) bunch length with energy equal to 100 MeV after self-injection (courtesy of M.R. Islam).

emittance after self-injection shown in Figure 1.12 might be a numerical artifact, as discussed in Ref. [53].

LWFA: List of symbols

Symbol	Definition
m_e, e	electron's mass, charge
c	speed of light
λ_p, k_p, ω_p, n_e	plasma wavelength, wavenumber, frequency, density
n_{cr}	critical density
δn	density perturbation
a	normalised (to $m_e c$) laser intensity
λ, k, ω, τ	laser central wavelength, wavenumber, frequency, pulse duration
v_p, v_g	electromagnetic field phase velocity, group velocity
η	refractive index
r_0	laser spot size
z_R	Rayleigh range
λ_{Np}	Nonlinear plasma wavelength
v_ϕ	plasma wave phase velocity
E_z	plasma wave longitudinal electric field
E_r	plasma wave transverse electric field
E_{max}	plasma wave maximum amplitude
E_0	cold linear wavebreaking limit
E_{WB}	nonlinear wavebreaking limit
ψ	plasma wave electronstatic potential
$\zeta = z - v_\phi t$	coordinate of co-moving frame
W	maximum energy gain of electron in plasma wave
L_d	dephasing length
L_{pd}	pump depletion length
R	bubble radius
ϵ	electron beam emittance
$\sigma_{x,y}$, $\sigma'_{x,y}$	electron beam source size and divergence
σ_z	electron beam bunch duration

Chapter 2

Application of beam dynamics to laser-driven electron beams

Electron beams from laser wakefield accelerators are promising candidates to be the drivers of coherent radiation sources and free-electron lasers (FELs) [8,52,54]. Rapid advances in high power laser technology have led to many breakthroughs in LWFAs, which have reached electron energies beyond 1 GeV [19]. Currently, researchers are in the direction of investigating new acceleration mechanisms to further improve the quality of these electron beams, for example by using new plasma sources (tapered capillary waveguides and gas cells) [18,55], staged acceleration [20] and plasma density profile tailoring to control the injection [56, 57]. For an accelerator, reproducibility and stability are very important. However, LWFAs still suffer from large energy spread and divergence. To date, the smallest energy spread measured is in the order of a few percent ($< 1\,\%$) [20, 58, 59], while the smallest rms divergence achieved is ~ 1 mrad [18, 60].

An equally important part of making laser wakefield acceleration (LWFA) drivers of the next generation radiation sources is their development as "accelerators", such that they are easily accessible to application users on a daily basis. This requires a good transport system, capable of maintaining the electron beam properties during propagation. The beam quality is best quantified by its emittance, which is loosely defined as the volume occupied by the beam distribution in phase space (which defines the particle state in position and momentum coordinates). The smallest transverse normalised emittance directly measured so far for LWFA is $\sim 0.2\,\pi$ mm mrad for 250 MeV electron beams [28]. Small emittance indicates high focusability and the potential of generating high quality radiation sources. Moreover, emittance is a conserved quantity in linear systems, hence it can be considered as a figure of merit to describe the quality of the electron beam throughout the system. However, in practice, beams can experience nonlinear forces or other effects that can increase the emittance, such as chromatic aberration, transport system misalignment and scattering from foils or background gases.

This chapter focuses on the possibility of transporting laser produced elec-

tron beams and discusses the limitations that might arise using a simple linear beamline (shown in Figure 2.5) based on the current transport system of the ALPHA-X accelerator. A review of emittance and beam dynamics is first presented, which is mainly based on references [61–64]. The numerical analysis of the transport system is performed using GEANT4, a simulation toolkit for particle interaction with matter [65] capable of modelling non-ideal beams (using Monte-Carlo methods), such as those having large energy spread and shot to shot pointing stability (which are common issues with laser-driven electron beams). The geometry of the beamline, including optical elements such as quadrupoles, spectrometer and foils, can be modeled and determine the beam response upon propagation through these elements. Misalignments of beamline elements, such as rotation and translation errors, can also be investigated.

2.1 Beam emittance

2.1.1 Liouville's theorem

When dealing with many particles, the study of their motion can be facilitated by using canonical coordinates, $(\mathbf{q}(t), \mathbf{p}(t))$, where $\mathbf{q}$ and $\mathbf{p}$ are the particle position and canonical momentum. The coordinates $\mathbf{q}$ and $\mathbf{p}$ form a six-dimensional mathematical space known as phase space. At any time t, each particle is represented by a single point in phase space and the particles distribution occupies a volume $V(t)$. As particles move in time, the shape and orientation of the region they occupy will change, but for conservative systems its volume remains constant(i.e. $\mathrm{d}V(t)/\mathrm{d}t = 0$). This is known as Liouville's theorem and applies for example to systems of non-interacting particles subject to non-dissipative forces, such as magnetic fields and forces which do not depend on velocity.

The six-dimensional phase space volume can be decomposed into three phase space areas, by projecting on each planes. In cartesian coordinates, these three orthogonal phase spaces are $\mathbf{x} - \mathbf{p}_x$, $\mathbf{y} - \mathbf{p}_y$ and $\mathbf{z} - \mathbf{p}_z$, where $\mathbf{x}$ and $\mathbf{y}$ are the tranverse coordinates and $\mathbf{z}$ is the preferred propagation direction. If the motion of the particles is uncoupled along the three planes, then the area, $A(t)$, is also invariant with time.

2.1.2 Geometrical description of the beam

The motion of a particle can be described by its position components, x, y and z and mechanical momentum components, p_x, p_y and p_z. An ensemble of particles

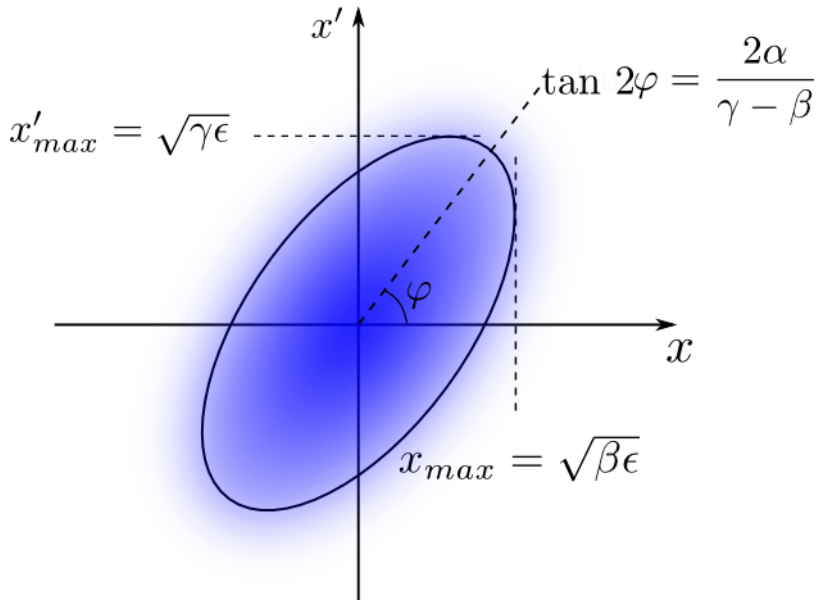

Figure 2.1: Trace-space ellipse in $x - x'$.

is considered a "beam" if the longitudinal momentum is much larger than the transverse momenta, i.e. $p_z \gg p_{x,y}$. Furthermore, in describing the properties of the beam, it is more convenient to use the slope of the particle trajectories, x', y', rather than the mechanical momenta. Using paraxial approximation, the horizontal transverse coordinate, x' can be expressed as

$$x' = \frac{\mathrm{d}x}{\mathrm{d}z} \approx \frac{\dot{x}}{\dot{z}} \approx \frac{p_x}{p_z} \,, \tag{2.1}$$

transitioning from the phase space to the trace space, $x - x'$. Unlike phase space where the coordinates are usually functions of time, the position in trace space is typically defined in terms of the longitudinal coordinates (i.e. $x = x(z)$). For simplicity, most of the discussions here consider only the horizontal plane ($x - x'$), however, similar relations will also hold for $y - y'$ trace space.

It is often convenient to describe the beam distribution in trace space as an ellipse (shown in Figure 2.1) with equation

$$\gamma x^2 + 2\,\alpha x x' + \beta x'^2 = \epsilon_x \,, \tag{2.2}$$

where γ, α, β and ϵ are called Twiss parameters and $\beta\gamma - \alpha^2 = 1$. As the beam evolves, γ, α and β vary accordingly, resulting in changes of size and orientation of the trace space ellipse.

The area occupied by the ellipse is called the beam emittance, ϵ, given by

$$A_x = \int_{ellipse} \mathrm{d}x\,\mathrm{d}x' = \pi\,\epsilon_x\ . \tag{2.3}$$

This is sometimes called the geometrical emittance of the beam. It is common to drop the factor π in the calculation of the area and just attach it to the units of emittance, which is in π mm mrad. When dealing with real beams with complex shapes, geometrical emittance is often calculated by finding an ellipse which encloses 95 % of the particle distribution. However, this is an arbitrary condition and one can make different choices such as ellipses containing 90 % or 100 % of the beam distribution. The horizontal and vertical emittances, ϵ_x and ϵ_y, are called transverse emittances, while ϵ_z is the longitudinal emittance. Unless specified, this chapter focuses only on the transverse emittances of the beam.

2.1.3 Statistical description of the beam

The definition of emittance introduced in the previous section is tailored for a perfectly elliptical phase space distribution, however, in practice, not all beams have a well defined shape. Lapostolle [66] and Sacherer [67] proposed the concept of "equivalent beam", where two beams having different phase space distributions but with the same energy and charge density are equivalent if their first and second moments are the same. Therefore, these beams can be described using their rms values. The first moments, $\langle x\rangle$ and $\langle x'\rangle$, represent the mean position and pointing of the particle distribution, while the second moments, $\langle x^2\rangle$ and $\langle x'^2\rangle$, are the standard deviation from the mean, and can be used to quantify the beam width and divergence. The "rms emittance" is defined as:

$$\epsilon_{x,rms} = \left(\langle x^2\rangle\langle x'^2\rangle - \langle xx'\rangle^2\right)^{1/2}. \tag{2.4}$$

The term $\langle xx'\rangle^2$ gives the correlation between x and x', which for the ideal case approaches zero at the beam waist.

Equation 2.4 measures the spread of the particles, and is not limited to a well-behaved ellipse. Therefore, ϵ_{rms} defines the transverse quality of a beam, and can be viewed as the statistical "mean area" of the distribution. Unlike the geometrical emittance, ϵ_{rms} gives more weight to the sides and tails of the particle distribution in trace space. As a result, usually, $\epsilon_{rms} > \epsilon$. As an example, for a Gaussian beam distribution truncated at two sigma, $\epsilon_{rms} = 4\epsilon$. In transport systems where a beam passes through a series of focusing elements, the geometri-

cal emittance remains the same, however, the beam distribution is progressively distorted and deviates from being an ellipsoid. In this case the rms emittance increases.

Emittance alone does not completely define the quality of the beam. For applications where the beam current for a given emittance is more important, a parameter called beam "brightness" is commonly used. For a distribution that can be described using Equation 2.2 and has a total current, I, the average brightness, $\bar{B}$, is [62],

$$\bar{B} = \frac{2\,I}{\pi^2\,\epsilon_{x,rms}\,\epsilon_{y,rms}}. \tag{2.5}$$

For a focused charged particle beam, the brightness directly dictates the achievable highest intensity at the focus.

In systems where acceleration is involved, the longitudinal momentum increases while the transverse momenta usually remain constant, resulting in a decrease in divergence and therefore in rms emittance. It is useful to introduce a new definition of rms emittance which is invariant during acceleration. This is known as "normalised rms emittance",

$$\epsilon^n_{rms} = \beta\gamma\,\epsilon_{rms}\ , \tag{2.6}$$

where $\beta = v/c$ (v is the speed of the charged particle and c is the speed of light) and $\gamma = 1/\sqrt{1-\beta^2}$ is the Lorentz factor associated with the velocity v. The normalised rms emittance is usually convenient in comparing the quality of two beams with different energies. Similarly, the normalised brightness is

$$B^n = \frac{2\,I}{\pi^2\,\epsilon^n_{x,rms}\,\epsilon^n_{y,rms}} = \frac{\bar{B}}{\beta^2\,\gamma^2}\ . \tag{2.7}$$

The emittance considered so far is also called projected emittance to distinguish it from the emittance of a longitudinal slice of the electron bunch, which is known as slice emittance and will be introduced in Section 2.3.4.

2.1.4 Conservation of emittance

For paraxial beams propagating in linear systems, where the forces do not depend on the velocity, and when no acceleration or deceleration is involved, the trace space is approximately equal to the phase space, and the area in trace space is also invariant. In this special case, the Liouville theorem is valid also in the trace space and hence, emittance is conserved. However, in general, emittance is not

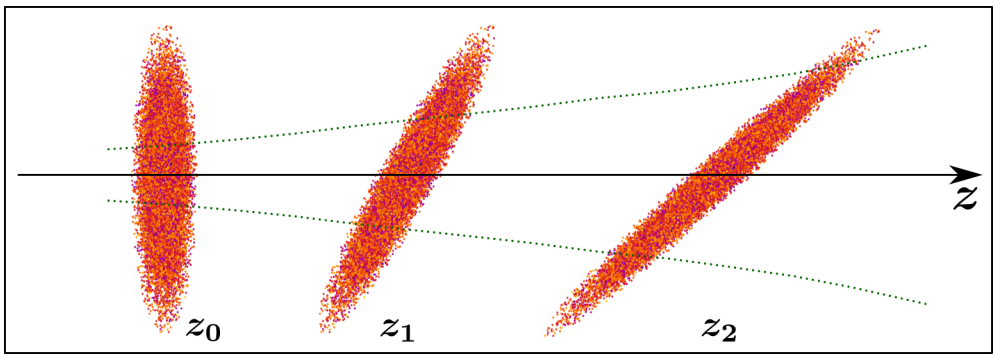

Figure 2.2: Transverse phase space evolution of an electron beam propagating in a drift space. The beam waist is at z_0. The dotted green curves show the beam envelope.

always time invariant. When there is acceleration, the emittance decreases with increasing longitudinal momentum. This leads to the introduction of normalised rms (or geometrical) emittance, which is constant during acceleration. Similarly, the normalised brightness is also a conserved quantity. Normalised emittance is very useful in designing a linear transport system. Ideally, normalised emittance is constant for linear beamlines, hence a growth indicates that there are nonlinear forces affecting the motion of the beam and degrading its quality. The main challenge in designing beam transport systems is the ability to preserve the normalised emitance and avoid sources of emittance growth.

2.2 Phase space evolution in a linear transport system

In the study of transport systems, beam properties are described using the Twiss parameters α, β and γ, which describes the beam envelope evolution in a given system. When a beam propagates in vacuum, the size and orientation of its phase space ellipse change while the area remains constant. As shown in Figure 2.2, the beam distribution in phase space rotates clockwise as the electron beam expands. The corresponding betatron function $\beta(z)$ is

$$\begin{aligned} \beta(z) &= \beta_0 - 2\alpha_0\, z + \gamma_0\, z^2 \\ \alpha(z) &= \alpha_0 - \gamma_0\, z \\ \gamma(z) &= \gamma_0\ , \end{aligned} \tag{2.8}$$

where α_0 , β_0 and γ_0 are the Twiss parameters at the beam waist.

The phase space ellipse at the beam waist is upright (as displayed in Fig-

ure 2.2), with no correlation between the position and divergence of the beam. Therefore, $\alpha_0 = 0$ and $\gamma_0 = 1/\beta_0$ (using the geometrical correlation of the Twiss parameters: $\beta\gamma - \alpha^2 = 1$). The rms width, Δx_0, and divergence , $\Delta x'_0$, at the waist are related to the Twiss parameters by:

$$\begin{aligned} \Delta x_0 &= \sqrt{\beta_0 \epsilon} \\ \Delta x'_0 &= \sqrt{\gamma_0 \epsilon}. \end{aligned} \tag{2.9}$$

Hence, at the beam waist, the emittance is just the product of the beam width and divergence.

Away from the waist, $\alpha \neq 0$ and the ellipse is tilted. Therefore, the parameter α indicates the inclination angle of the ellipse at a given position. On the other hand, the parameters β and γ correspond to the beam envelope and divergence, with β evolving as $\beta(z) = \beta_0 + z^2/\beta_0$. Hence, at any point, the beam properties can be obtained from the Twiss parameters, if the initial conditions, β_0, α_0, γ_0 are known.

To guide electron beams in a beamline, focusing forces are needed, such as solenoids, magnetic dipoles and quadrupoles. A dipole magnet produces a uniform magnetic field over its length. Charged particle beams propagating through the magnetic dipole move in a circle in the direction orthogonal to the magnetic field. They are widely used in circular accelerators. In linear accelerators, quadrupoles are utilised to obtain strong focusing without changing the propagation direction of the beam. Quadrupoles have magnetic fields that increase linearly with the distance from the axis. They can be generated by orienting four magnetic poles as shown in Figure 2.3a.

For a positively charged beam propagating into the page, the arrangement presented in Figure 2.3 produces a force with a horizontal component directed towards the centre and a vertical component directed away from the axis. This is conventionally called a focusing quadrupole while a rotation by 90° converts the arrangement to a defocusing quadrupole. Hence, a single quadrupole focuses a beam on one direction and defocuses it in the other direction. Moreover, its focusing strength, k, depends on the beam momentum (energy), according to the equation

$$k = \frac{1}{B\rho}\frac{\partial B_y}{\partial x} = -\frac{1}{B\rho}\frac{\partial B_x}{\partial y}\ , \tag{2.10}$$

where $\partial B_y/\partial x = -\partial B_x/\partial y$ is the magnetic field gradient and $B\rho$ is the magnetic rigidity, which is just another way of representing the momentum of a particle ($B\rho = p_z/e \approx E/(ec)$ for relativistics electrons).

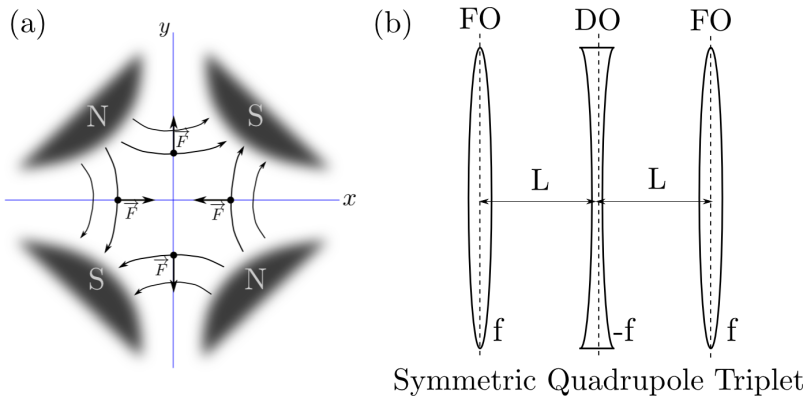

Figure 2.3: (a) Schematic diagram of a magnetic quadrupole, where N-north and S-south indicate the polarity of each magnet. The length of the magnets extends along the particle's propagation direction, z. On the horizontal axis, a positively charged particle moving into the page will experience a force towards the centre (focusing), while it will be pushed away from the centre in the vertical axis (defocusing).
(b) Illustration of a symmetric triplet with focal lengths $|f|$ and separation L.

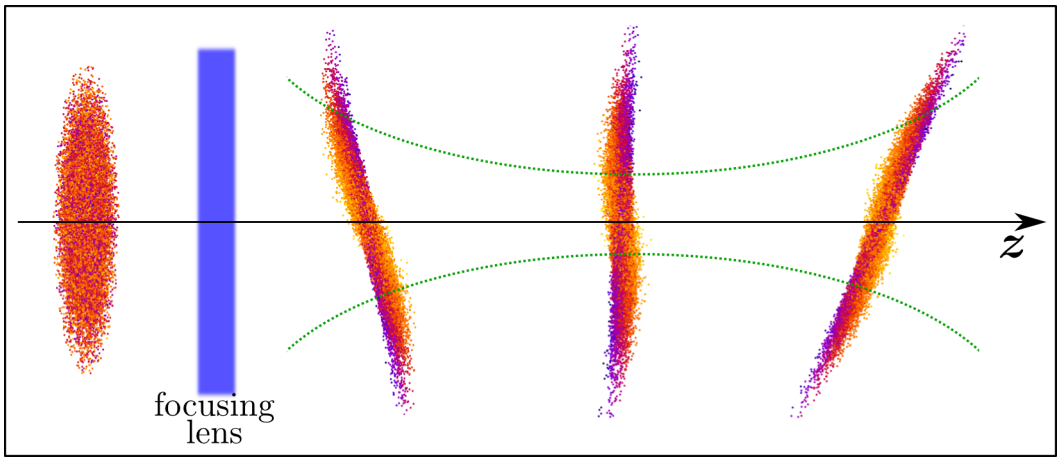

Figure 2.4: Phase space evolution of an electron beam passing through a focusing quadrupole placed after the beam waist. The color of each particle represents its energy, where yellow is highest and purple is lowest. The dotted green curves shows the beam envelope.

When the effective length of the quadrupole, l_e, is much smaller than its focal length, the factor $k\,l_e$ is constant as l_e approaches zero. Here, the focal length is estimated to be $f^{-1} = k\,l_e$, and the quadrupole is considered as a thin lens. This approximation is useful in analytical calculations of simple beam dynamics with quadrupoles. An important characteristic of a quadrupole is the linearity of the force, which means that there is no coupling between the motion in the horizontal and vertical directions. As a result, transport systems containing only dipoles and/or quadrupoles are called linear systems.

Series of quadrupoles are often combined to create lens systems that are capable of focusing the beam in both horizontal and vertical directions. Figure 2.3b shows a symmetric triplet where three quadrupoles with equal strength are arranged in a focusing-defocusing-focusing configuration, which is usually preferred because it produces an effective focusing strength that is stronger than the individual quadrupoles.

The phase space evolution of a beam passing through a quadrupole is shown in Figure 2.4, including the effect of a non-zero energy spread. The energy dependence of the focusing strength is clearly evident in the distortion of the ellipse which causes an increase in the area occupied by the beam, and therefore of the transverse emittance. This emittance growth will be discussed more in detail in the next section.

2.3 Laser-driven electron beam transport using a strong focusing system

Laser driven electron beams can have a large energy spread and divergence. Hence, it can be difficult to transport these beams while preserving their properties. This section discusses the transport of electron beams for the ALPHA-X beamline shown in Figure 2.5. The final properties of the electron beam are calculated at 4.17 m from the accelerator, which is the centre of the undulator.

The beamline has two quadrupole triplets, where the first set is composed of minituarised permanent quadrupoles (PMQs) with strong magnetic field gradients ($\sim 500\,\mathrm{T/m}$) to minimise the beam divergence upon reaching the second triplet. The second triplet consists of electromagnetic quadrupoles (EMQs) where the focusing strength can be varied by supplying a different current. The complete beamline parameters are listed in Table 2.1. The separation distances of the PMQs and the electric currents for the EMQs are calculated using the MAD-X software [68], searching for configurations where the electron beam is focused

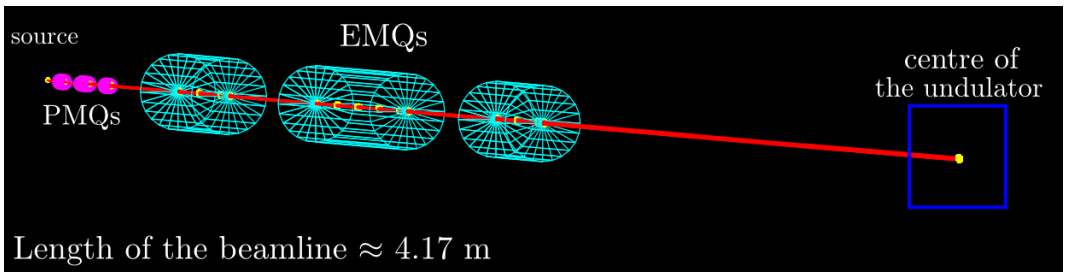

Figure 2.5: The ALPHA-X beamline. It is composed of a triplet of permanent quadrupoles (PMQs) and a triplet of electromagnetic quadrupoles (EMQs) located 9 cm and 161.5 cm from the accelerator, respectively. Simulations have been performed for a total length of 4.17 m, ending at what is assumed to be the centre of a 1.5 m long undulator.

	PMQs	**EMQs**
Magnetic field gradient (T/m)	480, 507, 480	$0.0123I$, $0.0122I$, $0.0123I$ *
Effective length (cm)	1.06, 1.81, 1.06	12.16, 21.8, 12.16
Separation distance (cm)	5.435	37.7
Triplet orientation in the vertical plane	F-D-F	F-D-F
Distance of the triplet centre from the accelerator (cm)	9	161.5

Table 2.1: Specifications of the permanent (PMQs) and electromagnetic (EMQs) quadrupoles used in the simulations. (*Where I is the supplied current (in amperes) that is dependent on the electron beam energy to be optimised.)

down to a size $\sim$ 50 µm at the centre of the undulator for energies between 120 MeV and 170 MeV. The optimisation assumes a normalised rms emittance of 1 π mm mrad, both in horizontal and vertical axis, and negligible rms energy spread, $\Delta E/E$. As shown in Figure 2.6, the focal lengths of the two combined triplets are not the same in x and y.

The magnetic field of the quadrupoles is modeled in GEANT4 using the following equations

$$B_x = k\,x, \quad B_y = -\,k\,y, \quad B_z = 0\,, \tag{2.11}$$

with k as the magnetic field gradient given in Equation 2.10. Equation 2.11 assumes a magnetic field with a sharp boundary, where the field is constant within the effective length of the quadrupole and zero outside of it. The results of GEANT4 simulations have been compared with other available particle tracking codes (GPT and MAD-X) and found to be in good agreement. More details will

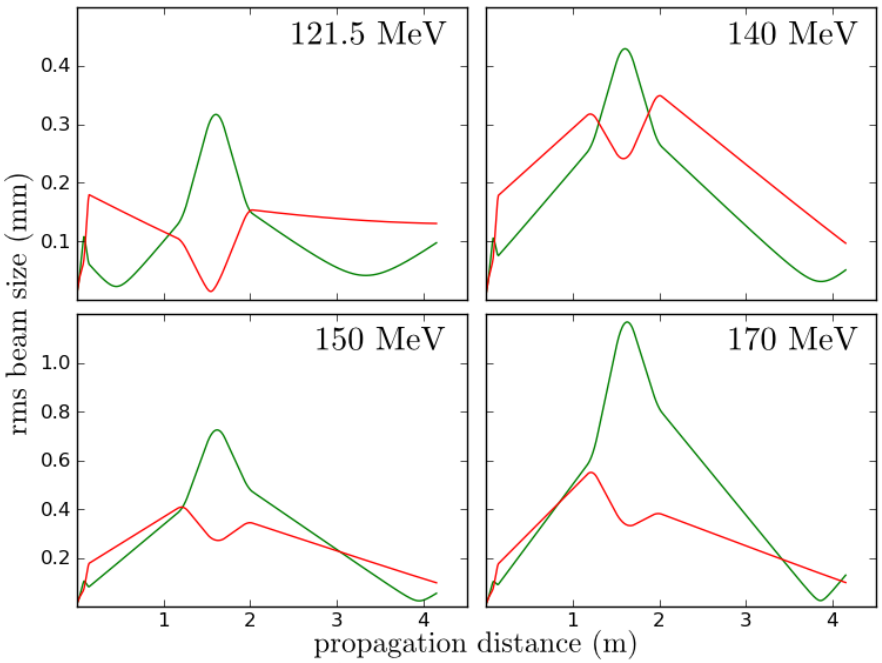

Figure 2.6: Electron beam trajectories in the horizontal x (green line) and vertical y (red line) planes for different energies, in the ALPHA-X beamline. Source parameters: initial $\epsilon^n_{rms} = 1 - 1.3\,\pi$ mm mrad and rms energy spread $\Delta E/E = 0.5\,\%$.

be given in Chapter 5, including simulations where quadrupoles are modeled by a smooth field map.

The initial electron beam profile in the GEANT4 simulations is transversely (x, y) and longitudinally (z) Gaussian with (rms) radius of $\sigma_r^2 = \sigma_x^2 + \sigma_y^2$ and bunch length σ_z. The beam is assumed to be at the waist and therefore the initial rms transverse emittance in one axis is $\epsilon_{source,x,(y)} = \sigma_{x,(y)} \cdot \sigma'_{x,(y)}$, where $\sigma'_{x,(y)}$ is the rms divergence. The rms emittance is calculated for approximately 95 % of the beam distribution. The unit of rms emittance used in this study is in π mm mrad, which is the usual convention used of the LWFA community.

The emittance growth is calculated using the following equation:

$$\Delta\epsilon/\epsilon_{source} = (\epsilon_f - \epsilon_{source})/\epsilon_{source} \tag{2.12}$$

where ϵ_f is the rms transverse emittance at the centre of the undulator.

2.3.1 Space charge effects

In the GEANT4 simulations, the particle-particle interaction is not accounted for, hence it is assumed that the electron beam is emittance and not space charge dominated. The space charge force, F_{sc}, is inversely proportional to electron energy, i.e. $F_{sc} \propto 1/\gamma^2 \simeq 1/(2E)^2$. As the energy increases, the defocusing (due to Coulomb repulsion) and focusing (due to $\mathbf{v} \times \mathbf{B}$ term) balance out, thus the effect of space charge is reduced. F_{sc} also depends on the electron source size, as space charge fields are stronger for higher charge density. Typically, LWFA produces electron beams with source sizes smaller than 10 µm and charge in the order of pC. Because of the short bunch duration, the charge density can be high and space charge can also induce bunch lengthening.

To check the effect of space charge, the propagation of electron beams over a 1 m long drift space is simulated using GEANT4 (no space charge) and GPT (including space charge). Figure 2.7c compares the final bunch length of the electron beam for 5 pC charge, 4 µm source size and 1.2 µm (4 fs) initial bunch length. Space charge increases the bunch length by an amount between 1.5 % and 3 %, which is equivalent to less than a micron. The transverse size is 1 mm in both cases, implying that in these conditions, space charge does not significantly affect the beam transverse properties. As expected, the bunch lengthening decreases with energy. There is also no significant change in bunch length when the electron beam source size is reduced to 1 µm, as shown in Figure 2.7a-b. Similar values are obtained when the charge is increased to 10 pC. Thus, GPT simulations show that neglecting the space charge is valid for charges less than 10 pC and for bunch length that are considered. In the ALPHA-X beamline, charges in the order of 2 – 7 pC are typically obtained.

2.3.2 Chromaticity

The focusing strength of a quadrupole depends on the energy of the beam, i.e. the higher the energy the weaker the focusing strength for a constant magnetic field gradient. On the other hand, low energy beams experience larger deflection leading to shorter focal length (according to Eqn. 2.10). Hence, an electron beam with a finite energy spread propagating through a quadrupole will have a spread on focal points, known as chromatic aberration.

X. J. Wang derived a simple 1D analytical model to estimate the effect on the beam emittance [69] . When an additional spread, $\delta = \Delta E/E$, on the energy is considered, the corresponding quadrupole focusing strength varies accordingly

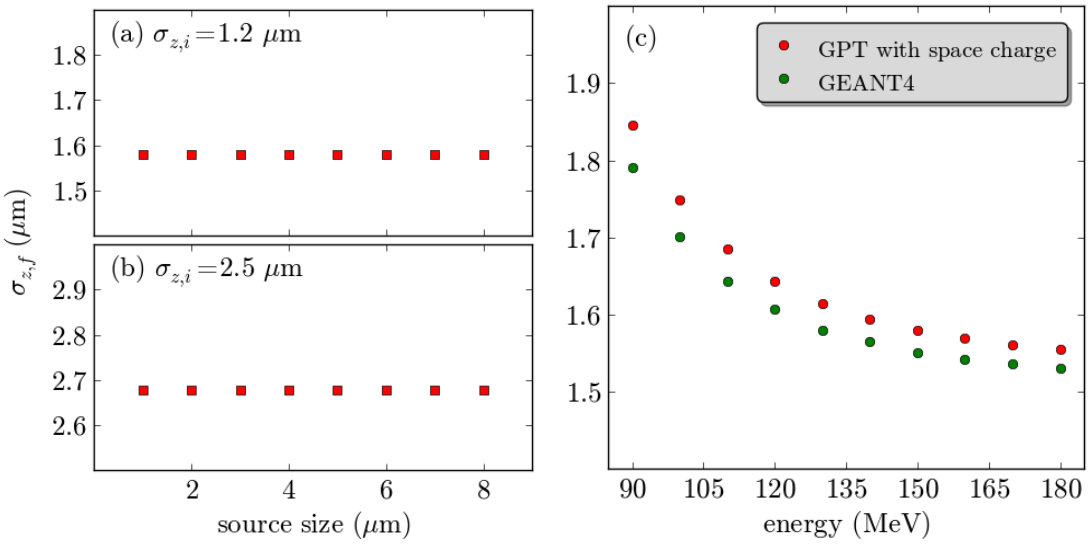

Figure 2.7: Final bunch length after 1 m drift propagation for 5 pC, 150 MeV ± 3 %, 1 mrad electron beams using GPT with space charge for (a) 1.2 µm and (b) 2.5 µm. Comparison with GEANT4 varying the energy is also shown in (c) for initial normalised $\epsilon^n_{rms} = 1\,\pi$ mm mrad.

and is now a function of energy spread,

$$\begin{aligned} (B\rho)^* &= \frac{1}{ec}\,(E + \Delta E) = B\rho\,(1+\delta) \\ k^* &= \frac{k}{1+\delta} \end{aligned} \tag{2.13}$$

where k is the focusing strength of the quadrupole for zero energy spread. A particle with an initial position x_o and zero transverse momentum, $x'_o = 0$, will exit a thin quadrupole at the same position x_o, i.e $\Delta x = 0$. However, the slope of the trajectory changes due to the additional energy spread. Using the transformation matrix of a thin focusing lens [62], the corresponding second moments are

$$\begin{aligned} \langle x_o^2 \rangle &= 0 \\ \langle x_o'^2 \rangle &= \langle x_o^2 / f(1+\delta)^2 \rangle \\ \langle x x' \rangle^2 &= \langle x_o^2 / f(1+\delta) \rangle^2 \end{aligned} \tag{2.14}$$

Assuming that the transverse positions and beam energy have no correlation, the change in emittance is approximately

$$\Delta\epsilon_{rms} \approx \frac{1}{f}\,\langle x_o^2 \rangle \delta_{rms} \tag{2.15}$$

where f is the quadrupole focal length, $\langle x_o^2 \rangle$ is the rms beam size at the entrance of

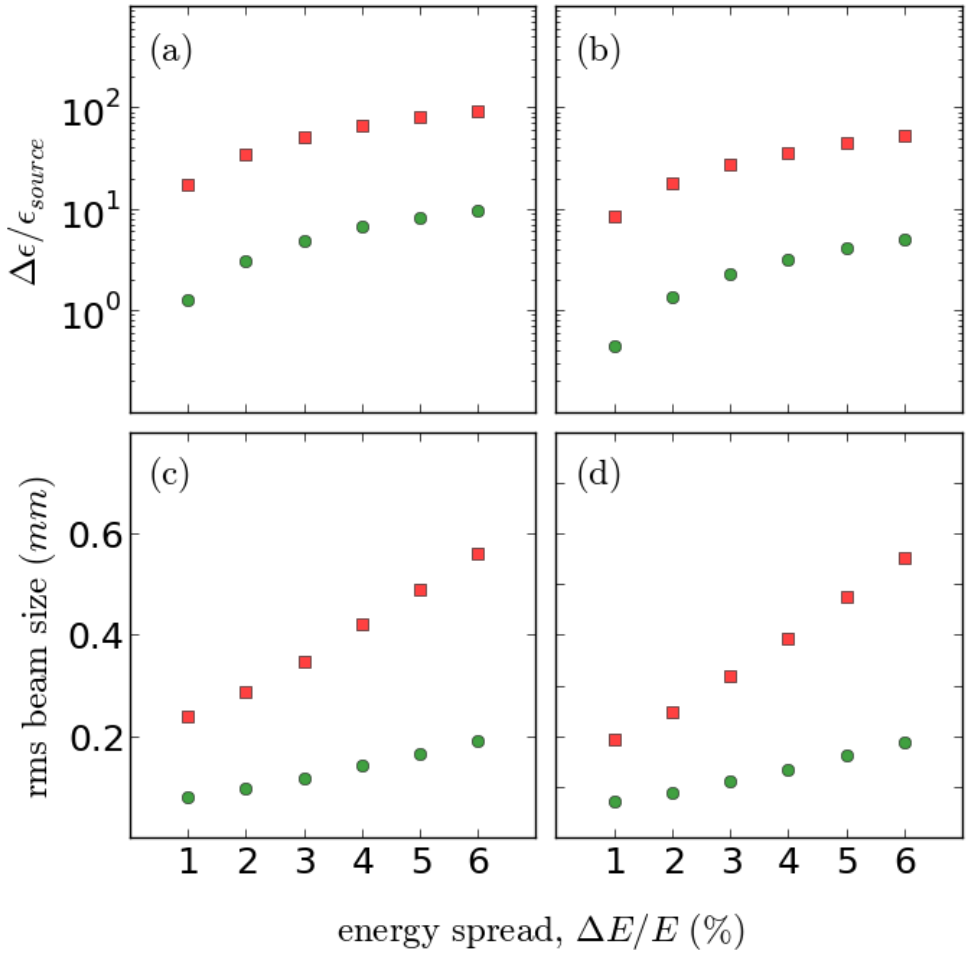

Figure 2.8: RMS beam size and emittance growth in x (figs. (a) and (c)) and in y (figs. (b) and (d)) for a 150 MeV electron beam with an initial normalised rms emittance of $1.2\,\pi$ mm mrad after propagation through the ALPHA-X beamline for divergence of 1 mrad (green circles) and 3 mrad (red squares).

the quadrupole and δ_{rms} is the rms relative energy spread of the beam. Equation 2.15 shows that chromaticity couples the transverse and longitudinal properties of the beam inducing an emittance growth which increases proportionally to the energy spread and to the beam size at the entrance of the quadrupole. Moreover, the chromatic emittance growth decreases as $1/f$, i.e. lower energy is more prone to chromaticity. It is worth noting that there is no chromatic effect when the energy spread of the beam is zero.

GEANT4 simulations have been performed for the geometry in Figure 2.5 and electron beams with energy $E = 150$ MeV (Lorentz factor $\gamma = 295$), which is at the centre of the energy window for the optimised beam transport.

Figure 2.8 shows emittance growth of an electron beam with an initial $\epsilon^n_{rms} =$

$1.2\,\pi$ mm mrad after propagation through two sets of triplets. The gaps between the PMQs are fixed (where the distances are given in Table 2.1), while the currents supplied through the EMQs are obtained from the optimisation done in MAD-X. As the rms energy spread increases ($\Delta E/E > 1\,\%$), the rms emittance grows by more than an order of magnitude, with a corresponding blow up of the transverse beam size as shown in Figure 2.8 c and d. In fact for $\sigma'_x = 3\,\text{mrad}$, the rms beam size rapidly grows reaching 1 mm at $\Delta E/E = 6\,\%$, implying that the transport system is loosing its focusing ability. Since the transport system has more focusing elements oriented along the vertical axis, the emittance growth in x is significantly larger (almost double) than in y. To avoid the rapid emittance growth due to chromaticity along the beamline, energy spread of less than or equal to 1 % and divergence of 1 mrad are needed.

In addition to degrading the emittance, large energy spreads also change the beam envelope evolution as shown in Figure 2.9a. The spot size increases significantly with larger energy spread, implying that the phase space portraits are distorted. It is also interesting to note that the huge jump in emittance occurs at the second EMQ, where the electron beam experiences the largest focusing field in x.

On the other hand, varying the divergence while keeping the energy spread constant does not distort the beam, as shown in Figure 2.9b. The focal position is maintained and the growth in emittance is only due to the large transverse size of the beam at the entrance of the triplets (consistent with Equation 2.15). According to Figure 2.9, the increase in emittance is more pronounced for electron beams with large energy spread rather than large divergence. In ideal case, where the energy spread is zero, electron beams with 1 mrad and 3 mrad will both have the same emittances and no emittance growth due to chromaticity.

The difference in the effect of divergence and energy spread is clearly seen on the phase space portraits taken after propagation through the two triplets, as shown in Figure 2.10. The phase space distributions of a 2 mrad electron beam are just magnified versions of those obtained for a 1 mrad beam. The transverse beam size increases but the shape is similar and no distortion occurs.

However, the phase space distribution of an electron beam with 2 % energy spread is distorted and occupies a larger area. The spatial profile displays aberrations since different energies are focused at different spatial locations. Since the emittance growth due to energy spread is geometrical and therefore reversible, it can be corrected by using other conventional accelerator devices such as sextupoles.

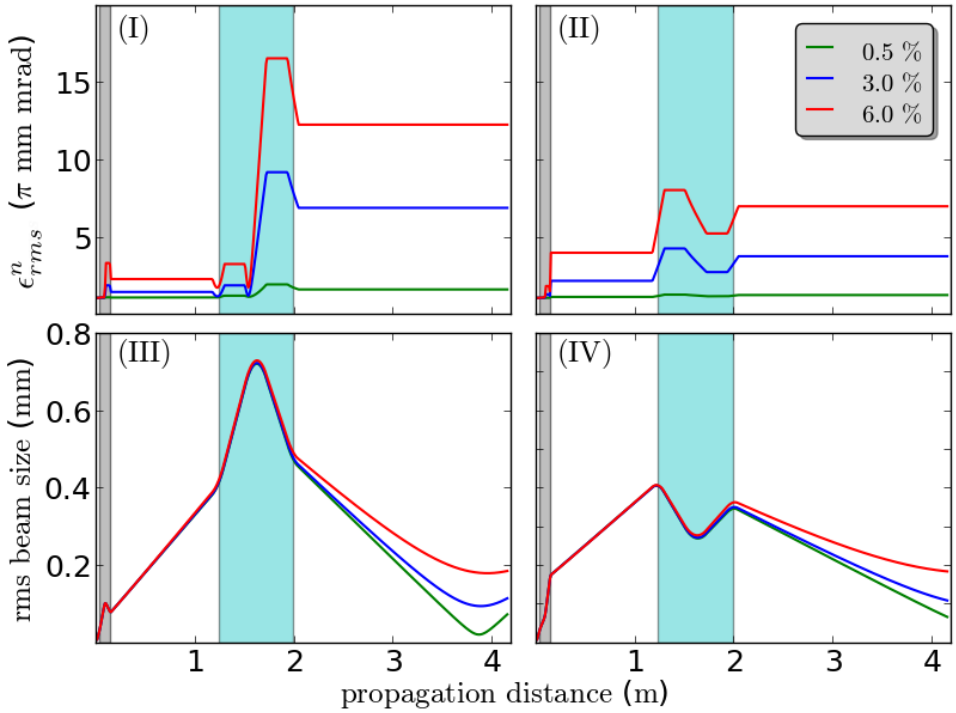

(a)

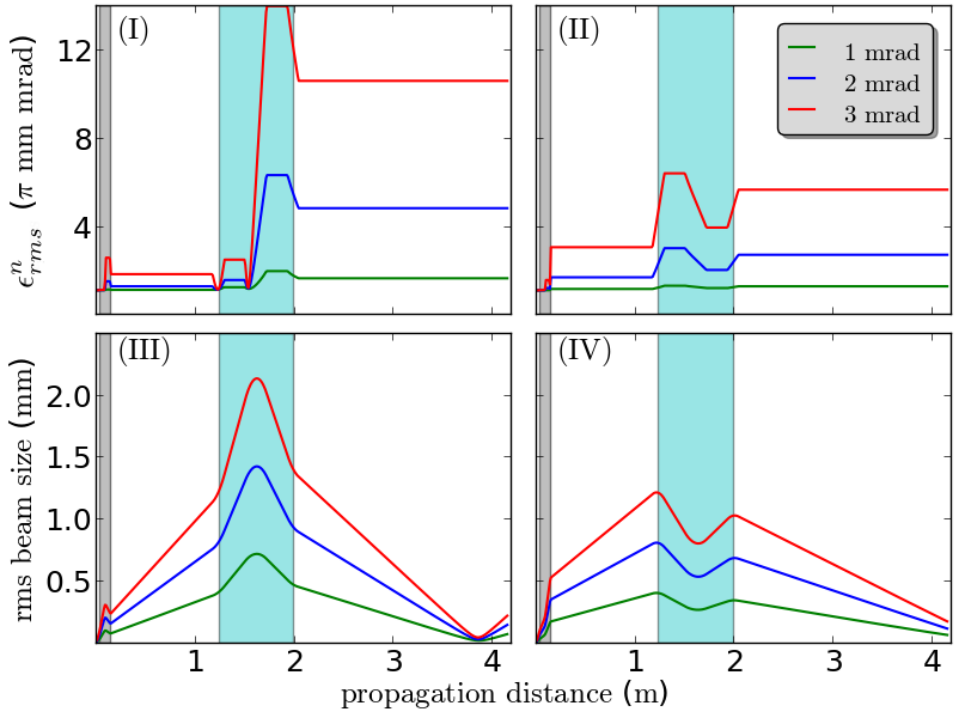

(b)

Figure 2.9: Evolution of the normalised rms emittance and rms beam size of an electron beam with energy of 150 MeV and normalised rms emittance of 1.2 π mm mrad (a) versus rms energy spread for a divergence of 1 mrad and (b) versus the divergence for an rms energy spread of 0.5 %. Figures I and III correspond to the horizontal plane, while figures II and IV to the vertical plane. The grey and blue shaded regions are the locations of the PMQs and EMQs in the beamline.

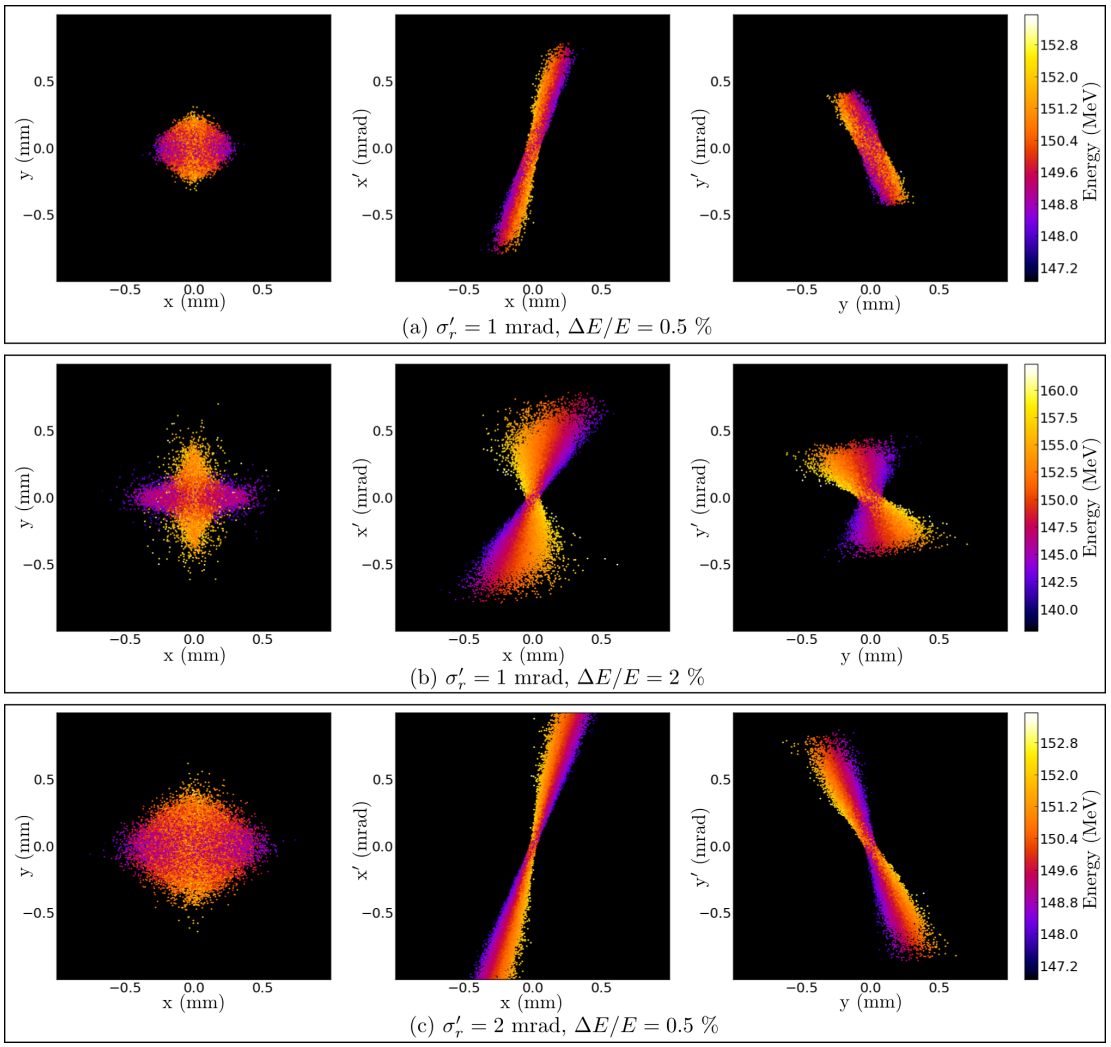

Figure 2.10: Spatial and phase space profiles at the center of the undulator for an electron beam with energy of 150 MeV and normalised rms emittance of $1.2\,\pi$ mm mrad after propagation through the triplets. The colors represent the energy of each particle, as indicated by the colorbar on the right.

The numerical analysis shows that the current beamline is very sensitive to the properties of the electron beam, and therefore unable to maintain important parameters, such as transverse emittance and beam size. The chromatic increase of emittance is mainly due to different tilting of the phase space ellipses for different energy. This growth is therefore reversible and can be solved by installing additional quadrupoles and sextupoles to correct the chromatic effects. However, there is still the problem of beam blow up due to large divergence. A 3 mrad electron beam can have a one to two orders of magnitude transverse emittance growth even at a relatively low energy spread of 1 – 3 %. This is undesirable since the obtainable intensity at the focal position is greatly reduced. Although a more complex beamline could mitigate this problem, it is important to improve the performance of the laser wakefield accelerator to produce low divergence electron beams, for example by devising new injection mechanisms. Similar results have also been shown by [70].

2.3.3 Multiple scattering from thin foils

In most laser-wakefield accelerator setups, a thin foil is placed along the transport system to block the laser beam propagating collinearly with the electron beam. An aluminium foil with thickness ranging from 0.8 to 25 µm is commonly used (in the ALPHA-X beamline) as a laser beam block. Since the foil is very thin, the electron beam size does not grow by passing through it, however, the divergence increases due to the collisions of the electrons with the atoms of the foil. The beam deflection, $\theta_{s,rms}$, after propagation through a scattering material with thickness L is [71]

$$\theta_{s,rms} = \frac{17.5\,\mathrm{MeV}}{\gamma mc^2}\sqrt{\frac{L}{L_R}}\left[1 + 0.125\log_{10}\left(\frac{L}{0.1\,L_R}\right)\right] \tag{2.16}$$

where γmc^2 (in MeV) is the electron energy and L_R is the radiation length of the scattering material, which is directly related to the high energy loss experienced by a particle after interacting with the material. The scattering angle is larger for low energy beams.

The multiple scattering effect on the beam envelope has been analysed by Reid [72], using a one dimensional analytical approach which assumes an electron beam with negligible initial energy spread. At the exit of a foil placed at a distance z from the waist, the divergence of an electron beam is

$$\begin{aligned} x_f'^2 &= x'^2 + \theta_{s,rms}^2 \quad \text{or} \\ x_f' &= x'\left(1+\xi\right)^{1/2}, \end{aligned} \tag{2.17}$$

where $\xi = \theta_{s,rms}^2/x'^2$ and $x'^2 = \epsilon/\beta(z_f)$. The sign of z_f depends on whether the foil is placed before (+) or after (-) the waist. Assuming that the initial emittance is much smaller than the final emittance, the growth in emittance with the foil included is

$$\begin{aligned} \epsilon_f &= \epsilon\ (1+\xi)^{1/2} \quad \text{or} \\ \frac{\Delta\epsilon}{\epsilon} &= (1+\xi)^{1/2}\,. \end{aligned} \tag{2.18}$$

Therefore, ξ dictates the emittance growth due to multiple scattering from a thin foil. This factor is minimised when the foil is placed exactly at the beam waist, where $x'^2 \approx \epsilon/\beta_0$ reaches its maximum and the beam size is the smallest. Furthermore, a very thin foil decreases $\theta_{s,rms}$, (as shown in Figure 2.11a) and significantly reduces the emittance growth. Electron beams with finite energy spread and large divergence have larger transverse sizes at the focus. Hence, aside from the chromatic emittance growth discussed in Section 1.4.1, the emittance will have an additional growth due to multiple scattering as shown in Figure 2.11a-(III).

In a transport system designed to focus a beam inside (at the centre) an undulator, it is not possible to install the foil at the beam waist. Moreover, the foil should be thick enough to block the intense laser radiation. To find a suitable location for an Al foil in the ALPHA-X beamline, GEANT4 simulations have been carried out for the geometry of Figure 2.5. A 150 MeV electron beam with a small energy spread ($\Delta E/E = 0.5\,\%$) is chosen to eliminate the chromatic emittance growth. As shown in Figure 2.11b, $\Delta\epsilon$ is minimised when the Al foil is placed right after the PMQ triplet (15 cm from the accelerator), however, this is experimentally not practical as the foil can be easily destroyed by the intense laser beam. Another option is to place the Al foil at the entrance of the undulator, where the beam is tightly focused by the EMQs. At this location, the emittance increases by a factor of 10 or less. However, an increase in the rms beam size at the focus is unavoidable, with the spot size almost twice as big both in the horizontal and vertical directions.

The additional scattering angle induced by the Al foil completely modifies the beam properties, as shown in Figure 2.12. The location of the focus is displaced proportionally to the distance of the foil from the ideal beam waist and the focused spot size increases. In fact, at $z_f = 1$ m, the EMQ triplet is no longer capable of focusing the beam when the initial values of current for the EMQs are used. As the beam propagates through the foil, the material induces random scattering

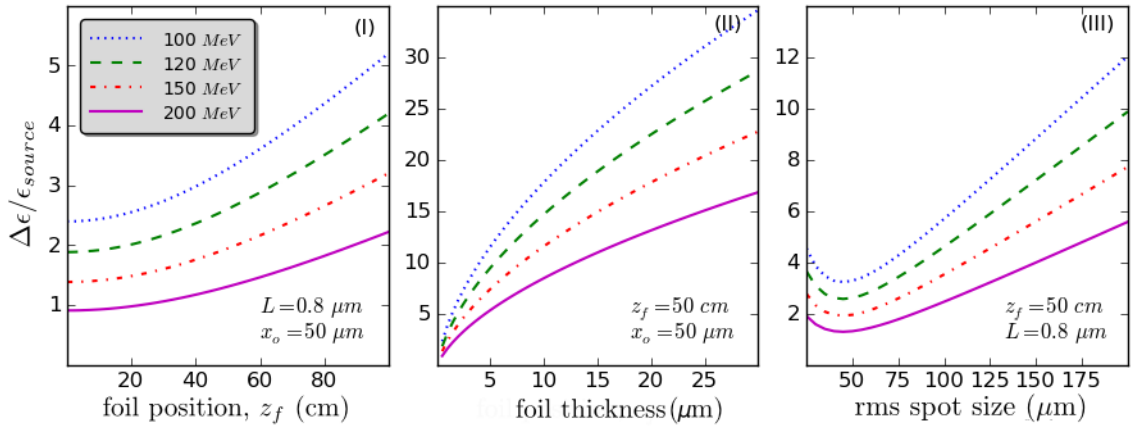

(a) Calculated emittance growth (in one axis) due to multiple scattering in an Al foil using Eqn. 2.18.

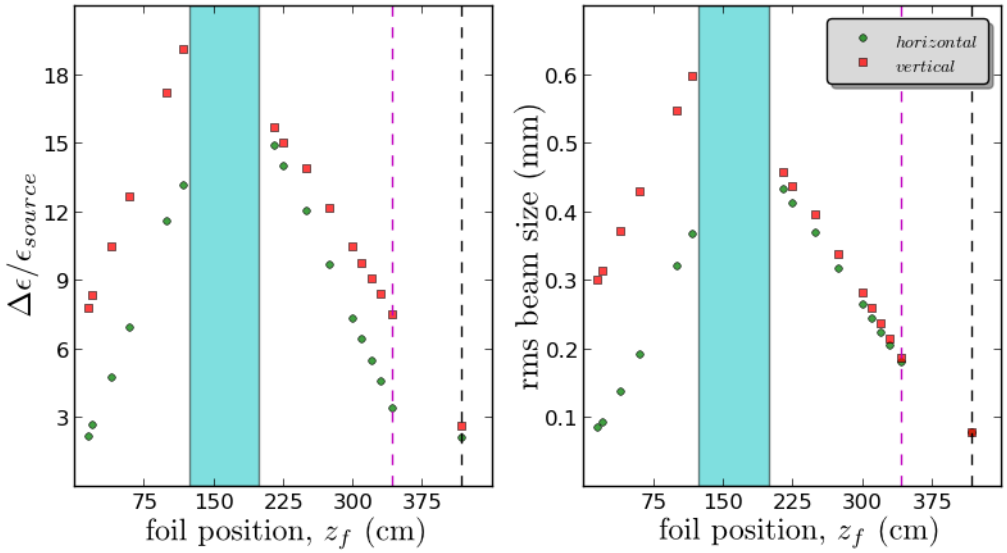

(b) Results of GEANT4 simulations showing the emittance growth and beam size at the centre of the ALPHA-X undulator versus the distance of an 0.8 µm thick Al foil from the accelerator. The electron beam has the following initial parameters: 150 MeV ± 0.5 %, $\epsilon^n_{rms} = 1\,\pi$ mm mrad. The position of the EMQ triplet in the beamline is indicated by the blue shaded region, while the purple and black dashed lines correspond to the entrance and centre of the undulator.

Figure 2.11: Emittance growth due to multiple scattering in an Al foil.

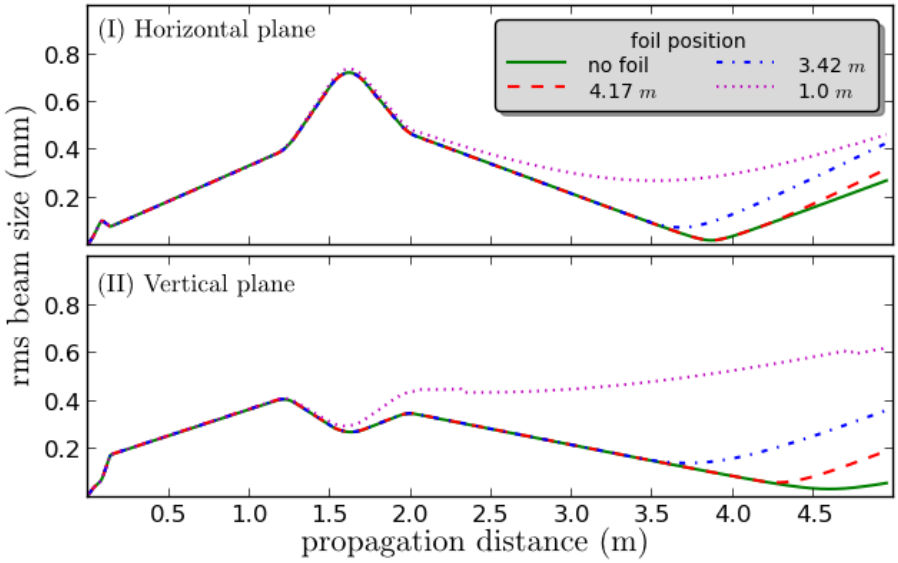

Figure 2.12: Envelope of a 150 MeV ± 0.5 % electron beam passing through a 0.8 µm Al foil placed at different locations in the beamline: 1 m (just before the first EMQ), 3.42 m (undulator entrance) and 4.17 m (centre of undulator).

resulting in an increased in the total divergence. In phase space, this means that foil introduces an additional tilting of the phase space ellipse.

With the Al foil in the beamline, the scattering further increases the emittance growth and gives an additional divergence due to multiple scattering from the foil, as shown in Figure 2.13 for an electron beam with initial rms normalised emittance of $1.2\,\pi$ mm mrad. The emittance grows by 6 – 8 times independently of the energy spread. This is also reflected in the rms beam size at the centre of the undulator, which grows by $\sim 100\,\mu$m both in x and y, independent of the energy spread. The addition of the foil is an example of irreversible emittance growth.

As shown in this analysis, the Al foil introduces additional distortions in the electron beam properties and produces a step-wise increase in the emittace, hence, it is necessary to include the foil transfer matrix in modelling a transport system, particularly for high-brightness beam applications. In this case, a new optimisation configuration is obtained with the Al foil included in the beamline. It is also possible to remove the foil from the beamline by separating the propagation axis of the electron and laser beams. This is achieved by designing a transport system with a chicane type or dog-leg structure, where the electron beam is bent away from the laser axis. However, this will require larger physical space and complex beamline design.

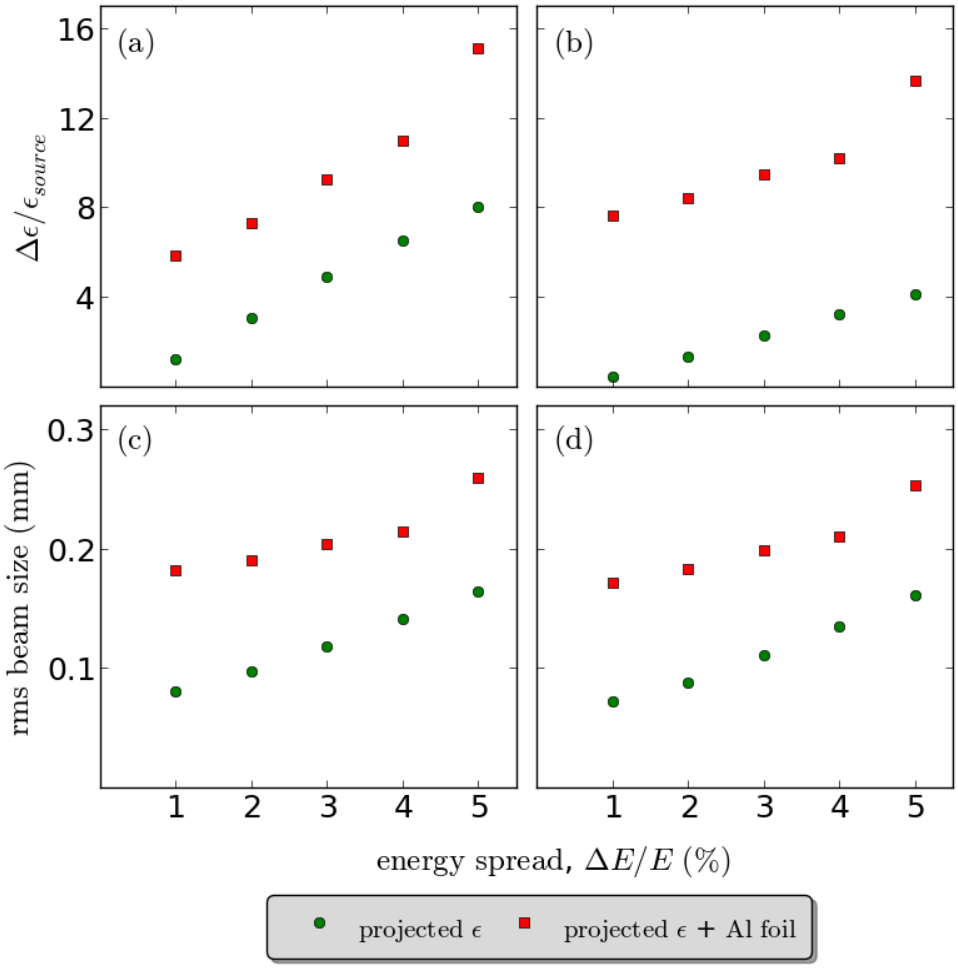

Figure 2.13: Emittance growth and beam sizes in x (figs. (a) and (b)) and y (figs. (c) and (d)) of a 150 MeV electron beam (initial $\epsilon^n_{rms} = 1.2\,\pi$ mm mrad) after propagation through the beamline with (red squares) and without (green circles) the 0.8 µm Al foil located at the entrance of the undulator.

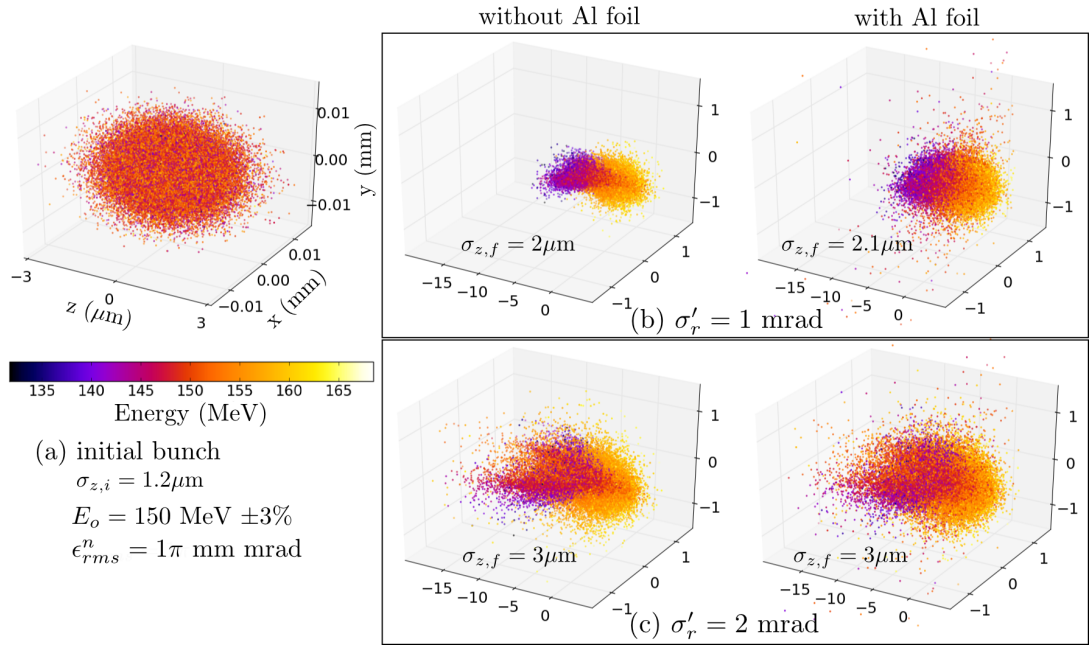

Figure 2.14: Electron bunch distribution at the (a) accelerator and after 4.17 m propagation through the designed beamline with rms divergence of (b) 1 mrad and (c) 2 mrad, where x and y are the transverse coordinates and z is the propagation axis. The color represents the energy of each particle, indicated by the colorbar. The effect of including the Al foil on the bunch distribution is also shown.

2.3.4 Electron bunch lengthening

Laser-driven electron beams inherently have ultrashort (fs range) bunch duration, which is difficult to achieve in conventional particle accelerators. However, divergence and energy spread can cause the bunch to lengthen during propagation. A symmetric bunch where particles with different energies are uniformly distributed will evolve, as shown in Figure 2.14. The high energy part of the beam travels faster than the low energy part, resulting in longitudinal bunch spreading. A large divergence (2.14c) further stretches the bunch, producing an asymmetric bunch distribution, with a long low-energy tail. This can be clearly seen in the histograms of the bunch distribution shown in Figure 2.15. The electron bunch is further distorted when an Al foil is inserted at the entrance of the undulator, resulting in an additional spread in the transverse direction. It is interesting to note that the Al foil has a larger effect on the transverse properties of the beam, with a $\sim 25\,\%$ increase in beam size in contrast to a $1.5\,\%$ increase in bunch length.

The LWFA theory predicts that electron beams are produced with a longitudinal energy chirp [10]. Both positive and negative chirp is achievable by stopping the acceleration before or after the dephasing length. The influence of a

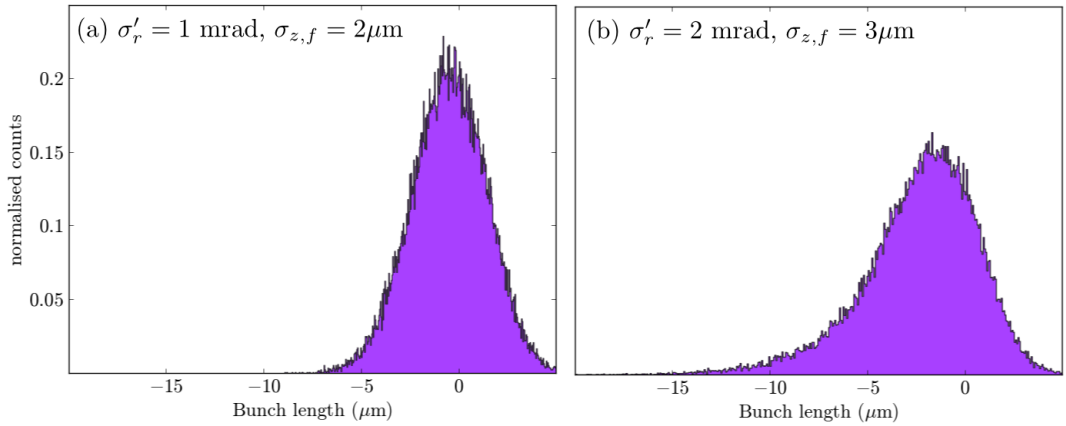

Figure 2.15: Electron bunch distribution for 1 mrad and 2 mrad electron beams.

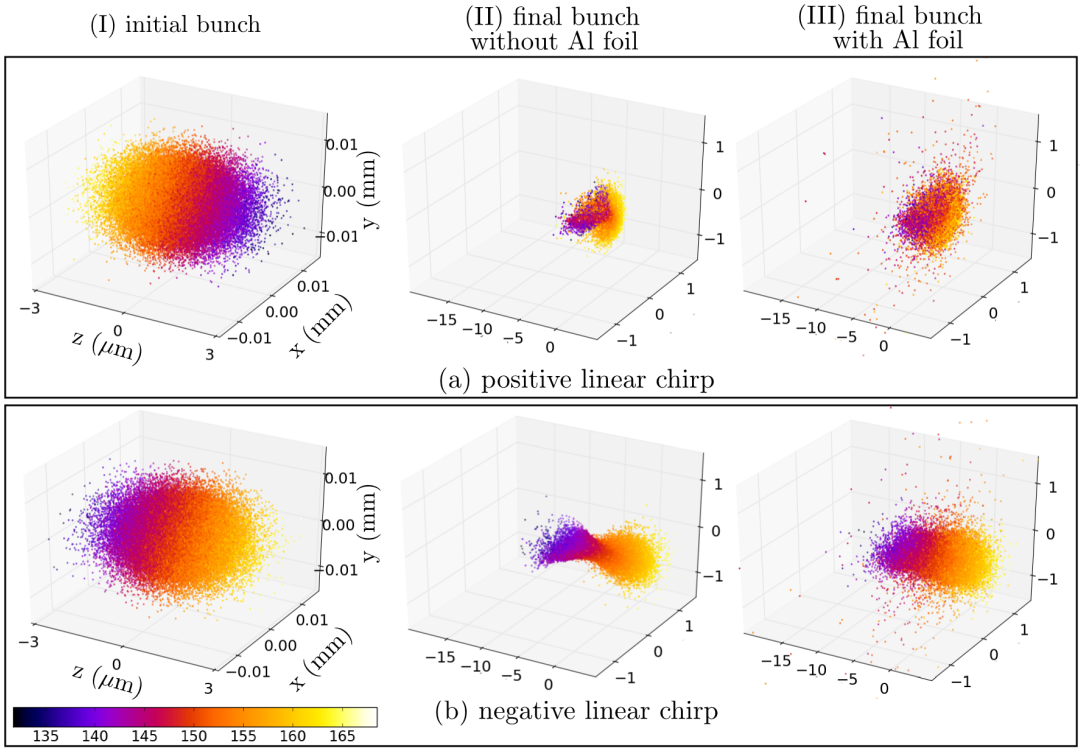

Figure 2.16: Electron bunch distribution for a (a) positive and (b) negative linear energy chirp with peak energy of 150 MeV and energy spread of 3 %. The electron beam has an initial emittance of 1 π mm mrad and initial bunch length of 0.9 µm (3 fs). The colors represent the energy of each particle as shown in the colorbar.

linear chirp on bunch length has been investigated using GEANT4 simulations. Although GEANT4 code does not consider the space charge effect, GPT simulations show that for an electron beam with 5-10 pC, the space charge can be neglected for energy ≥ 150 MeV with bunch length of less than 4 µm and source size of 4 µm (see Section 2.3.1). As shown in Figure 2.16, the leading edge of a bunch is occupied by the low energy particles in the case of positive chirp and by the high energy particles in the case of negative chirp. A positively chirped bunch will compress during propagation since the low energy component will catch the high energy component. On the other hand, a negative chirp enhances the bunch lengthening since the high energy part will move farther ahead, as shown in Figure 2.16 for an electron beam with initial emittance of $1\,\pi$ mm mrad and rms divergence of 1 mrad. As shown in the 3D graphs of the bunch, the addition of the Al foil has a negligible effect on the longitudinal bunch, since the increase in bunch length is less than a micron ($< 2\,\%$). The foil only scatters the beam in the transverse directions.

The beam divergence greatly affects the bunch length as shown in Figure 2.17. Electron beams with large divergence have longer path length, stretching the beam. For 1 to 2 mrad and no energy chirp (i. e. the energy distribution is independent of longitudinal position), the bunch duration increases with the energy spread. The growth is faster for a negative chirp. Introducing a positive chirp reduces this effect and for energy spreads greater than 1 %, bunch compression can be easily achieved. As the foil does not distort the longitudinal bunch, compression is still possible. However, the bunch compression effect is not very effective for 3 mrad divergence, when the bunch duration is already large even for small energy spread. In these conditions, the effect of the divergence dominates, resulting in a long bunch with duration almost unaffected by the energy spread.

2.3.5 Effects on the slice emittance

The emittance growth analysed in the previous sections considers the projected emittance for approximately 95 % of the beam distribution. For applications like free-electron lasers, an important parameter for the production of coherent radiation is the slice energy spread. Although laser-produced electron beams can have large integrated energy spreads, it was indirectly shown that the corresponding slice energy spread is significantly lower [73]. The large integrated energy spreads is a consequence of having longitudinal energy chirp. Moreover, simulations demonstrated that this so called "uncorrelated slice energy spread" (estimated to range between 0.5 and 1 %) is enough to obtain high gain for FEL

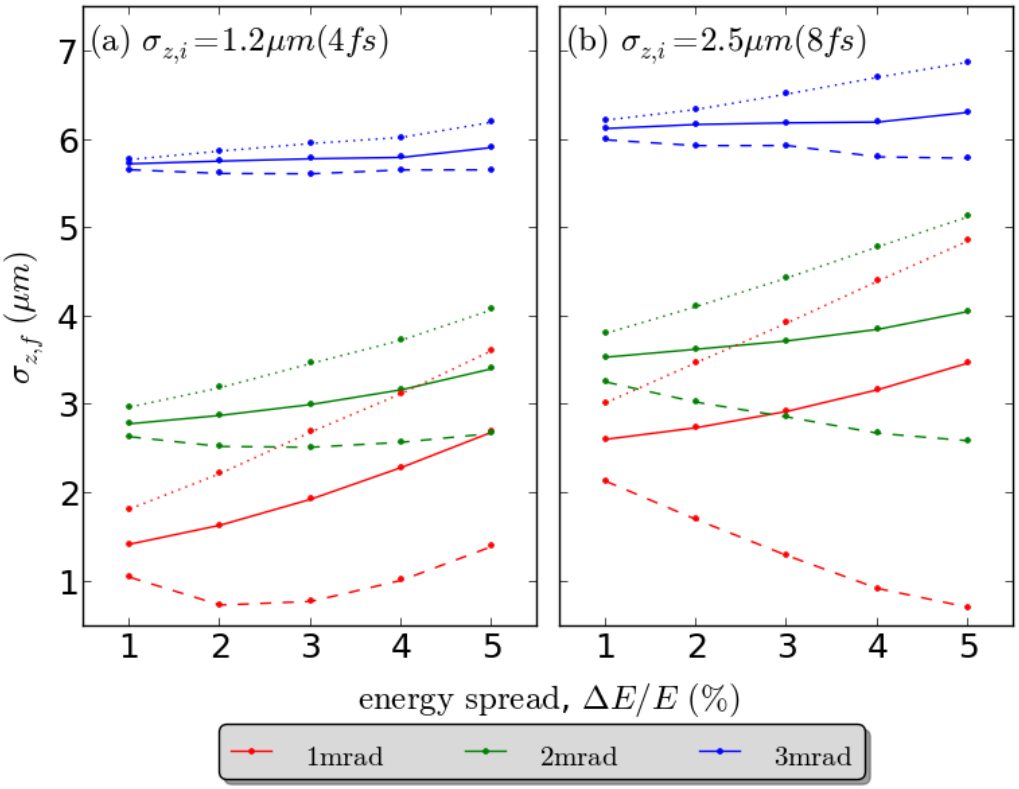

Figure 2.17: Bunch length, $\sigma_{z,f}$, after 4.17 m propagation through the ALPHA-X beamline for an electron beam with energy of 150 MeV and source size of 4 µm versus energy spread and divergence (solid lines: no energy chirp; dashed lines: positive linear chirp; and dotted lines: negative linear chirp). The bunch length at the source is (a) 1.2 µm and (b) 2.5 µm.

operation [10, 74], provided that the peak current can exceed 10 kA.

Different longitudinal slices of the electron beam occupy different regions in transverse phase space, leading to the definition of a slice beam emittance. To check how the corresponding slice emittance, ϵ_s, evolves, electron beams with initial negative energy chirp are divided into 10 equal slices (i.e. each slice contains 10 % of the beam particles). The energy chirp is chosen such that the head of the bunch has the high energy component, which is the preferred orientation for FELs operation. For simplicity, only three slices are shown here, defined as,

- front slice: 10 % beam distribution ahead of $\langle z \rangle$
- middle slice: 10 % beam distribution centred on $\langle z \rangle$
- back slice: 10 % beam distribution at the back of $\langle z \rangle$

where $\langle z \rangle$ is the longitudinal mean position of the bunch. The bunch slicing is illustrated in Figure 2.18, with the corresponding phase space profiles of the front, middle and back slices. For these slices, the corresponding slice energy spreads are between 0.5 and 1.2 %, increasing with larger integrated $\Delta E/E$.

Although the projected emittance rapidly grows with large $\Delta E/E$, the slice emittance increases slowly and is an order of magnitude lower than the projected emittance for electron beams with 1 mrad divergence, as shown in Figure 2.19. The slice emittance growth indicates that the beamline is not capable of properly aligning the slices. The emittance is nearly identical for the three slices, and is independent of the location of the slices. If the rms divergence is increased from 1 to 3 mrad, the electron beam becomes divergence dominated, and the growth in ϵ_s converges with ϵ_{rms} for large energy spreads, particularly for the back slice, which contains the low-energy component. As shown in Figure 2.18, different slices of the beam have different tilt in phase space, hence the sum of these slices leads to an increase in the projected area, while the slice ellipses have equal areas for a constant energy spread. Similar to projected emittance, the growth in x is larger than y, particularly when considering the end slice of the beam, which is a consequence of the design of the transport system. Although these results show that the corresponding slice emittance grows less than the projected emittance, the number of particles decreases when slicing the beam, resulting in reduced effective brightness. To counter this effect, it would be preferable to produce electron beams with higher charge (> 100 pC) within the usable energy component.

On the other hand, when the Al foil is in the beamline, the multiple scattering further increases the slice emittance, which is no longer significantly different from

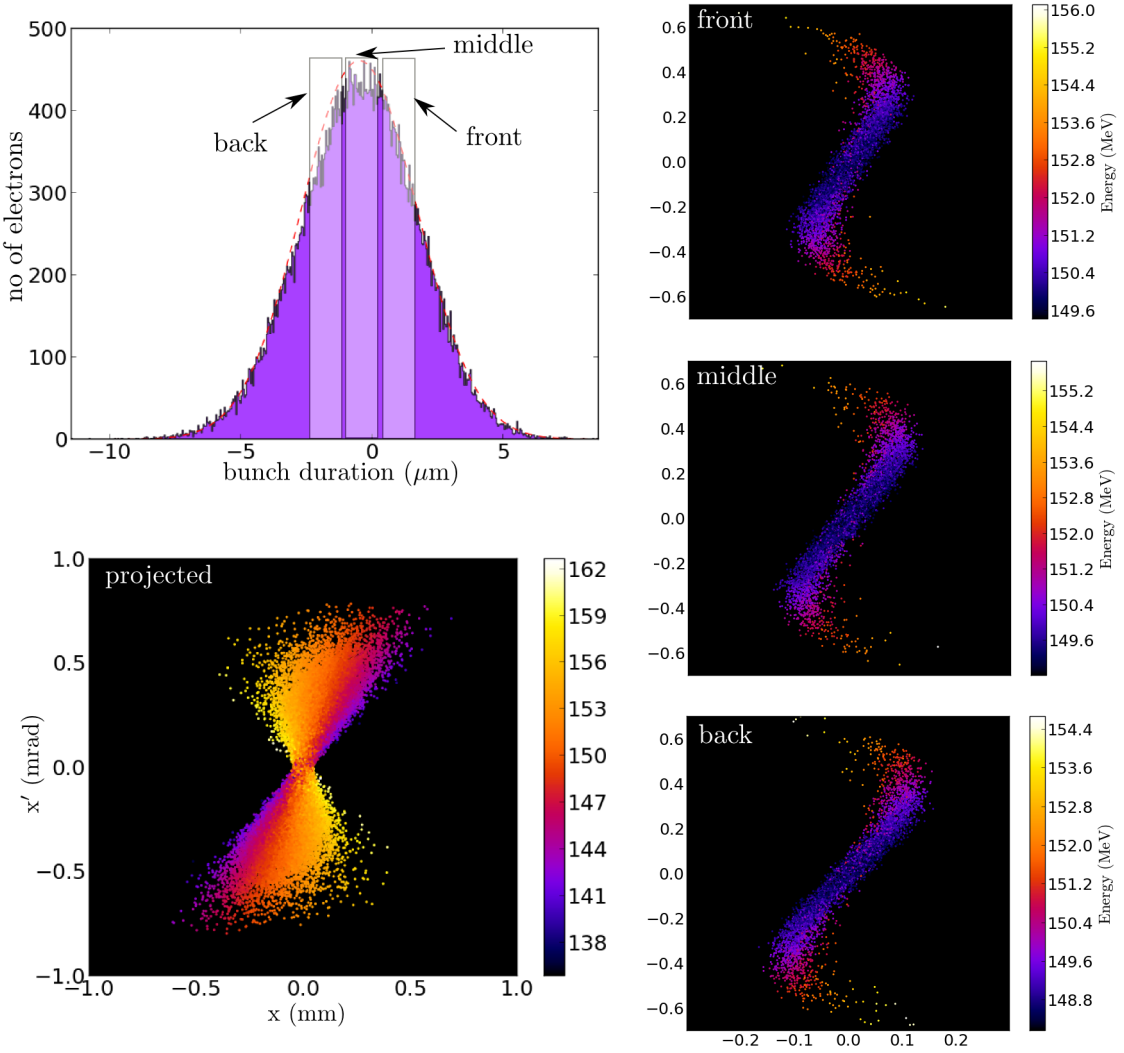

Figure 2.18: Illustration of longitudinal bunch slicing for slices containing 10 % of the total number of particles. The corresponding phase space profiles (front, middle and back slices) are also shown for an energy chirped electron beam with 150 MeV ± 1 %, initial bunch length of $\sigma_{z,i} = 1.2\,\mu\text{m}$ and initial $\epsilon^n_{rms} = 1\,\pi$ mm mrad.

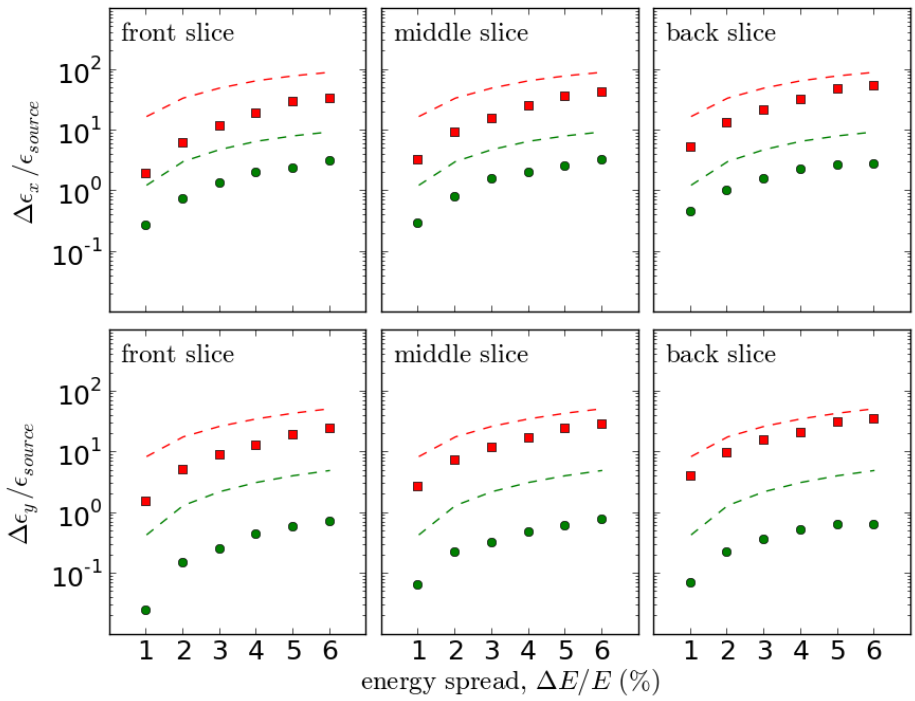

(a) Without Al foil

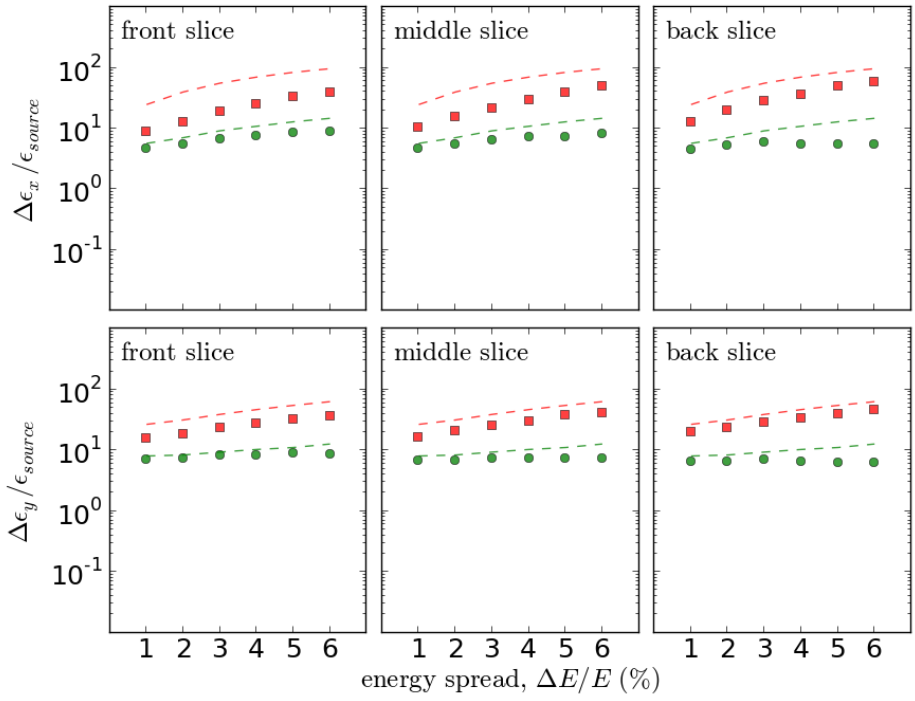

(b) With Al foil

Figure 2.19: Growth in x and y slice emittances (front, middle and back slices) of a 150 MeV electron beam with an initial $\epsilon^n_{rms} = 1.2\,\pi$ mm mrad and $\sigma_{z,i} = 1.2\,\mu$m for 1 mrad (green circles) and 3 mrad divergences (red squares) with (b) and without (a) a 0.8 µm Al foil (placed in front of the undulator). The corresponding projected emittance growth is shown by the dashed lines for reference.

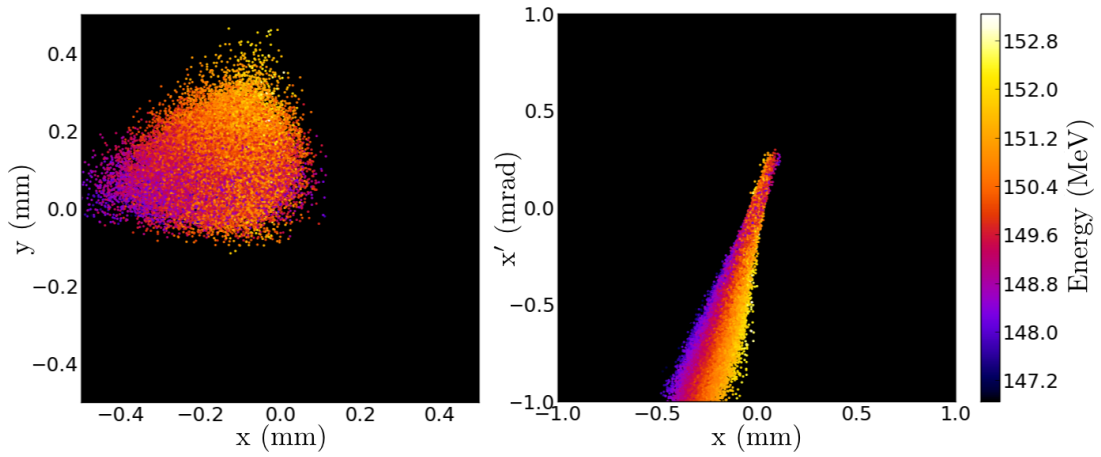

Figure 2.20: Spatial and phase space profiles of a 150 MeV ± 0.5 % electron beam emitted +2 mrad off-axis in both x and y, with initial emittance of $\epsilon^n_{rms} = 1\,\pi$ mm mrad.

its corresponding projected emittance, for both 1 mrad and 3 mrad divergence, as shown in Figure 2.19b. A 1 mrad electron beam already shows a large slice emittance growth for 1 % energy spread, remaining approximately unchanged for large energy spreads, while the slice emittance of a 3 mrad beam continues to increase slowly with the energy spread. However, since for large divergences, the emittance is already huge, the effect of the Al foil is not so important.

2.3.6 Electron beam pointing fluctuations

Another important issue affecting laser produced electron beams is the large shot to shot fluctuation in pointing. To date, the typical electron beam pointing reported is $\geq 1 - 2$ mrad [18, 60]. Furthermore, the mean pointing angle can be several mrad off-axis, probably due to problems with the laser such as non-uniform transverse intensity profiles and wavefront distortions. Such instabilities should be minimised, since electron beams emitted at an angle experience larger dispersion when passing through a series of quadrupoles, resulting in deformed spatial profiles and displacement from the beamline axis, as shown in Figure 2.20. There is also a significant increase in the rms beam sizes as the electron beam propagates further away from the beam axis, as shown in Figure 2.21. Moreover, the beam dispersion also causes growth of the projected emittance, as seen in the phase space distribution of electron beams propagating off-axis.

As shown in Figure 2.21, the projected emittance of an electron beam emitted at an angle of 1 mrad grows by almost 22 %, for a 0.5 % energy spread and by 40 % for a 3 % energy spread. This is expected since the electron beam effectively

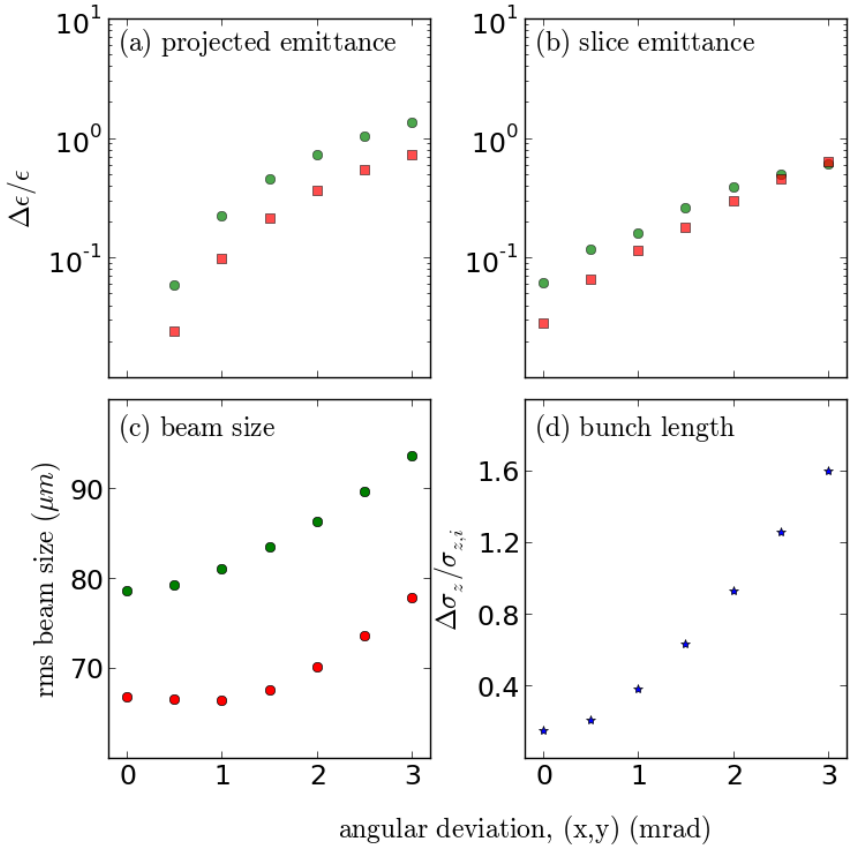

Figure 2.21: Effect of pointing stability on the beam transport. (a) Projected and (b) slice emittance growth, (c) rms beam sizes and (c) bunch lengthening calculated at the centre of the undulator for electron beam with energy of 150 MeV $\pm$ 0.5 % and initial emittance of $\epsilon^n_{rms} = 1\,\pi$ mm mrad (green circles: horizontal, red squares: vertical).

experiences a dipole field in a quadrupole as it moves away from the beamline axis, resulting in large dispersion. This dipole field also causes deflection of the electron beam away from the centre. The slice emittance (middle slice corresponding to a 10 % of the bunch distribution) is also affected by these fluctuations, having a similar growth to the projected emittance. Furthermore, pointing fluctuations also affect the bunch length, which doubles for electron beams emitted at 3 mrad.

2.4 Summary

This chapter discussed the possibility of transporting laser-driven electron beams using a simple strong focusing system based on the current beamline of the ALPHA-X accelerator, which consists of two quadrupole triplets: a permanent

quadrupole triplet positioned close to the accelerator and a conventional electromagnetic quadrupole triplet located 200 cm from the accelerator.

Large energy spreads induce projected emittance growth due to the chromaticity of the quadrupoles. However, the slice emittance remains one order of magnitude lower, increasing mainly with the divergence. This is a reversible growth, which can be corrected by adding other conventional devices such as a sextupoles to the beamline.

On the other hand, LWFA setups use Al foils to block the laser radiation. Multiple scattering in foils introduces irreversible emittance growth, which also affects significantly the slice emittance. The Al foil increases the overall beam divergence, leading to a growth in the slice ellipse area. As this growth cannot be corrected, it is recommended to design a system where the foil can be avoided. One possibility are transport systems where the electron beam propagation axis is translated using a dog-leg structure [75] or has a detour using chicane structure. The basic chicane structure composes of four dipoles with equal magnetic field bending the electron beam, however, the axis of propagation is the same at the exit of the chicane [76]. Moreover, chicane is also capable of bunch compression.

The main challenge for the transport of laser-produced electron beams is the intrinsic large divergence. Beams suffer from rapid blow up even at short distances. Moreover, the large divergence also causes pronounced growth of the electron bunch length. Although it was seen that introducing a positive linear chirp (where the high enery part is at the tail or back of the bunch) can compress the bunch, the beam becomes divergence dominated at $\sigma'_{x,y} = 3\,\mathrm{mrad}$, where compression is no longer significant. Pronounced bunch compression for larger energy spread can be seen if a divergence of less than 2 mrad is obtained.

This analysis also suggests that a simple beamline consisting of only two quadrupole triplets is not capable of transporting electron beams with energies, divergence and pointing varying over large parameter spaces. Although a single strong permanent quadrupole triplet is compact, the large magnetic field gradient of each PMQ defocuses the beam in one direction, resulting in huge jumps in projected emittance. Therefore, it is very crucial to have a proper optimisation. For instance, the PMQ triplet used in this study (the separation distance of 5.435 cm) has effective focal lengths of 18.3 cm in horinzontal plane and 8.14 cm in vertical plane for 150 MeV, and therefore its current location might be too close to the accelerator. It is also recommended to have a gradual focusing, which might include series of PMQs with lower field gradients.

Chapter 3

Experimental methods

This chapter describes the experimental setup and diagnostics at the **A**dvanced **L**aser–**P**lasma **H**igh-energy **A**ccelerator towards **X**-ray (ALPHA-X) beamline. A layout of the beamline is shown in Figure 3.1. The ALPHA-X project is commissioned to produce and apply ultra-short electron bunches and radiation sources. The accelerator is driven by high power, ultra-short laser pulses focused onto the front edge of a plasma target with densities in the order of 10^{19} cm^{-3}. As discussed in Chapter 1, for irradiance beyond 10^{18} W/cm^2 the ponderomotive force of the laser can generate plasma waves capable of accelerating electron beams to relativistic energies. The laser system, plasma source and diagnostics are described in the first two sections.

The electron beams are monitored and optimised using three removable scintillating screens (KODAK Lanex), L1, L2 and L3, installed at different locations along the beamline. These screens are coupled with lenses and CCD cameras for imaging. Three electromagnetic quadrupoles (EMQs), Q1, Q2 and Q3, are used to focus the electron beams towards the magnetic dipole electron spectrometer or to the 1.5 m long undulator. A compact miniaturised permanent quadrupole triplet (PMQs) is easily placed and removed (remotely) from the accelerator. The current position of hte PMQs is close from the accelerator (3 – 10 cm)to reduce the beam divergence. the triplet aperture is 6 mm. The drift distances between the PMQs can be adjusted between 1.5 and 5 cm to optimise the transport of different energy ranges. The gas target, PMQs and the first lanex, L1, are installed inside the accelerator main chamber, which is approximately 1 m long.

Optimisation techniques and basic properties of the electron beams are also presented in this chapter, focusing mainly on measurements of the electron energy, which are supported by numerical simulations using GEANT4.

3.1 The laser system

The experiments are carried out using a high power Ti:sapphire laser system, which delivers 800 nm, 35 – 40 fs laser pulses at a repetition rate of 10 Hz, with energy of ~ 0.6 J (within the FWHM) on target. After being focused down to a

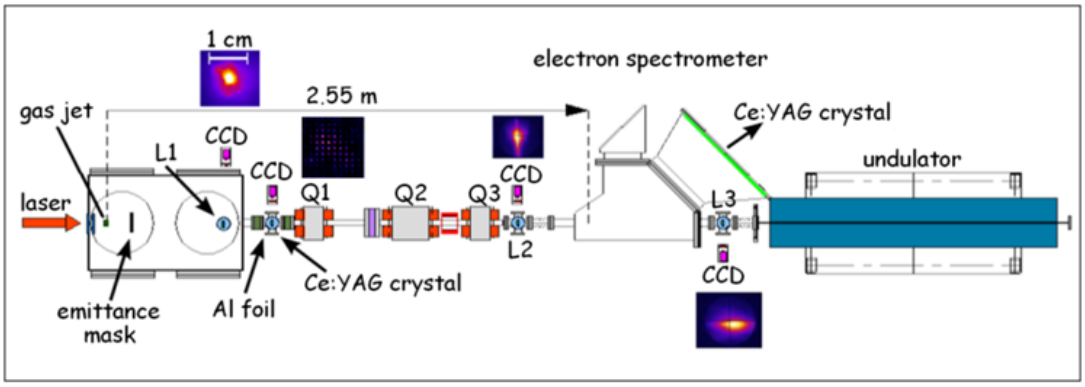

Figure 3.1: Schematic diagram of the ALPHA-X beamline, approximately 5 m in length. A series of quadrupoles (Q1, Q2, Q3) are used to transport the beam towards the electron spectrometer and 1.5 m long undulator. A permanent quadrupole triplet (PMQ) is located right after the gas jet to decrease the beam divergence. Lanex (L1, L2, L3) screens are used as spatial beam monitors, while a magnetic dipole is used for energy measurements. Also shown here are the Al foil and mask + YAG:Ce screen installed for transition radiation and emittance measurements.

40 µm spot size ($1/e^2$ diameter), by an f/18 spherical mirror, and undergoing self-focusing (through laser plasma interaction), the peak irradiance reaches 2×10^{18} W/cm^2, corresponding to a normalised vector potential $a_0 \simeq 1$. The layout of the laser system, which is based on chirped pulse amplification (CPA) technology is shown in Figure 3.2. The front end consists of an oscillator, a stretcher and a pre-amplifier, which includes a regenerative and a multi-pass amplifier. After two more multipass amplification stages, a maximum energy output of 1.55 J at 10 Hz is reached. The laser is compressed to $\sim 35 - 40$ fs using a vacuum grating compressor.

The Ti:sapphire oscillator generates pulses with duration of 18 – 20 fs and repetition rate 75 MHz. The spectral bandwidth is very broad, tuned to operate at a central wavelength of 800 nm. A stretcher negatively chirps the pulse to a duration of about 250 ps by using a single reflective grating in combination with concave and convex mirrors. Telescopic mirrors are used instead of lenses to remove spherical aberrations. Pulse stretching is a common technique used in CPA-laser systems to reduce the peak irradiance of the pulse and avoid optical damage during amplification. A Pockels cell (pulse picker) is installed in between the oscillator and stretcher to reduce the laser repetition rate down to 10 Hz.

The stretched pulse is first amplified through the regenerative (regen) amplifier's resonator cavity with Ti:sapphire crystal as the gain medium. It utilises two Pockels cells in combination with wave plates, as seeding and output cou-

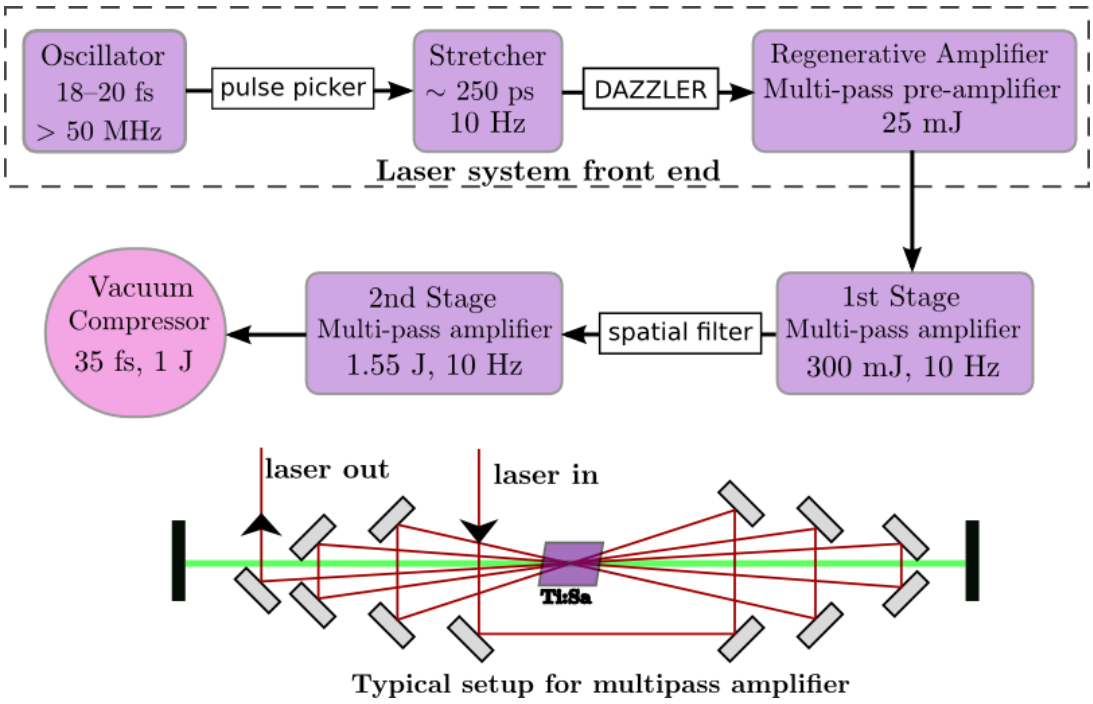

Figure 3.2: Schematic diagram of the ALPHA-X 15 TW laser. Also shown is the setup for a multi-pass amplifier.

pler. The polarisation of the laser is flipped to enter the cavity where the pulses resonate many times gaining energy. When sufficient amplification is achieved, the polarisation is flipped again to exit the cavity. The regen has a low gain in a single pass, thereby preventing the build-up of amplified spontaneous emission (ASE). However, since the cavity is electronically switched, the laser can pass hundreds of times, resulting in an overall high gain amplification, reaching almost 10^4–10^5. The output energy from the regen is usually < 1 mJ. Another Pockels cell (the pulse cleaner) is placed right after the regenerative amplifier to remove the ns pre-pulse before the second stage of pre-amplification in a multi-pass amplifier, schematically shown in Figure 3.2. The beam passes through a Ti:sapphire crystal five times, reaching an output energy of 20 – 25 mJ.

The two final amplification stages are both based on multi-pass amplifiers. The first amplifier is pumped by two Nd:YAG lasers with combined energy of 1 J. After three passes, the output energy is typically 260 – 300 mJ. The second amplifier is pumped by three Nd:YAG lasers with combined energy of 2 J. The Ti:sapphire crystal used in the final amplification stage is cryogenically cooled to prevent thermal lensing. The laser final energy can reach up to 1.6 J. A spatial filter is placed in between the two power amplifiers to remove low frequency components that could damage the last amplifier crystal.

A vacuum grating compressor (with transmission efficiency of 63 – 68 %) based

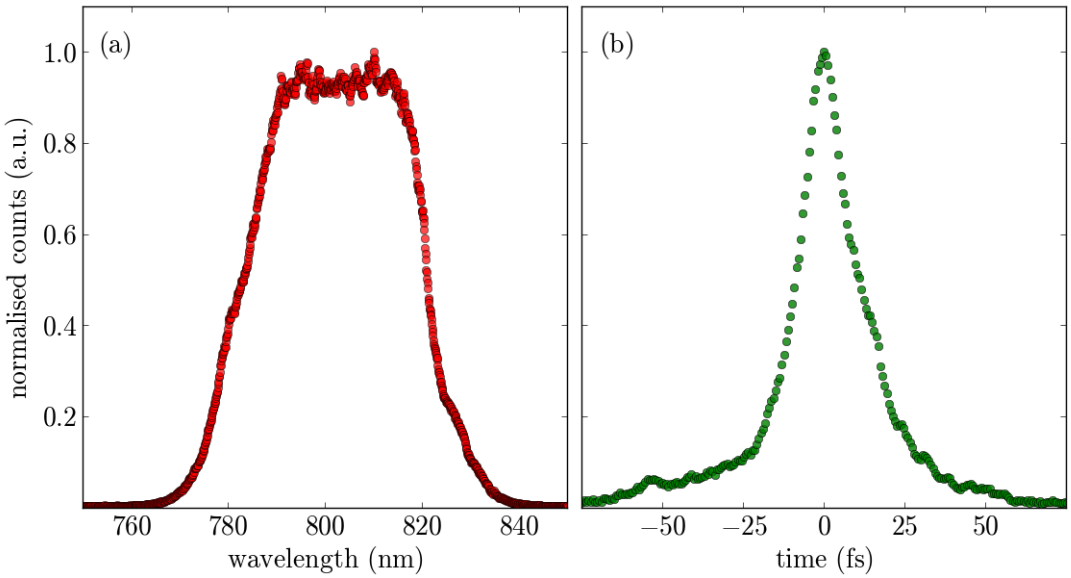

Figure 3.3: Measured laser properties: (a) spectrum (taken after the first stage power amplifier) and (b) pulse duration (obtained after compression using an auto-correlator).

on two parallel gratings reduces the pulse duration to 35 – 40 fs. Ideally, the compressor and the stretcher are exactly conjugate. However, additional dispersion can occur. Hence, an acousto-optic programmable dispersive filter (DAZZLER from Fastlite) is installed after the stretcher to fine-tune the group delay dispersion for the non-ideal conjugation between the stretcher and compressor. Moreover, it is also used to compensate for the gain narrowing that might occur during amplification.

For laser wakefield acceleration experiments, it is important that the laser meets crucial requirements, such as high peak power, good contrast ratio (preferably $> 10^6$), aberration-free focal spot and symmetric broad spectrum. Poor laser quality can results in electron beam large shot to shot pointing and energy fluctuations, low charge and large divergence. Hence certain diagnostics are always performed during experiments. The spatial profile from the laser front end should have uniform intensity distribution with measured rms energy stability of less than 5 %. The laser spectrum is measured after the spatial filter, with the first stage power amplifier switched on. A broad bandwidth (40 nm), approximately flat-top profile is an indication of good alignment of the stretcher and regenerative amplifier, as shown in Figure 3.3. The ns pre-pulse is normally monitored using a fast photodiode placed after the first power amplifier. Pre-pulses are not ideal since they can alter the mechanism of interaction between the main pulse and the gas target. This type of pre-pulse can be reduced by adjusting the last

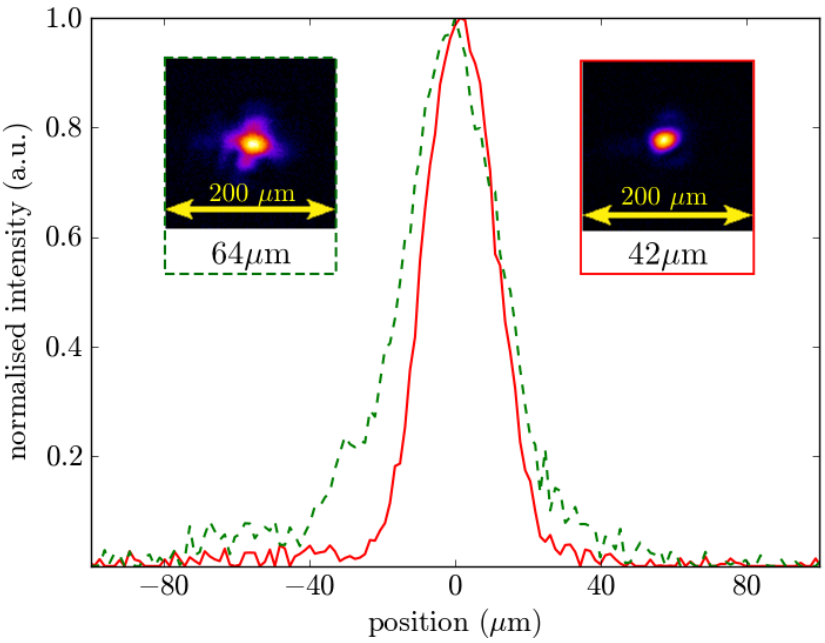

Figure 3.4: Measured laser focal spot inside the main chamber at low power (only the laser front end is operated) for a misaligned (dashed green line) and aligned (solid red line) spherical mirror. Measured spot sizes are given in $1/e^2$ diameter.

Pockels cell located after the regen. The pulse duration is also regularly checked using an auto-correlator, as shown in Figure 3.3.

Fine alignment of the spherical mirror is very important in producing an aberration-free laser spot. At the focus, most of the laser energy has to be contained within the central core (FWHM), as shown in Figure 3.4, since the nonlinear processes necessary to reach the bubble regime require extremely high intensity gradients. A spot size from a misaligned spherical mirror is also shown, revealing significant energy loss to wings outside the beam core.

3.2 Plasma sources

Laser-wakefield acceleration experiments use gas targets as plasma source. Different designs of supersonic gas nozzles and laser machined capillary waveguides are available at the ALPHA-X beamline. Gas filled (usually H_2 is used) capillary waveguides are typically 200 – 300 µm in diameter and 30 – 40 mm long [55, 77]. The laser pulses are guided through the waveguide, resulting in a longer interaction length. A high voltage electrical discharge pulse is applied to the waveguide, pre-ionising the gas before arrival of the laser pulse. Plasmas from capillary waveguides are characterised by parabolic density profiles with densities between 10^{17} and 10^{18} cm^{-3}. Laser wakefield acceleration experiments using linear and

newly-developed tapered capillary discharge waveguides are discussed in the Ph.D thesis of S. Abuazoum [78].

On the other hand, all of the experiments presented in this thesis use supersonic gas jet targets generated by gas nozzles with different geometrical designs. Nozzles are connected to a pulsed gas valve synchronised with the laser and opened for 2 to 3 ms. Helium gas is typically used. Since the threshold intensity for ionisation is on the order of 10^{15} W/cm^2, the front of the laser completely ionises the gas target, creating a plasma, which will be exposed to the full laser irradiance.

The gas profile coming out from the exit of the nozzle dictates the density profile of the plasma. Here, de Laval nozzle designs are implemented to generate supersonic gas jets. An example is shown in Figure 3.5a. These types of nozzles produce density profiles with an approximately constant central region between rising and falling density ramps. The length of the central region can vary from $\sim$ 0.5 to 5 mm, depending on the exit diameter of the nozzle.

Plasma densities from the He gas jet targets are in the order of $\sim 10^{19}$ cm^{-3}. The plasma channel produced from these targets is always monitored during experiments by imaging the top-view of the nozzle. An example is shown in Figure 3.5b. The plasma density is varied by changing the backing gas pressure or the distance between the nozzle exit and the laser beam. Figure 3.5c shows the variation in plasma density profiles for different heights from the nozzle exit, at a constant backing pressure of 30 bar. These are obtained from FLUENT simulations, assuming complete ionisation of the gas. Large density fluctuations (shocks) occur very close to the nozzle exit, while the slope of the ramp increases with height. Typically, experiments are performed with background gas pressure between 25 and 35 bar, and the laser focus is positioned between 2 and 3 mm above the nozzle exit. At these settings, the central region of the density profile is approximately flat-top and the ramps are not very large (the ramp is estimated to extend between 200 and 300 µm).

3.3 Electron beam optimisation

The electron beam characteristics depend strongly on the stability and quality of laser pulses and gas jets. With respect to the gas jets, the valve flow and stability is monitored using a transducer. Under normal operation, a gas valve should have a constant pressure difference within the opening time, as shown in Figure 3.5d. Depending on the backing pressure, the gas pressure drop can range between 200

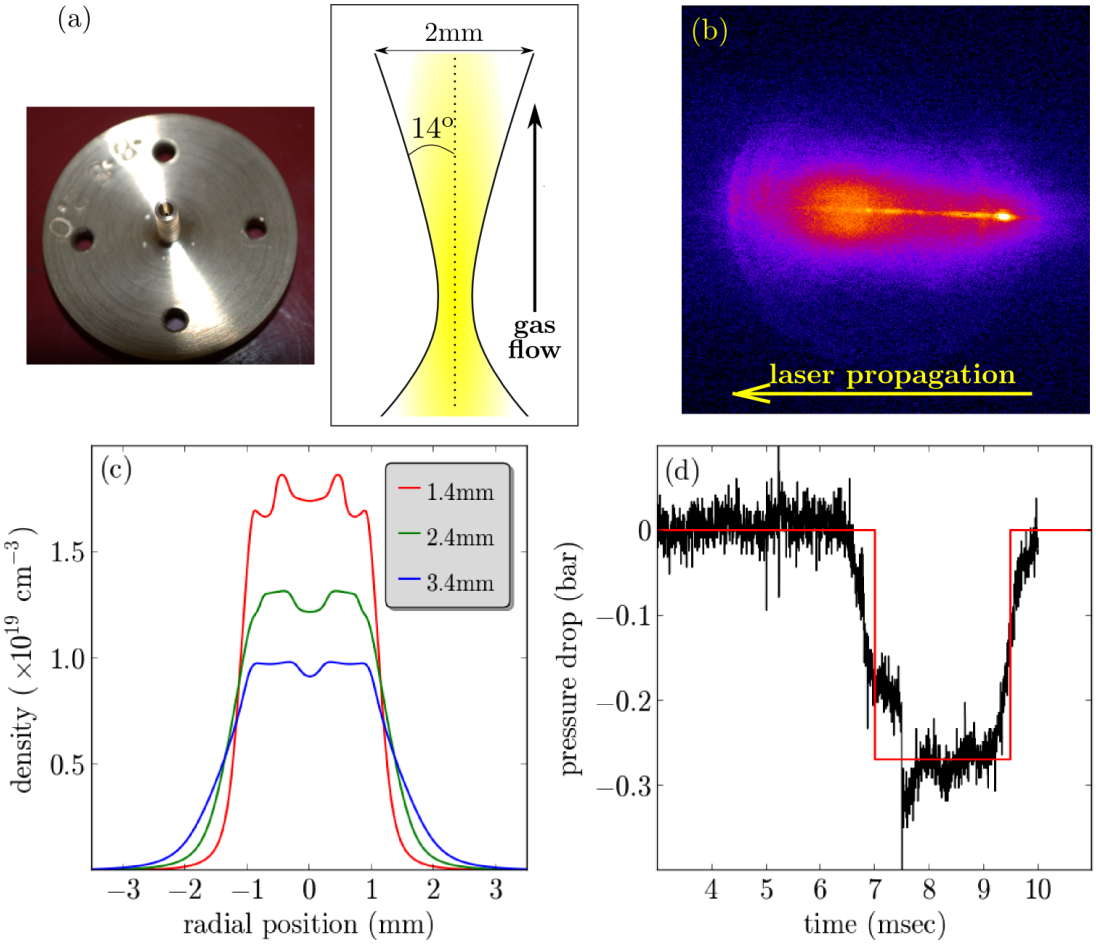

Figure 3.5: Gas jet target. (a) Photograph of a nozzle used in the experiment with an example layout of the structure producing supersonic gas flow, (b) laser-induced plasma channel at 2.5 mm from the nozzle exit and backing gas pressure of 30 bar, (c) density profiles at different heights from the nozzle exit with backing gas pressure of 30 bar (density profiles were obtained from CFD simulations in FLUENT 6.23 using the structure in figure (a) courtesy of C. Aniculaesei) and (d) pressure difference from the valve measured with a gas transducer, where the red outline indicates the valve opening time.

and 450 mbar. Detailed discussions on nozzle designs and valve stability analysis will be presented in the Ph.D thesis of C. Aniculaesei (*in preparation*).

The relative position between laser and gas jet is optimised by looking at the quality of the electron beams detected downstream on the first Lanex scintillating screen, L1, which has a viewing area of 30 × 40 mm. It is located 64 cm from the accelerator and tilted horizontally by 45° with respect to the beamline axis. Images are recorded with a CCD camera equipped with a zooming lens for an overall resolution of 1 pixel = 43 and 31 µm in x and y, respectively.

The behaviour of the electron beam can give insight into the performance of the laser. As an example, electron beams recorded for three consecutive laser shots are shown in Figure 3.6 for different conditions. In the case of Figure 3.6a, large shot to shot pointing instability (> 20 mrad) and large divergence are observed. Only less than 50 % of 100 consecutive laser shots accelerate electron beams. Moreover, electron beams have low charge (the camera had to be operated at maximum gain in order to obtain a measurable signal) and have large background halo. The corresponding laser-produced plasma channel is also shown in the insets. The channel length is not the same for every shot, indicating that the interaction between laser and plasma is not properly optimised. The fluctuations in plasma channel length indicates that the energy of the laser is fluctuating or that the intensity at the focus is not high enough to reach a stable regime of relativistic self-focusing. This can also show that the laser parameters are not properly matched with the gas jet density.

On the other hand, a high quality laser beam properly matched with the plasma density produces electron beams with good pointing stability and high charge, as shown in Figure 3.6b, where the camera is saturated despite being operated at zero gain and with a 0.5 ND filter in front of it. The high charge region is concentrated on the beam core, resulting in low background halo. The shot to shot pointing stability in this run is less than 10 mrad and the rms divergence is between 2 and 6 mrad, for 100 consecutive laser shots. Furthermore, the corresponding plasma channels are very similar, and start forming before the flat-top density profile, indicating that the rising density ramp can also be part of the acceleration process.

Under optimal conditions, the ALPHA-X accelerator is capable of producing electron beams with pointing stability of less than 5 mrad, as shown in Figure 3.7 for 500 consecutive laser shots. Here, 100 % of the laser shots accelerate electron beams, indicating a very good reproducibility. However, these beams are emitted 4 mrad off-axis which is probably due to the tilting of the laser beam wavefront.

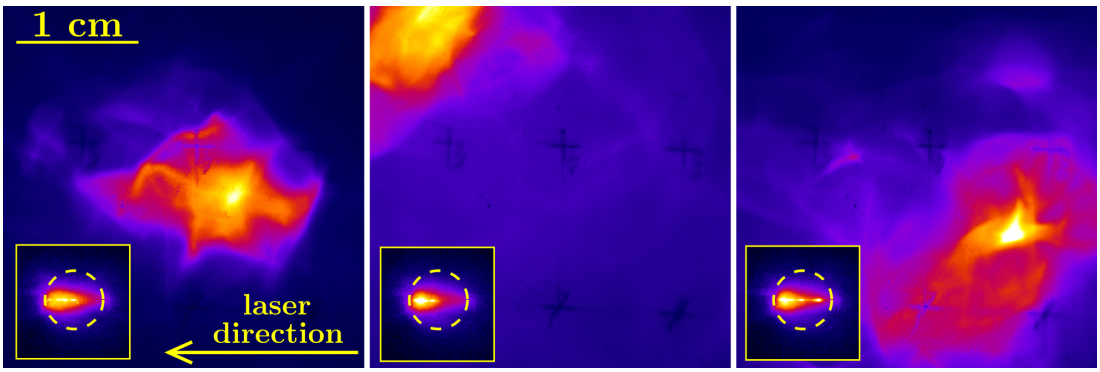

(a) Unstable plasma channel and large shot to shot pointing of the electron beam (The camera gain is increased to $\times 10^{15}$ to properly resolved the signal).

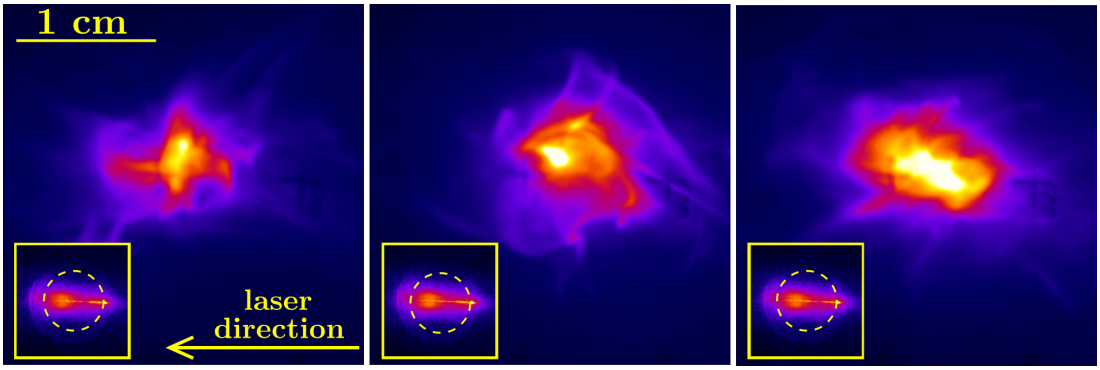

(b) Consistent plasma channel length with good pointing stability of the electron beam. (A 0.5 ND filter is placed infront of the camera with zero gain to reduce intense signal).

Figure 3.6: False-colour images of electron beam detected on the first Lanex (64 cm from the accelerator) from three consecutive laser shots for (a) ummatched and (b) matched laser parameters with the He gas jet plasma density (backing gas pressure of 27 bar and laser is focused 2.2 mm above the nozzle exit). Insets show the false-colour image of plasma channel created for each electron beam, where the nozzle inner wall is indicated by the circle lineout, with a diameter of 2 mm.

The electron beam shot to shot fluctuation is larger in x, which is the polarisation plane of the laser. As shown in the inset of Figure 3.7, the accumulated electron beam images form an elliptical distribution due to different stability in x and y. The corresponding rms divergence is between 4 and 6 mrad, in both horizontal and vertical directions. The electron beam centroid is independent of the charge. However, the divergence seems to depend on the charge, as shown in Figure 3.8.

These measurements of the electron beam transverse profile do not provide any information on the energy. It is possible for the high energy components to be concentrated at the core of the beam on top of a large halo made of low energy electrons. This high divergence, low energy component would be quickly lost during propagation through the beamline, especially if quadrupoles are used. In this case, measurements on L1 would overestimate the beam size and divergence. In Chapters 4 and 5, beam profiles measurements obtained on a YAG:Ce scintillating screen positioned 100 cm from the accelerator will be presented, showing smaller divergences. However, this second screen has a smaller size (2×2 cm) and can effectively select beams with divergence low enough to fit without clipping, possibly leading to an underestimation of the real beam divergence.

As discussed in Chapter 2, the electron beam transport can be improved by using permanent quadrupoles triplet (PMQs) to decrease the beam divergence right after the gas jet. By changing the spacing between each quadrupole, the transport of different energy windows can be optimised and three configurations have been employed in the experiments so far. In Figure 3.9, GEANT4 simulations are presented showing the expected beam size on L1 as a function of energy for the three configurations, for beams with normalised $\epsilon^n_{rms} = 1\,\pi$ mm mrad, 1 mrad rms divergence and 1 % energy spread. All settings are unable to provide equal focusing on the horizontal and vertical directions, leading to an elliptical beam after propagation through the focusing system. Moreover, longer drift separations between quadrupoles increases the focusing strength of the triplet.

Shown in Figure 3.10 are the accumulated electron beams from 200 consecutive laser shots (recorded on L1) using three different drift separations between PMQs. The electron beam pointing stability for each PMQs settings is also recorded for 100 consecutive laser shots. Among the three settings, the beam size is smallest, approximately 2.4 mm (in x) and 1.7 mm (in y) mean sizes, when the drift separation is 5.45 cm. With the measured (rms) divergence of 4 – 6 mrad, the estimated energy range is between 120 and 140 MeV. The triplet also reduces the background halo, effectively removing the low energy components of the electron beam. However, the spatial profiles are slightly distorted owing to the large

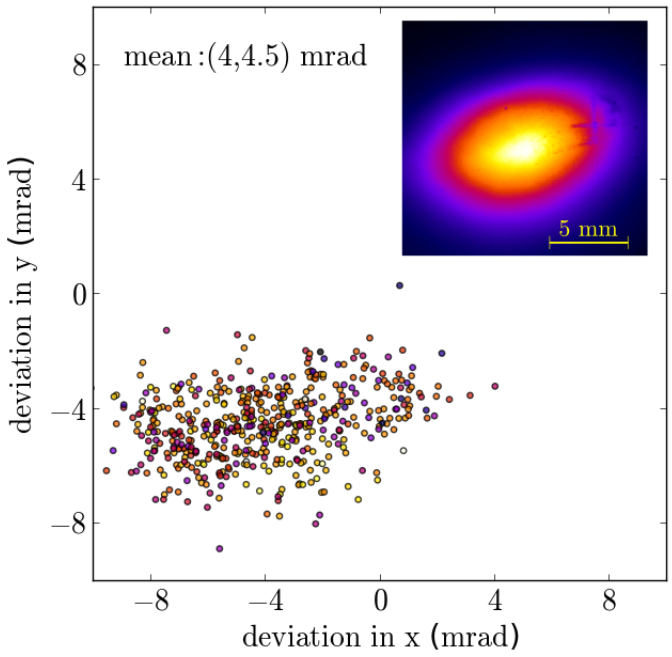

Figure 3.7: Typical shot to shot electron beam pointing fluctuations of the ALPHA-X accelerator, obtained from 500 consecutive laser shots on the first Lanex screen. The colors of each point represents the relative integrated charge of each electron beam. Inset shows the false-colour image of the accumulated electron beam.

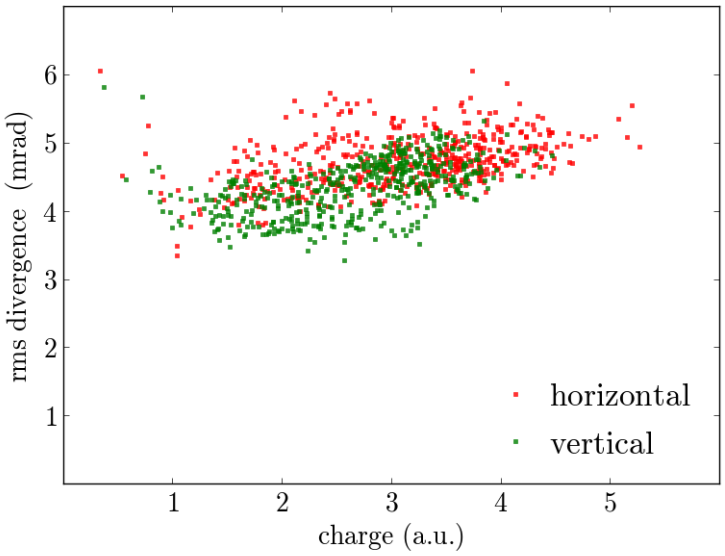

Figure 3.8: Integrated charge vs rms divergence in horizontal (red) and vertical (green) directions for the same data of Figure 3.7.

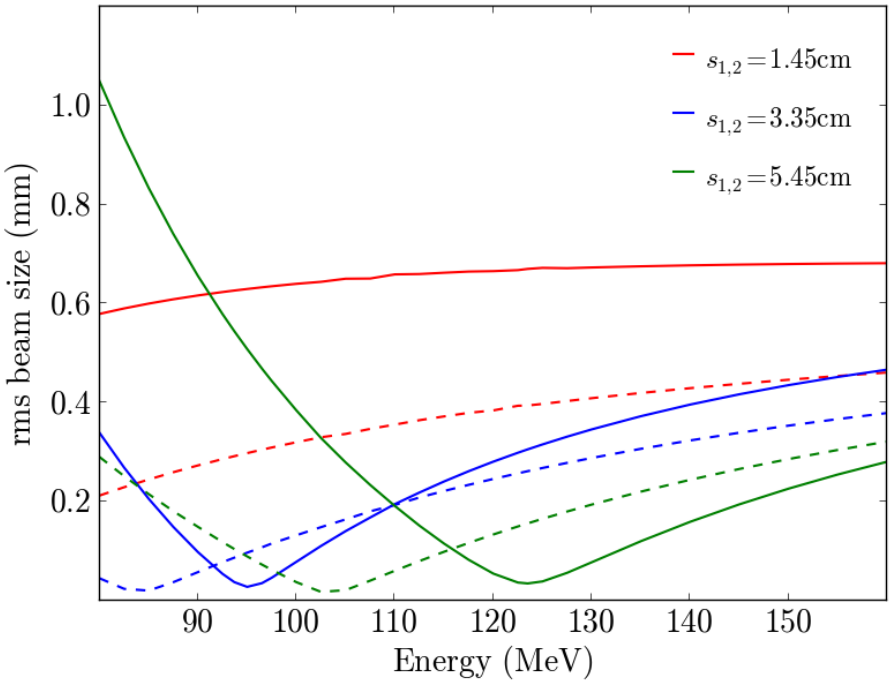

Figure 3.9: RMS beam size (horizontal: solid lines, vertical: dotted lines) as a function of energy for three different PMQs triplet configuration, where $s_{1,2}$ is the drift distance between quadrupoles. Beam sizes are calculated at the position of L1. (Constant parameters: $\epsilon^n_{rms} = 1\,\pi$ mm mrad, $\sigma'_r = 1\,$mrad and $\Delta E/E = 1\,\%$.)

energy spreads and the energy dependence of the PMQs focusing strength. The ellipticity of the electron spatial profile increases as the drift separations of PMQs increases since strongly focusing configurations are more sensitive to the shot to shot pointing fluctuations. Moreover, some laser shots produce multiple electron beams emitted at different angles and with different energies. A more detailed discussion will be presented in Chapter 5.

3.4 Energy spectra measurements

The electron beam energy is measured with a spectrometer located 256 cm from the accelerator and activated by supplying currents to the dipole electromagnets. The layout of the spectrometer is shown in Figure 3.11. At the entrance, the magnets are arranged at a 43° angle from the beamline axis, a design which produces a magnetic field capable of focusing vertically the beam, thus improving the detectability of the spectrometer. Since this focusing effect is insufficient at high energies, an electromagnetic quadrupole triplet (EMQs) is also installed. The maximum obtainable magnetic field is 1.65 T, corresponding to a maximum observable energy range between 245 and 657 MeV. A 300 mm x 10 mm x 0.150 mm YAG:Ce scintillating screen is located at the focusing plane and electron spectra are recorded with a 14bit CCD camera. Since the electron spectrometer is designed to focus both in the horizontal and vertical directions, information on the beam divergence is lost.

3.4.1 Spectrometer resolution

The resolution of the electron spectrometer is studied using GEANT4 simulations. Since the spectrometer is located more than 2 m from the accelerator and the electron beam size rapidly increases, EMQs are always necessary to re-focus the beam and minimise the signal lost during transport. However, this results in a strong dependence of the spectrometer performance on the beam energy and on the EMQs supplied currents. As an example, Figure 3.12 shows how electron beams with energies of 100, 125 and 150 MeV are expected to appear on the spectrometer screen for two EMQs configurations (using GEANT4). The supplied currents of the EMQs are obtained from GPT simulations, looking for smallest beta function on the screen. Since the higher current (6.5 A, -5.5 A, 6.5 A) setting provides better resolution, this will be chosen for this analysis. This setting is optimised for stronger focusing of energies between 125 and 135 MeV, but other energies are not degraded. For the following discussions, the term

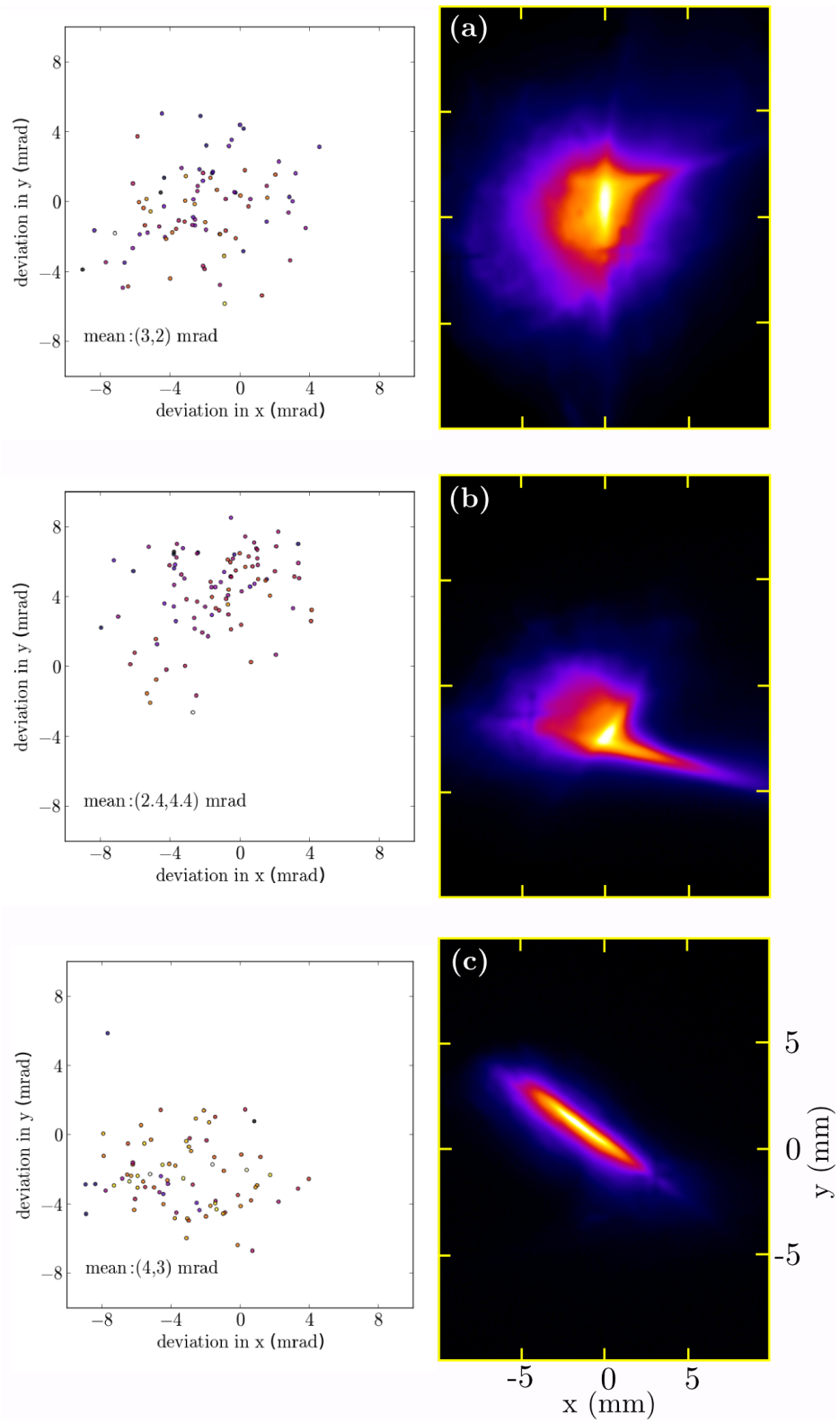

Figure 3.10: False colour accumulated image of electron beams from 200 consecutive laser shots recorded on L1 after propagation through PMQs using three different drift separations: (a) 1.45 cm; (b) 3.35 cm; and (c) 5.45 cm. The electron beam centroid distribution is also included, obtained for 100 consecutive laser shots.

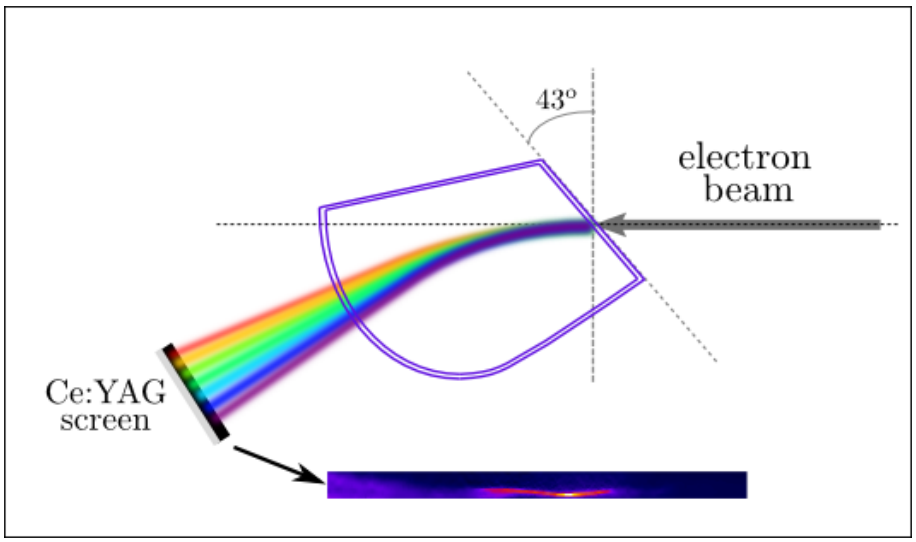

Figure 3.11: Schematic diagram of electron spectrometer.

"measured" energy spread is the value predicted by the GEANT4 simulations on the spectrometer screen, while the term "source" energy spread is the theoretical/actual value of the input beam. Simulations do not include eventual scattering or nonlinearities in the YAG:Ce crystal.

The vertical focusing ability of the electromagnets reduces with increasing beam divergence, resulting in poorer image resolution, as shown in Figure 3.13 a & b where a 125 MeV electron beam with normalised rms emittance of $1\,\pi$ mm mrad is transported through the electron spectrometer. Although the use of EMQs triplet provides better resolution, the measured energy spread increases with divergence. To be able to measure an energy spread of 0.5 % for 125 MeV, the source divergence must be less than 0.5 mrad, thus limiting the smallest possible energy spread measurable directly. If the electron beam divergence is known, the resolution can be improved by deconvolving the spectrometer response from the measured spectra. For the energies considered here, this is not required when $\Delta E/E > 3 - 4\,\%$, when the measured energy spread approaches the real value.

As the beam transport is energy dependent, the resolution will also depend on the EMQs current settings and will decrease at high energy as shown in Figure 3.13 c & d. Moreover, for the settings considered here, energy spreads greater than 15 % are discarded because of beam clipping on the YAG:Ce screen. This can be avoided by increasing the currents supplied to EMQs and spectrometer. In this case, both the current of the EMQs and spectrometer should have to be increased for realiable high energy measurements.

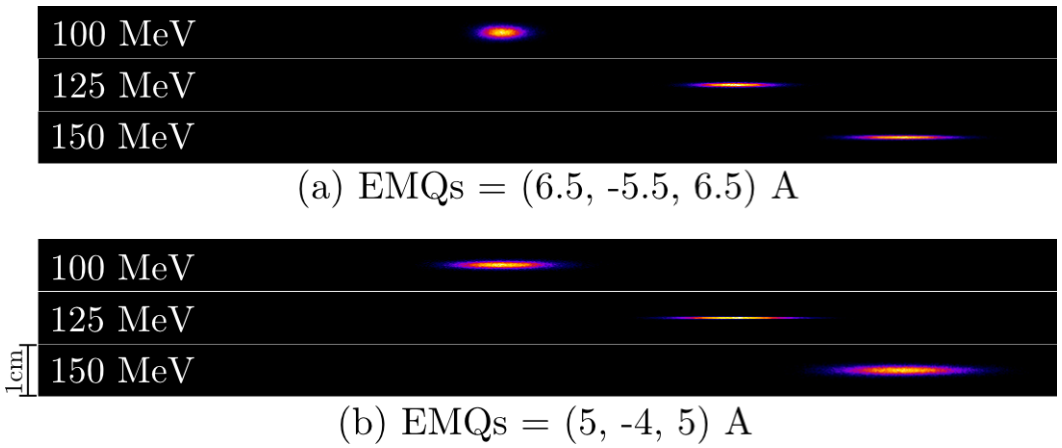

Figure 3.12: Simulated electron beam output on the spectrometer screen for two different EMQs settings and spectrometer current of 55 A (energy window is 75 to 180 MeV). The electron beams have rms divergence of 2 mrad, $\Delta E/E = 1\,\%$ and charge of 0.1 pC.

3.4.2 Noise analysis

The previous section shows that the spectrometer resolution is dominated by the beam divergence and varies with the electron energy and with the current supplied to the EMQs. However, this analysis is for an ideal situation where background signals, such as scattering from laser light and camera noise, are not accounted for. Example of an experimentally obtained raw image of an electron spectrum is shown in Figure 3.14a. The EMQs and spectrometer currents are similar to those used in the numerical analysis of the previous section. Several sources of noises can be seen embedded with the signal, in particular the laser light on the left side and scattering at the edges of the YAG:Ce screen, which is made of three crystals glued in place. Experimental images are processed to filter and subtract the background noise. However, some information can be lost, since the spectrometer performance also becomes charge-dependent.

The error induced by background signals has been estimated by merging electron spectra simulated with GEANT4 into experimentally recorded images which include camera noise and laser background. Electron beam properties are calculated after subtracting the same background image, ignoring the shot to shot variation of the background noise, which would require further filtering and introduce additional errors. Despite its limitations, this method allows to estimate the best spectrometer performance possible with the current setup. An example of an experimental background image combined with an appropriately scaled simulated spectrum is shown in Figure 3.14c. Figure 3.15 summarises the measured energy spread for electron beams with 2 mrad divergence and with different en-

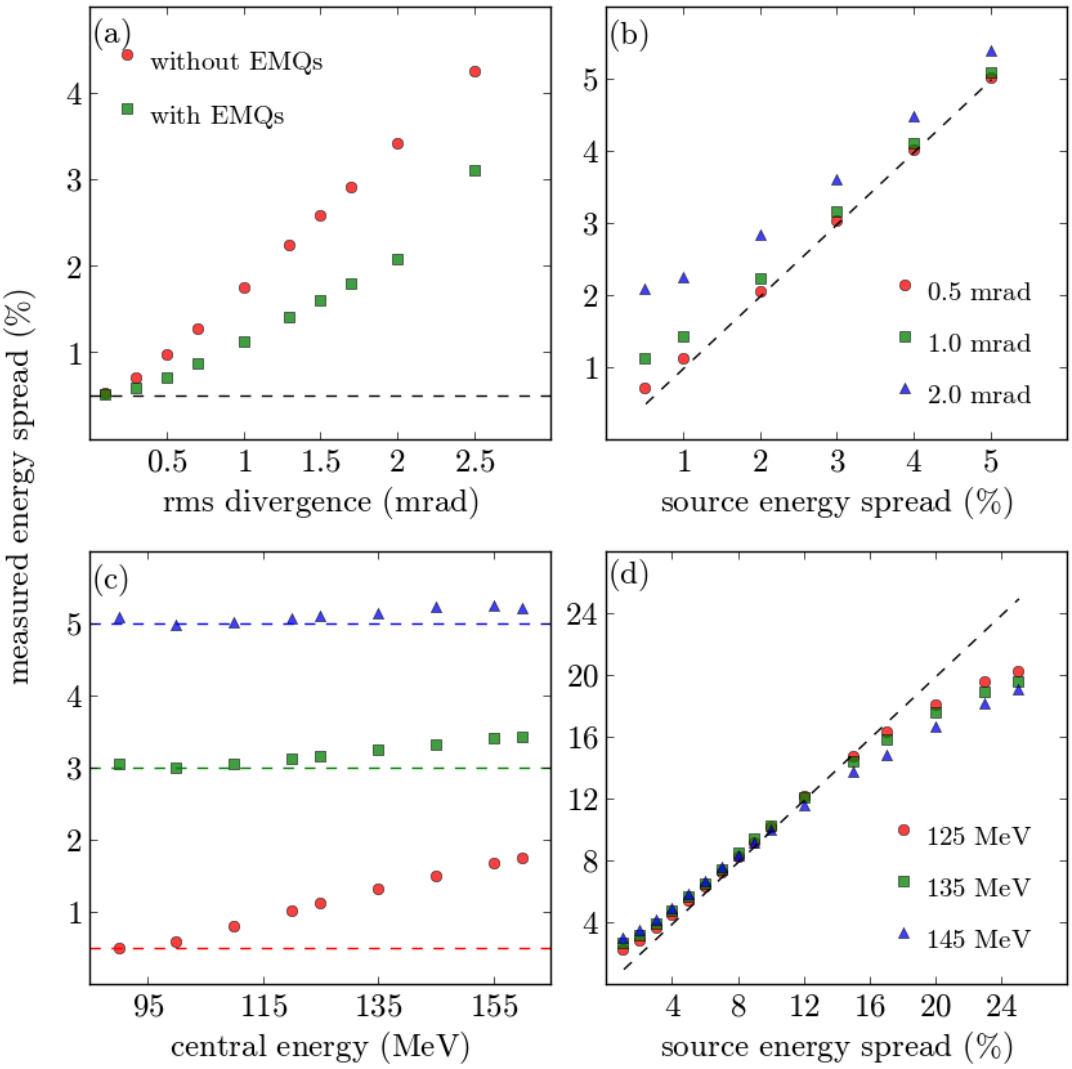

Figure 3.13: Resolution dependence of electron spectrometer. Measured energy spread on the spectrometer screen using 125 MeV electron beam and normalised rms emittance of $1\,\pi$ mm mrad for (a) varying divergence with source energy spread of 0.5 % and (b) varying energy spread for three different rms divergence. (c) and (d) Dependence of measured energy spread on peak energy for 2 mrad electron beam. The supplied current for the spectrometer is $I = 55$ A and the EMQs currents are 6.5, 5.5 and 6.5 A. The dashed lines are the theoretical/actual energy spread.

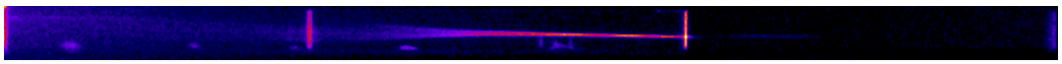

(a) Experimental raw data

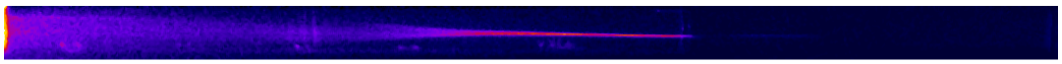

(b) Processed data (background, noise and charge corrected)

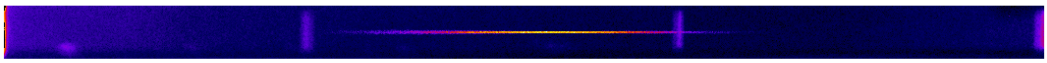

(c) Simulated electron spectrum with background noise

Figure 3.14: Experimentally measured eletron energy spectrum (a) before and (b) after image processing (background subtraction and noise filtering). A simulated (c) energy spectrum immersed in replicated background noise is also shown.

ergy, charge and energy spread sent to the electron spectrometer for two EMQs configurations. When noise is included, the resolution becomes charge dependent. In general, for beams with less than 1 pC, the measured energy spread is always less than the actual value since the signal to noise ratio is low, and spectrometer detectability suffers. Moreover, the difference between the two EMQ settings is no longer significant indicating that the divergence is no longer the main factor affecting the energy measurements. These results suggest that low energy spread beams can produce strong signals and even saturate the camera for modest charges. On the other hand, low charge and high energy spread beams cannot be reliably measured in the presence of large noise levels.

3.4.3 Effect of Al foil

The background noise in the electron spectrometer measurements can be reduced by using a thin foil. In the ALPHA-X beamline, an Al foil is normally used to block off the intense laser radiation which can cause permanent damage to detectors (such as expesive CCD cameras) looking directly to the beamline axis. During energy measurements, a removable 0.8 µm thick Al foil is placed at the entrance of the spectrometer. As discussed in Section 2.3.2, the addition of the foil in the beamline induces growth in the divergence of the beam, and therefore reduces the vertical focusing effect of the spectrometer, leading to an increase in the vertical beam width on the YAG:Ce screen. This also implies that the signal will be lower. Experimental energy measurements are performed, where electron beams are recorded for 200 laser shots with and without the Al foil, consecutively for five runs to obtain enough statistics. The electron spectrometer current is $I = 65.8$ A, corresponding to an observable energy range of 87 MeV to

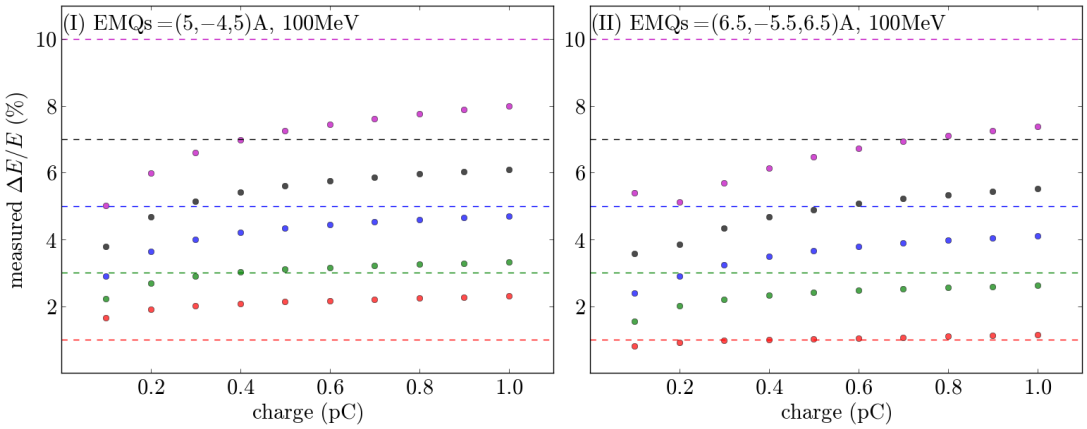

(a)

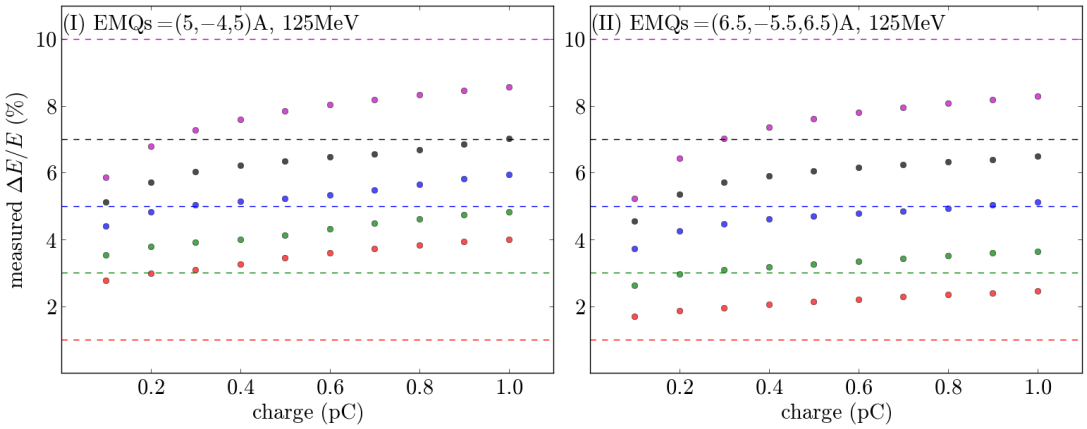

(b)

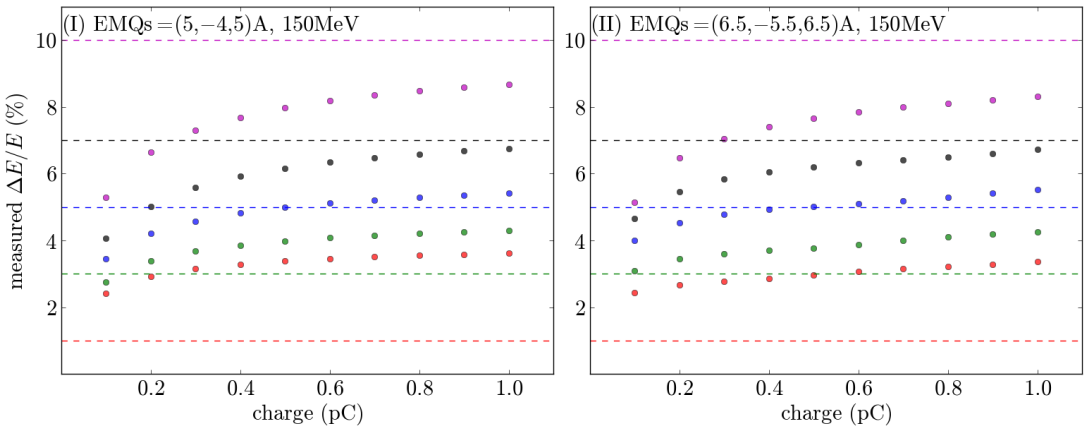

(c)

Figure 3.15: Measured energy spread vs charge. Energy spread measurements for simulated electron spectra embedded with noise for a 2 mrad electron beam and peak energy of (a) 100 MeV, (b) 125 MeV and (c) 150 MeV. The dotted lines indicate the theoretical/actual energy spread. Figures on the left are with EMQs current of (5,-4, 4) A, while figures on the right are for EMQs current of (6.5,-5.5, 6.5) A.

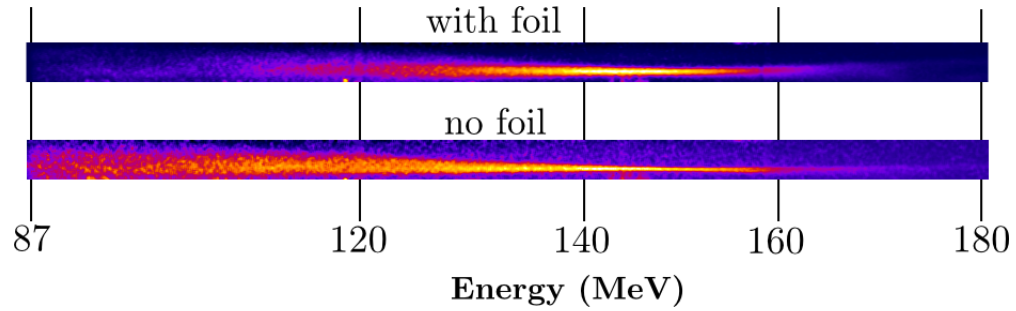

Figure 3.16: False colour image of the accumulated electron beam spectra with and without Al foil placed at the entrance of the spectrometer.

200 MeV. The EMQ currents are (5.5, -5.7, 5.5)A for all the measurements.

Shown in Figure 3.16 are the accumulated images of the electron spectra with and without the Al foil. For the spectrometer and EMQ currents used, energies below 120 MeV (the low energy tail) are not focused, resulting in a larger vertical width, which is noticable when the Al foil is not used. When the foil is used, the multiple scattering further increases the divergence, resulting in a larger dispersion of the low energy components of the electron spectra, which are no longer measurable. The high energy tail is also shorter. The scattering leads to a small reduction in integrated charge as shown in the comparison of charge distributions in Figure 3.17a. As the signal is lower with the foil, the measured energy spread is also reduced, as shown in Figure 3.17b, consistently with the noise analysis results of Section 3.4.2. As noted in the previous section, the beam energy spread is actually higher for measured $\Delta E/E$ greater than 15 %. Here, the energy spread is calculated for the energy range of 87 MeV to 180 MeV. Figure 3.17c shows that there is also a significant increase (up to ~ 5 MeV) in the measured central energy, which is caused by the missing low energy components. The vertical widths with and without the foil are also compared. However, since they are calculated by integrating along the vertical direction, the overall width is larger without the foil due to the defocused low energy components. But, if the integration considers only the energy between 140 and 160 MeV (where the beam is tightly focused), the width is obviously wider with the foil. These measurements show that a thin foil at the entrance of the electron spectrometer strongly affect the electron beam properties. It is therefore desirable to reduce the background noise by attaching an Al foil to the front of the YAG:Ce crystal.

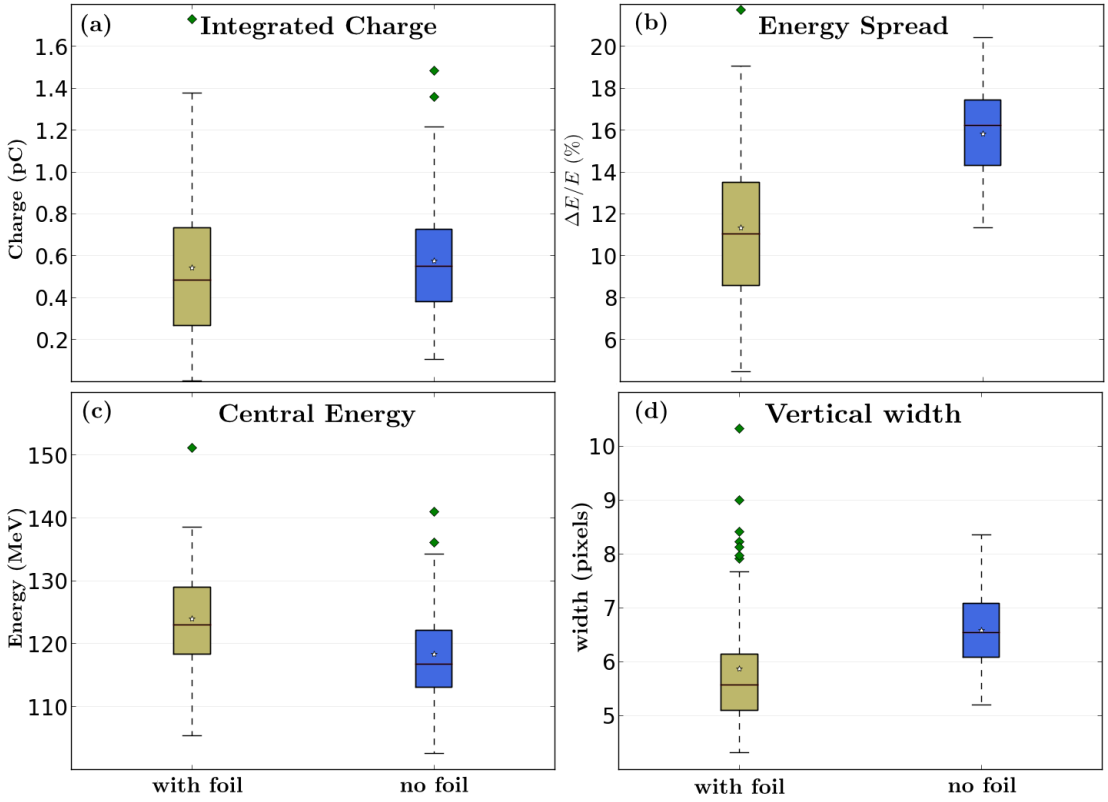

Figure 3.17: Box plots comparison with and without the foil for (a)integrated charge, (b) energy spread, (c) central energy and (d) vertical width of the electron spectrum. The line inside the box plots are the median of the distribution while the star symbols are the mean values. Each group of data has been obtained for 200 consecutive laser shots.

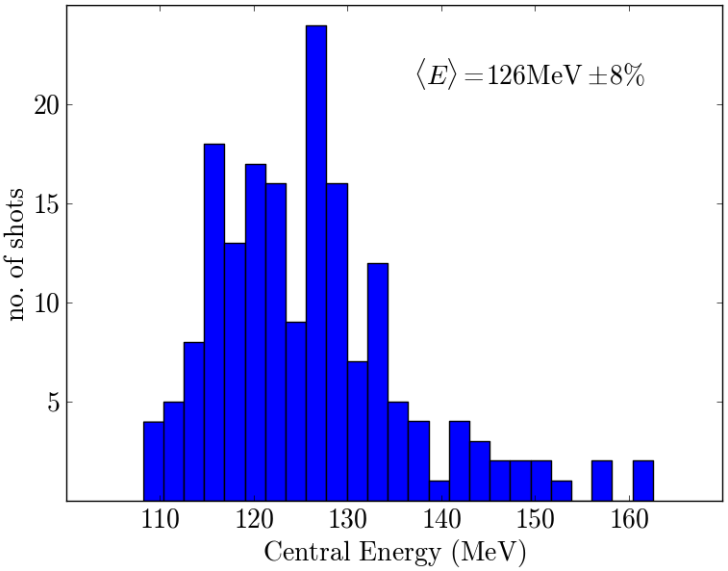

Figure 3.18: Measured energy distribution for 177 consecutive laser shots with mean value of 126 MeV and energy jitter of 8 % (spectrometer current is 65.7 A and EMQs have currents of (5.4,-5.7, 5.4) A).

3.4.4 Experimental results

Energy measurements are obtained at the same laser and plasma conditions of Figure 3.6b. The charges are between 0.5 and 2 pC, and therefore the measured energy spread will be resolution limited due large noise levels. Shown in Figure 3.18 are the measured central energies for 177 consecutive laser shots with mean energy of 126 MeV and energy jitter of 8 %. The energy spread measured in this set ranges from 5 to 15 %. This value will be used as the normalisation factor for the emittance measurements presented in Chapter 5.

3.5 Summary

The experimental methods for laser wakefield acceleration at the ALPHA-X beamline are presented in this chapter. The process of optimising the laser-plasma interaction to obtain high quality electron beams is presented. Results show that electron beams from the ALPHA-X accelerator have pointing stability and divergence less than 10 mrad, which is already acceptable for radiobiology experiments [79, 80]. However, these values can still can be improved.

As the accelerator is currently relying on the self-injection mechanism, the electron beam fluctuations are hard to control. Other methods, such as tailoring the plasma density to improve the stability are being currently investigated.

This chapter also discusses the resolution limitations of the ALPHA-X electron spectrometer. It was shown that the measured energy spreads are dominated by the divergence and charge. It was seen that for reliable energy spread measurements, charges greater than 1 pC must be obtained to improve the signal to noise ratio. Since the main source of noise is the laser, it is suggested to block it with a thin Al foil. The foil cannot be placed at the entrance of the spectrometer, where it would alter the beam properties, therefore it is better to attach it to the YAG:Ce screen.

Chapter 4

Transverse emittance measurement using pepper-pot technique

The quality of laser-driven electrons is directly related to the characteristics of the accelerator itself. Therefore, information obtained from the properties of electron beams can be used to further improve the accelerator. Basic diagnostics, such as energy and beam profile measurements, as discussed in Chapter 3, are well established and widely implemented as day-to-day tools for laser wakefield accelerator (LWFA) experiments [81, 82]. This chapter introduces more advanced diagnostics able to directly measure the beam transverse emittance. High-brightness beam applications require electron beams that can be focused down to small sizes ($\sim$ few μm scale) and transported along beamlines with minimal dispersion. In medical imaging, low-emittance electron beams are needed to generate resolvable images. With these requirements, transverse rms emittance can be used as figure of merit. Electron beams with low transverse emittance are capable of producing high-quality radiation. However, maintaining low emittance is one of the challenges in designing transport systems.

In conventional accelerators, several emittance measurement methods are already well developed. The most common is the quadrupole scan technique [83–85]. The spatial size of the beam is measured by varying the focusing strength of a quadrupole or by changing the position of a scintillating screen. Another method is based on optical-transition-radiation (OTR) screens [86], where screens are placed at different locations along the beamline to determine the beam waist. These two methods are multishots, and indirectly measure the tranverse emittance by obtaining the overall beam matrix. However, they are difficult to apply to laser-driven electron beams. For both cases, it is necessary to have a stable beam and a well designed beamline where dispersion and other non-linear effects are negligible. For quadrupole scanning, the large energy spread produced by LWFA causes chromatic aberrations, resulting in added complication. Moreover, this method is better suited for higher energy beams, less susceptible to space charge induced blow-up when focused down.

In this chapter, direct single shot measurements of transverse emittance of

laser driven electron beams are presented using the pepper-pot technique [23], where beams are converted into smaller beamlets by passing through an array of holes. This technique is insensitive to large shot to shot fluctuations of the electron beam properties, making it suitable for LWFAs as the transverse emittance is obtained in a single measurement. It has been successfully tested both for low (20 MeV to 55 MeV) and high (508 MeV) energy electron beams [24, 25, 87].

It is widely used in conventional linear accelerators as the holes transform the space-charge dominated beams by reducing the charge density, letting the beamlets drift under the influence of emittance alone [88, 89]. Although LWFA generated electron beams have short bunches, it was shown in Chapter 2 that for modest charges, space charge can be neglected. Hence, the following discussions of the electron beam properties are valid without considering the effect of space charge.

4.1 The pepper-pot technique

The transverse emittance is measured using a mask with a "pepper-pot" design, as illustrated in Figure 4.1. Particles propagating through the holes form beamlets, which drift downstream hitting a scintillating screen. The width of each beamlet on the screen represents the spread on the transverse momentum of the beam, while the location of the beamlet centre (on the screen) is the mean position of the particles passing through each hole. This information is used to reconstruct the transverse trace space profile of the beam, and calculate the rms emittance.

M. Zhang derived an equation for the calculation of the transverse rms emittance that solely depends on the position of the holes and orientation of the beamlets on the screen [90]. The rms emittance for the horizontal (x) direction is given by:

$$\begin{aligned}\epsilon_{x,rms}^2 &= \langle x^2\rangle\langle x'^2\rangle - \langle xx'\rangle^2 \\ &\approx \frac{1}{N^2}\left[\sum_{j=1}^{p} n_j(x_j-\bar{x})^2\right]\left[\sum_{j=1}^{p} n_j\sigma_{x'_j}^2 + n_j(\bar{x}'_j-\bar{x}')^2\right] \\ &\quad - \frac{1}{N^2}\left[\sum_{j=1}^{p} n_j x_j\bar{x}'_j - N\bar{x}\bar{x}'\right]^2,\end{aligned} \tag{4.1}$$

where x_j and $x'_j = (X_j - x_j)/L$ are the position and divergence of the particles in the j^{th} beamlet, while $\bar{x}$ and $\bar{x}'$ are the mean position and divergence of all

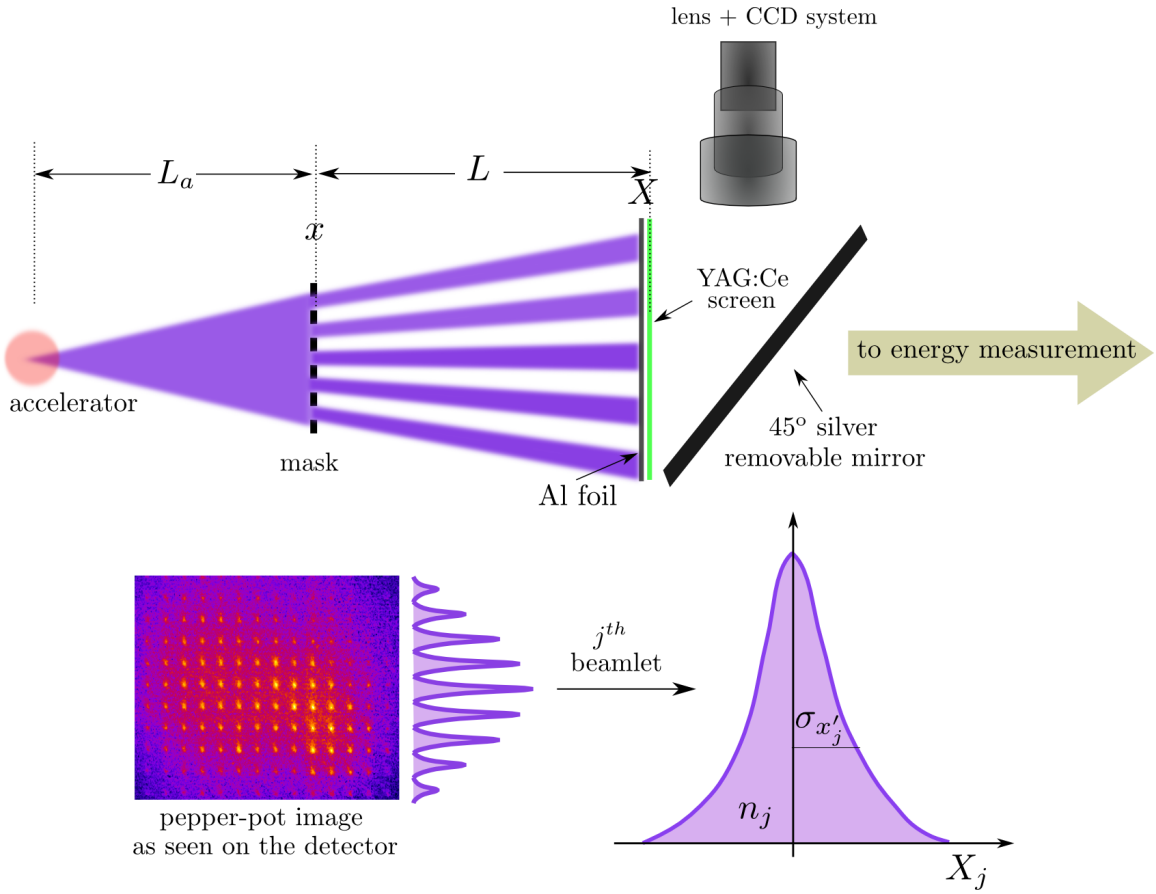

Figure 4.1: Schematic diagram (top view) of the transverse emittance measurement using pepper-pot technique, where L_a is the accelerator to mask distance and L is the mask to YAG:Ce scintillating screen distance. The apertures on the mask are defined by the x coordinate, while the beamlets on the screen are defined by the X coordinate. The Al foil, YAG:Ce scintillating screen and silver mirror are installed in a single housing that can be remotely removed for electron energy measurement.

beamlets, respectively. The factor $N = \sum_{j=1}^{p} n_j$ (n_j is the number of particles in the j^{th} beamlet and p is the total number of beamlets) is directly related to the total charge, while $\sigma_{x'_j}$ is the rms divergence of the j^{th} beamlet.

The rms divergence of a beamlet is obtained by deconvolving in quadrature the hole projection on the screen and the optical resolution of the imaging system, R, from the rms beamlet size on the screen, ω_{X_j}, [91], i.e.

$$(\sigma_{x'_j} L)^2 = \omega_{X_j}^2 - R^2 - (M\, d/\sqrt{12})^2 \,, \tag{4.2}$$

where M is the geometrical magnification and the factor $\sqrt{12}$ comes from the rms hole projection on the screen by assuming a flat-top profile. The magnification is defined as $M = (L_a + L)/L_a$, where L_a is the distance of the accelerator to the mask and L is the mask to screen distance. Similar relations hold for the vertical plane $(y - y')$.

In designing the mask, the hole size must be very small to make the beamlet distributions approximately independent from the mask geometry. If the particles have an angular spread of $\delta\theta$ after the hole and drift downstream toward the screen, the hole diameter, d, must satisfy the following condition:

$$\delta\theta\, L \gg d \,. \tag{4.3}$$

This condition implies that the hole diameter's acceptance angle must be larger than the angular spread of the beamlets, to accomodate electron beams with large divergence. It also states that the resolution of the beamlets is improved by increasing L, provided that the beamlets can produce a measurable signal on the detector.

Ideally, a thick mask is needed to entirely stop the beam and only allow passage to the particles encountering the holes. However, a thick mask can effectively act as a collimator, leading to an under-estimation of the rms emittance. It is also more difficult to manufacture. To avoid the overlapping of the beamlets on the screen, wider hole separations are desirable.

These experiments have been carried out with tungsten masks having a thickness of 125 µm. Tungsten is preferable as it can withstand exposure to the intense laser radiation to be found close to the accelerator. This material also has a large scattering effect, creating a uniform background noise even if the thickness is not enough to block the entire beam. Two masks have been used with hole diameter of 16 ± 2 µm and 21.5 ± 5 µm, respectively. Shown in Figure 4.2 are light trans-

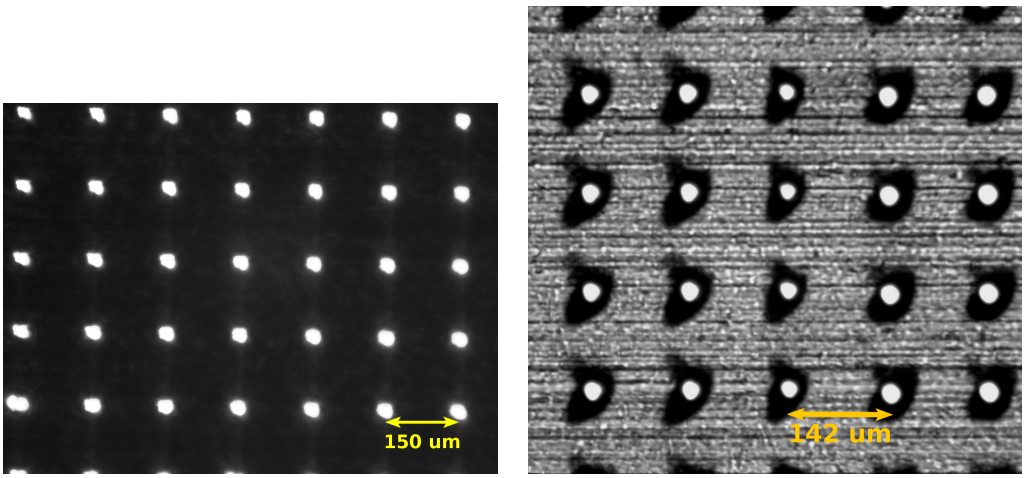

(a) (b)

Figure 4.2: Light transmission images of a portion from a 125 µm thick tungsten mask with hole diameter and hole separation of (a) 21.5 ± 5 µm and 150 µm and (b) 16 ± 2 µm and 142 µm.

mission images of a portion of the two pepper-pot masks. The uncertainty in the hole diameters comes from small irregularities of the hole shape.

The tungsten masks are modeled using GEANT4 showing that the thickness is enough to produce detectable beamlets on a screen 70 cm from the mask, as shown in Figure 4.3, for a hole diameter of 16 ± 2 µm. Although the background noise level increases with the energy for a divergence of 1 mrad, the beamlets are measurable, for charges ≥ 0.2 pC.

A 150 µm thin YAG:Ce scintillating screen is chosen as a detector. Its emission peaks at 530 – 550 nm, making it highly compatible with photodetectors like CCD cameras. Several studies have shown that the beam size measured on YAG:Ce screens is larger as compared to other beam profile monitors such as OTR screens and wire scanners and that the beam size measured on the crystal increases proportionally with both the crystal thickness and electron charge [91, 92]. A. Murokh et al. showed that for an electron beam of 300 pC and 66 MeV, an rms beam size of 50 µm is measured for a 250 µm thick YAG:Ce, which is 67 % larger than wire scan measurements [92]. Since, in the pepper-pot method, only a few percent of the entire beam is hitting the screen ($\sim$ 1 pC or less), and the crystal is almost twice as thin, the accuracy is expected to be better.

The final resolution depends both on the imaging system and YAG:Ce screen characteristics. For the imaging lens and CCD camera used in the experiments, the optical resolution is 6 – 10 µm per pixel, while the 150 µm thin YAG:Ce crystal has a resolution of 10 µm (provided by the manufacturer). Therefore the

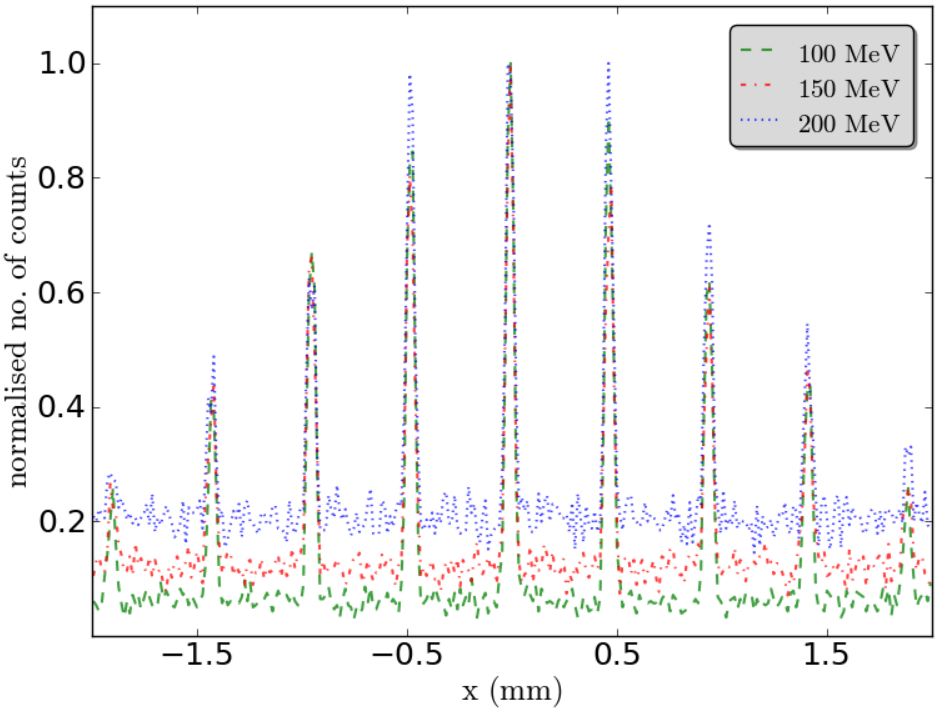

Figure 4.3: Background noise level vs beamlet signal for different central energies based on simulated pepper-pot images for 0.2 pC, 1 mrad, 1 π mm mrad electron beams.

final resolution is taken to be 10 µm.

4.2 Numerical analysis

GEANT4 simulations of the pepper-pot measurements have been performed for the geometry of Figure 4.1. The experimental resolution has been reproduced by convolving the results with a Gaussian function having a width of $\sigma = 10\,\mu$m. Figure 4.4a shows simulated pepper-pot images for a 1 mrad, 130 MeV electron beam and two different source sizes. For the chosen divergence, the beamlet size generated by a beam with an emittance of 4 π mm mrad is more than 100 % larger than the beamlet size for 1 π mm mrad. The dependence of beamlet size on source size is shown in Figure 4.4b. For a 1 mrad divergence, the smallest possible beamlet size that the current pepper-pot setup can measure is $\sim 16\,\mu$m, which is the hole diameter of the mask. For $\sigma_r \leq 4\,\mu$m (equivalent to $\leq 1\,\pi$ mm mrad), the variation in beamlet sizes is very small, setting a limit to the smallest measurable emittance.

On the other hand, a larger divergence increases the number of beamlets and

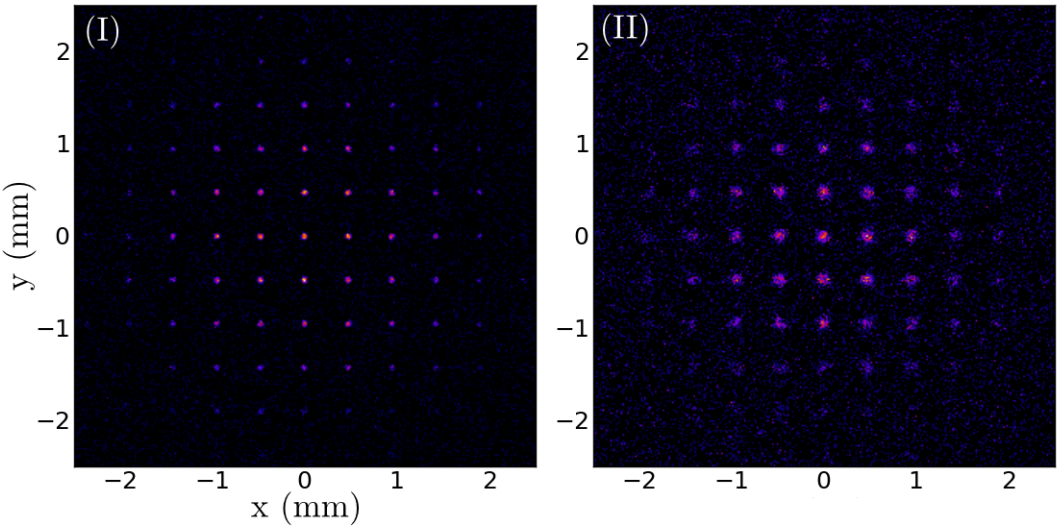

(a)

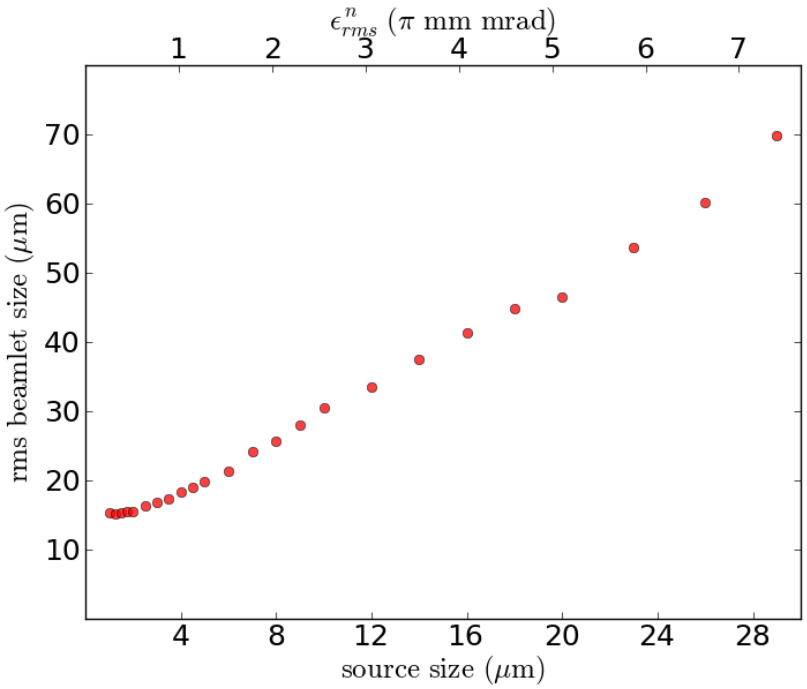

(b)

Figure 4.4: (a) False-colour simulated pepper-pot images for a 130 MeV ± 3 % electron beam with (I) $\epsilon^n_{rms} = 1\,\pi$ mm mrad and (II) $\epsilon^n_{rms} = 4\,\pi$ mm mrad. (b) RMS beamlet size calculated on the screen (70 cm from the mask) vs source size for rms divergence of 1 mrad. (The tungsten mask used here is located 30 cm from the accelerator, with hole diameter of 16 ± 2 µm and hole separation of 142 ± 2 µm)

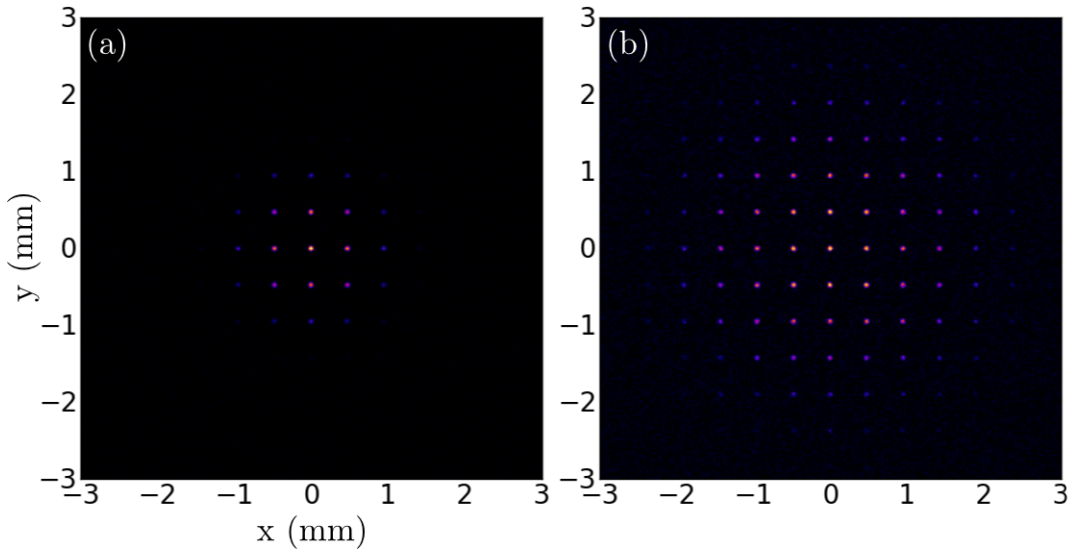

(a)

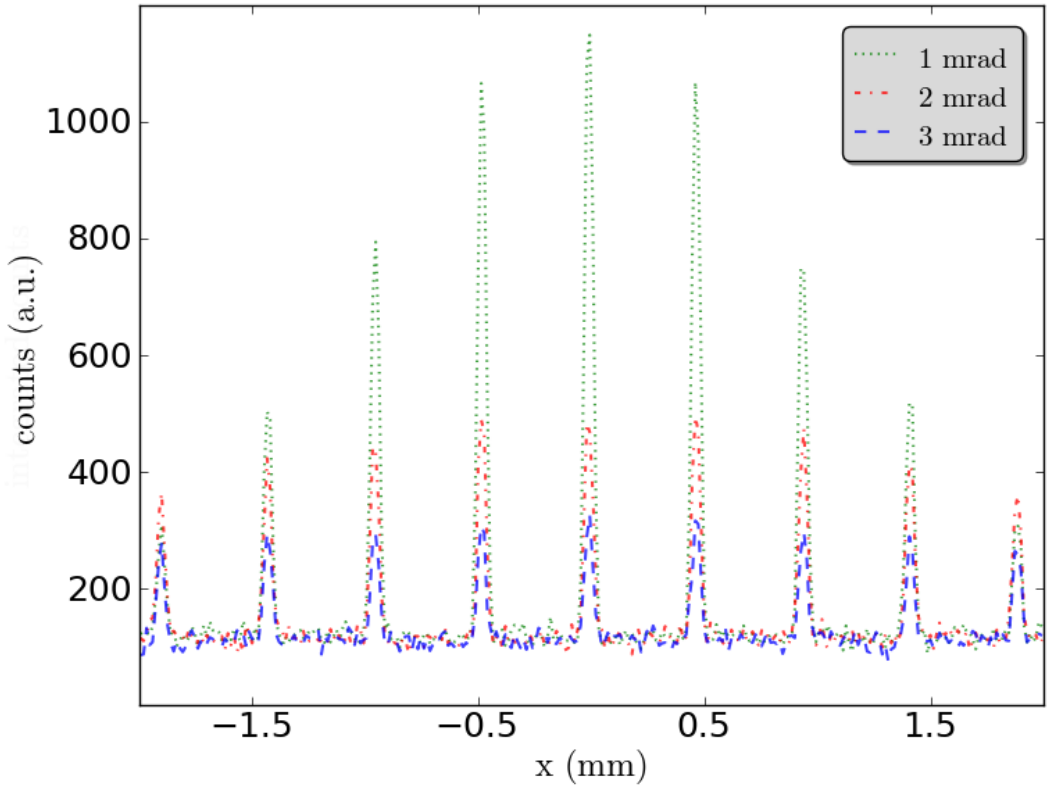

(b)

Figure 4.5: (a) False-colour simulated pepper-pot images for (I) 0.5 mrad and (II) 1 mrad divergence and (b) beamlet signal vs divergence. (Constant source parameters: $\sigma_r = 4\,\mu\text{m}$, $E = 130\,\text{MeV} \pm 3\,\%$)

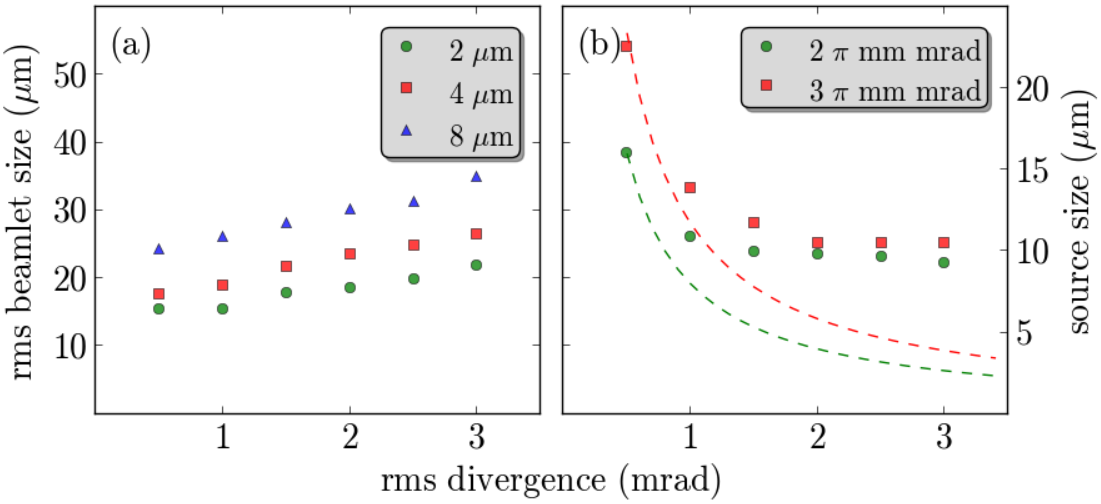

Figure 4.6: RMS beamlet size vs divergence for 0.5 pC 130 MeV ± 3 % with constant (a) source size and (b) normalised rms emittance. The corresponding source size is indicated by the dashed lines in Figure (b).

reduces the individual beamlet signal on the screen, as illustrated in Figure 4.5a. As shown in Figure 4.5b, when σ_r' reaches 3 mrad, the signal to noise ratio is very low. Simulations show that to have a measurable signal, the charge should be $\geq$ 0.5 pC for $\sigma_r' \geq$ 3 mrad. Hence, the beam divergence has two implications on the experiment: (1) electron beams with large divergence and large pointing fluctuations are clipped on the mask, decreasing the number of usable pepper-pot images. (2) As the screen is moved farther away from the mask, clipping becomes more severe. Therefore, the distance between mask and screen cannot be too large.

Since the electron beam size on the mask is much larger than the hole size, the beamlet size should be independent of divergence. This has been verified for a beam with a charge of 0.5 pC, which is high enough to produce beamlets detectable against the background noise for divergences up to 3 mrad. As shown in Figure 4.6a, the beamlet size grows by only 34 – 40 % as σ_r' is increased from 1 to 3 mrad, which is due low signal to noise ratio at the screen for larger divergence. On the other hand, when the emittance is kept constant by varying both the source size and divergence at the same time, the beamlet size changes following the dependence curve on source size. This is shown in Figure 4.6b, where both the source and beamlet sizes are plotted against the divergence. Here, the rms beamlet size decreases with the source size.

The analysis discussed in this section shows that (1) although the mask is too thin to stop the electron beam, it is able to generate detectable beamlets

on top of a nearly uniform background noise, that can be easily subtracted. (2) The smallest rms emittance that can be measured using this method is limited by the drift distance between the mask and the screen. For this configuration, emittances smaller than $1\,\pi$ mm mrad cannot be measured. And (3), for large divergences beamlets are difficult to resolve and clipping can occur, limiting the largest possible distance between the mask and the screen.

4.3 Experimental results

The schematic diagram of the transverse emittance measurements using pepper-pot technique is shown in Figure 4.1. As a first experiment, a tungsten mask with thickness of 125 µm, containing 27 x 27 laser drilled holes, with a diameter of 21.5 ±5 µm and separated by a distance of 150 µm, is used. The accelerator to mask distance is $L_g = 29.5$ cm while the mask to screen distance is $L = 61$ cm. The mask is attached to a rotating motor that can be remotely controlled to move it in and out from the beamline. A 20 x 20 x 0.15 mm YAG:Ce scintillating screen is used as detector and is positioned orthogonally to the beam path. A silver mirror tilted by 45° is located right at the back of the YAG:Ce screen to image the beamlets towards a 14-bit charged coupled device (CCD camera) combined with a compact imaging lens ($f = 108$ mm). The detection system has an overall 10 µm resolution, limited by the YAG:Ce screen. The scattering due to the laser beam is blocked off using a thin Al foil, placed very close to the YAG:Ce screen to avoid the additional effect of the foil to the acquired data. GEANT4 simulations show that over such short distances the scattering in the foil is negligible. The YAG:Ce screen and Al foil are connected to an actuator and only activated during emittance measurements.

In this experiment, the electron beam energy is 125 MeV with 3 % shot-to-shot fluctuations. The rms divergence in x and y are $\sigma'_x = 2.5 \pm 0.2$ mrad and $\sigma'_y = 2.0 \pm 0.5$ mrad (Figure 4.7b), while the shot to shot pointing stabilities are 1.5 and 0.7 mrad in x and y, as shown in Figure 4.7a. Due to the large divergence and pointing fluctuations, images that showed beam clipping and low signal were disregarded resulting in only 15 % of the shots produced useful pepper-pot images.

A false-colour image of a typical pepper-pot pattern captured in the YAG:Ce screen is shown in Figure 4.8. An electron beam profile without the mask is also shown for reference. The rms emittance in x and y is calculated for 64 out of 400 consecutive laser shots using the relation given in Equation 4.1. The distribution of x and y normalised rms emittances for this experiment is shown in

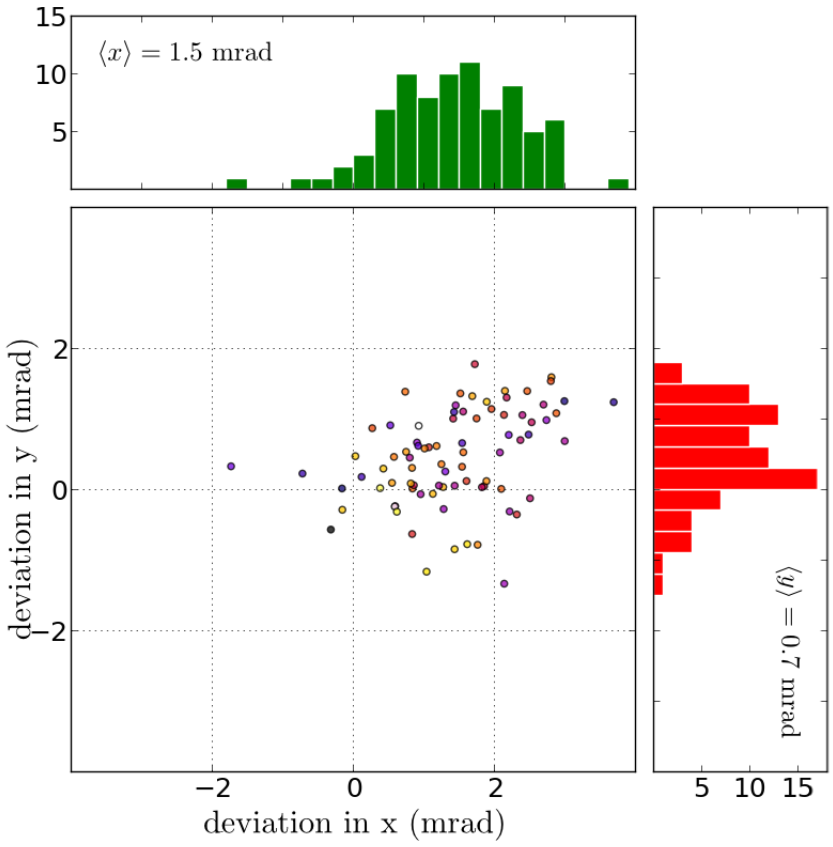

(a)

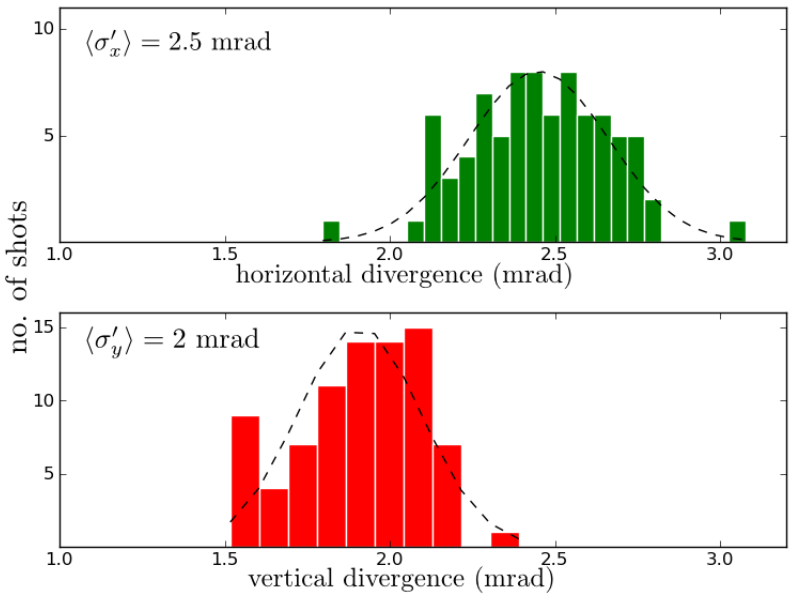

(b)

Figure 4.7: (a) Shot-to-shot pointing fluctuation and (b) rms divergence of electron beams from 82 consecutive laser shots.

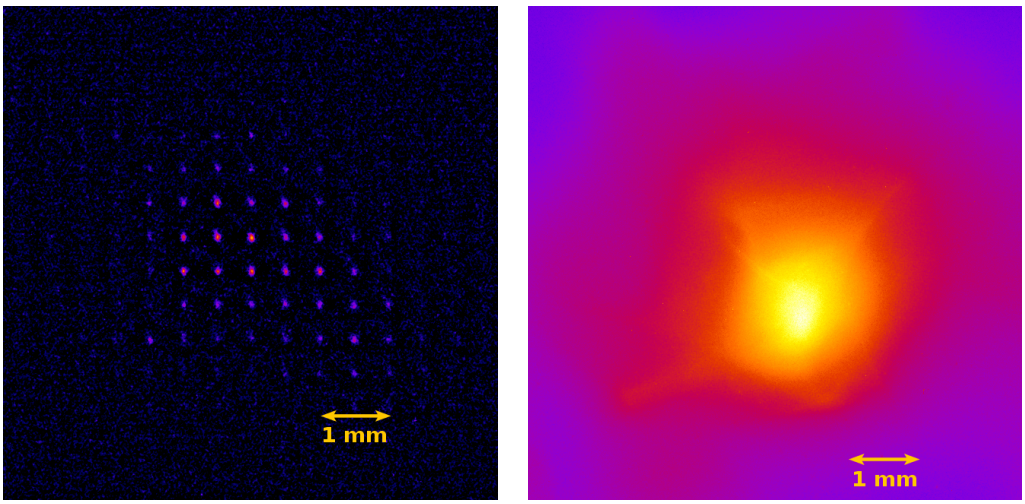

(a) (b)

Figure 4.8: False colour and background subtracted images of the electron beam as detected on the YAG:Ce screen (a) with and (b) without the tungsten mask in the beamline. The calculated normalised rms emittance in this image is 1.9 and 2.0 π mm mrad for x and y, respectively.

Figure 4.9, obtaining mean values $\epsilon^n_{x,rms} = 2.2 \pm 0.7\,\pi$ mm mrad and $\epsilon^n_{y,rms} = 2.3 \pm 0.6\,\pi$ mm mrad. The calculated rms emittances are comparable with those of conventional linear accelerators [93]. An emittance as low as $1.1 \pm 0.1\,\pi$ mm mrad was measured which corresponds to the resolution limit of the detection system. For a divergence of 2 – 3 mrad, the corresponding source size is estimated to be less than 4 – 5 µm.

The emittance experiment is repeated using the second mask shown in Figure 4.2b (16 ± 2 µm hole diameter). The number of holes is also increased to improve the collection efficiency. Furthermore, the mask to screen distance is increased to 70 cm and a CCD camera with larger viewing area (2448 x 2048 pixels) is installed. Here, a total of 20 out of 300 (7 %) usable pepper-pot images were recorded, two of these shots are presented in Figure 4.10. The emittances in x and y have an average value of 1.6 ± 0.5 π mm mrad normalised to 126 MeV (pointing, divergence and emittance distributions are shown in Chapter 5). The improved setup has decreased the background noise, leading to more resolvable beamlets, however, fewer images were obtained due to the electron beams lower charge and higher divergence as compared with the first measurement.

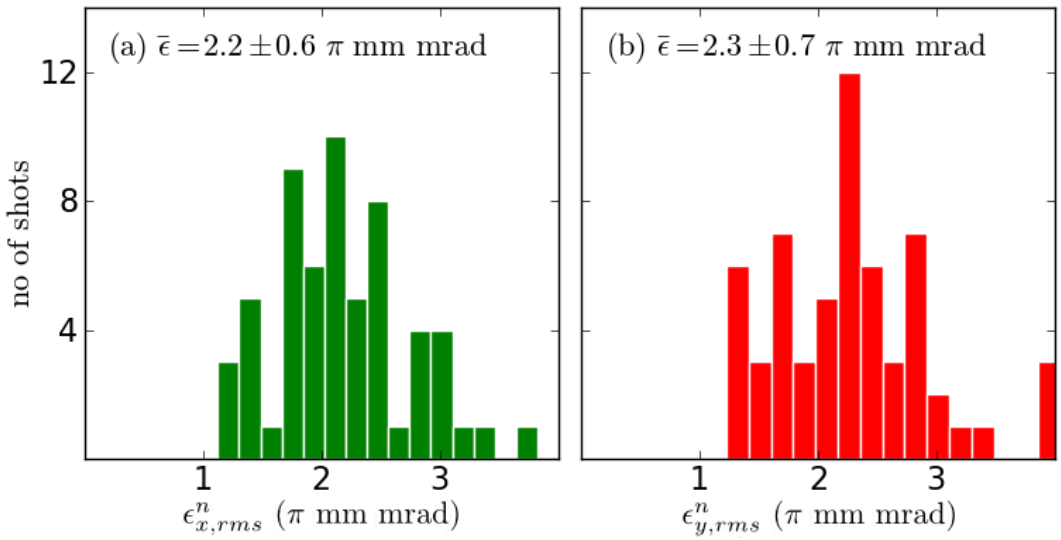

Figure 4.9: Distribution of the normalised rms emittance in x and y using 64 (out of 400) pepper-pot images [23, 94].

4.4 Discussions

The accurary of pepper-pot method for emittance measurements mainly depends on: (1) mask hole size, (2) screen/detector resolution and (3) image magnification (i.e. mask to screen distance). The improvements done for the second batch of measurements are the following:

- Used a mask with smaller hole diameter – from 25 µm to 16 µm and more holes.
- Increased the mask to screen distance – from 61 cm to 70 cm. Although the setup magnification is only increased by 11 %, the smaller hole diameter compensates for it, reducing the weight of the hole correction in the beamlet measurement.
- Installed a CCD camera with larger viewing area – from 1.2 MP to 5 MP to increase the collection efficiency of the measurement.
- Reduced the background noise by improving the housing of the Al foil and YAG:Ce crystal.

The emittances obtained here are similar to the results of other groups that have used the pepper-pot technique [25, 28]. These are the first direct measurements of transverse emittance of laser-produced electron beams, showing that

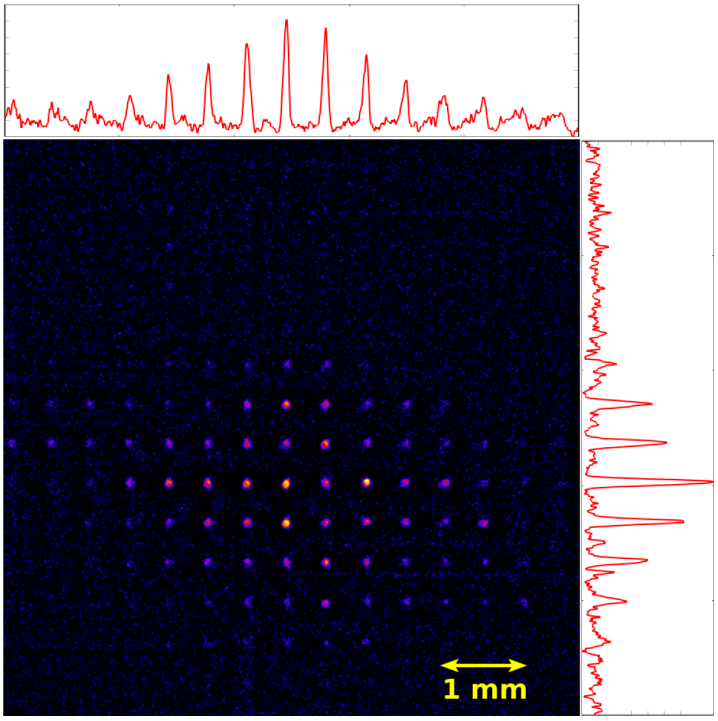

(a)

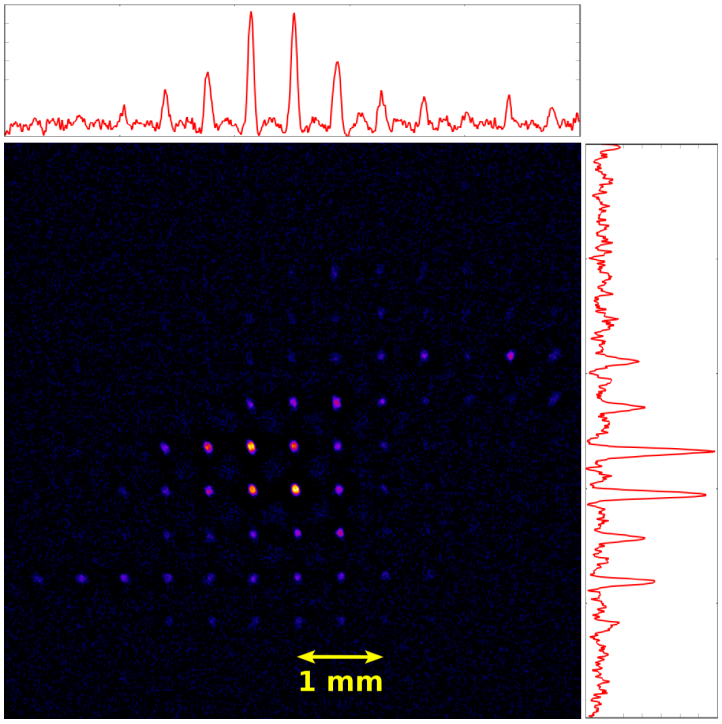

(b)

Figure 4.10: Background-subtracted pepper-pot images as captured on the YAG:Ce screen using the second batch of tungsten mask, with the corresponding rms emittance of (a) $\epsilon^n_{x,y,rms} = 2.2 \pm 0.7\pi$ mm mrad and (b) $\epsilon^n_{x,rms} = 1.8 \pm 0.7\pi$ mm mrad, $\epsilon^n_{y,rms} = 2.2 \pm 0.7\pi$ mm mrad both normalised to 126 MeV.

they can have values in the order of $1\,\pi$ mm mrad. However, recent simulations in bubble regime have shown that transverse emittances can be lower than $1\,\pi$ mm mrad if the trapped electrons are injected on-axis [23, 27, 42].

Recent works on transverse emittance measurements from LWFA using different techniques have been published obtaining values smaller than $1\,\pi$ mm mrad. G.R. Plateau et al. used x-ray spectroscopy, where an approximation of the electron beam source size is obtained by matching the x-ray spectrum emitted by the accelerated electrons in the plasma to betatron radiation models [27]. Together with simultaneous divergence and energy measurements, a transverse emittance of $\sim 0.1\,\pi$ mm mrad normalised to 460 MeV is estimated. However, as the method only inferred the emittance through the beam source size in the bubble, it does not take into consideration the possible emittance growth in the plasma to vacuum transition. In the works of R. Weingartner et al, quadrupole scan technique is utilised to estimate the beam spot size and the divergence is measured separately. Their measurements are done after the electron are dispersed using an electron spectrometer to remove the emittance blow up due to chromaticity. Here, an estimated normalised rms emittance of $\sim 0.2\,\pi$ mm mrad is obtained for 245 MeV electron beams [28]. A summary of these measurements is shown in Figure 4.11. The main limitation of the pepper-pot technique is the resolution, whereas the other methods have better accuracy but are indirect and require multiple shots.

To evaluate if the pepper-pot technique has the possibility of measuring such small emittances, the following limitations have to be considered.

Magnification

It was shown in the simulations that electron beams with transverse emittances below $1\,\pi$ mm mrad generate beamlets with dimensions close to the mask hole diameter. As shown in Figure 4.4b, the beamlet widths are almost constant below $\sigma_r = 4\,\mu$m, resulting in indistinguishable source size variations. Ideally, this can be improved by increasing the magnification of the system. Figure 4.12 plots the beamlet size of an electron beam with $\sigma_r' = 1$ mrad and normalised emittances of $0.5\,\pi$ mm mrad and $1\,\pi$ mm mrad for varying setup magnification. Electron beams with 0.5 pC charge are considered to remove errors due to low signals. Here, the magnification is improved by increasing the mask to screen distance. To have a good statistics, the beamlet size on the screen should be more than two to three times the hole diameter and the growth of the beamlets for two different emittances considered should be largely different. This is obtained when the screen is located farther than 200 cm from the mask, which is physically difficult

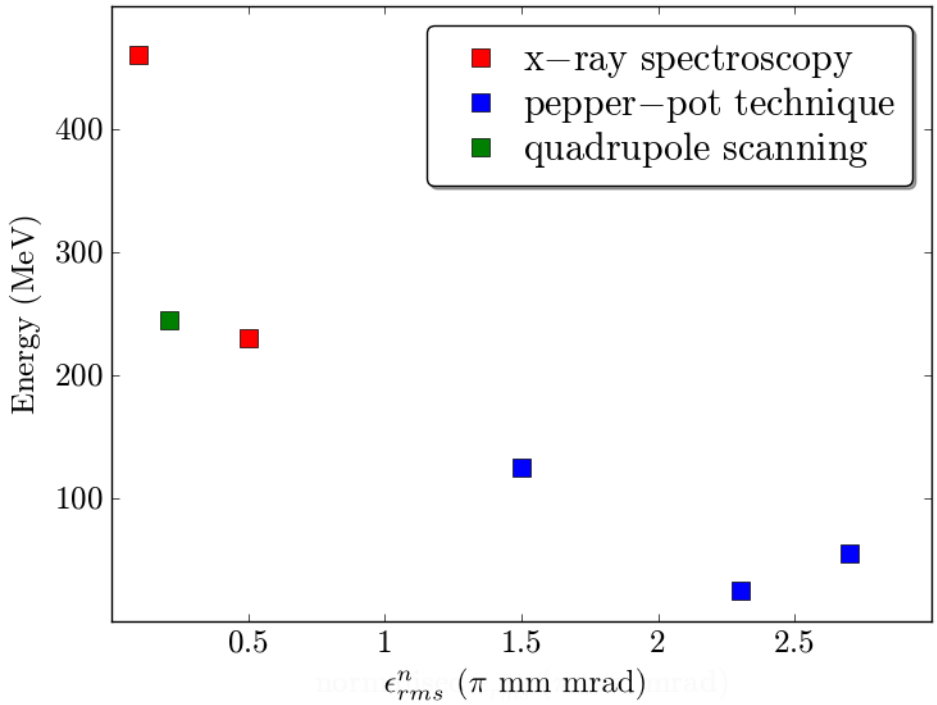

Figure 4.11: Measured transverse emittance of electron beams from LWFA. Data with blue marker employed pepper-pot technique (electrons from 0.3–3 mm long gas jet targets with plasma density between 2 and 5×10^{19} cm^{-3}), while data with red and green markers are from other indirect measurements (electrons from preformed plasma channel using capillary discharge waveguides and gas cell with plasma density between 3 and 6×10^{18} cm^{-3}), based from [23–28].

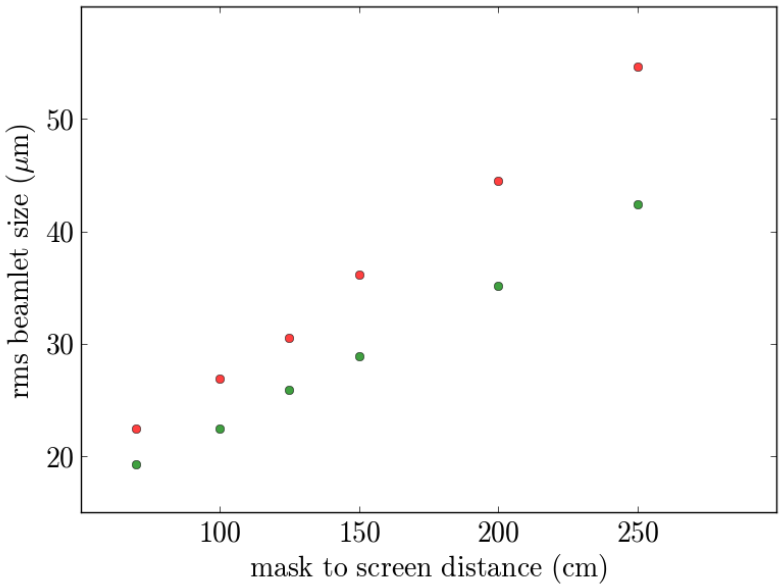

Figure 4.12: RMS beamlet size vs mask to screen distance (L) of electron beams with divergence of 1 mrad, 0.5 pC and normalised emittances of 0.5 π mm mrad (green marker) and 1 π mm mrad (red marker).

to achieve since (1) the current beamline will not be able to accomodate such long distance and (2) a larger beamlet size also implies a weaker signal to be detected. If the beam divergence is more than 1 mrad, higher charge is required. Moreover, a bigger crystal and an imaging system capable to see the whole pattern is required.

Another possibility is to have a high resolution screen such that the resolution limit is improved. Figure 4.13 shows the results of GEANT4 simulations obtained after deconvolving with Gaussian functions with smaller σ, therefore reproducing a higher resolution screen. The rms beamlet size is calculated for normalised emittances less than 1 π mm mrad and mask to screen distance of 100 cm. It can be seen that the growth of beamlet sizes are the same for increasing screen resolution, indicating that at this setup, high resolution screen is not really necessary.

Mask hole diameter

Ideally, a mask with infinitely small hole diameter (i.e. hole diameter smaller than the electron beam source size) is required to make the hole correction negligible. However, small hole sizes decrease the beamlet intensity on the screen, making it difficult to distinguish the beamlet signal from the background noise. For example, a mask with 4 µm hole diameter requires electron beams of 1 mrad and

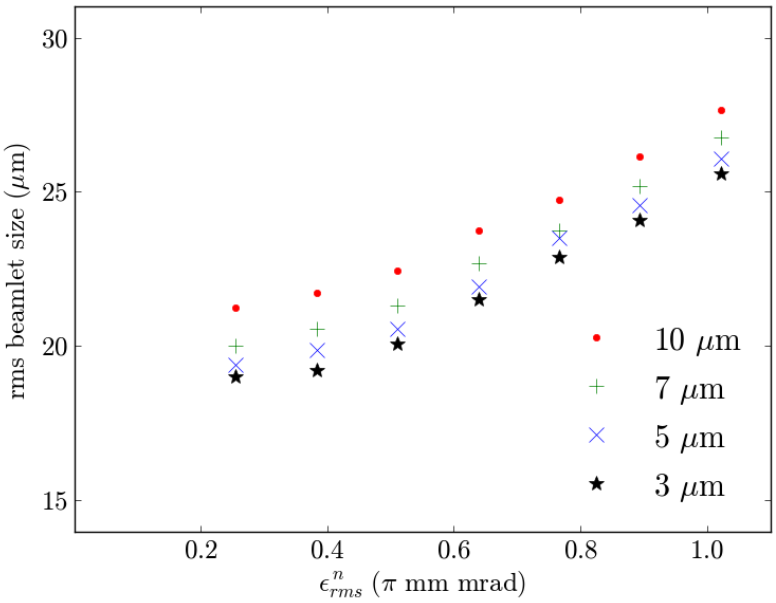

Figure 4.13: RMS beamlet size of electron beams with divergence of 1 mrad and normalised emittances less than 1 π mm mrad for varying (YAG:Ce) screen resolution. The mask to screen distance is set to 100 cm.

0.8 pC to have detectable beamlets. This means that for larger divergence, higher charges are needed. Moreover, smaller hole diameters are difficult to manufacture.

If, however, a mask with small hole diameter is available, the magnification should be improved to achieve larger variations in beamlet sizes for emittances lower than 1 π mm mrad. As shown in Figure 4.14, the current setup ($L = 70$ cm and $M = 3.3$) produces only 5 µm difference from 0.2 to 1 π mm mrad when a mask with hole radius of 4 µm is used. However, if the mask to screen distance is increased to 170 cm ($M = 6.7$), the beamlet sizes vary from 20 to 30 µm, which is enough to measure emittance down to $\sim 0.25\,\pi$ mm mrad. As stated in the previous section, higher magnification requires larger crystal and imaging system to obtain the whole pepper-pot pattern and to avoid beam clipping.

It is also worth to note that although smaller mask hole diameter requires higher screen resolution, the beamlet variations are not improved. This means that to measure emittances less than 1 π mm mrad using the pepper-pot method, large mask to screen distance is the primary requirement. However, for laser produced electron beams, this post a problem due to inherent large divergence.

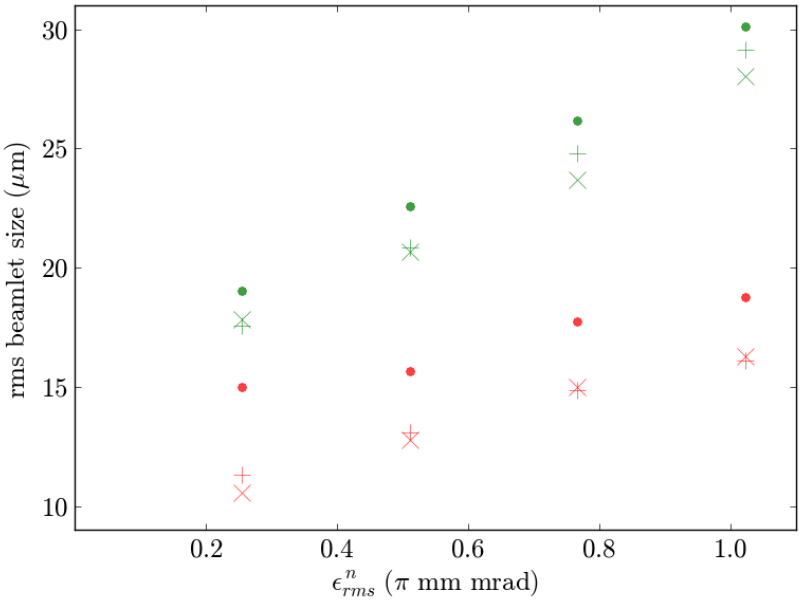

Figure 4.14: RMS beamlet size vs rms emittance (less than $1\,\pi$ mm mrad) of electron beams with 130 MeV $\pm$ 3 % energy, 0.8 pC charge and 1 mrad divergence for $M = 3.3, L = 70$ cm (red markers) and $M = 6.7, L = 170$ cm (green markers), using a tungsten mask with hole radius of 4 µm. Different symbols indicate the screen resolution used : 10 µm (•), 5 µm (+) and 3 µm (×) .

4.5 Summary

In this chapter, direct single-shot transverse emittance measurements using the pepper-pot method are presented. One main drawback of the pepper-pot technique is its low resolution, which does not allow to measure transverse emittances lower than 1 π mm mrad due to physical constraints. Simulations show that improving the setup magnification or mask design is not enough to resolve emittances below $1\,\pi$ mm mrad.

Chapter 5

Electron beams diagnostics using pepper-pot and quadrupoles

The divergence of laser-driven electron beams ranges between 1 and 4 mrad [18, 24, 95], causing the beam size to blow up quickly during propagation over long drift distances. A strong focusing system is required in order to reduce the electron beam size. For better control and efficiency, the focusing system should be compact so that it can be positioned close to the accelerator. This requirement can be accomplished by using miniature permanent quadrupole (PMQ) lenses. Usually, PMQs have strong magnetic field gradients ($\sim$ 500 T/m) and therefore strong focusing power over short distances, making them attractive tools for laser-driven electron beam transport.

As shown in Chapters 2 and 3, three PMQs have been designed for the ALPHA-X beamline to form a compact focusing triplet with length between 4 and 12 cm, depending on the desired energies to optimise. It can be positioned very close to the accelerator and it can be inserted or removed from the beamline by using a remotely controlled translation stage. The effective focal length of a triplet depends on the quadrupoles magnetic gradients and drift separations. Since the magnetic strengths of PMQs are fixed, the drift separations are adjusted to optimise the transport of the required energies.

The PMQs compact size requires precise design and alignment. Detailed studies on the fabrication, fine tuning and beam transport simulation of PMQs as a focusing system have been reported [96,97]. It has also been shown that PMQs can act as an energy filter, therefore, decreasing the electron beam energy spread [98]. However, less has been said on the PMQs' capability of preserving the emittance of the beam and their limitation on improving the beam's pointing stability. In this chapter, a method of characterising electron beams using a PMQ triplet is presented. Here, the pepper-pot method and PMQs are combined to simultaneously determine the electron beam projected emittance with the quadrupoles and quantify the performance of the focusing system. In the experiment here reported, the electron beams pass through a focusing triplet and then through a pepper-pot mask. The outgoing beamlets are detected by a YAG:Ce screen cou-

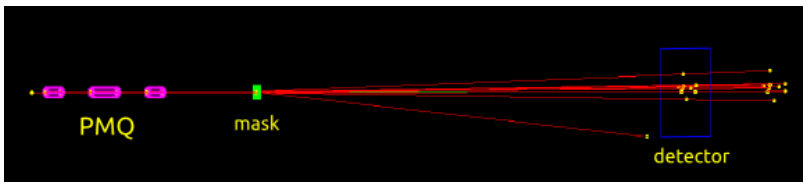

Figure 5.1: Schematic diagram of the modeled experiment using GEANT4 visualization.

pled with a high-resolution optical system. Details on the emittance measurement using the pepper-pot technique have been discussed in Chapter 4.

5.1 Numerical analysis

5.1.1 Beam propagation with PMQ triplet

Simulations using GEANT4 are performed to evaluate the PMQ triplet behaviour for the geometry shown in Figure 5.1. A detailed description of the quadrupoles has been presented in Chapter 2. The permanent quadrupoles have been modelled using a magnetic structure simulator to obtain a field map. Gradients have been extracted to match this field distribution as closely as possible with the quadrupole equations given in Equation 2.11. The quadrupole equations used in GEANT4 and field maps from GPT both produce the same results, as shown in Figure 5.2. The effective length and magnetic gradients of the PMQs are given in Table 2.1. GEANT4 results have been convolved with a Gaussian with $\sigma = 10\,\mu m$ to match the experimental resolution.

The triplet is arranged with alternating signs of magnetic gradient, having a similar configuration as the electromagnetic triplet of the ALPHA-X beamline. The drift separations between the first and the second PMQs (s_1) and between the second and third PMQ (s_2) are $s_1 = s_2 = 3.35\,cm$. With this configuration, the triplet has an effective focal lengths of 15.5 cm (horizontal plane) and 12 cm (vertical plane) for 130 MeV. The triplet configuration is set to optimise the matching of the transport for electron energies between 100 MeV and 150 MeV. The centre of the triplet is placed at a distance of 10.6 cm from the accelerator. The mask is 30 cm from the accelerator and the scintillating screen is 70 cm from the mask, matching the experimental setup. A transverse symmetric Gaussian beam distribution is initialized to simplify the analysis, with initial emittance, $\epsilon_{source,x} = \sigma_x \cdot \sigma'_x$, where σ_x and σ'_x are the rms source size and divergence in the horizontal direction, respectively. Similar relation also applied to the vertical

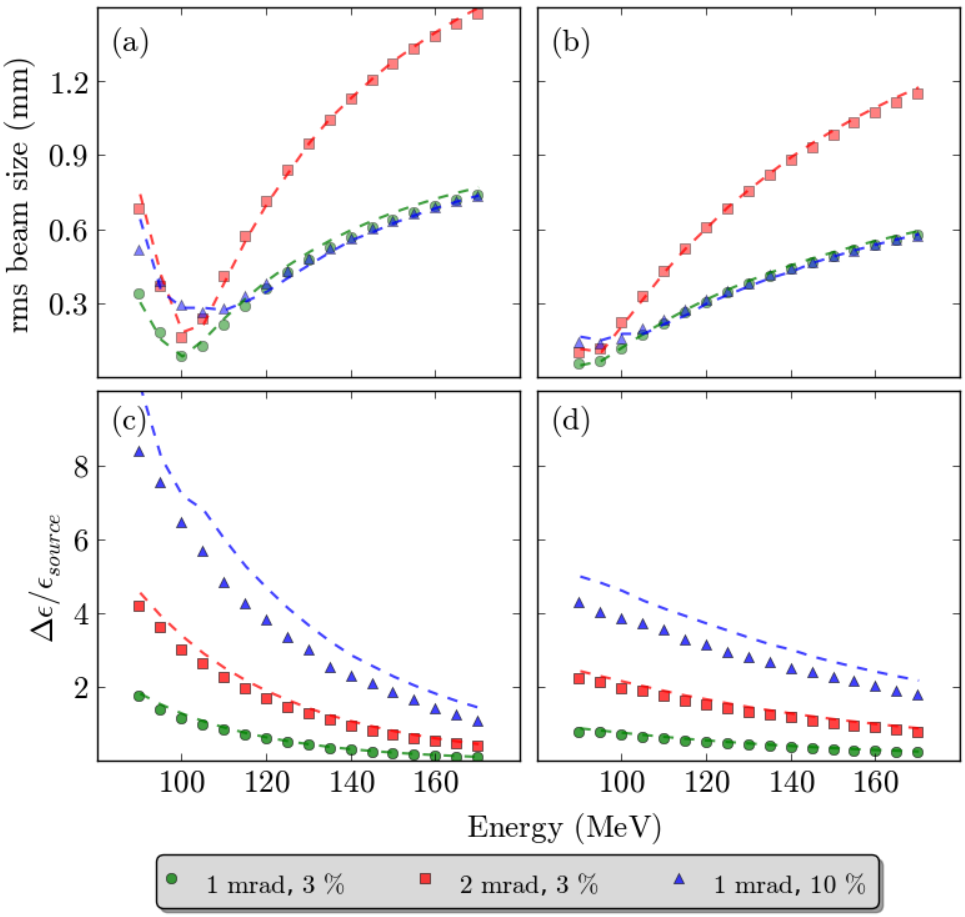

Figure 5.2: RMS beam size and emittance growth at a distance of 100 cm from the accelerator, after propagation through the PMQ triplet. Figures a and c show the beam evolution in the horizontal plane, Figures b and d in the vertical plane. The initial beam size is kept to 4 µm (initial $\epsilon^n_{rms} = 0.7 - 1.3\,\pi$ mm mrad). The dashed lines are obtained using the field map (GPT) and the symbols using Equation 2.1 (GEANT4).

direction. In the simulation, it is assumed that $\sigma_x = \sigma_y$, unless specified.

Without the focusing system, an electron beam with an initial rms size σ_x of 4 µm and rms divergence σ'_x of 2 mrad can grow as much as 2 mm after a drift distance of 100 cm. However, with the PMQ triplet positioned along the beamline, the beam size evolution becomes energy dependent. As shown in Figure 5.2, the beam can still be reduced at energies beyond 150 MeV, where PMQs focusing ability is weaker.

The energy dependence of the beam envelope is shown in Figure 5.3. For energies lower than 100 MeV, the focusing power in the horizontal and vertical planes is very different. In the horizontal plane, the electron beam is tightly focused by the middle quadrupole and diverges rapidly after propagation through

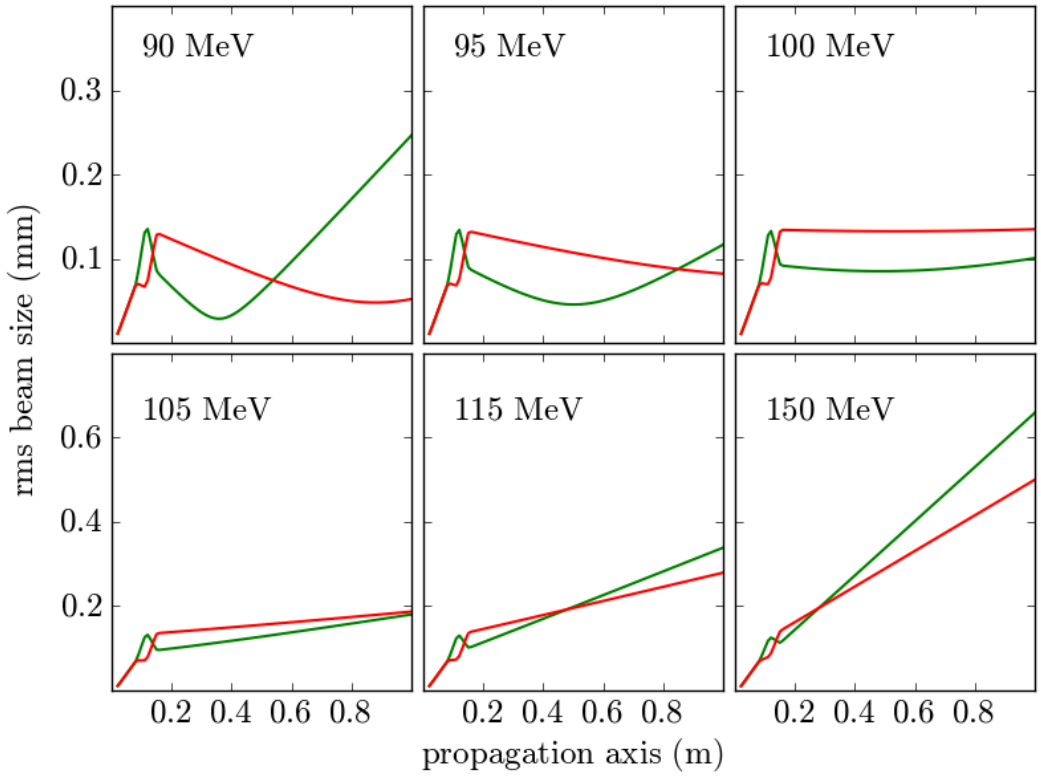

Figure 5.3: Effect of the PMQ triplet on the electron beam evolution (green lines for x and red lines for y) for different energies. (Source parameters: $\epsilon^n_{rms} = 1\,\pi$ mm mrad and $\Delta E/E = 3\,\%$)

the triplet. In the vertical plane, the focusing is weaker, leading to a highly elliptical transverse beam profile. For energies between 100 MeV and 105 MeV, the electron beam remains roughly collimated to a size of about 200 µm within 1 m from the accelerator. For emittance less than $1\,\pi$ mm mrad and negligible energy spread, the PMQs are able to keep the size of 100 MeV electron beams below 100 µm. For energies higher than 105 MeV, the strength of the PMQs decreases resulting in a reduction of divergence by a few percent. In fact, at 170 MeV, the beam trajectory is already similar to an electron beam without PMQs. Since the PMQ triplet has stronger focusing power in the vertical plane (y in Figure 5.3), the divergence is smaller than in the horizontal plane (x in Figure 5.3), resulting in elliptical transverse beam profiles.

The corresponding chromatic growth in projected emittance ($\Delta\epsilon/\epsilon_{source}$) due to the triplet is also shown in Figure 5.2 c & d for 3 % and 10 % energy spreads ($\Delta E/E$). Since the beam transport in the horizontal and vertical planes is very different at low energies, the projected emittance and the corresponding beam size in x is larger compared to y. In contrast, for higher energies the emittance growth is approximately the same in both axes. The projected emittance gets worse for

large $\Delta E/E$, growing by almost an order of magnitude. An effect of the chromatic aberration is the additional beam blow out, however this is only observable for energies below 120 MeV, where the electron beams are tighly focused. Larger divergence can also contribute to the geometric increase of projected emittance as the chromatic effect of the PMQs is also dependent on the input beam size (cf. to Section 2.4.1).

5.1.2 Pepper-pot simulations with PMQ triplet

The tungsten mask used in the simulations has holes with diameter of 16 µm, separated by 142 µm. When no focusing elements are utilised, the longitudinal characteristics of the electron beam do not have any effects on the pepper-pot images. For the geometry of the pepper-pot experiment, the spacing between beamlets (detected on the screen 70 cm from the mask) is $\sim$ 470 µm, consistent with the magnification ($M = 3.3$) of the setup. The shape and number of beamlets are solely related to the electron beam source size and divergence. However, with the addition of PMQs, the position and shapes of the beamlets depend on the energy, as shown in Figure 5.4. The triplet also decreases the effective "source" divergence of the beam, thus improving the signal to noise ratio as compared with pepper-pot images without the triplet.

For electron energies lower than 100 MeV, the strong difference in focusing power between the horizontal and vertical planes produces highly distorted beamlets. At 100 MeV, the focusing effect is the strongest and the hole separation in the mask is too wide to create beamlets, even if the beam divergence is increased to 2.5 mrad. Therefore useful pepper-pot images can be obtained experimentally only for energies higher than 100 MeV.

For fixed initial divergence, the number of beamlets increases with the energy. Moreover, different energies produce different separations between beamlets in x (d_x) and y (d_y) planes, as shown in Figure 5.5a for an electron beam with $\sigma_x = 4$ µm, $\sigma'_x = 1$ mrad and $\Delta E/E = 3$ %. Both d_x and d_y rapidly increase until 140 MeV, and then stabilise to a value which slowly approaches 470 µm, indicating that the electron trajectories are no longer significantly affected by the quadrupoles. Since the overall focusing effect is stronger on the vertical plane, d_x is always greater than d_y, in agreement with the results of Figure 5.3. Moreover, the difference between d_x and d_y is $\sim$ 100 µm, independent of energy. The focusing power of the triplet is energy dependent, making the beamlet separation energy dependent as well. Therefore, d_x and d_y give an insight on the range of electron beam energies. Although a 1 mrad electron beam is used in the simulations, the

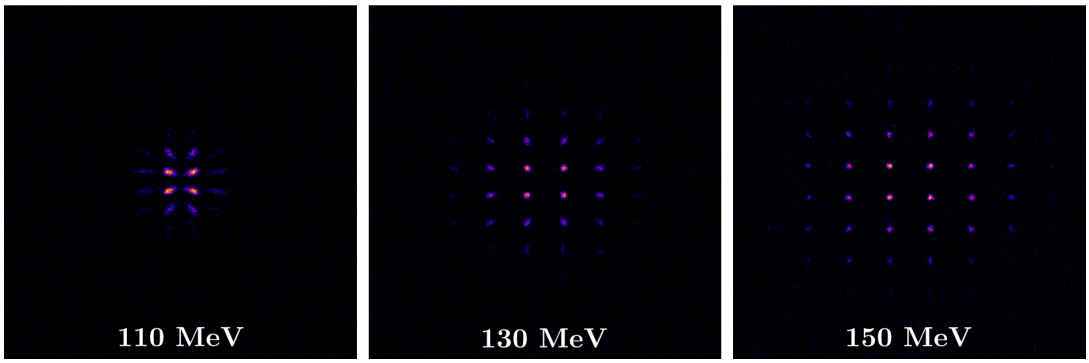

(a) $\Delta E/E = 3\,\%$

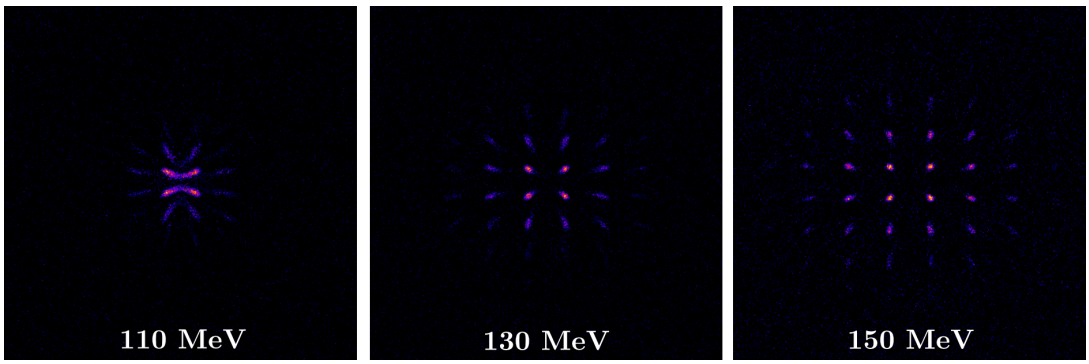

(b) $\Delta E/E = 7\,\%$

Figure 5.4: Simulated pepper-pot images after propagation through the PMQ triplet for (a) 3 % and (b) 7 % energy spread. (Source parameters: $\sigma_x = 4\,\mu\text{m}$, $\sigma'_x = 1\,\text{mrad}$)

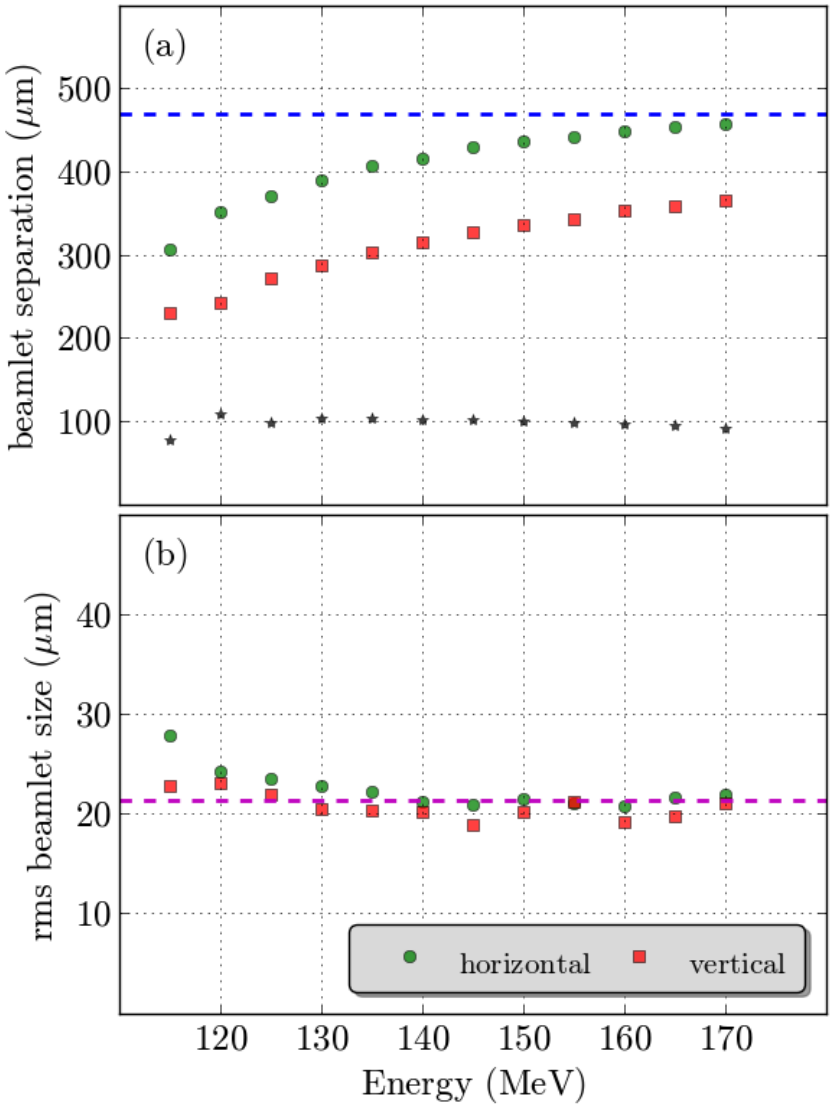

Figure 5.5: (a) Mean spacing between beamlets and (b) rms beamlet size of the simulated pepper-pot images as a function of electron beam energy. The rms size and beamlet separations are calculated for the horizontal and vertical axes. The black stars are the difference of horizontal (d_x) and vertical (d_y) beamlet separations. The dashed lines indicate the spacing between beamlets (blue) and beamlet size (purple) without using the triplet. (Source parameters: $\sigma_x = 4\,\mu\text{m}$, $\sigma'_x = 1\,\text{mrad}$, $\Delta E/E = 3\,\%$).

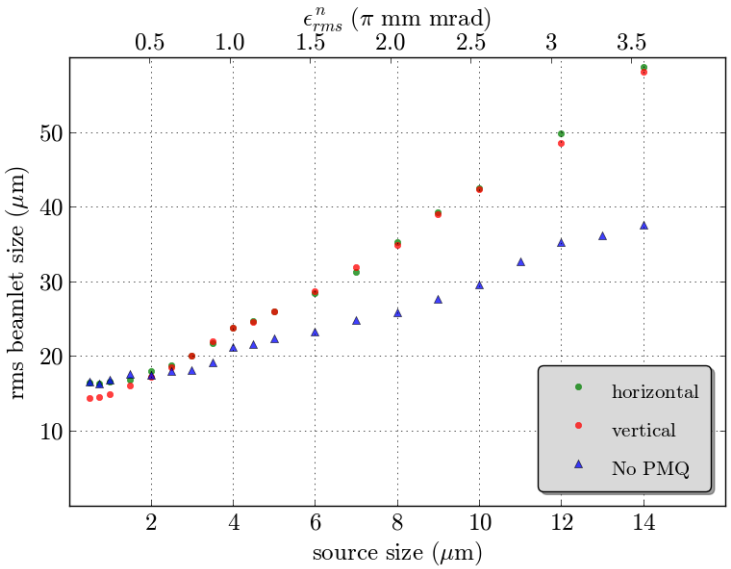

Figure 5.6: Dependence of beamlet size on source size with $\sigma'_x = 1\,\text{mrad}$ and energy of 130 MeV $\pm$ 3 %.The corresponding beamlet size without the PMQs is also included for comparison.

divergence only increases the number of beamlets detected on the screen but does not change the beam trajectory, hence there will be no significant effect on the spacing between beamlets.

The rms beamlet size does not vary much for energies greater than 120 MeV, as shown in Figure 5.5b. Using the same source parameters of Figure 5.5a, the beamlet size remains close to $\sim$ 20 µm for energy between 120 MeV and 170 MeV. There is a small difference ($\sim$ 2 to 3 µm) between the beamlet sizes calculated along the x and y directions, a consequence of having different magnetic strength in the two axes.

Since it was shown that the beamlet size is independent of the energy, from here on, the simulations will only focus on a single energy to explore other parameters. A 130 MeV electron beam is chosen to match the mean experimental energy obtained from the accelerator.

Dependence on emittance and divergence

The beamlet size is strongly dependent on the electron's emittance, which can be varied numerically by the source size σ_x, as shown in Figures 5.6 & 5.7a for fixed initial divergence of $\sigma'_x = 1\,\text{mrad}$ and 2 mrad. The beamlet size evolution without the triplet is also included for comparison. With the addition of the triplet, the smallest possible beamlet size decreases to $\sim$ 15 µm. The beamlet considered in this calculation is located close to the axis and therefore experiences chromatic

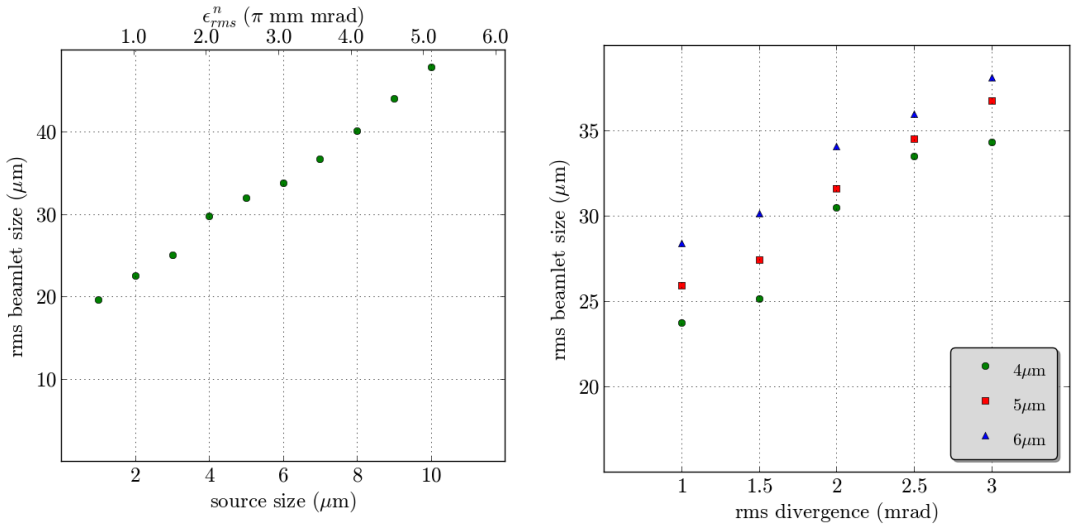

(a) (b)

Figure 5.7: RMS beamlet size (a) vs initial emittance (source size) with σ'_x = 2 mrad and (b) vs divergence for 130 MeV ± 3 % electron beams.

effects. In a quadrupole, the chromatic aberration is also dependent on the initial beam size. Larger source sizes enhance the chromatic emittance growth, resulting in a larger final beam size after the PMQs. This is evident in Figure 5.6 which shows that the beamlet size increases more rapidly with a larger source size in comparison with the case without a triplet.

When the focusing system is not used, the larger divergence increases the number of beamlets detected on the screen but the integrated beamlet signal is reduced, as shown in Figure 5.12. For a constant source size, the beamlet size increases by ∼8 µm when the rms divergence goes from σ'_x = 1 to 3 mrad (cf. Section 4.2). Similar behaviour of the beamlets is obtained when the triplet is used, as shown in Figure 5.7b. For σ_x = 4 to 6 µm, the beamlet size has increased by 7 – 10 µm when σ'_x = 3 mrad, showing that changes in beamlet shape are dominated by the emittance. Moreover, with the PMQs the minimum charge to have resolvable beamlets is only 0.3 pC for a divergence between 2 – 3 mrad and negligible energy spread.

For ideal quadrupoles, the focusing powers in horizontal and vertical planes are uncoupled. Hence, if the initial beam distribution is elliptical (either the source size or divergence in x and y are different), the beamlets properties change only in the same plane. For instance, for a 1 mrad beam with source sizes of 4 µm and 6 µm in x and y, the resulting beamlets will have bigger height (∼ 28 µm) than width (∼ 21 µm), similar to the trend in Figure 5.6. If the elliptical distribution is caused by a different x and y divergence instead, only the number

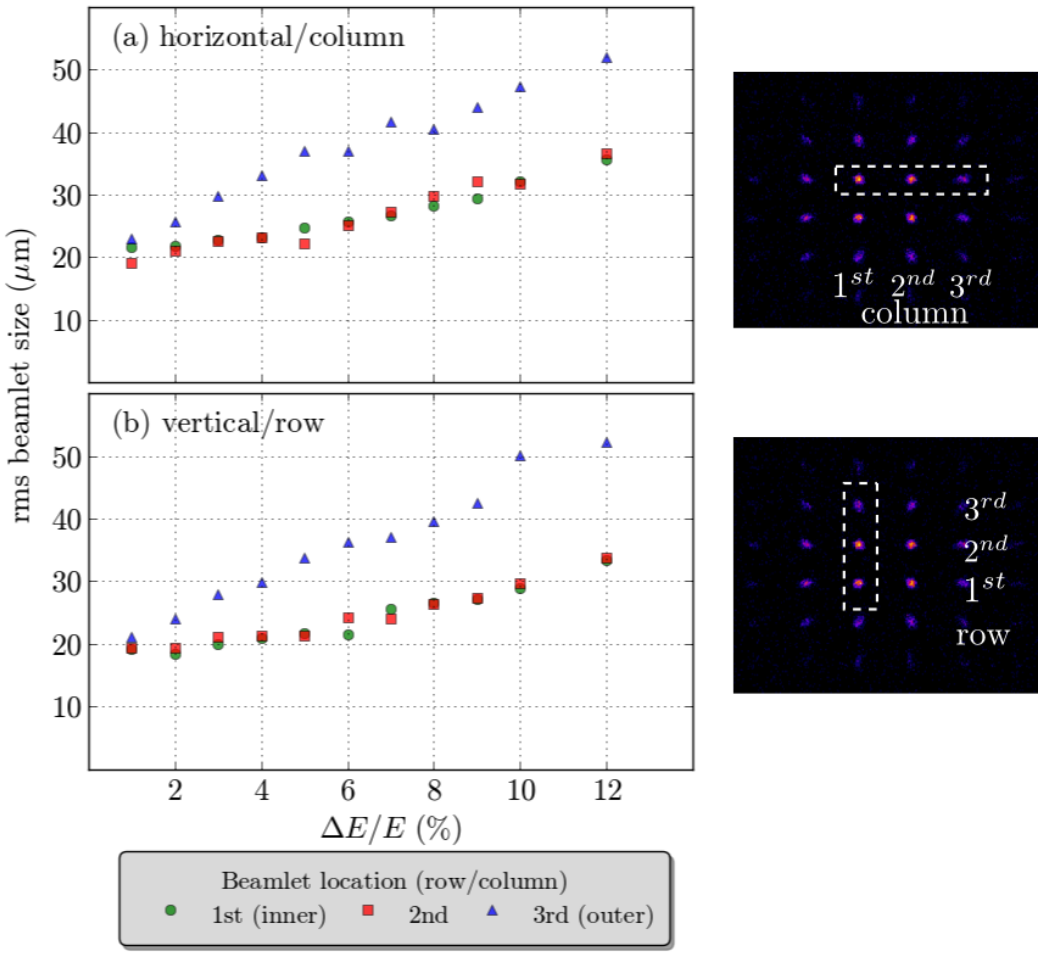

Figure 5.8: RMS beamlet size as a function of $\Delta E/E$ after propagation through the triplet, measured along the (a) horizontal and (b) vertical planes. The size is calculated for three different locations of the beamlet, as indicated on the false-colour images on the right. (Source parameters: 130 MeV, initial $\epsilon^n_{rms} = 1\,\pi$ mm mrad, $\sigma'_x = 1$ mrad)

of beamlets along rows and columns changes, indicating that the variation in the x and y beamlet sizes are independent with each other.

Dependence on energy spread

In addition to the source size, the electron beam energy spread also causes emittance growth, changing the beamlet size (see Figure 5.4-b). For larger $\Delta E/E$, the beamlets are bigger and the quality is degraded. Moreover, the size of the beamlets is no longer uniform in a single row or column. The beamlets farther from the centre of the image are highly distorted and tilted as compared to the beamlets located at the centre. The centred beamlet whis is closed to the axis are less affected by the triplet chromaticity than the beamlets farther from the

axis. Figure 5.8 shows the expected beamlet sizes for an electron beam with $\Delta E/E$ of 1 to 12 % keeping the initial rms emittance and divergence constant, $\epsilon^n_{rms} = 1\,\pi$ mm mrad and $\sigma'_x = 1\,$mrad. Three different rows and columns are considered, where the first and second rows (columns) are the beamlet located in between the central axis of the image, while the third row (column) is the beamlet located far from the axis. This is illustrated on the images provided in Figure 5.8. For beamlets in the first and second rows (columns), the rms size remains close to 20 µm until $\Delta E/E = 6\,\%$, growing slowly as the energy spread is further increased. Both beamlets experience less chromatic effects from the triplet. There is no much difference in the calculated beamlet sizes for the first and the second rows since they are both located very close to the axis (right before and after the center). However, the beamlet size increases faster for beamlets located far from the beamline axis, reaching 40 µm for $\Delta E/E = 8\,\%$. This is more than 10 µm larger than the beamlet located at the centre. As $\Delta E/E$ increases, the beamlets size variation also grows in a single row or column. For instance, at $\Delta E/E = 4\,\%$, the difference between beamlets in a column is only 10 µm, whereas at $\Delta E/E = 10\,\%$, the difference reaches 20 µm. This effect is clear evidence of chromatic aberration induced by the PMQs. Moreover, the orientations of the beamlets are degraded as they start to tilt in all directions. Although the simulations assume an electron beam with $\sigma'_x = 1\,$mrad, the effect of divergence on the beamlet size is very small, as observed when the PMQs are not used. For instance, the beamlet size grows only by 3 µm with $\sigma'_x = 2\,$mrad for $\Delta E/E = 1 - 12\,\%$.

Dependence on pointing stability

The beamlet size is also sensitive to the relative alignment between the axis of the triplet and the direction of the electron beam. Experimentally, this can vary as result of fluctuations in the pointing of the electron beam or misalignment of the triplet with respect to the beamline axis. As shown in Figure 5.9, without the triplet, an off-axis electron beam simply results in translated images with no differences in the properties of the beamlets. However, with the triplet in place, the emittance growth is larger for beams propagating off-axis and beamlets are more distorted and tilted towards the given direction. Figure 5.10 compares the growth of the beamlet size for electron beams on-axis ($\vartheta = 0$) and off-axis ($\vartheta = (1.5, 1.5)$ mrad) with beamlets located at the centre and on the far side of the image.

The distortion of the beamlets off-axis and on-axis is very similar, with an

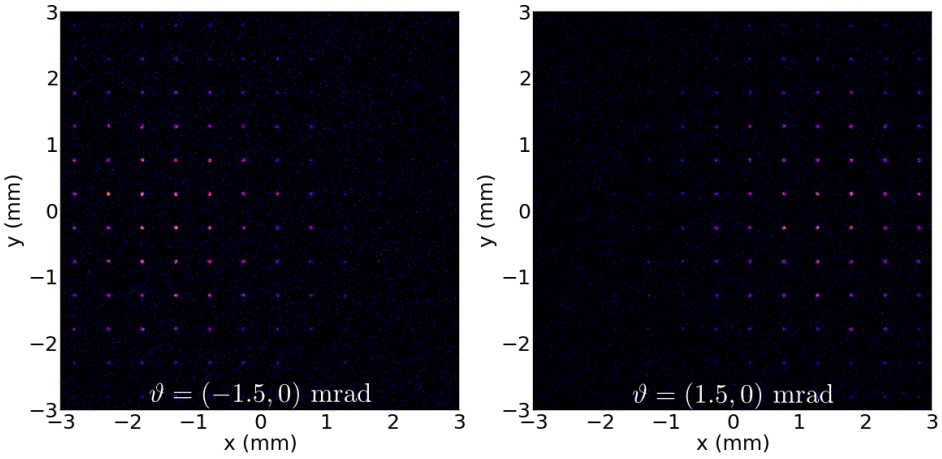

(a) Without PMQ

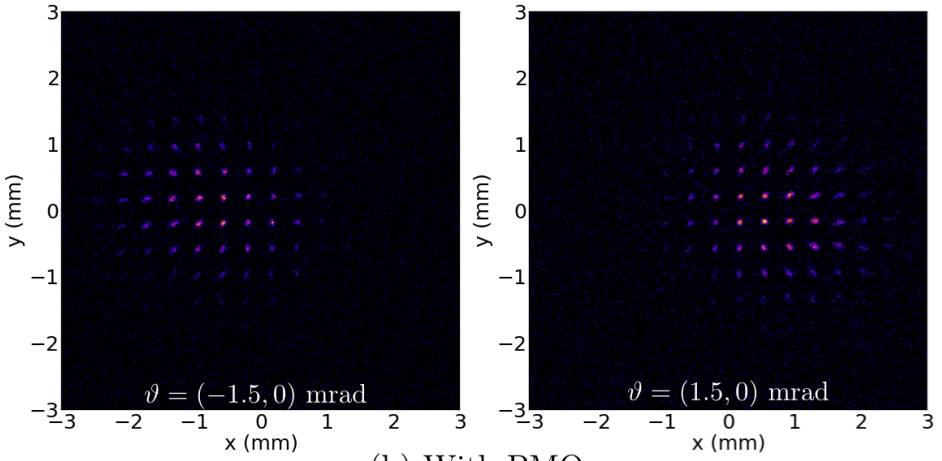

(b) With PMQ

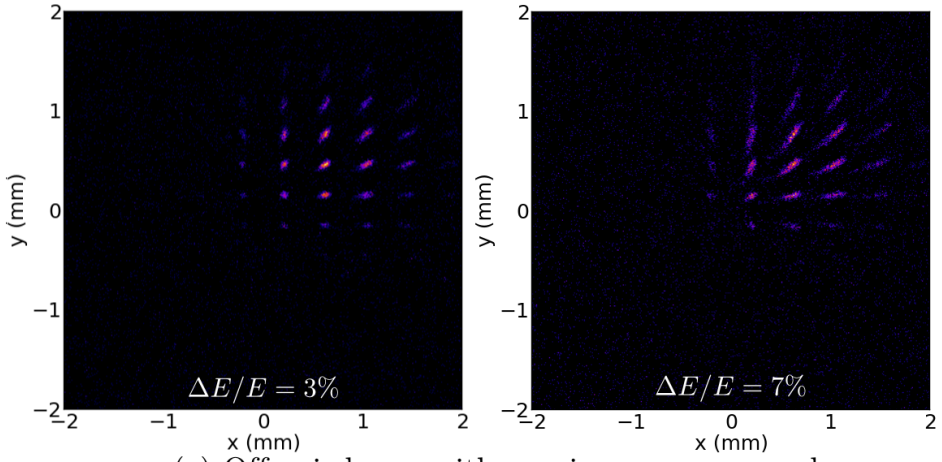

(c) Off-axis beam with varying energy spread

Figure 5.9: Simulated pepper-pot images for different beam pointing, (a) without and (b) with PMQs for 130 MeV ± 3 %. Figure (c) compares the effect of large $\Delta E/E$ for $\vartheta = (1.5, 1.5)$ mrad. (Source parameters: initial $\epsilon^n_{rms} = 1\,\pi$ mm mrad, $\sigma'_x = 1$ mrad)

increase both in width and height. For off-axis beams, the central beamlet size increases by only 5 – 10 % for energy spreads more than 6 %, as shown in Figure 5.10. On the other hand, the outer beamlet size grows by almost 20 – 25 % compared with the case of on-axis propagation. Moreover, the shape of the beamlets become elliptical and tilted in the direction given by ϑ. In fact, the beamlets are like lines as the energy spread is further increased, as shown in Figure 5.9c.

Indirect measurement of rms emittance

Although the magnification of the combined PMQ-pepper-pot system is energy dependent, the hole diameter correction term in Equation 4.2 can be estimated from the curve in Figure 5.11, showing that its effect on the emittance calculation is small. Therefore this diagnostic is capable to directly measure the beam emittance after propagation through the PMQs in a single shot.

However, as shown in Figures 5.9 & 5.12, large divergence, energy spread and pointing fluctuations strongly broaden and distort off-axis beamlets, making them too weak to be detected for the charge levels obtained in the experiments. This results in a large underestimation of the divergence and therefore of the measured emittance.

Nevertheless, it is still possible to indirectly estimate the beam emittance. The source size can be obtained by measuring the smallest beamlets, which are expected to be located close to the centre of the image and to have a size in the range of 20 – 40 µm for energy spreads less than 12 %. As shown in Figure 5.8, their size also depends on the energy spread, but the magnitude of this contribution can be estimated from the variation in beamlet size between different rows. Therefore, if the divergence is known from separate measurements, an estimate for the beam emittance can be obtained.

5.1.3 Effect of focusing system uncertainties on the beamlets properties

Figure 5.13 shows the triplet installed in the ALPHA-X beamline, with the three quadrupoles mounted together using a perspex holder. Fine alignments along horizontal and vertical axes are optimised using the (black) mount attached to the exit of the triplet. The PMQs alignment with respect to the laser axis is normally checked before the experiment using pinholes with diameter of 1 mm. Despite fine alignments, serious problems within the triplet configuration can still

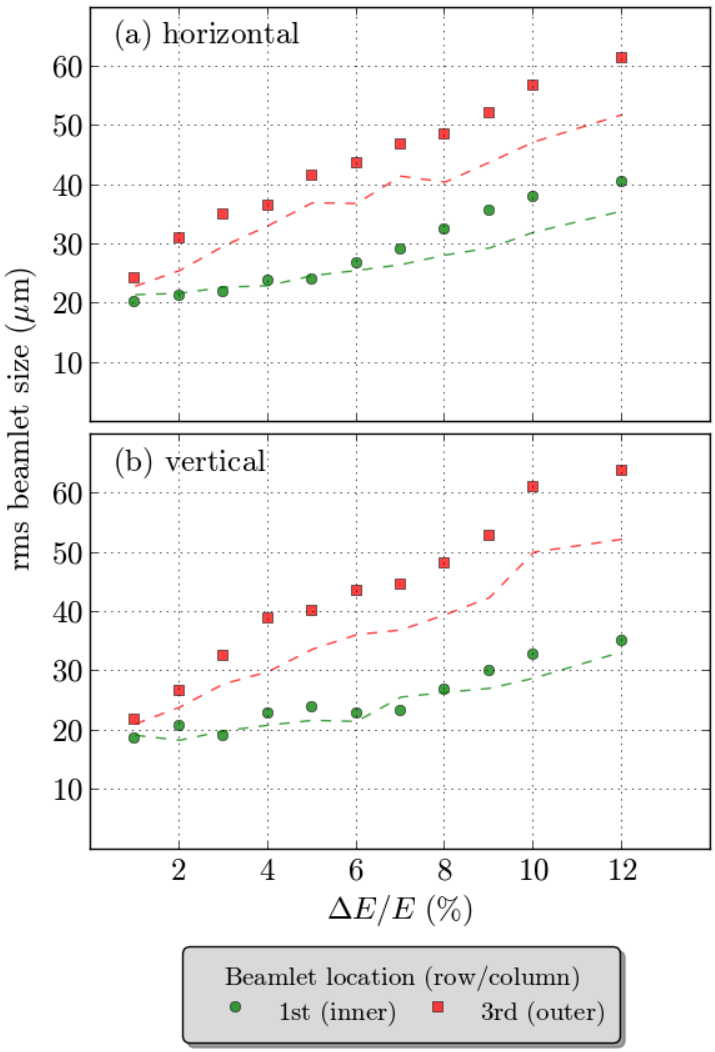

Figure 5.10: RMS beamlet size with varying $\Delta E/E$ for beams emitted $\vartheta = (+1.5, +1.5)$ mrad off-axis. The first and third rows/columns are at the same locations as in Figure 5.8. The dashed lines correspond to beams emitted on-axis. (Source parameters: 130 MeV, initial $\epsilon^n_{rms} = 1\,\pi$ mm mrad).

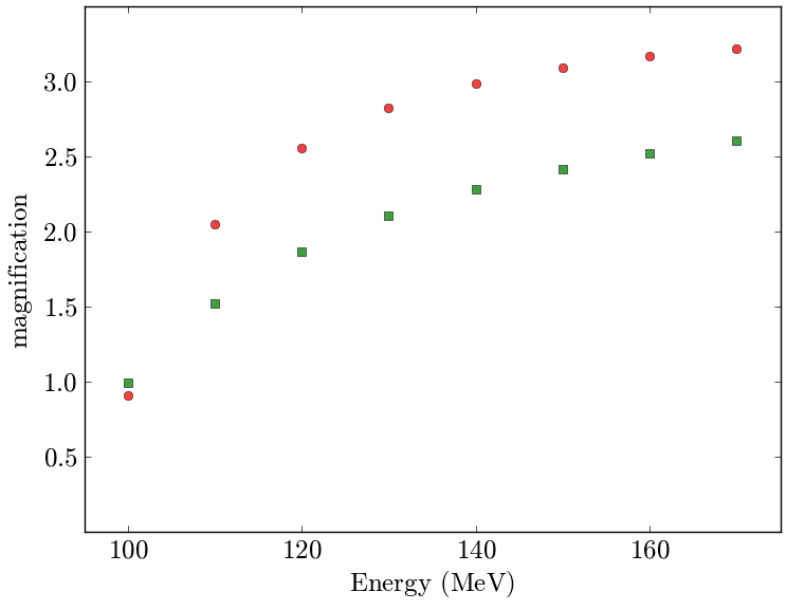

Figure 5.11: Setup magnification vs energy for electron beams with $\Delta E/E = 1\,\%$, $\sigma'_x = 1\,\text{mrad}$ and $\epsilon^n_{rms} = 1\,\pi$ mm mrad for horizontal (red) and vertical (green) directions.

arise and possibly affect the properties of the beamlets. The main problems that will be discussed here are the following: (1) uncertainties in the magnitude of the magnetic gradient, (2) uncertainties in the triplet configurations (i.e. drift separations, s_1 and s_2) and (3) rotational misalignment of the quadrupoles.

Triplet configuration uncertainties

As discussed in Section 5.1.1, the field gradients are obtained by matching a simulated field map to the results given by Equation 2.11, which can have small deviation from the actual field. Moreover, although the position of the triplet and the drift separation between PMQs are precisely measured, small deviation ($\pm$ 1 mm) can still occur. Due to the compact size of the triplet, these two small errors can alter the effective focal length of the triplet, resulting in a modified beam transport. As a consequence, the beamlet separations are particularly affected when these errors are included in the pepper-pot simulations. However, since the triplet is a linear focusing device, the x and y trajectories are uncoupled, making it easier to determine on which planes each triplet parameter has an influence.

Simulations show that the horizontal beam trajectory is significantly modified when small changes in s_1 and in PMQ-2 gradient are included; the vertical trajectory is strongly affected by s_2 and by the gradients of PMQ-1 and PMQ-3.

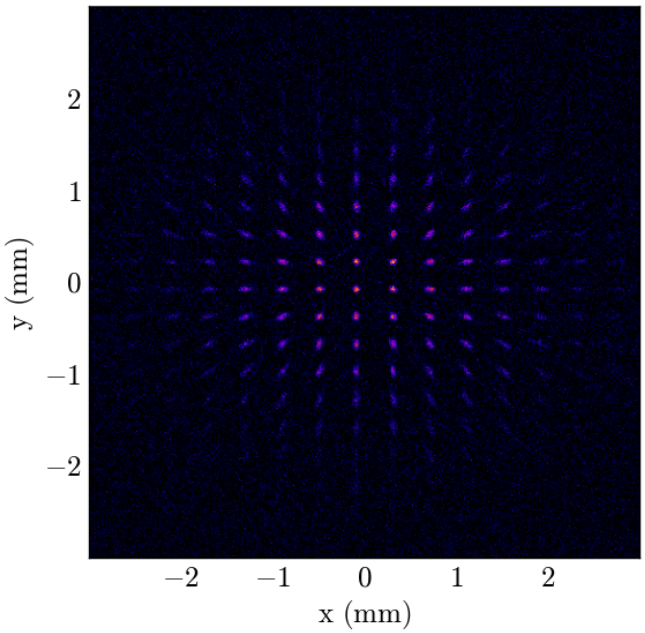

(a)

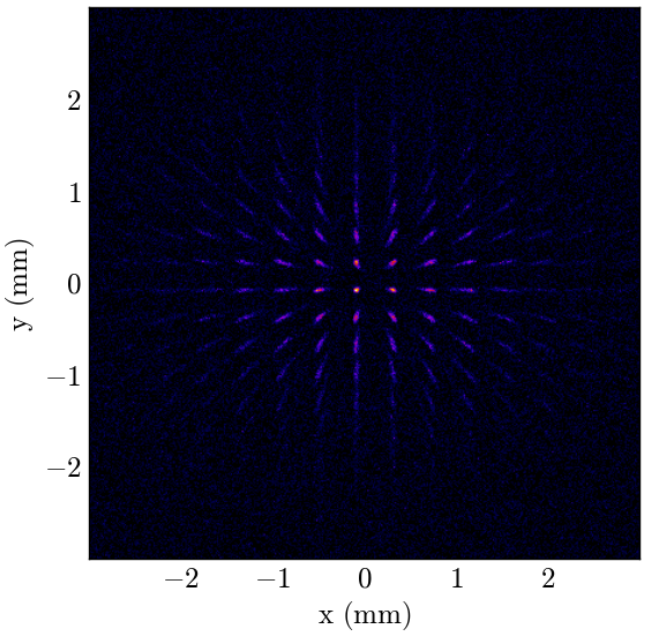

(b)

Figure 5.12: Simulated pepperpot images of electron beams with $\epsilon^n_{rms} = 2\,\pi$ mm mrad, $\sigma'_x = 2.5\,$mrad, $0.3\,$pC, energy of $130\,$MeV and energy spreads of (a) $3\,\%$ and (b) $7\,\%$.

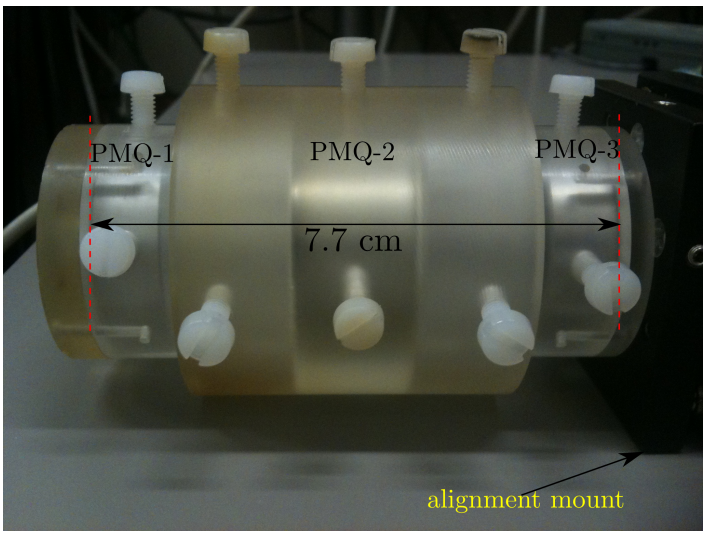

Figure 5.13: Actual image of the triplet (total length of 7.7 cm) used in the experiments here discussed. Also shown in the photo is the mount attached to the exit of the triplet used for fine alignment.

Here, energies between 100 and 150 MeV are considered. For 100 MeV, the beam evolution is highly sensitive to these deviations. As an example, a small error ($\delta s = \pm 3\,\% = \pm 1\,\text{mm}$) is added to the drift separations, s_1 and s_2. As shown in Figure 5.14a, the beam trajectories for 100 MeV drastically change from collimated to focusing or diverging, giving huge variations in the final x and y rms beam sizes. The rms size in x changes as much as 50 % of its expected size when an error of $\delta s = \pm 1\,\text{mm}$ is added to both s_1 and s_2. Similarly, modifying only the PMQ-2 gradient by $\delta G = \pm 2\,\% = \pm 10\,\text{T/m}$, can also induce pronounced changes in the horizontal trajectory, leading to more than 60 % rms beam size deviation. A positive δG_2 corresponds to a stronger horizontal focusing power, leading to beam compresssion in x.

On the other hand, the rms size along y can almost change by 20 % when only the error in s_2 is added. Simultaneous alteration in the PMQ-1 and PMQ-3 gradients gives a similar effect, leading to almost 40 % deviation in the vertical rms beam size. Similar to the PMQ-2 behaviour, a positive $\delta G_{1,3}$ corresponds to a stronger vertical focusing power, leading to higher beam compression in y while defocusing in x. If $\delta G_{1,2,3}$ is added to the gradients of the three PMQs simultaneously, the effect is just a combination of the two previous cases. Hence, a reduction in the PMQ gradient weakens its effective focusing power, resulting in an additional growth in both x and y beam sizes.

A similar pattern is observed when energies higher than 100 MeV are considered. However, since the theoretical triplet configuration only reduces the

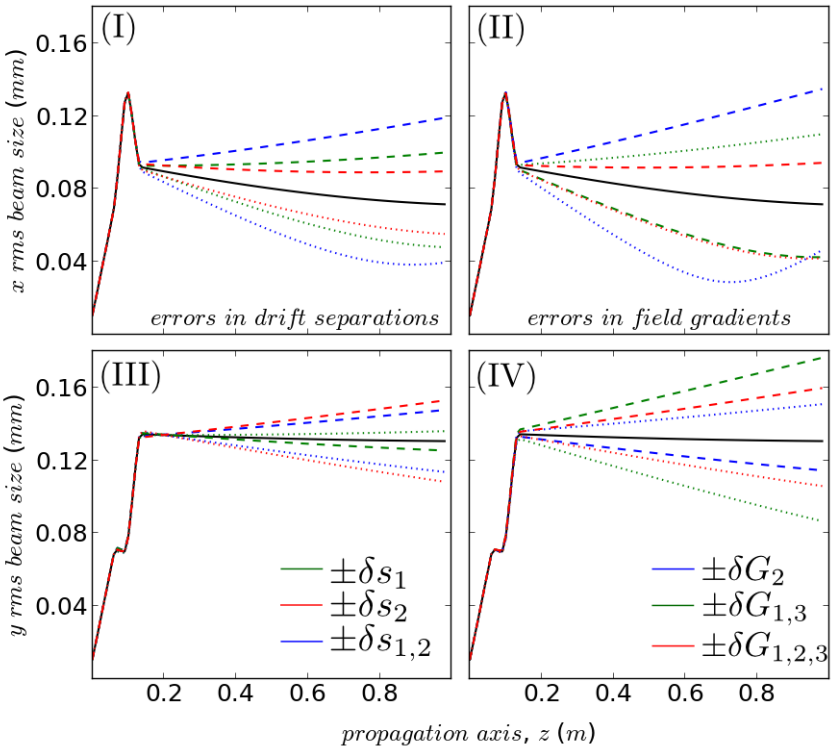

(a) 100 MeV ± 0.5 %

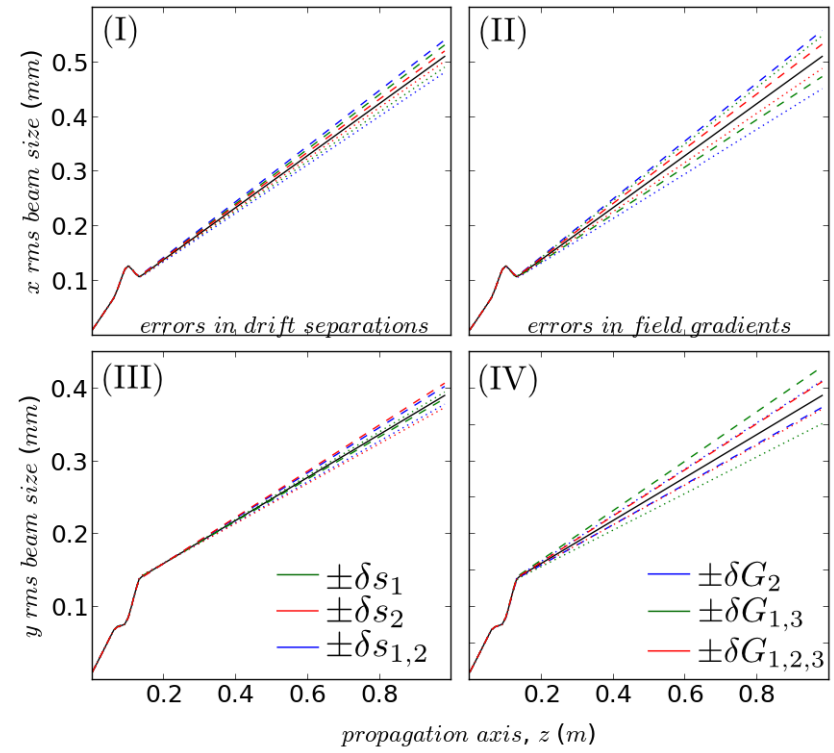

(b) 130 MeV ± 0.5 %

Figure 5.14: Beam trajectories for 100 and 130 MeV when errors in the drift separations ($\delta s_{1,2} = \pm 3\,\%$) and PMQs field gradients ($\delta G_{1,2,3} = \pm 2\,\%$) are added (dotted lines are for + and broken lines for −). The black lines represent trajectories when these errors are not included.

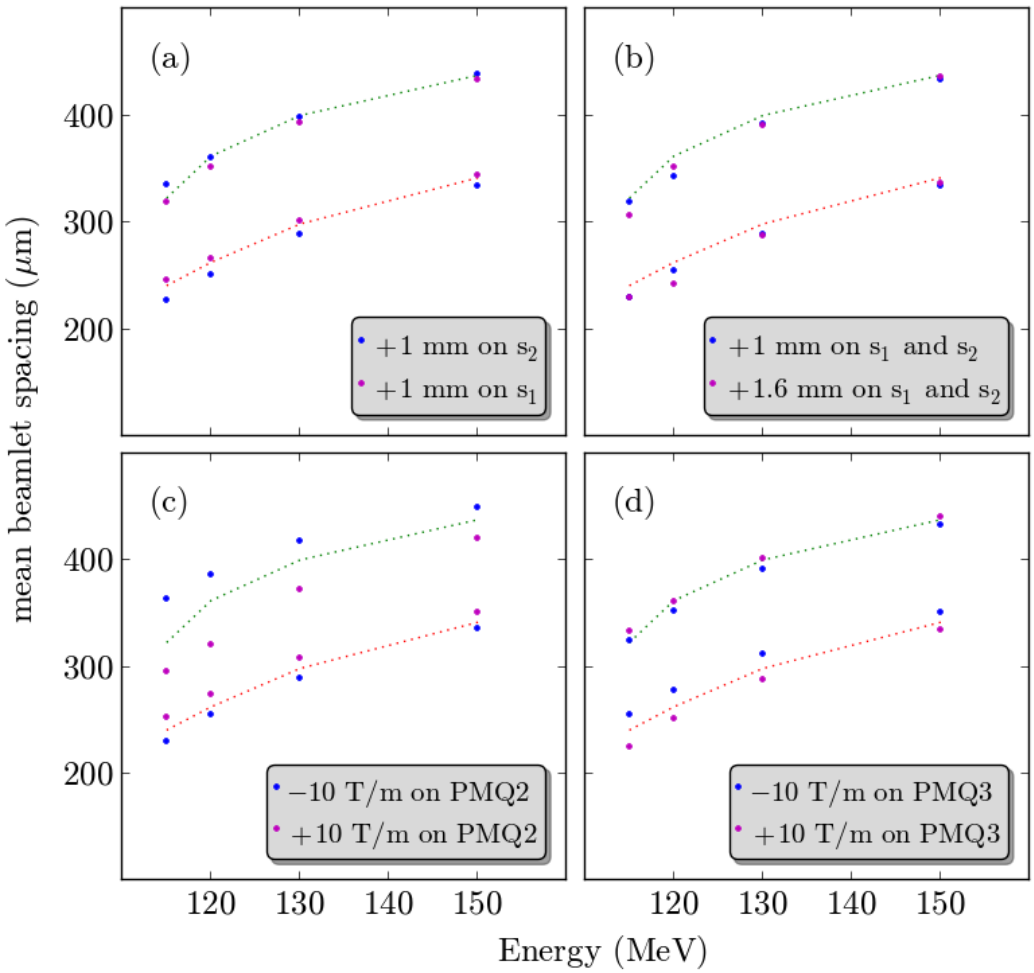

Figure 5.15: Effect of uncertainties in PMQs characteristics on the beamlet spacings. Figures (a) and (b) consider small variations in the distances separating the first and second PMQs (s_1) and the second and third PMQs (s_2), while variations in the field gradients are shown in (c) and (d). The green and red dashed lines are the beamlet spacings without off-set in x and y axes, respectively.

divergence for these energies, the trajectories do not drastically change, but a small variation in the beam size may occur, as shown in Figure 5.14b. In fact, a maximum change of only 10 % in beam size is obtained when one of the deviations is added to a 130 MeV beam. Simulations also show that energies higher than 150 MeV are less sensitive to small deviations on drift separations and field gradients. It is worth to note that the changes in the field gradients have higher impact on the beam trajectories than errors in the drift separation between the quadrupoles. Although the changes in d_x and d_y varies for different energies, a pattern can be extracted on how they behave for each deviation in the triplet parameters, listed in Table 5.1.

Triplet errors	Δd_x	Δd_y
$\pm\delta s_{1,2}$	$\mp$	$\mp$
$\pm\delta G_{1,2,3}$	$\mp$	$\mp$
$\pm\delta G_{1,3}$	$\pm$	$\mp$
$\pm\delta G_2$	$\mp$	$\pm$

Table 5.1: The corresponding behaviour of the beamlets separations, d_x and d_y for each triplet parameters deviations. A positive sign indicates growth while a negative sign is for reduction.

These deviations are then included in the pepper-pot simulations. As expected, only the beamlet separations are sensitive to these changes. As shown in Figure 5.15a, a + 1 mm off-set in s_2 induces a $\sim$ 13 µm difference from the expected d_y, while a similar off-set in s_1 does not have any significant effect in d_y. Changes in d_x occur if s_1 and s_2 are both misaligned by + 1 mm simultaneously, giving a $\sim$ 13 µm difference, as shown in Figure 5.15b. This implies that for a given range of energies, a huge variation in d_y indicates error in the s_2 parameter. On the other hand, small deviation of the PMQ-2 gradient alone changes d_x, where a $\pm$ 10 T/m error gives almost $\mp$ 40 µm change from the expected value, while only $\pm$ 12 µm in y, as shown in Figure 5.15c-d. Uncertainties in either the first or third PMQ gradient alter mostly d_y, giving a $\mp$ 16 µm uncertainty for a $\pm$ 10 T/m, while changes in d_x are beyond the resolution of the detection system. If both the first and third quadrupole gradients are off-set by the same amount, the change in d_y is almost 30 µm.

Rotational errors of PMQs

Rotational misalignments of PMQs should also be addressed since they can cause additional tranverse emittance growth, and possibly affect the beamlets properties. Rotation misalignment can be classified into three cases: (1) a rotational misalignment of the entire PMQ assembly relative to the beamline axis during triplet installation, (2) a rotational misalignment of each PMQ with respect to each other, or (3) both.

For the first case, the triplet assembly should be misaligned by more than 0.1 rad to induce an rms emittance growth of 4 % in x and y. However, the corresponding rms beam sizes have no significant increase. On the other hand, a small rotational misalignment between quadrupoles can already result in a significant rms emittance growth. In the simulations, each quadrupole is rotated clockwise, one at a time. The projected emittance grows by a factor of three

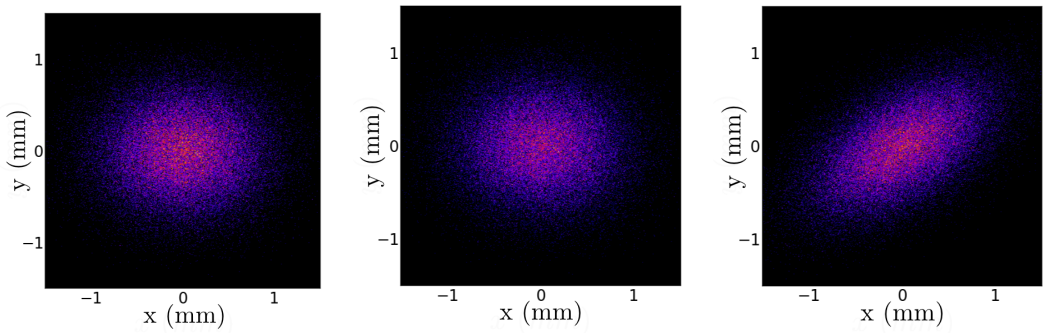

(a) No rotation on the triplet assembly

(b) Triplet assembly rotated 0.05 rad clockwise

(c) Only PMQ-2 rotated 0.03 rad clockwise

Figure 5.16: Spatial profiles of a 130 MeV ± 3 % electron beam after propagation with skewed PMQs.

after passing through a triplet with just a small rotation of 0.03 rad, as shown in Figure 5.17 for a 130 MeV ± 3 % electron beam. Although the rms divergence of the beam is maintained, there is a slight increased in the beam size, resulting in the small increase of emittance. Moreover, the spatial profile becomes highly elliptical, in particular when PMQ-2 is skewed, as shown in Figure 5.16.

Simulations indicate that a diagonal misalignment of the beamlets is a consequence of rotation error of the PMQs. When the first case is considered in the pepper-pot analysis, the triplet should be rotated by more than 0.12 rad to produce a noticeable effect on the pepper-pot images. Moreover, the angle of the beamlet does not vary much with the electron energy, producing images where the beamlets are always tilted by the same amount.

On the other hand, rotation errors in between the three PMQs result in a larger degree of skewness, as shown in right images of Figure 5.17. This effect has been investigated for a clockwise rotation by 0.03 rad of each PMQ one at a time with respect to the beamline axis. Table 5.2 shows the calculated rotation angle of the beamlets with respect to the vertical axis for three different electron energies. The slanting angle of the beamlet's axis decreases with higher energy, since high energy beams experience smaller deflections from the triplet. Among the three PMQs, the middle quadrupole produces the highest skew angle since its effective length is almost twice as long as the other two quadrupoles.

It is worth to note that although rotation errors in between the three PMQs increases the rms emittance by a few percent and give larger slanting angle to the beamlets, the beamlet size and separations have high degree of tolerance to these errors. For an electron beam with initial normalised $\epsilon^n_{rms} = 1\,\pi$ mm mrad and a triplet with rotation error of 0.03 rad in PMQ-2, $d_{x,y}$ is almost constant and the

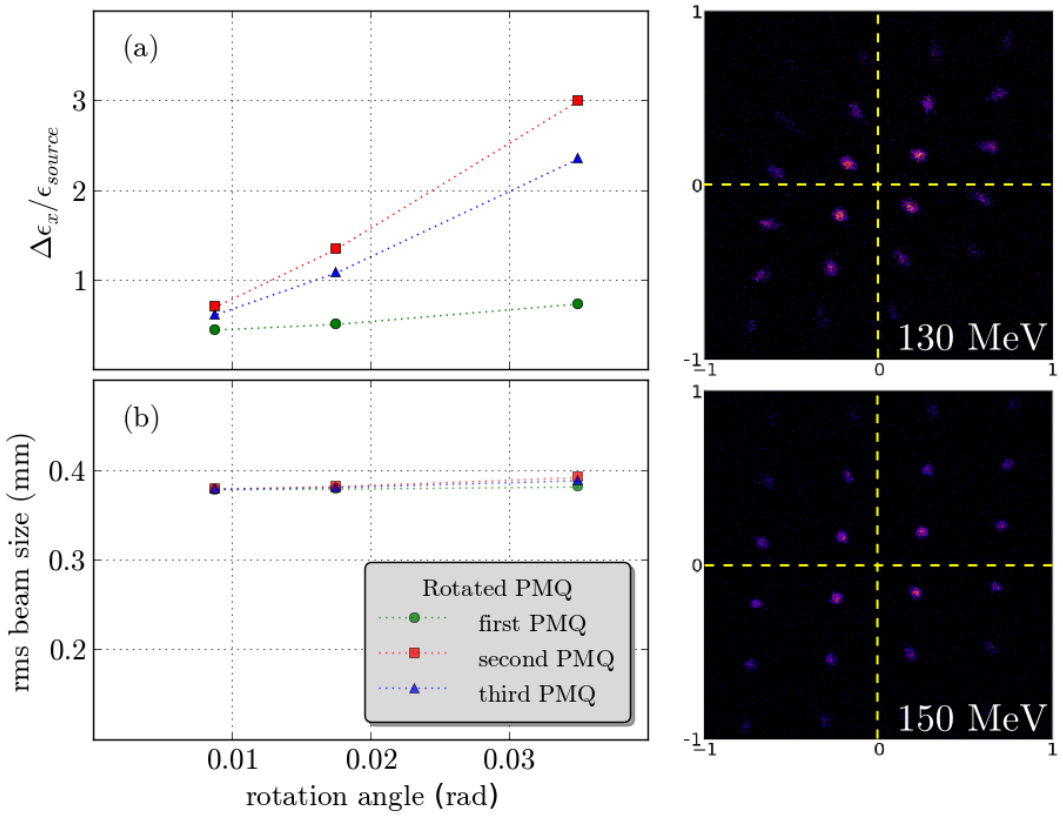

Figure 5.17: Calculated (a) emittance growth and (b) rms beam size of a 130 MeV ± 3 % after passing through a skewed PMQ (with initial normalised $\epsilon^n_{rms} = 1\,\pi$ mm mrad). The effect of a rotation error (0.03 rad) introduced in the second PMQ to the pepper-pot images is shown on the left figure for two different electron beam energies.

E (MeV)	**PMQ-1** (rad)	**PMQ-2** (rad)	**PMQ-3** (rad)
115	0.07	0.31	0.21
130	0.03	0.16	0.10
150	0.02	0.08	0.07

Table 5.2: Measured slanting angle (in rad) of the beamlets axis with respect to y plane for three electron energies. Each PMQ is given a clockwise rotation of 0.03 rad with respect to the beamline axis, one at a time.

beamlet size is maintained to 20-22 µm.

5.1.4 Summary of pepper-pot numerical analysis

The results of the numerical simulations on the pepper-pot technique combined with propagation through a PMQ triplet can be summarised as follows:

- The PMQ triplet couples the transverse and longitudinal characteristics of the electron beam. The size of the individual beamlets is not only a function of the source size, but also of the energy spread. Moreover, the shape of the beamlets can be distorted by pointing fluctuations of the electron beam. The difficulty of detecting broad beamlets with small charges implies that the pepper-pot method provides a direct measurement of the rms emittance only for on-axis beams with very small energy spread and divergence.

- For large energy spread and divergence, the projected emittance can be estimated by measuring the smallest beamlet size assuming that the divergence of the electron beam is known. However, uncertainties due to large energy spreads and pointing fluctuations must be accounted for.

- The pepper-pot technique with PMQs can visually show (through the images) the quality of the electron beam. A constant beamlet size for each row or column implies small energy spread, while ellipticity of the outer beamlets indicates fluctuations in beam pointing.

- While the electron beam properties highly affect the shape and orientation of the beamlets, uncertainties and rotation errors on the triplet assembly can change the beamlet separations and the overall structure of the beamlet alignment.

5.2 Experimental results

5.2.1 Electron beam properties

The emittance measurements have been performed at the ALPHA-X beamline described in Chapter 3. A CPA laser system with a central wavelength of 800 nm and pulse duration of 35 fs is focused down to a 40 µm diameter onto a 2 mm long He gas target ($n_e \simeq 10^{19}$ cm^{-3}) to produce mono-energetic electron beams, with mean energy of 126 MeV, energy jitter of 8.3 % and charge of $\sim$ 1 pC. The spatial profile of the electron beam is detected using a YAG:Ce screen located

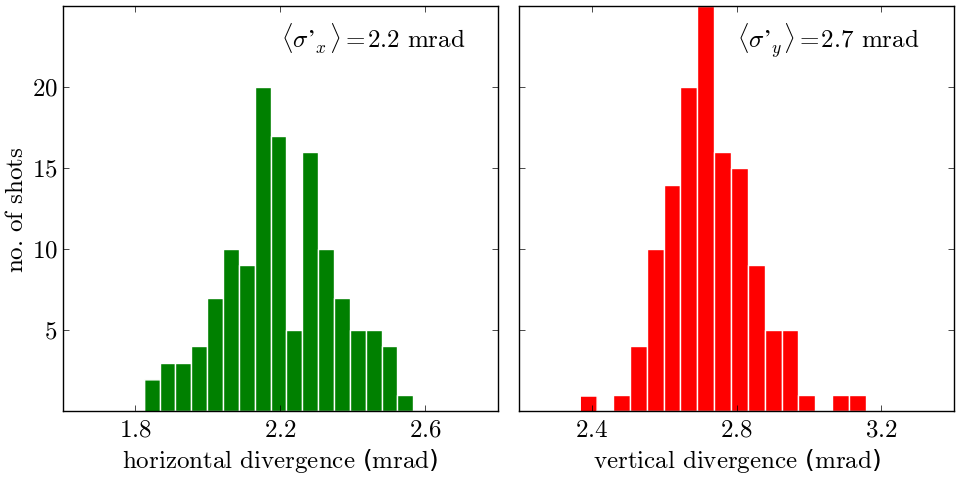

Figure 5.18: Distribution of rms divergence for 100 consecutive shots along the horizontal and vertical axes.

at 100 cm from the accelerator. (This is the same detector used for the emittance measurements of Chapter 4). The distribution of the electron beam rms divergence for 100 consecutive shots is shown in Figure 5.18, with mean value of $\sigma'_{x,y} = (2.2, 2.7)$ mrad. The divergence measured here is lower than the results of Chapter 3, which were obtained on the first Lanex screen, L1. As discussed in Section 3.3, transverse profiles measured on L1 may include a low energy halo that leads to an overestimation of the divergence. On the other hand, these measurements obtained on a smaller screen farther away from the accelerator may effectively select only the best shots and underestimate the divergence. The smallest divergence measured is $\sigma'_{x,y} = (1.8, 2.4)$ mrad. Most of the beams are elliptical with larger size along the vertical axis. As shown in Section 5.1.2, an elliptical beam distribution results in beamlets with different size along x and y.

The pointing stability of the beam is obtained by measuring the position of the electron beam centroid (in x and y) with respect to the centre of the screen. As seen in Figure 5.19a, the electron beam is emitted at a mean angle $\langle x \rangle = 1 \pm 0.6$ mrad and $\langle y \rangle = 0.7 \pm 0.5$ mrad. Since the laser beam is horizontally polarised, the electron beam fluctuations are larger along the horizontal plane. Moreover, the position of the electron beam is independent of its charge. The variation of the electron beam pointing is reduced when the PMQ triplet is used, as shown in Figure 5.19b. However, since most of the electron beams are off-axis, the beam trajectories are further deflected away from the centre, a behaviour observed also in GEANT4 and GPT simulations. The spatial profile of the beam is asymmetric with some beams having long tails along one axis. The asymmetry might be due

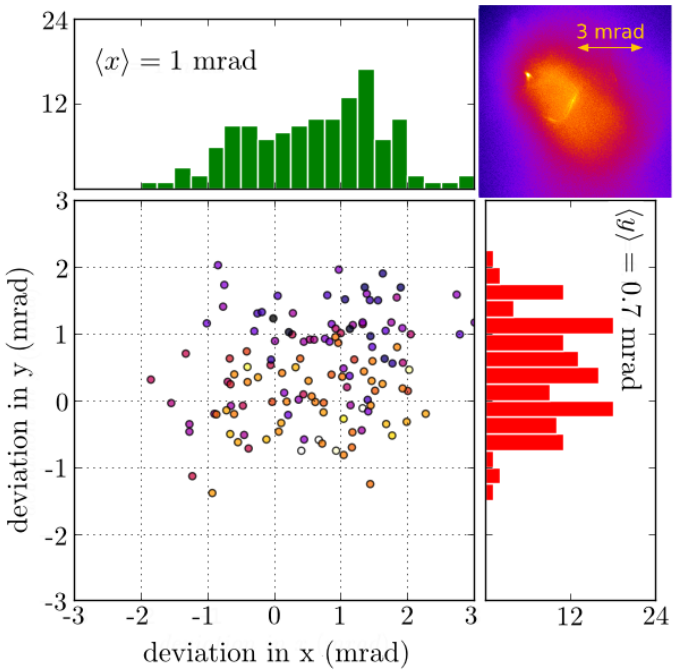

(a) Pointing stability without the PMQs triplet.

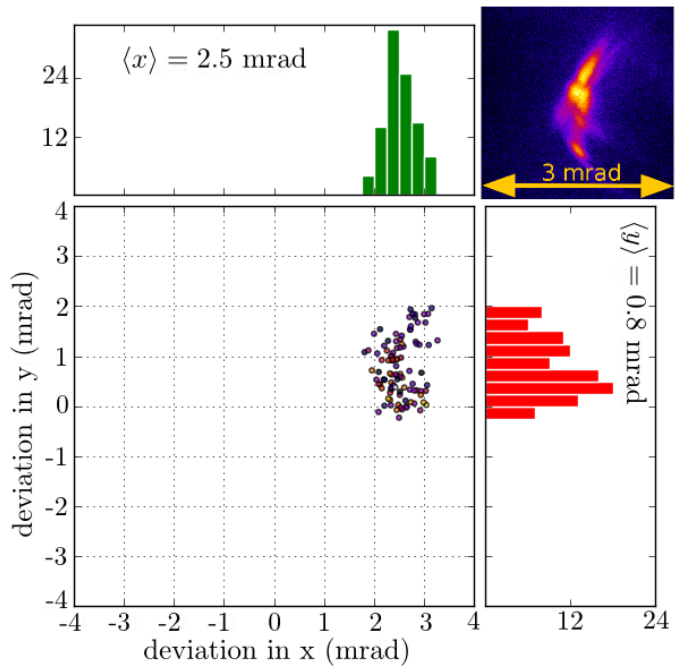

(b) Pointing stability with the PMQ triplet in place.

Figure 5.19: Comparison of electron beam pointing with and without the PMQs. The colors of each point represent the relative charge (red-highest, blue-lowest) of each electron beam shot. The histograms represent the electron beam centroid distribution along the x (top) and y (right) axes. Shown on the top right is a false-colour image of the electron beam as seen from the YAG:Ce screen.

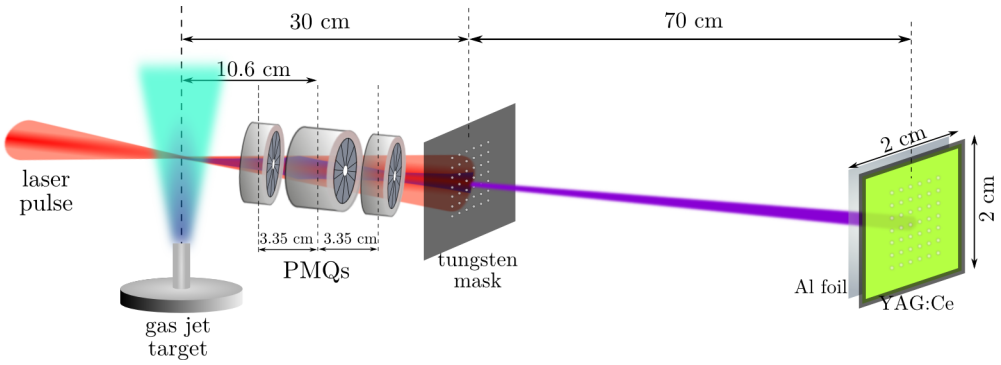

Figure 5.20: Experimental setup for electron beam characterisation by combining the pepper-pot technique and PMQs triplet.

to defocused low energy components of the electron beam or misalignment of the PMQs.

5.2.2 Pepper-pot measurements with PMQ triplet

Figure 5.20 shows the experimental setup. The tungsten mask has 54 x 54 holes (16 ± 2 µm diameter) separated by 142 ± 2 µm. The mask thickness is 125 µm, the same as the one used for the emittance measurements of Chapter 4. The beamlets are detected using the same YAG:Ce crystal, which is now at 70 cm from the mask. A new housing for the detector is installed allowing the Al foil to be placed at only a few mm from the crystal. A 2448 x 2048 pixels CCD camera is also installed with an overall resolution of 10 µm.

The transverse emittance of the electron beam is measured without the triplet for reference. An example of the pepper-pot images as seen on the YAG:Ce screen is shown in Figure 5.21. The rms emittance of 20 out of 200 laser shots, normalised to 126 MeV energy, is ϵ^n_{rms} =1.6 ± 0.5 π mm mrad for both the horizontal and vertical directions (as presented in the second batch of measurements in Chapter 4). Since the electron beams fluctuate by 1.5 mrad, only 7 % of the shots reached the detection system. Moreover, beams with rms divergence greater than 2 mrad suffer from low signal to noise ratio.

With a measured rms divergence of 2 - 3 mrad, the source size of the electron beam was estimated to be 4 - 5 µm. The measured beamlet size for this set of data ranges from 25 µm to 40 µm, as shown in Figure 5.21. The smallest rms emittance measured is $\epsilon^n_{rms} = 1$ π mm mrad, with corresponding measured beamlet size of 25 µm, consistent with the predicted values in Figure 5.6 (when $\sigma'_x = 2$ mrad). The average beamlet separation without the triplet in both x and y directions is $\langle d_{x,y} \rangle = 470$ µm, as expected from simulations.

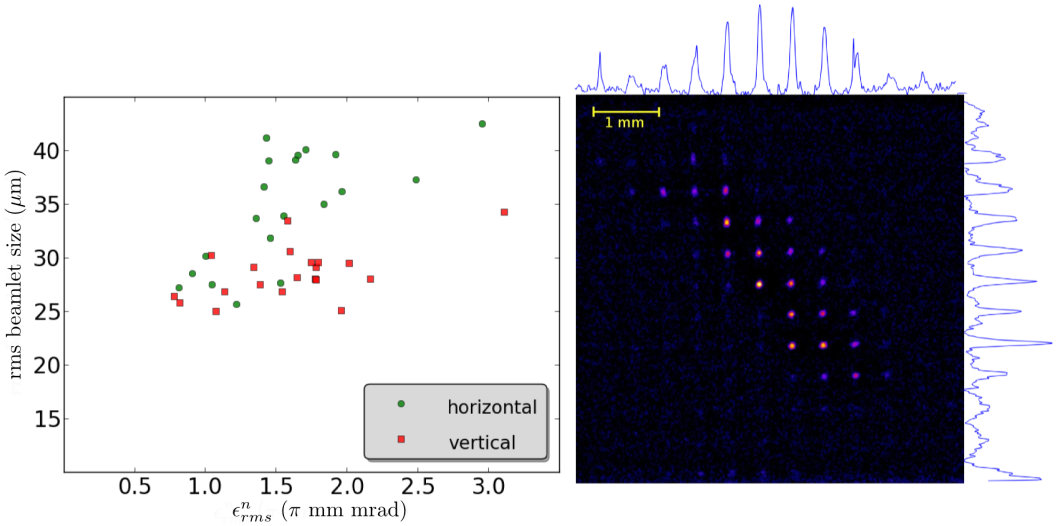

Figure 5.21: RMS beamlet size with the corresponding normalised rms emittance in the horizontal and vertical axes without the PMQs. An example of false-colour and background subtracted pepper-pot image is also shown.

Pepper-pot images with PMQs triplet in line are recorded. Out of 400 laser shots, 28 pepper-pot images are analysed by measuring the corresponding beamlet size and spacing. Images with (nearly) overlapping and/or highly distorted beamlets are not included for the calculation of beamlet sizes and separations. A separate discussion on these images is provided in Section 5.2.4.

In general, the experimental images behave as predicted by the numerical analysis presented in the previous section. As expected, the smallest beamlets are mostly located close to the centre of the image, with the smallest beamlet along the horizontal not always corresponding to the smallest beamlet in the vertical direction. The distribution of the smallest beamlet sizes in every image is shown in Figure 5.22a, with an average $\langle w_{x,y} \rangle = 30 \pm 4\,\mu\text{m}$ in x and y. As discussed in Section 5.1, the source size and therefore the emittance can be estimated from the beamlet size after identifying the growth due to energy spread, divergence and pointing fluctuations.

The electron beams obtained in this experiment are emitted at a mean angle of $\sim 1\,\text{mrad}$ off-axis and have energy spreads $\geq 7\,\%$. Therefore, based from Figure 5.10, the corresponding contribution to the beamlet size is $\sim 3 - 4\,\mu\text{m}$. The measured divergence of $\sim 2.5\,\text{mrad}$ induces a $\sim 3\,\mu\text{m}$ growth for $\Delta E/E = 1-12\,\%$ (as mentioned in Section 5.1.2). Taking into account these contributions, the mean beamlet size is $\simeq 24\,\mu\text{m}$, indicating a source size between 2 and $4\,\mu\text{m}$, which corresponds to an estimated transverse emittance at the source between 1 and $4\,\pi$ mm mrad, comparable to the measurements without the PMQs.

Moreover, it has been observed that in all recorded images, the alignment of the beamlets along the rows (horizontal axis) and columns (vertical axis) are skewed. The skewness is mostly in the clockwise direction, but the angle varies hugely from image to image. The images have to be rotated between 0.03 and 0.1 rad counterclockwise to make each column perfectly aligned along the vertical axis. On the other hand, to align the horizontal axis, the images should be rotated between 0.03 and 0.2 rad. Since the degree of skewness among the recorded pepper-pot images has a huge variation, it is evident that a rotation error in between the three PMQs has occured. Based on Table 5.2 (assuming that the mean energy is around 130 MeV), one of the PMQs is probably misaligned by $0.03\,\text{rad} \simeq 2°$, leading to an emittance growth of less than 3 % (based on Figure 5.17). However, this growth is small relative to uncertainties introduced by energy spread and pointing fluctuations, and as shown in Section 5.1.3, the beamlet size is not significantly affected.

The corresponding beamlet separations in x have a mean of $\langle d_x \rangle = 460 \pm 13\,\mu\text{m}$. As shown in Figure 5.22b, d_x is always similar to the spacing without PMQs in place and varies less between the images. On the other hand, there are significant fluctuations in d_y, with an average $\langle d_y \rangle = 390 \pm 25\,\mu\text{m}$. Compared to the expected beamlet separations from the numerical analysis, the difference between d_x and d_y is $70 \pm 30\,\mu\text{m}$ (cf. Figure 5.5a).

Separation between beamlets depends weakly on the position of the mask or the scintillating screen, which should be misaligned by more than 3 cm to produce an additional 5 µm on both d_x and d_y. On the other hand, as shown in Section 5.1.3, errors on the PMQ gradients highly affect the beam transport, resulting in changes in the expected $d_{x,y}$. Since the experimental $d_{x,y}$ are both higher than the expected values, it can be inferred that the triplet magnetic field gradients are lower than the theoretical values as given in Table 2.1. Moreover, big variations in d_y imply that $s_1 > s_2$. When a deviation of $\delta G_{1,2,3} = -12\,\%$ is added to the theoretical gradients and s_1 is set to be 2 mm greater than s_2, the numerical beamlets separations are now comparable with the experiment, as shown by the shaded region in Figure 5.22b. In this proposed triplet configuration, the beamlet separations are calculated for energies range between 130 and 165 MeV, consistent with the energy measurements performed.

The proposed triplet configuration changes the overall beam transport, allowing energies as low as 100 MeV to produce useful pepper-pot images, but the corresponding $d_{x,y}$ is much smaller compared to what have been measured. As shown in Figure 5.23, the transverse emittance grows by an order of magnitude

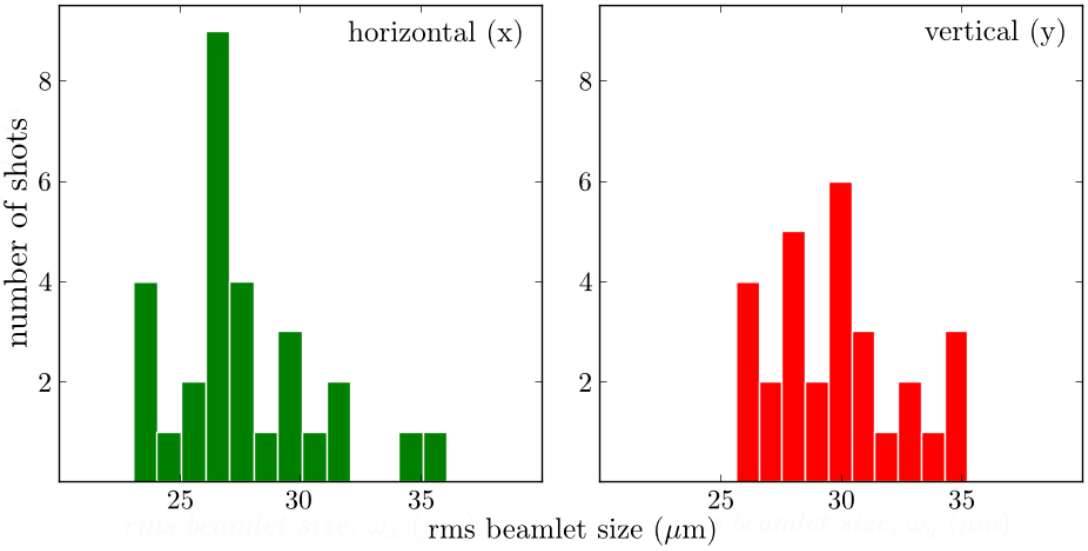

(a) Distribution of the measured smallest beamlet size, $\omega_{x,y}$.

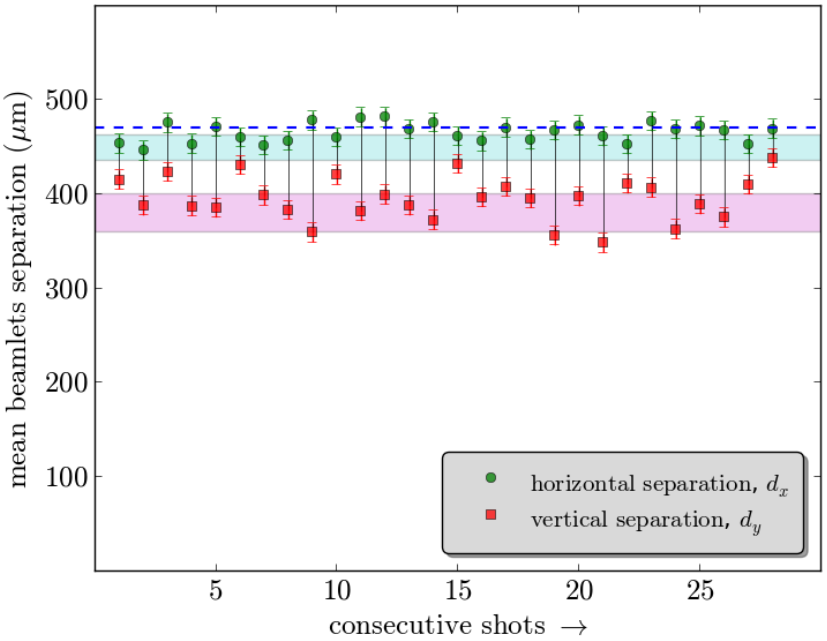

(b) Experimental $\langle d_x \rangle$ and $\langle d_y \rangle$ for each pepper-pot image considered. The blue dashed line is the measured spacing without the PMQs, while the red and green shaded regions are the numerical d_x and d_y for the proposed triplet configurations for energies between 130 and 165 MeV.

Figure 5.22: Measured smallest beamlet size and separation between beamlets in x and y axes for 28 consecutive shots with propagation through PMQs.

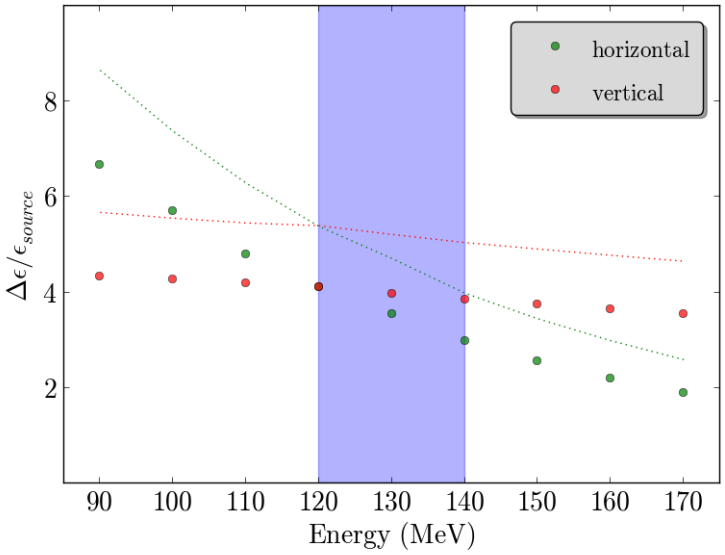

Figure 5.23: Simulated emittance growth of electron beams with $\Delta E/E = 7\,\%$ and 2 mrad divergence after propagation through PMQs using the proposed configuration. The symbols correspond to electron beams emitted on-axis and the dotted curves to the electrons beams emitted off-axis ($\vartheta = (1.5, 1.5)$ mrad). The shaded area indicates the range of energy in these measurements.

for electron beams with $\Delta E/E = 7\,\%$ and 2 mrad divergence (matching the experimental parameters). Hence, the estimated transverse emittance after the PMQs is between 5 and $20\,\pi$ mm mrad for on-axis propagation and between 6 and $24\,\pi$ mm mrad for off-axis propagation (based from Figure 5.23).

5.2.3 Analysis of individual pepper-pot images

Among the shots that show resolvable beamlets, only 25 % are hitting the centre of the detector and almost 50 % are hitting the upper right corner, consistently with the observed average pointing offset of the electron beam presented in Section 5.2.1.

Images produced by beams propagating approximately on-axis ($\vartheta = 0$) are shown in Figure 5.24. The measured smallest beamlet sizes, $\omega_{x,y}$, for the two images are similar (a: (25, 30) µm and b: (27, 30) µm), implying that the corresponding transverse emittances are also similar. With measured divergence of ∼2.5 mrad, these measured beamlet sizes correspond to source sizes of 3 – 4 µm, and a normalised emittance of $\sim 2\,\pi$ mm mrad. However, Figure 5.24a shows more uniform beamlets. The beamlet size ranges from 26 to 38 µm, going from the first column until the fifth column. From this range, an energy spread of less than 6 % is inferred (referring to Figure 5.8). On the other hand, Figure

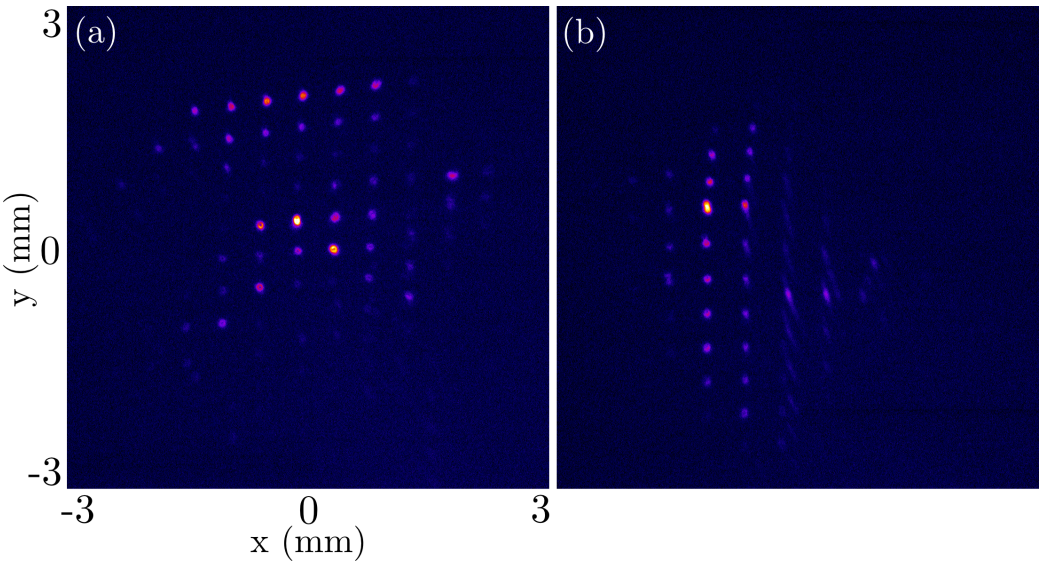

Figure 5.24: False-colour pepper-pot images as detected by the YAG:Ce crystal. The corresponding smallest beamlet size measured in these images are: (a): 25 µm and (b): 27 µm.

5.24b shows a big increase in beamlet size from the first column to the third. The range of beamlet sizes in this case is 25 to 57 µm. The non-uniformity of these beamlets indicates that the electron beam in this image has a large energy spread. It can be estimated that $\Delta E/E$ is greater than 8 %.

Pepper-pot images with beams propagating off-axis are shown in Figure 5.25. Both images have fewer beamlets compared to other pepper-pot images, implying that the electron beams have low divergence ($\sim$ 1 to 2 mrad). The minimum beamlet sizes for Figures 5.25a-b are (29, 28) µm and (27, 27) µm, respectively. In Figure 5.25a, the ratio of ω_x and ω_y is mostly $\sim$ 1, going from the inner row/column to the outer row/column. The maximum beamlet size measured from this image is 33 µm, which is just a few µm larger than the minimum beamlet. An energy spread between 4 – 8% can be deduced. However, the beamlets start to tilt more as their location moves farther away from the screen's centre. It is also worth noting that the direction of the tilt indicates the pointing direction of the electron beam.

Figure 5.25b displays a completely different behaviour. The tilt direction of the beamlets is quite random on different rows and columns. Moreover, the maximum beamlet size is measured to be 43 µm, which is more than 15 µm larger than the smallest beamlet. This shows that the electron beam has a large energy spread. The combined effect of a large energy spread and off-axis electron beam propagation is shown in Figure 5.26.

The electron beam energy spread can be estimated by the beamlets variations

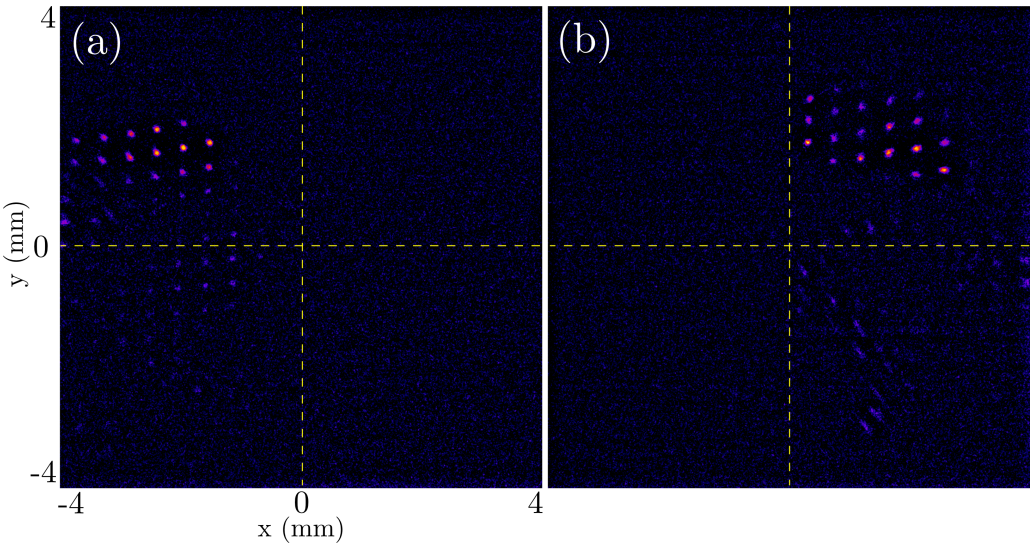

Figure 5.25: False-colour pepper-pot images as detected on the YAG:Ce crystal for electron beams propagating off-axis.

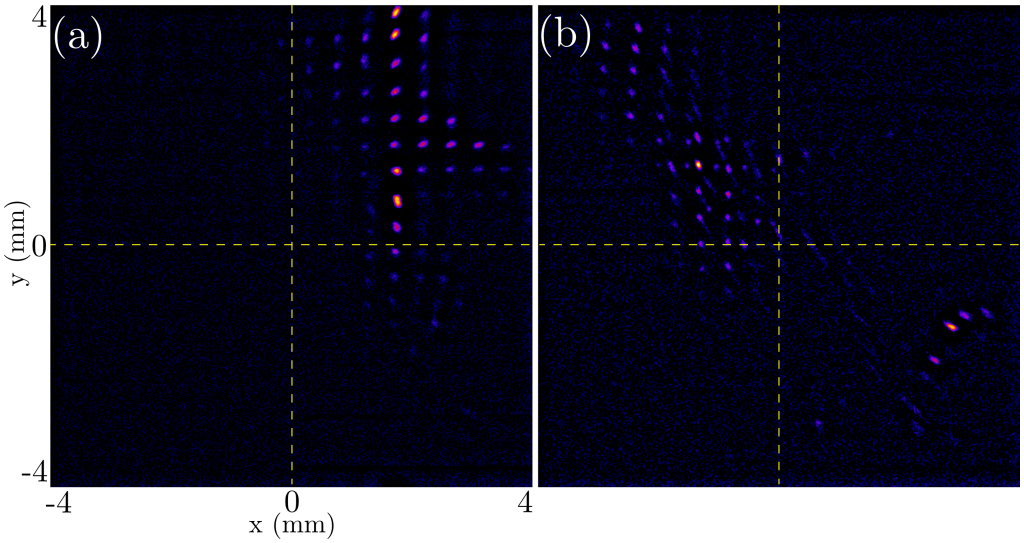

Figure 5.26: False-colour pepper-pot images as detected on the YAG:Ce crystal for electron beams having large energy spread and propagating off-axis.

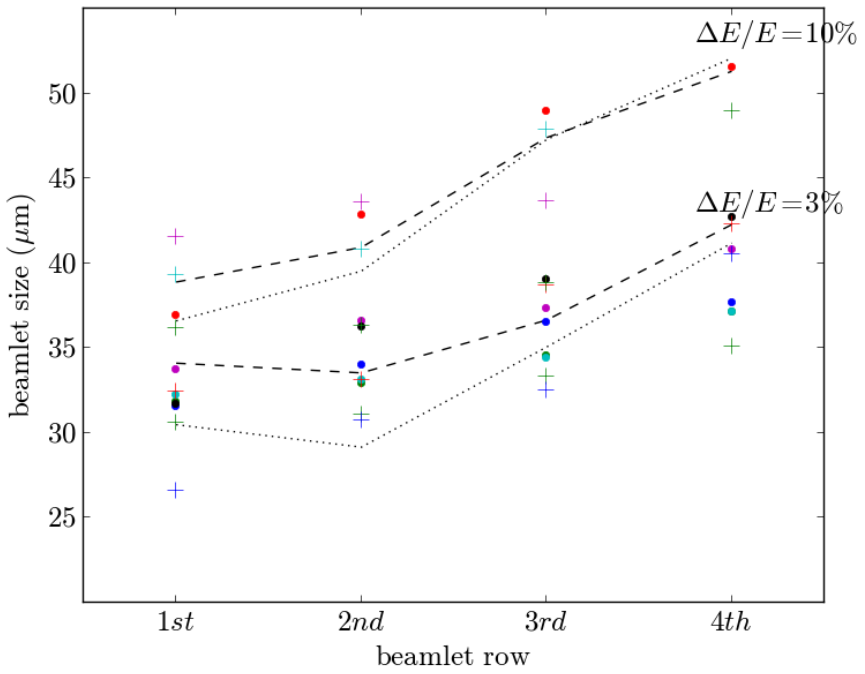

Figure 5.27: Measured beamlets for different rows using 11 pepper-pot images, same color represents single image. Simulated beamlet sizes are also indicated by dashed lines ($\sigma_x = 6\,\mu m$) and dotted lines ($\sigma_x = 4\,\mu m$) for electron beams with $\sigma'_x = 2\,mrad$.

along the rows or columns. As shown in Figure 5.27, four consecutive beamlets in a row are considered, starting from the smallest beamlet size. For the estimated source size of 4 –6 µm, the variations of the beamlet sizes fall between 3 and 10 % energy spread. It is also worth noting that the predicted parameters from the simulations agree well on the experiments.

5.2.4 Observation of multiple peak electron beam

Among the recorded pepper-pot images, almost 10 % are characterised by unique beamlets structures, where beamlets are nearly overlapping, as shown in Figure 5.26b. When the triplet is not used, the positions of the beamlets are solely dependent on the geometrical configuration of the pepper-pot setup, i.e. on the position of the mask and the detection system. Thus, the position of the beamlets on the scintillating screen is independent of the divergence or pointing fluctuations of the electron beam, provided that the geometrical properties of the pepper-pot setup are maintained. The addition of the triplet in the pepper-pot setup effectively varies the position of the "source" beam with energy, leading to an energy dependence of the detection system magnification. Hence, an electron

beam with multiple energy peaks will show two different magnifications of the beamlets. Examples of recorded pepper-pot images with these unique beamlets structures are shown in Figure 5.28. The images also indicate that the two energy peaks have different divergence as the double beamlets are only seen on a small portion of the whole image. As seen in Figure 5.28a, the shape and orientation of the beamlets are also different implying that these two energy peaks have different energy spread.

Simulations are performed to analyse the possible cases for these beamlet structures with the proposed triplet configuration used in Figure 5.22b. Moreover, a slight rotation error (0.02 rad) in between the PMQs is included to match the experimental results. If the two energy peaks are emitted at the same angle, multiple beamlets structures are obtained when the energy difference between two peaks is $\delta E_o \geq 30$ MeV, independent of energy, as shown in Figure 5.29b. Electron beams with two peaks separated by less than 30 MeV will produce beamlets similar to a single peak with large energy spread. Beamlets having different energy peaks are further apart when they are emitted at a different angle from the accelerator, as shown in Figure 5.29a. These results show that the accelerator has produced electron beams with more than one bunch and these bunches have different spatial properties. Evidence of multiple electron bunches has also been observed by R. Shanks in measuring the electron bunch length using transition radiation spectrum [94]. This can be an important result as it implies that the pepper-pot and PMQs combined can be used as an alternative diagnostics in characterising the properties of electron beam in terms of having double peaks and how they are ejected from the accelerator.

5.3 Summary

A method for the characterisation of electron beams focused by a PMQ triplet has been presented. In this chapter, the pepper-pot technique and PMQs are combined to simultaneously determine the projected emittance of the electron beam after passing through the PMQs and quantify the effectiveness of the focusing system. Although the PMQs triplet increases the signal to noise ratio and improves the resolution of the pepper-pot method, it also couples the transverse and longitudinal characteristics of the electron beam, making the beamlets dependent on other electron beam parameters in addition to the source size and divergence. In this case, the rms transverse emittance is estimated from the measurement of the minimum beamlet size, provided that the divergence is known.

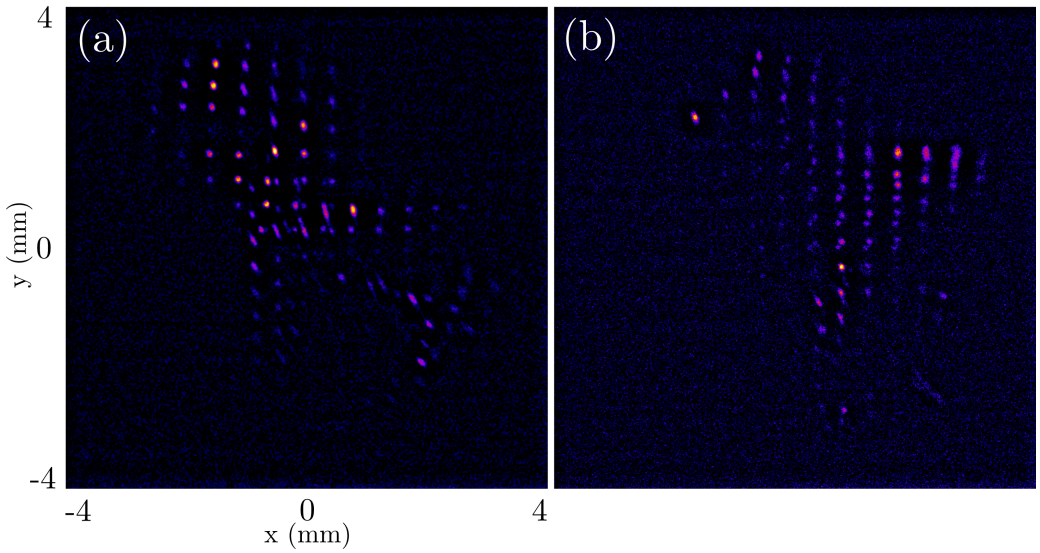

Figure 5.28: Recorded pepper-pot images after propagation through the triplet with multiple beamlets structures.

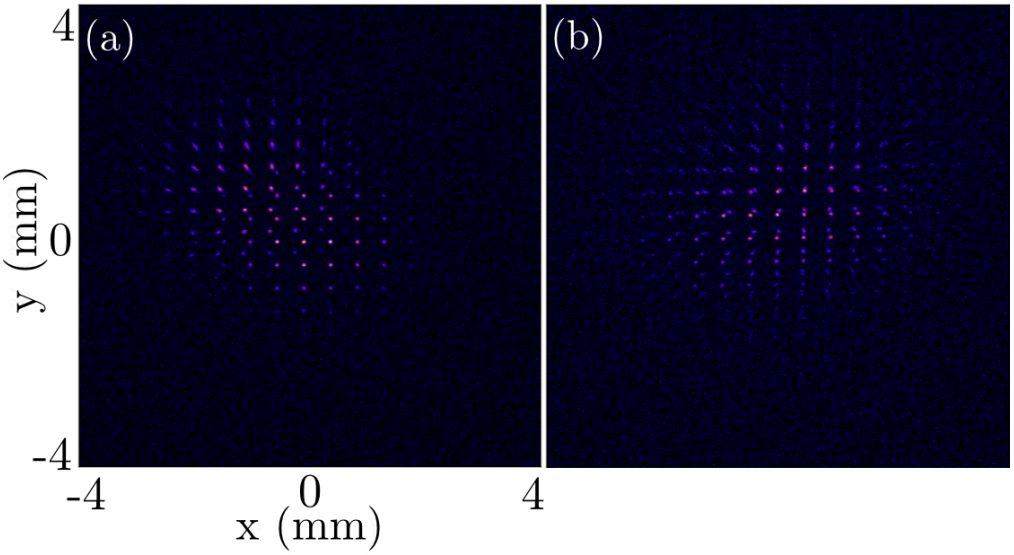

Figure 5.29: Simulated pepper-pot images after propagation through the triplet having double peak energies. Figure (a) is for $\delta E_o = 25\,\mathrm{MeV}$,where the lower energy peak is emitted at an angle, while the higher energy is emitted on-axis. Figure (b) is for $\delta E_o = 35\,\mathrm{MeV}$, with two peaks both emitted at the same angle. In both figures, the lower energy peak have energy spread of 6 %, while the higher energy peaks have 3 %.

The minimum beamlet sizes for 28 shots have an average of $w_{x,y} = 30 \pm 4\,\mu m$ which correspond to an estimated emittance of $1 - 4\,\pi$ mm mrad at the source after subtracting the contribution of large energy spreads and beam pointing. After the quadrupoles, the transverse emittance of a beam with rms energy spread 7 % of is estimated to increase reaching values between 5 and $20\,\pi$ mm mrad when beam pointing is not included and between 6 and $24\,\pi$ mm mrad for beams propagating 1.5 mrad off-axis (i. e. pointing fluctuation is included). The pepper-pot images are also used to simultaneously characterise the electron beam in terms of pointing stability and energy spread.

Double beamlet structures in some recorded pepper-pot images indicate that electron beams with double peak energies are generated. Simulations shows that these structures are visible for central energies separated by more than 30 MeV. The characteristics of each energy peak are inferred from the shapes and orientation of the beamlets. This important result shows that if the PMQs are properly characterised and installed (i.e. if the gradients of the quadrupoles are known and if individual quadrupoles are aligned with high precision), the combination of pepper-pot mask and PMQs can be an alternative diagnostic tool for simultaneous measurement of spatial properties and energy of the electron beam.

In addition, the alignment of the focusing system is analysed using the pepper-pot images. A small change in magnetic field gradients ($\pm$ 10 T/m) and separation distances ($\pm$ 1 mm) between PMQs can already alter the transport of the electron beams as indicated by the variation in the separations between beamlets. It was also shown that the tilting of the beamlet axis is a consequence of the rotation error in between the quadrupoles and rotation misalignment of the triplet with respect to the beamline axis. Based from the pepper-pot images, it is more likely that the there is a rotation error in between the PMQs. It is recommended to design a better mounting of the quadrupoles. In particular, a method to accurately align the quadrupoles with respect to each other should be implemented, having a precision ≤ 0.01 rad since the rotation error between quadrupoles has less tolerance, as suggested in Ref. [96]. The alignment of the quadrupoles is very important because these additional errors can further degrade the transverse emittance of the beam.

Chapter 6

Conclusions

6.1 Summary

This thesis provided numerical and experimental studies on the possibility of using laser wakefield accelerators as compact sources of high quality electron beams. The electron beam transverse properties were studied in details, particularly the rms emittance which is considered as a figure of merit to define the quality of electron beams.

Basic diagnostics to measure the electron beam divergence and pointing stability were presented in Chapter 3. The shot to shot fluctuations are always less than 10 mrad, while the divergence is between 2 and 4 mrad both in x and y. The measurements show good reproducibility as similar values are obtained for different experimental conditions. Pointing instability is one of the main disadvantages of acceleration in the bubble regime as the properties of the electron beams are strongly dependent on the injection mechanism. Since acceleration relies on self-injection, it is difficult to control, leading to instabilities.

On the other hand, the energy measurements showed that the integrated electron energy spread is greater than 5 %. Although there are a few shots with $\Delta E/E$ less than 5 %, they have charges of less than a pC, which may be too low for many applications, as well as difficult to measure with accuracy due to limitations with the current configuration of the electron spectrometer.

The transverse emittance depends on the transverse forces that the electrons experience during the self-injection process. Since the accelerating force is approximately linear inside the bubble and constant transversely, the geometrical emittance during acceleration is approximately constant. Hence, the growth in emittance is primarily dictated by the transverse forces during self-injection, which were found to scale with the bubble radius. Therefore to have low emittance, small bubble radius is preferred.

To measure the transverse emittance of the ALPHA-X accelerator, the pepper-pot method was employed. A normalised rms emittance in the range of 1 – 2 π mm mrad was measured in two different experimental conditions. The ob-

tained emittance is comparable with what can be produced by conventional linear accelerators. Recent emittance measurements based on different techniques have shown that the transverse emittance of laser driven electrons can be an order of magnitude lower than that measured here. In Chapter 4, the resolution of the pepper-pot technique was analysed showing that this method is unable to measure emittances lower than $1\,\pi$ mm mrad due to practical constraints dictated by the charge, stability and divergence of the electron beams.

In Chapter 5, the pepper-pot technique was combined with a permanent quadrupole (PMQ) triplet to measure the emittance after propagation through the triplet. As the energy spread was large and the PMQs couple the transverse and longitudinal properties of the electron beam, the method described in Chapter 4 cannot be directly used to calculate the rms emittance. However, assuming that the divergence (measured separately) is known, the beamlet size can be indirectly related to the source size and therefore, to the rms emittance. It was shown that with PMQs, the transverse emittance at the source is between 1 – $4\,\pi$ mm mrad when the uncertainties due to energy spread, pointing fluctuations and divergence are subtracted. After the PMQs, the transverse emittance is inferred to be between 5 and $20\,\pi$ mm mrad for beams propagating on-axis and between 6 and $24\,\pi$ mm mrad for beams propagating 1.5 mrad off-axis. These measurements imply that the PMQs increases the transverse emittance and the electron beam quality is degraded during propagation. This is an important result as these focusing devices are necessary in transporting electron beams for most potential applications. The pepper-pot images are also used to simultaneously characterise the electron beam in terms of pointing stability and energy spread.

The possibility of using conventional systems for the transport of laser produced electron beams with the properties measured here is analysed numerically in Chapter 2. In order to deliver a "useful" beam, the transport system must be able to preserve the emittance. It was shown that the possible sources of emittance growth are chromaticity (due to large energy spread), scattering from Al foil and pointing fluctuations. In the case of chromatic growth, the slice emittance has a slow growth compared to its corresponding projected emittance, implying that this source of growth is reversible and thus can be corrected. However, both Al foil and pointing fluctuations induce additional dispersion which cause an almost identical growth both in projected and slice emittances. It was shown that the laser produced beams are divergence dominated and that the beam quality degrades rapidly when the initial divergence is large (i.e. $\sigma_r' > 2\,\text{mrad}$). This is mainly due to the large energy spread produced from the LWFA. The large

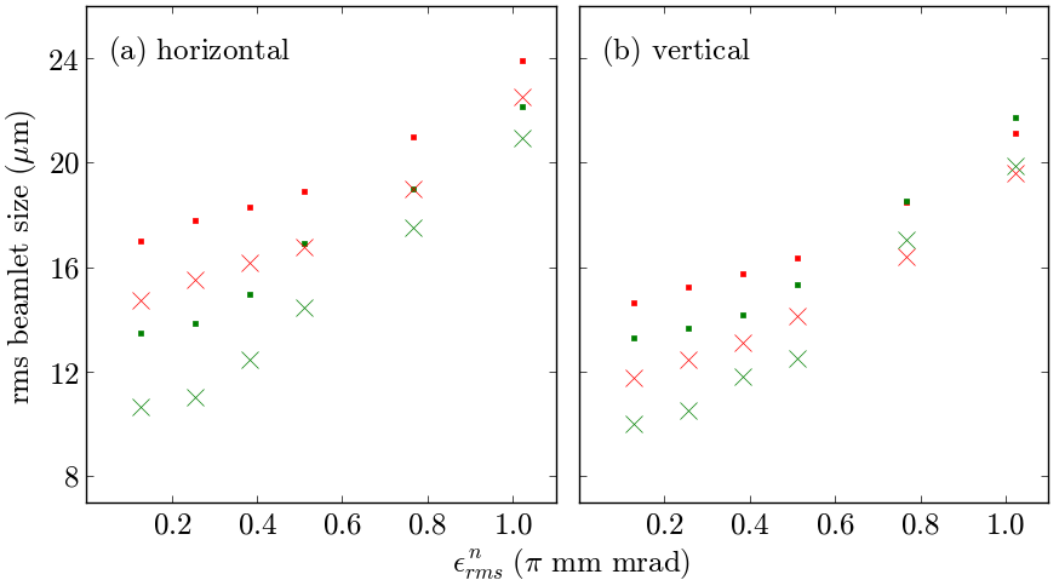

Figure 6.1: RMS beamlet size vs normalised ϵ^n_{rms} for electron beams with 130 MeV $\pm$ 1 % energy and 1 mrad divergence using PMQs and a mask with hole diameter of 8 µm (green symbols) and 16 µm (red symbols) using two different screen resolutions: •: 10 µm, ×: 5 µm.

divergence also causes significant bunch lengthening, although an initial positive linear chirp can lead to bunch compression, provided that the divergence is less than 3 mrad.

6.2 Outlook

Emittance measurement

The combination of pepper-pot mask and PMQs can be used as a a diagnostic tool for high resolution emittance measurements of electron beams with negligible energy spread, low divergence and propagating on-axis. It was shown in Figure 5.6 that emittances less than 1 π mm mrad have more beamlet size variations. For electron beams with energy spread of 1 % and divergence of 1 mrad, the current setup ($L = 70$ cm) can resolve beamlet sizes with (normalised) emittances down to $\sim 0.5\,\pi$ mm mrad, as shown in Figure 6.1. Moreover, the setup magnification can be further improved using a mask with 8 µm hole diameter, without increasing the mask to screen distance. However, the smallest beamlet size reaches the resolution limit of the screen, therefore high resolution YAG:Ce crystal and improved imaging system are required.

Energy measurement

The combination of pepper-pot mask and PMQs is also a potential alternative diagnostic for energy and transverse properties measurements simultaneously. When using PMQs, the magnification becomes energy dependent and differences in energy can be seen in pepper-pot images. An evidence of this is the double beamlet structures found in some recorded pepper-pot images, indicating that the accelerator has produced double bunches. It was shown that with the PMQs configuration used in Chapter 5, an energy difference $\geq 30\,\mathrm{MeV}$ can be resolved. It is also possible to obtain additional information from the shape and orientation of the beamlets. This diagnostics enables to explore the validity of different theories on the injection mechanism in the accelerator, leading to a better understanding of the LWFA process.

However, the potential of this method highly depends on the accuracy of installation and alignment of the PMQs. Currently, the PMQs housing is not ideal as it is prone to misalignment. This is undesirable, since, as shown in Chapter 2, a slight misalignment in PMQs can highly affect the beam trajectories in the EMQs. Moreover, it is necessary to measure the exact magnetic gradient.

Recommendations

Recent results from laser wakefield acceleration have shown that it can produce short energy bunches and small transverse normalised emittance. The biggest challenge now is to go beyond high energy with good repeatability and stability. Moreover, improving the energy spread is also needed specifically for applications where long transport systems are required. These challenges require new techniques such as developing new electron injection (and not relying on self-injection in bubble regime) to have better control of the acceleration.

As shown from the numerical analysis of the ALPHA-X beamline, in-depth optimisation should be done using sophisticated numerical tools such as MAD-X or ELEGANT to obtain proper configurations for the two triplets currently installed.

Bibliography

[1] E. Blum, U. Happek, and A. Sievers, "Observation of coherent synchrotron radiation at the cornell linac," Nuclear Instruments and Methods in Physics Research Section A: Accelerators, Spectrometers, Detectors and Associated Equipment **307**, 568 – 576 (1991).

[2] T. Shintake, H. Tanaka, T. Hara, T. Tanaka, K. Togawa, M. Yabashi, Y. Otake, Y. Asano, T. Bizen, T. Fukui *et al.*, "A compact free-electron laser for generating coherent radiation in the extreme ultraviolet region," Nature Photonics **2**, 555–559 (2008).

[3] P. Emma, R. Akre, J. Arthur, R. Bionta, C. Bostedt, J. Bozek, A. Brachmann, P. Bucksbaum, R. Coffee, F.-J. Decker *et al.*, "First lasing and operation of an ångstrom-wavelength free-electron laser," Nature Photonics **4**, 641–647 (2010).

[4] M. Mitsumori, D. C. Shrieve, E. Alexander, U. B. Kaiser, G. E. Richardson, P. M. Black, and J. S. Loeffler, "Initial clinical results of linac-based stereotactic radiosurgery and stereotactic radiotherapy for pituitary adenomas," International Journal of Radiation Oncology* Biology* Physics **42**, 573–580 (1998).

[5] L. Xiang, B. Han, C. Carpenter, G. Pratx, Y. Kuang, and L. Xing, "X-ray acoustic computed tomography with pulsed x-ray beam from a medical linear accelerator," Medical Physics **40**, 010701 (2013).

[6] T. Tajima and J. M. Dawson, "Laser electron accelerator," Phys. Rev. Lett. **43**, 267–270 (1979).

[7] D. Strickland and G. Mourou, "Compression of amplified chirped optical pulses," Optics Communications **55**, 447 – 449 (1985).

[8] D. Jaroszynski, R. Bingham, E. Brunetti, B. Ersfeld, J. Gallacher, B. van der Geer, R. Issac, S. Jamison, D. Jones, M. de Loos, A. Lyachev, V. Pavlov, A. Reitsma, Y. Saveliev, G. Vieux, and S. Wiggins, "Radiation sources based on laserplasma interactions," Philosophical Transactions of the Royal Society A: Mathematical, Physical and Engineering Sciences **364**, 689–710 (2006).

[9] F. Grüner, S. Becker, U. Schramm, T. Eichner, M. Fuchs, R. Weingartner, D. Habs, J. Meyer-ter Vehn, M. Geissler, M. Ferrario, L. Serafini, B. van der Geer, H. Backe, W. Lauth, and S. Reiche, "Design considerations for table-top, laser-based vuv and x-ray free electron lasers," Applied Physics B **86**, 431–435 (2007).

[10] A. R. Maier, A. Meseck, S. Reiche, C. B. Schroeder, T. Seggebrock, and F. Grüner, "Demonstration scheme for a laser-plasma-driven free-electron laser," Phys. Rev. X **2**, 031019 (2012).

[11] K. Nakajima, T. Kawakubo, H. Nakanishi, A. Ogata, Y. Kitagawa, R. Kodama, K. Mima, H. Shiraga, K. Suzuki, K. Yamakawa, T. Zhang, Y. Kato, D. Fisher, M. Downer, T. Tajima, Y. Sakawa, T. Shoji, N. Yugami, and Y. Nishida, "Proof-of-principle experiments of laser wakefield acceleration using a 1 ps 10 tw nd:glass laser," AIP Conference Proceedings **335**, 145–155 (1995).

[12] A. Modena, Z. Najmudin, A. Dangor, C. Clayton, K. Marsh, C. Joshi, V. Malka, C. Darrow, C. Danson, D. Neely *et al.*, "Electron acceleration from the breaking of relativistic plasma waves," Nature **377**, 606–608 (1995).

[13] V. Malka, S. Fritzler, E. Lefebvre, M.-M. Aleonard, F. Burgy, J.-P. Chambaret, J.-F. Chemin, K. Krushelnick, G. Malka, S. P. D. Mangles, Z. Najmudin, M. Pittman, J.-P. Rousseau, J.-N. Scheurer, B. Walton, and A. E. Dangor, "Electron acceleration by a wake field forced by an intense ultrashort laser pulse," Science **298**, 1596–1600 (2002).

[14] S. P. D. Mangles, C. D. Murphy, Z. Najmudin, A. G. R. Thomas, J. L. Collier, A. E. Dangor, E. J. Divall, P. S. Foster, J. G. Gallacher, C. J. Hooker, D. A. Jaroszynski, A. J. Langley, W. B. Mori, P. A. Norreys, F. S. Tsung, R. Viskup, B. R. Walton, and K. Krushelnick, "Monoenergetic beams of relativistic electrons from intense laser-plasma interactions," Nature **431**, 535–538 (2004).

[15] C. G. R. Geddes, C. Toth, J. van Tilborg, E. Esarey, C. B. Schroeder, D. Bruhwiler, C. Nieter, J. Cary, and W. P. Leemans, "High-quality electron beams from a laser wakefield accelerator using plasma-channel guiding," Nature **431**, 538–541 (2004).

[16] J. Faure, Y. Glinec, A. Pukhov, S. Kiselev, S. Gordienko, E. Lefebvre, J. Rousseau, F. Burgy, and V. Malka, "A laser-plasma accelerator producing monoenergetic electron beams," Nature **431**, 541–544 (2004).

[17] S. Karsch, J. Osterhoff, A. Popp, T. P. Rowlands-Rees, Z. Major, M. Fuchs, B. Marx, R. Hrlein, K. Schmid, L. Veisz, S. Becker, U. Schramm, B. Hidding, G. Pretzler, D. Habs, F. Grner, F. Krausz, and S. M. Hooker, "GeV-scale electron acceleration in a gas-filled capillary discharge waveguide," New Journal of Physics **9**, 415 (2007).

[18] J. Osterhoff, A. Popp, Z. Major, B. Marx, T. P. Rowlands-Rees, M. Fuchs, M. Geissler, R. Hörlein, B. Hidding, S. Becker, E. A. Peralta, U. Schramm, F. Grüner, D. Habs, F. Krausz, S. M. Hooker, and S. Karsch, "Generation of stable, low-divergence electron beams by laser-wakefield acceleration in a steady-state-flow gas cell," Phys. Rev. Lett. **101**, 085002 (2008).

[19] C. E. Clayton, J. E. Ralph, F. Albert, R. A. Fonseca, S. H. Glenzer, C. Joshi, W. Lu, K. A. Marsh, S. F. Martins, W. B. Mori, A. Pak, F. S. Tsung, B. B. Pollock, J. S. Ross, L. O. Silva, and D. H. Froula, "Self-guided laser wakefield acceleration beyond 1 GeV using ionization-induced injection," Phys. Rev. Lett. **105**, 105003 (2010).

[20] B. B. Pollock, C. E. Clayton, J. E. Ralph, F. Albert, A. Davidson, L. Divol, C. Filip, S. H. Glenzer, K. Herpoldt, W. Lu, K. A. Marsh, J. Meinecke, W. B. Mori, A. Pak, T. C. Rensink, J. S. Ross, J. Shaw, G. R. Tynan, C. Joshi, and D. H. Froula, "Demonstration of a narrow energy spread, 0.5 GeV electron beam from a two-stage laser wakefield accelerator," Phys. Rev. Lett. **107**, 045001 (2011).

[21] A. Reitsma, R. Trines, and V. Goloviznin, "Energy spread in plasma-based acceleration," Plasma Science, IEEE Transactions on **28**, 1150–1154 (2000).

[22] T. Mehrling, J. Grebenyuk, F. S. Tsung, K. Floettmann, and J. Osterhoff, "Transverse emittance growth in staged laser-wakefield acceleration," Phys. Rev. ST Accel. Beams **15**, 111303 (2012).

[23] E. Brunetti, R. P. Shanks, G. G. Manahan, M. R. Islam, B. Ersfeld, M. P. Anania, S. Cipiccia, R. C. Issac, G. Raj, G. Vieux, G. H. Welsh, S. M. Wiggins, and D. A. Jaroszynski, "Low emittance, high brilliance relativistic electron beams from a laser-plasma accelerator," Phys. Rev. Lett. **105**, 215007 (2010).

[24] C. M. S. Sears, A. Buck, K. Schmid, J. Mikhailova, F. Krausz, and L. Veisz, "Emittance and divergence of laser wakefield accelerated electrons," Phys. Rev. ST Accel. Beams **13**, 092803 (2010).

[25] S. Fritzler, E. Lefebvre, V. Malka, F. Burgy, A. E. Dangor, K. Krushelnick, S. P. D. Mangles, Z. Najmudin, J.-P. Rousseau, and B. Walton, "Emittance measurements of a laser-wakefield-accelerated electron beam," Phys. Rev. Lett. **92**, 165006 (2004).

[26] S. Kneip, C. McGuffey, J. L. Martins, M. S. Bloom, V. Chvykov, F. Dollar, R. Fonseca, S. Jolly, G. Kalintchenko, K. Krushelnick, A. Maksimchuk, S. P. D. Mangles, Z. Najmudin, C. A. J. Palmer, K. T. Phuoc, W. Schumaker, L. O. Silva, J. Vieira, V. Yanovsky, and A. G. R. Thomas, "Characterization of transverse beam emittance of electrons from a laser-plasma wakefield accelerator in the bubble regime using betatron x-ray radiation," Phys. Rev. ST Accel. Beams **15**, 021302 (2012).

[27] G. R. Plateau, C. G. R. Geddes, D. B. Thorn, M. Chen, C. Benedetti, E. Esarey, A. J. Gonsalves, N. H. Matlis, K. Nakamura, C. B. Schroeder, S. Shiraishi, T. Sokollik, J. van Tilborg, C. Toth, S. Trotsenko, T. S. Kim, M. Battaglia, T. Stöhlker, and W. P. Leemans, "Low-emittance electron bunches from a laser-plasma accelerator measured using single-shot x-ray spectroscopy," Phys. Rev. Lett. **109**, 064802 (2012).

[28] R. Weingartner, S. Raith, A. Popp, S. Chou, J. Wenz, K. Khrennikov, M. Heigoldt, A. R. Maier, N. Kajumba, M. Fuchs, B. Zeitler, F. Krausz, S. Karsch, and F. Grüner, "Ultralow emittance electron beams from a laser-wakefield accelerator," Phys. Rev. ST Accel. Beams **15**, 111302 (2012).

[29] T. Boyd and J. Sanderson, *The Physics of Plasmas* (Cambridge University Press, 2003).

[30] E. Esarey, C. B. Schroeder, and W. P. Leemans, "Physics of laser-driven plasma-based electron accelerators," Rev. Mod. Phys. **81**, 1229–1285 (2009).

[31] P. Sprangle, E. Esarey, J. Krall, and G. Joyce, "Propagation and guiding of intense laser pulses in plasmas," Phys. Rev. Lett. **69**, 2200–2203 (1992).

[32] C. D. Decker and W. B. Mori, "Group velocity of large amplitude electromagnetic waves in a plasma," Phys. Rev. Lett. **72**, 490–493 (1994).

[33] D. Jaroszynski, R. Bingham, and R. Cairns, *Laser-Plasma Interactions*, Scottish Graduate Series (Taylor & Francis, 2010).

[34] P. Sprangle, E. Esarey, A. Ting, and G. Joyce, "Laser wakefield acceleration and relativistic optical guiding," Applied Physics Letters **53**, 2146–2148 (1988).

[35] J. M. Dawson, "Nonlinear electron oscillations in a cold plasma," Phys. Rev. **113**, 383–387 (1959).

[36] P. Sprangle, E. Esarey, and A. Ting, "Nonlinear theory of intense laser-plasma interactions," Phys. Rev. Lett. **64**, 2011–2014 (1990).

[37] P. Sprangle, E. Esarey, and A. Ting, "Nonlinear interaction of intense laser pulses in plasmas," Phys. Rev. A **41**, 4463–4469 (1990).

[38] E. Esarey and M. Pilloff, "Trapping and acceleration in nonlinear plasma waves," Physics of Plasmas **2**, 1432–1436 (1995).

[39] W. Lu, M. Tzoufras, C. Joshi, F. S. Tsung, W. B. Mori, J. Vieira, R. A. Fonseca, and L. O. Silva, "Generating multi-GeV electron bunches using single stage laser wakefield acceleration in a 3D nonlinear regime," Phys. Rev. ST Accel. Beams **10**, 061301 (2007).

[40] R. A. Fonseca, L. Silva, F. Tsung, V. K. Decyk, W. Lu, C. Ren, W. Mori, S. Deng, S. Lee, T. Katsouleas *et al.*, "Osiris: a three-dimensional, fully relativistic particle in cell code for modeling plasma based accelerators," in "Computational ScienceICCS 2002," (Springer, 2002), pp. 342–351.

[41] P. Mora and T. M. Antonsen, "Electron cavitation and acceleration in the wake of an ultraintense, self-focused laser pulse," Phys. Rev. E **53**, R2068–R2071 (1996).

[42] A. Pukhov and J. Meyer-ter Vehn, "Laser wake field acceleration: the highly non-linear broken-wave regime," Applied Physics B **74**, 355–361 (2002).

[43] I. Kostyukov, E. Nerush, A. Pukhov, and V. Seredov, "Electron self-injection in multidimensional relativistic-plasma wake fields," Phys. Rev. Lett. **103**, 175003 (2009).

[44] S. Kalmykov, S. Yi, V. Khudik, and G. Shvets, "Electron self-injection and trapping into an evolving plasma bubble," Phys. Rev. Lett. **103**, 135004 (2009).

[45] A. Pukhov and S. Gordienko, "Bubble regime of wake field acceleration: similarity theory and optimal scalings," Phil. Trans. R. Soc. A **364**, 623 – 633 (2006).

[46] E. Esarey, B. Shadwick, C. Schroeder, and W. Leemans, "Nonlinear pump depletion and electron dephasing in laser wakefield accelerators," in "AIP Conference Proceedings," , vol. 737 (2004), vol. 737, p. 578.

[47] B. A. Shadwick, C. B. Schroeder, and E. Esarey, "Nonlinear laser energy depletion in laser-plasma accelerators," Physics of Plasmas **16**, 056704 (2009).

[48] S. Wilks, T. Katsouleas, J. M. Dawson, P. Chen, and J. J. Su, "Beam loading in plasma waves," Plasma Science, IEEE Transactions on **15**, 210 –217 (1987).

[49] C. B. Schroeder, C. Benedetti, E. Esarey, and W. P. Leemans, "Nonlinear pulse propagation and phase velocity of laser-driven plasma waves," Phys. Rev. Lett. **106**, 135002 (2011).

[50] C. D. Decker, W. B. Mori, K.-C. Tzeng, and T. Katsouleas, "The evolution of ultra-intense, short-pulse lasers in underdense plasmas," Physics of Plasmas **3**, 2047–2056 (1996).

[51] W. Lu, "Nonlinear plasma wakefield theory and optimum scaling for laser wakefield acceleartion in the blowout regime," Ph.D. thesis, University of California- Los Angeles (2006).

[52] S. Cipiccia, M. R. Islam, B. Ersfeld, R. P. Shanks, E. Brunetti, G. Vieux, X. Yang, R. C. Issac, S. M. Wiggins, G. H. Welsh *et al.*, "Gamma-rays from harmonically resonant betatron oscillations in a plasma wake," Nature Physics (2011).

[53] R. Lehe, A. Lifschitz, C. Thaury, V. Malka, and X. Davoine, "Numerical growth of emittance in simulations of laser-wakefield acceleration," Phys. Rev. ST Accel. Beams **16**, 021301 (2013).

[54] H.-P. Schlenvoigt, K. Haupt, A. Debus, F. Budde, O. Jäckel, S. Pfotenhauer, H. Schwoerer, E. Rohwer, J. Gallacher, E. Brunetti *et al.*, "A compact synchrotron radiation source driven by a laser-plasma wakefield accelerator," Nature Physics **4**, 130–133 (2007).

[55] S. Abuazoum, S. M. Wiggins, B. Ersfeld, K. Hart, G. Vieux, X. Yang, G. H. Welsh, R. C. Issac, M. P. Reijnders, D. R. Jones, and D. A. Jaroszynski, "Linearly tapered discharge capillary waveguides as a medium for a laser plasma wakefield accelerator," Applied Physics Letters **100**, 014106 (2012).

[56] C. G. R. Geddes, K. Nakamura, G. R. Plateau, C. Toth, E. Cormier-Michel, E. Esarey, C. B. Schroeder, J. R. Cary, and W. P. Leemans, "Plasma-density-gradient injection of low absolute-momentum-spread electron bunches," Phys. Rev. Lett. **100**, 215004 (2008).

[57] A. Gonsalves, K. Nakamura, C. Lin, D. Panasenko, S. Shiraishi, T. Sokollik, C. Benedetti, C. Schroeder, C. Geddes, J. Van Tilborg *et al.*, "Tunable laser plasma accelerator based on longitudinal density tailoring," Nature Physics **7**, 862–866 (2011).

[58] G. Welsh, S. Wiggins, R. Issac, E. Brunetti, G. Manahan, M. Islam, S. Cipiccia, C. Aniculaesei, B. Ersfeld, and D. Jaroszynski, "High resolution electron beam measurements on the alpha-x laser–plasma wakefield accelerator," Journal of Plasma Physics **78**, 393–399 (2012).

[59] S. M. Wiggins, M. P. Anania, E. Brunetti, S. Cipiccia, B. Ersfeld, M. R. Islam, R. C. Issac, G. Raj, R. P. Shanks, G. Vieux, G. H. Welsh, W. A. Gillespie, A. M. MacLeod, and D. A. Jaroszynski, "Narrow spread electron beams from a laser-plasma wakefield accelerator," pp. 735914–735914–10 (2009).

[60] S. M. Wiggins, R. C. Issac, G. H. Welsh, E. Brunetti, R. P. Shanks, M. P. Anania, S. Cipiccia, G. G. Manahan, C. Aniculaesei, B. Ersfeld, M. R. Islam, R. T. L. Burgess, G. Vieux, W. A. Gillespie, A. M. MacLeod, S. B. van der Geer, M. J. de Loos, and D. A. Jaroszynski, "High quality electron beams from a laser wakefield accelerator," Plasma Physics and Controlled Fusion **52**, 124032 (2010).

[61] H. Wiedemann, *Particle Accelerator Physics* (Springer, 2007).

[62] M. Reiser, *Theory and Design of Charged Particle Beams* (Wiley-VCH Verlag GmbH, 2007).

[63] S. Humphries, *Charged Particle Beams*, A Wiley-Interscience publication (Wiley, 1990).

[64] J. Buon, "Beam phase space and emittance," CERN European organization for nuclear research-reports-CERN pp. 89–115 (1994).

[65] J. Allison, K. Amako, J. Apostolakis, H. Araujo, P. Dubois, M. Asai, G. Barrand, R. Capra, S. Chauvie, R. Chytracek, G. Cirrone, G. Cooperman, G. Cosmo, G. Cuttone, G. Daquino, M. Donszelmann, M. Dressel, G. Folger, F. Foppiano, J. Generowicz, V. Grichine, S. Guatelli, P. Gumplinger, A. Heikkinen, I. Hrivnacova, A. Howard, S. Incerti, V. Ivanchenko, T. Johnson, F. Jones, T. Koi, R. Kokoulin, M. Kossov, H. Kurashige, V. Lara, S. Larsson, F. Lei, O. Link, F. Longo, M. Maire, A. Mantero, B. Mascialino, I. McLaren, P. Lorenzo, K. Minamimoto, K. Murakami, P. Nieminen, L. Pandola, S. Parlati, L. Peralta, J. Perl, A. Pfeiffer, M. Pia, A. Ribon, P. Rodrigues, G. Russo, S. Sadilov, G. Santin, T. Sasaki, D. Smith, N. Starkov, S. Tanaka, E. Tcherniaev, B. Tome, A. Trindade, P. Truscott, L. Urban, M. Verderi, A. Walkden, J. Wellisch, D. Williams, D. Wright, and H. Yoshida, "GEANT4 developments and applications," Nuclear Science, IEEE Transactions on **53**, 270 –278 (2006).

[66] P. M. Lapostolle, "Possible emittance increase through filamentation due to space charge in continuous beams," Nuclear Science, IEEE Transactions on **18**, 1101 –1104 (1971).

[67] F. J. Sacherer, "RMS envelope equations with space charge," Nuclear Science, IEEE Transactions on **18**, 1105 –1107 (1971).

[68] http://mad.web.cern.ch.

[69] X. Wang, H. Kirk, C. Pellegrini, K. McDonald, and D. Russell, "The brookhaven accelerator test facility injection system," in "Particle Accelerator Conference, 1989. Accelerator Science and Technology., Proceedings of the 1989 IEEE," (1989), pp. 307 –309 vol.1.

[70] P. Antici, A. Bacci, C. Benedetti, E. Chiadroni, M. Ferrario, A. R. Rossi, L. Lancia, M. Migliorati, A. Mostacci, L. Palumbo, and L. Serafini, "Laser-driven electron beamlines generated by coupling laser-plasma sources with conventional transport systems," Journal of Applied Physics **112**, 044902–044902–9 (2012).

[71] V. L. Highland, "Some practical remarks on multiple scattering," Nuclear Instruments and Methods **129**, 497 – 499 (1975).

[72] M. B. Reid, "Electron beam emittance growth in thin foils: A betatron function analysis," Journal of Applied Physics **70**, 7185 –7187 (1991).

[73] C. Lin, J. van Tilborg, K. Nakamura, A. J. Gonsalves, N. H. Matlis, T. Sokollik, S. Shiraishi, J. Osterhoff, C. Benedetti, C. B. Schroeder, C. Tóth, E. Esarey, and W. P. Leemans, "Long-range persistence of femtosecond modulations on laser-plasma-accelerated electron beams," Phys. Rev. Lett. **108**, 094801 (2012).

[74] C. Schroeder, "Free-electron laser driven by the LBNL laser-plasma accelerator," in "13th Advanced Accelerator Concepts Workshops(AAC08)," (2010).

[75] W. K. Panofsky and J. McIntyre, "Achromatic beam translation systems for use with the linear accelerator," Review of Scientific Instruments **25**, 287–290 (1954).

[76] B. E. Carlsten and S. J. Russell, "Subpicosecond compression of 0.1-1 nc electron bunches with a magnetic chicane at 8 mev," Phys. Rev. E **53**, R2072–R2075 (1996).

[77] S. M. Wiggins, M. P. Reijnders, S. Abuazoum, K. Hart, G. H. Welsh, R. C. Issac, D. R. Jones, and D. A. Jaroszynski, "Note: Femtosecond laser micromachining of straight and linearly tapered capillary discharge waveguides," Review of Scientific Instruments **82**, 096104 (2011).

[78] S. Abuazoum, "Experimental study of laser driven electron and proton acceleration." Ph.D. thesis, University of Strathclyde (2012).

[79] V. Malka, J. Faure, and Y. A. Gauduel, "Ultra-short electron beams based spatio-temporal radiation biology and radiotherapy," Mutation Research/Reviews in Mutation Research **704**, 142 – 151 (2010).

[80] Y. A. Gauduel, "Laser-plasma accelerator based femtosecond high-energy radiation chemistry and biology," Journal of Physics: Conference Series **373**, 012012 (2012).

[81] A. Gamucci, N. Bourgeois, T. Ceccotti, S. Dobosz, P. D'Oliveira, M. Galimberti, J. Galy, A. Giulietti, D. Giulietti, L. A. Gizzi, D. J. Hamilton, L. Labate, J.-R. Marques, P. Monot, H. Popescu, F. Reau, G. Sarri, P. Tomassini, and P. Martin, "Advanced diagnostics applied to a laser-driven electron-acceleration experiment," Plasma Science, IEEE Transactions on **36**, 1699 –1706 (2008).

[82] S. P. D. Mangles, A. G. R. Thomas, O. Lundh, F. Lindau, M. C. Kaluza, A. Persson, C.-G. Wahlstrom, K. Krushelnick, and Z. Najmudin, "On the stability of laser wakefield electron accelerators in the monoenergetic regime," Physics of Plasmas **14**, 056702 (2007).

[83] X. Qiu, K. Batchelor, I. Ben-Zvi, and X.-J. Wang, "Demonstration of emittance compensation through the measurement of the slice emittance of a 10-ps electron bunch," Phys. Rev. Lett. **76**, 3723–3726 (1996).

[84] B. E. Carlsten, "Characterizing the emittance contribution due to rotated quadrupoles and canonical angular momentum using the quadrupole scan technique in electron accelerators," Review of Scientific Instruments **70**, 1672–1683 (1999).

[85] J. G. Power and M. E. Conde, "A 3.9 MeV photoinjector and delay system for wakefield measurements," Review of Scientific Instruments **69**, 1295–1297 (1998).

[86] F. Löhl, S. Schreiber, M. Castellano, G. Di Pirro, L. Catani, A. Cianchi, and K. Honkavaara, "Measurements of the transverse emittance at the FLASH injector at DESY," Phys. Rev. ST Accel. Beams **9**, 092802 (2006).

[87] N. Delerue, R. Bartolini, G. Doucas, P. Lau, K. Peach, A. Reichold, R. Senanayake, D. Urner, P. A. Walker, S. Bajlekov, N. Bourgeois, L. Caballero-Bendixsen, T. Ibbotson, S. Hooker, C. Thomas, G. Mazzitelli, and B. Buonomo, "Single-shot emittance measurement of a 508 MeV electron beam using the pepper-pot method," in "Particle Accelerator Conference, 2009. Proceedings of the 2009," (2009), pp. 3597–3599.

[88] Y. Yamazaki, T. Kurihara, H. Kobayashi, I. Sato, and A. Asami, "High-precision pepper-pot technique for a low-emittance electron beam," Nuclear Instruments and Methods in Physics Research Section A: Accelerators, Spectrometers, Detectors and Associated Equipment **322**, 139 – 145 (1992).

[89] S. G. Anderson, J. B. Rosenzweig, G. P. LeSage, and J. K. Crane, "Space-charge effects in high brightness electron beam emittance measurement," Phys. Rev. ST Accel. Beams **5**, 014201 (2002).

[90] M. Zhang, "Emittance formula for slits and pepper-pot measurement," 105 FNAL-TM–1988, Fermi National Accelerator Lab., Batavia, IL (United States) (1996).

[91] A. Lumpkin, A. Johnson, J. Ruan, J. Santucci, Y. Sun, and R. Thurman-Keup, "Spatial resolution limits of YAG:Ce powder beam profile monitors at the fermilab A0 photoinjector," Proceedings of FEL09, Liverpool p. 348 (2009).

[92] A. Murokh, J. Rosenzweig, I. Ben-Zvi, X. Wang, and V. Yakimenko, "Limitations on the resolution of YAG:Ce beam profile monitor for high brightness electron beam," in "Proceedings of the 19th Particle Accelerator Conference, Chicago, Illinois, 2001," (IEEE, 2001).

[93] J.-P. Carneiro, R. Carrigan, M. Champion, P. Colestock, H. Edwards, J. Fuerst, W. Hartung, K. Koepke, M. Kuchnir, J. Santucci, L. Spentzouris, M. Fitch, A. Melissinos, P. Michelato, C. Pagani, D. Sertore, N. Barov, and J. Rosenzweig, "First results of the fermilab high-brightness RF photoinjector," in "Particle Accelerator Conference, 1999. Proceedings of the 1999," , vol. 3 (1999), vol. 3, pp. 2027 –2029 vol.3.

[94] R. Shanks, "Comprehensive characterisation of laser plasma wakefield accelerated electrons," Ph.D. thesis, University of Strathclyde (2012).

[95] C. McGuffey, A. G. R. Thomas, W. Schumaker, T. Matsuoka, V. Chvykov, F. J. Dollar, G. Kalintchenko, V. Yanovsky, A. Maksimchuk, K. Krushelnick, V. Y. Bychenkov, I. V. Glazyrin, and A. V. Karpeev, "Ionization induced trapping in a laser wakefield accelerator," Phys. Rev. Lett. **104**, 025004 (2010).

[96] J. K. Lim, P. Frigola, G. Travish, J. B. Rosenzweig, S. G. Anderson, W. J. Brown, J. S. Jacob, C. L. Robbins, and A. M. Tremaine, "Adjustable, short focal length permanent-magnet quadrupole based electron beam final focus system," Phys. Rev. ST Accel. Beams **8**, 072401 (2005).

[97] S. Becker, M. Bussmann, S. Raith, M. Fuchs, R. Weingartner, P. Kunz, W. Lauth, U. Schramm, M. El Ghazaly, F. Grüner, H. Backe, and D. Habs, "Characterization and tuning of ultrahigh gradient permanent magnet quadrupoles," Phys. Rev. ST Accel. Beams **12**, 102801 (2009).

[98] R. Weingartner, M. Fuchs, A. Popp, S. Raith, S. Becker, S. Chou, M. Heigoldt, K. Khrennikov, J. Wenz, T. Seggebrock, B. Zeitler, Z. Major, J. Osterhoff, F. Krausz, S. Karsch, and F. Grüner, "Imaging laser-wakefield-accelerated electrons using miniature magnetic quadrupole lenses," Phys. Rev. ST Accel. Beams **14**, 052801 (2011).